Dynamic ANO1 Nanodomain Signalling Complexes in Nociceptive Neurons of the Dorsal Root and Trigeminal Ganglia

Char Palfrey

Submitted in accordance with the requirements for the degree of
Doctor of Philosophy

University of Leeds
School of Biomedical Sciences

September 2024

Acknowledgements

First and foremost, my most sincere gratitude and thanks go out to my supervisor, Professor Nikita Gamper, who believed in me from the very beginning and from whom I've gained so much knowledge and inspiration over the last five years that I've had the opportunity to be a member of his research group.

Thank you to Brain Research UK for the generous funding that allowed me to undertake this PhD and benefit from so many invaluable scientific experiences.

My research journey wouldn't have been what it was without all the wonderful members of Nikita's group, both past and present, who made every day in the lab something I looked forward to. An extra big thanks to the Philadelphia Dream Team – to Shab for teaching me everything he knows about ANO1, calcium imaging and PLA (and for occasionally buying me coffee), and to Vincenzo for always taking the time to discuss our ideas and for keeping me company working too late on the weekends. Thanks to Steve for always trying his best to keep us all in line and keep the lab up and running, and, of course, to V for being such a good friend in so many ways, but especially for always being ready to listen if I needed to complain when things went wrong.

I spent an awful lot of time in the Bioimaging Facility so also a big thank you to Ruth for teaching me the wonderful ways of the confocal and STED microscopes and for always helping with imaging advice.

Of course, all the love and appreciation in the world to Moum and Dad and Saz for their endless support (financially or otherwise!) and for always being proud of me. Couldn't have done it without you all.

Finally, a giant special thank you to my best friend and partner, Lucien, for all your love, patience and understanding and for always taking care of me, and to my sweet Potato for all the at-times-much-needed pet therapy. Love you both.

Abstract

In small-diameter nociceptive neurons of dorsal root ganglion (DRG) the Ca^{2+}-activated Cl^- channel anoctamin 1 (ANO1) confers a novel amplification mechanism of nociception via preferential coupling of ANO1 at the plasma membrane (PM) with IP_3-sensitive Ca^{2+} release channels (IP_3R1) present in the endoplasmic reticulum (ER). Close apposition of the ER and PM is crucial to maintain the proximity required between ANO1 and IP_3R1 such that these proteins directly interact in a junctional multiprotein signalling complex (JMSC). To date, experimental work towards uncovering the molecular mechanisms governing ANO1 signalling in nociceptive neurons has been limited to the DRG, however, as the cranial somatosensory analogue, it is of significant interest to investigate whether such mechanisms are conserved in the trigeminal ganglion (TG). Furthermore, molecular mechanisms modulating the functional organisation of ANO1 nanodomains are yet to be uncovered but may present novel therapeutic targets for the management of acute and chronic pain conditions.

This thesis presents novel experimental evidence demonstrating that the formation of ANO1 signalling nanodomains is under dynamic and stimulus-specific, activity-dependent control and that functional coupling between ANO1, IP_3R1 and the noxious heat and capsaicin receptor transient receptor potential vanilloid type 1 (TRPV1) is conserved between nociceptive neurons of the DRG and TG. Furthermore, this work characterises expression of a putative ER-PM junctional tether, extended synaptotagmin 1 (Esyt1), in the DRG and presents evidence in support of a functional interaction between Esyt1 and ANO1. While further experimental work is undoubtedly required to fully elucidate its functionality at nociceptive ER-PM contact sites, the evidence herein establishes Esyt1 as an intriguing addition to the nociceptive ANO1 signalling interactome in the DRG.

Table of Contents

List of Figures

List of Tables

Abbreviations

ADGRD1 - Adhesion G-protein-coupled receptor D1
AMPA - α-amino-3-hydroxy-5-methyl-4-isoxazolepropionic acid
ANO1 – Anoctamin 1
ATP – Adenosine triphosphate
B2R – Bradykinin receptor type 2
BAPTA - 1,2-bis(2-aminophenoxy)ethane-N,N,N',N'-tetra-acetic acid
BCA - Bicinchoninic Acid
BEC - Biliary epithelial cell
BK – Bradykinin
BSA – Bovine serum albumin
Ca^{2+} - Calcium cation
$[Ca^{2+}]_i$ – Intracellular calcium concentration
CaCC – Calcium-activated chloride channel
$CaCl_2$ – Calcium chloride
cAMP – cyclic adenosine monophosphate
CAP – Capsaicin
cDNA – Complementary DNA
CGRP – Calcitonin gene-related peptide
Cl^- - Chloride anion
$[Cl^-]_i$ – Intracellular chloride concentration
CLC – Chloride channel
CO_2 – Carbon dioxide
CRLR – Calcitonin receptor-like receptor
CNS -Central nervous system
CRAC – Calcium release-activated calcium channel
CRISPR - Clustered regularly interspaced short palindromic repeats
DAG – Diacylglycerol
DAPI - 4′,6-diamidino-2-phenylindole
DHPR - Dihydropyridine receptor
DIDS - 4,4′ Di-isothiocyanatostilbene-2,2′ -disulfonic acid
DMEM – Dulbecco's Modified Eagle's Medium
DNA – Deoxyribonucleic acid
DRG – Dorsal root ganglion
EC – Extracellular solution
E_{Cl} – Chloride equilibrium potential
EDTA - Ethylenediaminetetraacetic acid
ELISA – Enzyme-linked immunosorbent assay
EM – Electron microscopy
EPSC - Excitatory post-synaptic current
ER - Endoplasmic reticulum

Esyt1 – Extended synaptotagmin 1
EYFP – Enhanced yellow fluorescent protein
FBS – Foetal bovine serum
FRET - Fluorescent resonance energy transfer
Fura-2 AM - Fura-2-acetoxymethyl ester
FWHM - Full width at half maximum
GAPDH - Glyceraldehyde 3-phosphate dehydrogenase
GFP – Green fluorescent protein
GPCR – G protein-coupled receptor
GST - Glutathione-S-transferase
HBSS – Hank's Balanced Salt Solution
HCl – Hydrochloric acid
HEK293 – Human embryonic kidney 293
HEPES - 2-(4-(2-hydroxyethyl)piperazin-1-yl)ethanesulfonic acid
HRP – Horse radish peroxidase
IB4 – isolectin B4
ID – Integrated density
IP_3 - Inositol triphosphate
IP_3R1 – Inositol triphosphate receptor type 1
JMSC – Junctional multiprotein signalling complex
JPH – Junctophilin
K^+ - Potassium cation
KCl – Potassium chloride
LSM – Laser scanning microscope
mANO1 – Murine ANO1
MCS – Membrane contact site
$MgCl_2$ – Magnesium chloride
mRNA – Messenger RNA
mTRPV1 – Murine TRPV1
NA – Numerical aperture
NaCl – Sodium chloride
NaI – Sodium iodide
NF200 – Neurofilament 200 kDa
NFA – Niflumic acid
NGF – Nerve growth factor
NKCC1 – Sodium-potassium-chloride co-transporter
NND – Nearest neighbour distance
PAGE – Polyacrylamide gel electrophoresis
PAR-2 - protease-activated receptor 2
PB – Phosphate buffer
PBS – Phosphate buffered saline
PCC – Pearson's correlation coefficient

PDL - Poly-D-lysine
PFA - Paraformaldehyde
PIP2 – Phosphatidylinositol 4,5-bisphosphate
PKA – Protein kinase A
PKC – Protein kinase C
PLA – Proximity ligation assay
PLC – Phospholipase C
PLS – Phospholipid scramblase
PM – Plasma membrane
PMSF - Phenylmethylsulonyl fluoride
PNS – Peripheral nervous system
PPI - Protein-protein interaction
PSF - point spread function
PVDF - Polyvinylidene difluoride
QC – Quality control
RAMP1 – Receptor activity modifying peptide 1
RCA - Rolling circle amplification
RCP - Rolling circle product
RI – Refractive index
RIPA - Radioimmunoprecipitation assay
RNA – Ribonucleic acid
RNA-Seq – RNA sequencing
ROI – Region of interest
RyR – Ryanodine receptor
SD – Standard deviation
SDS – Sodium dodecyl sulfate
SEM – Standard error of the mean
SERCA – Sarco/endoplasmic reticulum calcium ATPase
SG – Substantia gelatinosa
SGC – Satellite glial cell
siRNA – Small interfering RNA
SMP - Synaptotagmin-like mitochondrial-lipid binding protein
SNAP - N-ethylmaleimide-sensitive factor attachment protein
SNARE – SNAP receptor
SOCE – Store-operated calcium entry
SR – Sarcoplasmic reticulum
STED – Stimulated emission depletion
STIM1 – Stromal interaction molecule 1
STORM - Super-resolution stochastic optical reconstruction microscopy
SP – Substance P
TG – Trigeminal ganglion

TIRF - Total internal reflection fluorescence

TNC - Trigeminal nucleus caudalis

TRAP-Seq – Translating ribosome affinity purification RNA sequencing

TRPC3 – Transient receptor potential canonical receptor type 3

TRPV1 – Transient receptor potential vanilloid receptor type 1

UAA - Unnatural amino acid

VGCC – Voltage-gated calcium channel

VGNC – Voltage-gated sodium channel

Y2H – Yeast two-hybrid

Chapter 1: Introduction

1.1 Overview of Nociception

1.1.1 Nociception and Pain

The ability to detect and respond to harmful stimuli (extreme temperature, corrosive chemicals or mechanical forces) is arguably one of life's most important survival mechanisms. Nociception refers to the biological processes by which stimuli that may cause actual or perceived tissue damage (noxious stimuli) are detected and transduced to electrochemical signals relayed from the peripheral nervous system (PNS) to the central nervous system (CNS), where they are typically perceived as pain. The International Association for the Study of Pain defines pain as 'an unpleasant sensory and emotional experience associated with actual or potential tissue damage' (Merskey, 1994). Therefore, while nociception refers primarily to the neural encoding of noxious stimuli, pain is considered a complex and subjective experience combining both sensory and cognitive components to react and respond with an appropriate behavioural adaptation.

1.1.2 Nociceptors are Specialised Sensory Neurons

Nociceptors are highly specialised somatosensory neurons responsible for detecting and transducing noxious stimuli in the peripheral nervous system. They can be classified into four sub-groups according to the region of the body that they innervate: muscle nociceptors, joint nociceptors, visceral (inner organs) nociceptors and cutaneous nociceptors, that innervate the skin (Raja et al., 1988). Cutaneous nociceptors are canonically classified as A- or C-fibre neurons according to their conduction velocity, axonal myelination, and the modality of the signal they transmit (Dubin and Patapoutian, 2010a, Gasser and Erlanger, 1929). Conduction velocity is closely linked to both the diameter of their axons and their degree of myelination (Djouhri et al., 1998), therefore, larger diameter, myelinated axons permit lower electrical resistance, allowing for more rapid signal propagation. Myelination is the process by which axons are ensheathed in an insulating multilamellar membrane (myelin) comprised primarily of lipids and proteins that are produced by specialised glial cells closely associated with the neuron (Nave, 2010). In the PNS, these glial cells are Schwann cells, while in the CNS, myelination is carried out by oligodendrocytes (Sherman and Brophy, 2005). Myelination further enhances signal propagation by facilitating saltatory conduction – the rapid transmission of action potentials whereby excitation only occurs along the axon at gaps in the myelin sheath known as the Nodes of Ranvier (Hartline and Colman, 2007).

A-fibre nociceptors are myelinated, with relatively large-diameter axons and somata, allowing rapid conduction speeds between 5 to 30 meters per second (Djouhri and

Lawson, 2004). These neurons are typically responsible for mediating the sensation of fast-onset, sharp pain ("first pain", also known as sensory-discriminative pain) (Campbell and LaMotte, 1983, Purves et al., 2004). Most A-fibre nociceptors are further classified as Aδ-fibre neurons and are primarily mechanosensitive and thermosensitive in modality (Cain et al., 2001). In contrast, C-fibre nociceptors are unmyelinated and have smaller-diameter axons and somata, resulting in slower conduction speeds of 0.4 to 1.4 meters per second (Djouhri and Lawson, 2004). C-fibre nociceptors are often polymodal, responding to a variety of noxious stimuli, including mechanical, thermal, and chemical stimuli, and are responsible for the sensation of slow-onset, dull, and diffuse pain, known as "second pain" (Van Hees and Gybels, 1981, Dubin and Patapoutian, 2010a, Price and Dubner, 1977). Somatosensory ganglia, including the dorsal root ganglia (DRG) and the trigeminal ganglia (TG), additionally contain large-diameter mechanosensitive and proprioceptive neurons that give rise to heavily myelinated Aα and Aβ nerve fibres which innervate the skin and primarily transduce innocuous (non-painful) stimuli with conduction speeds up to 120 meters per second (Olausson et al., 2024).

1.1.3 Nociceptive Pathways

The process of pain sensation can be divided into four key stages: transduction, transmission, modulation and perception (Ringkamp et al., 2018). Transduction describes the conversion of exogenous or endogenous noxious stimuli to electrochemical signals by specialised somatosensory nociceptors in the PNS, which originate from the DRG and TG (Woolf and Ma, 2007). Transmission (Figure 1.1) refers to the propagation of those electrochemical signals from first-order peripheral sensory neurons to second-order neurons. Primary sensory neurons originating from the DRG project from the periphery to the dorsal horn of the spinal cord, where they branch into ascending and descending bundles forming the dorsolateral tract of Lissauer before entering the grey matter of the spinal cord to synapse with second-order neurons at the dorsal horn laminae I (C-fibres and Aδ fibres) and V (Aδ-fibres) (Purves et al., 2004). Second-order neurons decussate at the spinal cord, crossing to the contralateral side, and project along afferent ascending nociceptive pathways (the spinothalamic tract) to synapse with third-order CNS neurons, which subsequently project to a wide variety of regions at the brainstem, mid-brain and fore-brain to mediate the sensory discriminative and affective-motivational aspects of pain (Purves et al., 2004). In contrast, primary somatosensory neurons originating from the TG initially project central axons down the spinal trigeminal tract to the spinal trigeminal nucleus in the medulla oblongata to synapse with second-order neurons, which then similarly decussate within the brainstem and project to higher brain regions including the thalamus (Purves et al., 2004). Modulation occurs at multiple levels along these pain transmission pathways. The gate

control theory of pain (Melzack and Wall, 1965) models a generally accepted mechanism of how descending central efferent fibres modulate the synaptic transmission of nociceptive signals from the peripheral afferents to the second-order neurons at the level of the dorsal horn of the spinal cord. These mechanisms are comprehensively reviewed by Millan (2002) but are outside the scope of this thesis, which will focus on molecular mechanisms of nociception in peripheral nociceptors of the DRG and TG, and so will not be discussed further. However, until recently, the consensus view was that the spinal cord was the first site of such modulation of nociception (Mendell, 2014), although recent experimental work contests that view and proposes the DRG as a novel site of initial modulation (Du et al., 2017, Fuller et al., 2023). Modulation of nociceptive signalling mechanisms at the level of the peripheral DRG, and indeed TG, neurons through pharmacological or genetic approaches, therefore, is a viable strategy for the development of novel therapeutics to manage acute and chronic pain conditions (Berta et al., 2017, Kc et al., 2022).

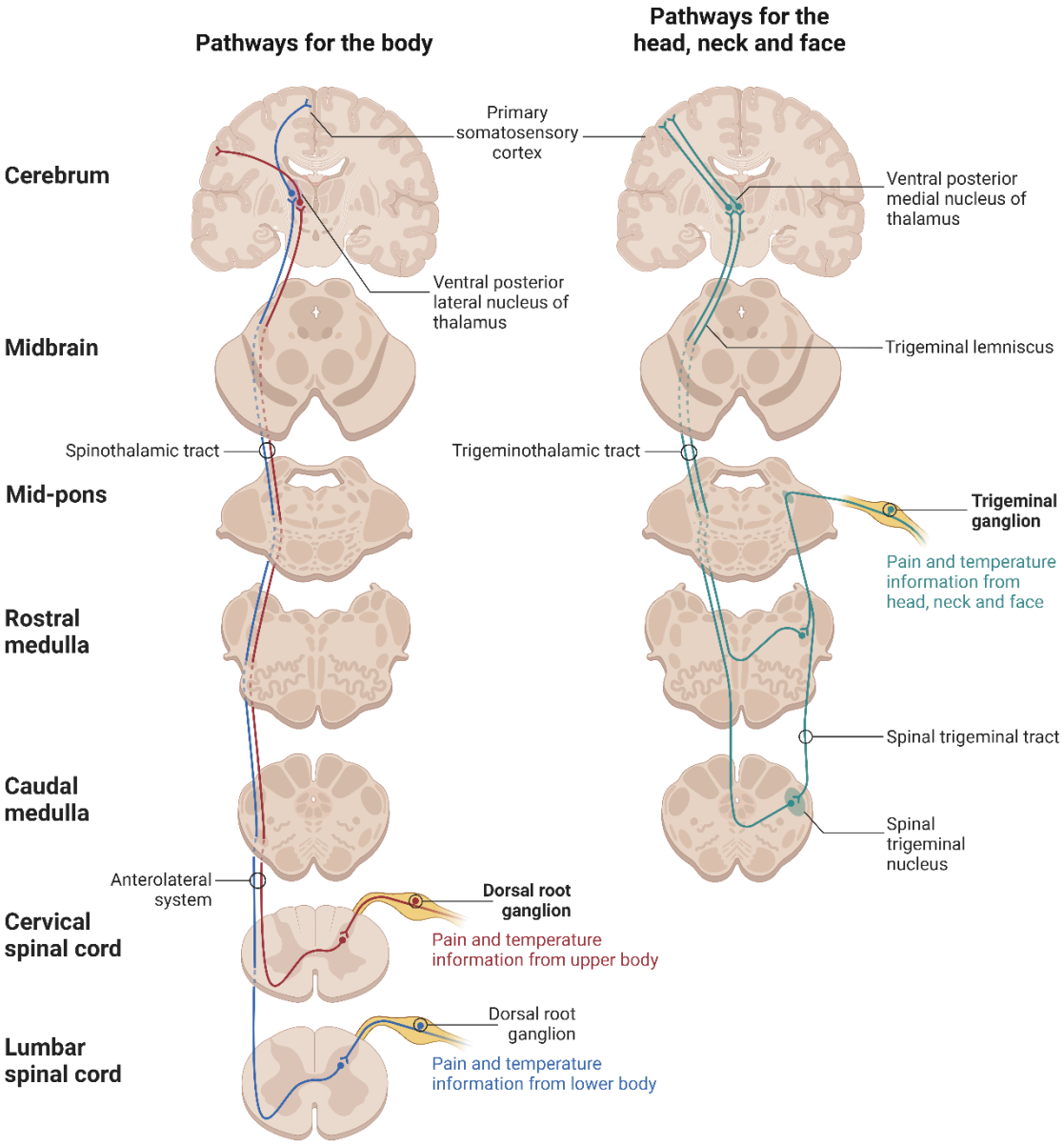

Figure 1.1: Transmission pathways of pain from the peripheral to central nervous system. Diagrams depicting the afferent transmission pathways for nociceptive input from DRG neurons (left) and TG neurons (right). Primary sensory pseudounipolar neurons synapse with second-order CNS neurons in the dorsal horn of the spinal cord (DRG) or spinal trigeminal nuclei of the medulla oblongata (TG). Second-order neurons ascend the spinothalamic (DRG) or trigeminothalamic (TG) tract which project to nuclei of the thalamus where they synapse with third-order neurons which project to higher fore-brain regions to mediate the perception of pain. Adapted from Purves et al,. 2004 and created using Biorender.com.

1.2 The Dorsal Root and Trigeminal Ganglia

While nociceptors originating from the DRG and TG do exhibit a high degree of functional similarity, there are significant differences with respect to their developmental lineage, their connections to the CNS (as described in Section 1.1.3), and furthermore, recent comprehensive transcriptomic profiling investigations suggest they possess distinct genomic signatures which undoubtedly reflect in specialised functionality (Megat et al., 2019b, Kogelman et al., 2017, Lopes et al., 2017a, Flegel et al., 2015). For example, analysis of the DRG and TG 'translatome' of actively translating mRNA in $Na_V1.8$-positive nociceptors using a translating ribosome affinity purification (TRAP) approach revealed a significant enrichment of transcripts for mechanistic target of rapamycin (mTOR)-related genes in the TG compared to the DRG, and conversely an enrichment in AMP-activated protein kinase (AMPK)-related genes in the DRG compared to the TG (Megat et al., 2019b). The AMPK signalling pathway functions as a negative regulator of mTOR-related signalling, therefore, these findings may highlight a differential balance in the function of these signalling mechanisms between DRG and TG nociceptive neurons.

The most apparent difference between the two ganglia with respect to their functionality is the somatic regions they innervate: intra- and extracranial structures, including the neck, are innervated by nociceptive afferent fibres originating from the TG and the DRG at the highest cervical level of the spine, while the remainder of the skin from the neck down is innervated exclusively by the DRG (Vermeiren et al., 2020).

Both ganglia share a similar structural organisation consisting of the cell bodies (somata) of pseudounipolar primary afferent neurons, their peripheral and central axonal processes, and closely associated satellite glial cells, which encapsulate the neuronal somata (Haberberger et al., 2023, Messlinger and Russo, 2019). The term psuedounipolar refers to the unique morphology of somatosensory neuronal processes *in vivo,* which consists of a single axon that bifurcates at a T-junction into a peripheral branch, which extends to the spinal nerve, and a central branch, which extends as the dorsal root towards the dorsal horn of the spinal cord (Matsuda et al., 1998). This arrangement allows sensory information to be transmitted rapidly and directly from the periphery to the CNS without requiring synaptic relay within the ganglion itself, although the stem axonal segment may serve to function as a low-pass filter limiting the frequency of action potential propagation to the CNS (Stoney, 1990, Du et al., 2014, Du et al., 2017, Hao et al., 2023).

In *Rattus norvegicus* (Wistar rats), the DRG are localised bilaterally within openings between the pedicles of the spinal vertebrae (intervertebral foramina) at the cervical (C), thoracic (T), lumbar (L) and sacral (S) divisions in the spinal column. In total, rats have between 30 and 31 individual pairs of DRG (Malin et al., 2007). In contrast, the TG are

two structures residing in Meckel's cavity at the petrosal region of the temporal bone at the base of the skull (Messlinger and Russo, 2019). The TG is comprised of three separate divisions, the ophthalmic (V1) division, the maxillary (V2) division and the mandibular (V3) division, which project to three individual branches of the fifth cranial nerve (trigeminal nerve) (Messlinger and Russo, 2019).

Despite mediating similar roles with respect to nociceptive transduction, the DRG and TG arise from distinct embryological origins (Lopes et al., 2017a). While DRG neurons are derived from the neural crest, TG neurons dually originate from the cranial neural crest and the trigeminal ectodermal placodes, suggesting they may exhibit differential patterns of gene expression (D'Amico-Martel and Noden, 1983, Krispin et al., 2010). Indeed, recently a considerable effort has been made to comprehensively characterise and compare the respective transcriptomes of the DRG and TG and several independently developed databases provide evidence for differential gene expression in the DRG and TG in naive tissue and models of chronic pain (Korczeniewska et al., 2020, Megat et al., 2019b, Bhuiyan et al., 2024, Korczeniewska et al., 2024).

While there are countless ionic and metabotropic receptors expressed by DRG and TG neurons which mediate a role in nociception, this introduction will focus in detail on the anion-permeable calcium-(Ca^{2+})-activated chloride-(Cl^-) channel (CaCC) that forms the basis of the experimental work for this thesis: anoctamin 1 (ANO1).

1.3 ANO1

1.3.1 The ANO Family of Proteins

Barish first described endogenous Ca^{2+}-activated Cl^- currents in Xenopus oocytes in 1983. However, the molecular identity of CaCCs remained a source of contention up to 2008, when three independent groups identified ANO1 as the mediator of endogenous CaCC activity in oocytes and epithelial cells (Yang et al., 2008, Schroeder et al., 2008, Caputo et al., 2008). Prior to this discovery, a number of candidate proteins were proposed as the mediators of CaCC activity, including human bestrophin 2, various Cl^- channel (CLC) subunits, and Tweety (Sun et al., 2002, Qu et al., 2003, Huang et al., 2001, Suzuki and Mizuno, 2004). However, cloning the ANO family of proteins revealed anion channels whose biophysical characteristics aligned much more closely with those of endogenous CaCCs (Yang et al., 2008, Schroeder et al., 2008, Caputo et al., 2008). Such characteristics included Ca^{2+}-activated Cl^- currents that demonstrate a pattern of outward rectification, synergistic Ca^{2+} and voltage dependence, comparable single-channel conductance and that were susceptible to classical CaCC inhibitors such as DIDS and niflumic acid (Yang et al., 2008, Caputo et al., 2008, Schroeder et al., 2008, Pedemonte and Galietta, 2014).

The ANO protein family consists of ten identified human homologues (ANO1 through ANO10) that share between 20% and 60% amino acid sequence identity, reflecting a wide range of physiological functionality that is yet to be fully elucidated (Falzone et al., 2018, Galietta, 2009, Duran and Hartzell, 2011, Suzuki et al., 2010). All members of the ANO family are transmembrane proteins that are functionally localised to the PM or to intracellular compartments (Kunzelmann et al., 2024). ANO1 and ANO2 have been identified as trans-PM anion channels exclusively mediating CaCC activity in a broad range of tissue types (Yang et al., 2008, Schroeder et al., 2008, Caputo et al., 2008, Stephan et al., 2009). In particular, ANO2 is expressed at the cilial membrane of olfactory sensory neurons where ANO2-mediated CaCCs contribute to canonical olfactory signal transduction pathways (Billig et al., 2011, Stephan et al., 2009). Contrary, other members of the ANO protein family have been identified as Ca^{2+}-dependent phospholipid scramblase (PLS) proteins, which mediate the substrate-specific rearrangement of phospholipids between the two leaflets of the cell surface PM bilayer (Suzuki et al., 2013, Williamson, 2015). For example, ANO6 contributes to the Ca^{2+}-dependent exposure of phosphatidylserine on the PM of platelets, initiating the clotting mechanism and heritable mutations in the *TMEM16F* gene encoding ANO6 lead to the clotting disorder Scott syndrome (Suzuki et al., 2010, Boisseau et al., 2018).

The physiology and function of the remaining ANO proteins has been less well characterised; ANO3 is known to function as an ER-resident PLS which may interact

with the Na^+-activated K^+ channel, SLACK, to reduce the excitability of DRG nociceptive neurons (Huang et al., 2013) and ANO4 has been implicated as a negative regulator of Ca^{2+}-activated aldosterone secretion by the adrenal glands (Maniero et al., 2019). Mutations in the *TMEM16E* gene encoding ANO5 are associated with autosomal recessive limb-girdle muscular dystrophy, and it has been hypothesised that ANO5 functions in skeletal myocytes as a Cl^- counterion channel required to compensate for excess ER Ca^{2+} uptake in response to cell damage (Soontrapa and Liewluck, 2022, Chandra et al., 2021). ANO9 has recently been characterised as a cation channel activated by cyclic adenosine monophosphate (cAMP)-dependent protein kinase A (PKA) activity and expressed in the olfactory epithelium where it confers an amplification of odorant-induced olfactory transduction (Kim et al., 2018, Kim et al., 2022). To further add to the variety of functions mediated by ANO proteins, ANO8 has been shown to function as a membrane tethering protein mediating the close apposition between the endoplasmic reticulum (ER) and PM required for the functional interaction between Ca^{2+} signalling proteins, stromal interaction molecule 1 (STIM1) and Orai1 (Jha et al., 2019).

1.3.2 Biophysiological Properties of ANO1

Single-particle cryo-electron microscopy (cryo-EM) has successfully resolved the structure of the murine ANO1 protein (mANO1) in the presence and absence of bound Ca^{2+} (Paulino et al., 2017). This analysis revealed that ANO1 is functionally expressed as a homodimer where each subunit consists of a cytosolic N- and C-terminus, ten membrane-spanning α-helix domains, and an extracellular domain (Figure 1.2). Homodimerisation is achieved through the interaction of amino acid residues localised to the α10 helix (Paulino et al., 2017). Each ANO1 monomer contains an hourglass-shaped ion permeation pore created by the α3- α8 helices, and the high density of basic amino acids confers a positive electrostatic environment favouring permeabilisation to negatively-charged anions (Arreola et al., 2024). The Ca^{2+}-dependent activation mechanism of ANO1 has been comprehensively studied, and three unique Ca^{2+} binding sites have been identified. Systematic mutagenetic analysis of amino acid residues lining the pore region identified the orthosteric Ca^{2+} binding site localised to six residues of α6-α8 that together form a binding pocket for 1 or 2 Ca^{2+} cations (Paulino et al., 2017, Dang et al., 2017). Therefore, the gating mechanism of ANO1 involves two main steps: the opening of an electrostatic gate and the subsequent opening of a hydrophobic gate. Initially, the binding of Ca^{2+} to the orthosteric binding site negates a negative electrostatic potential at the pore entrance (electrostatic gate), facilitating the conduction of anions. The hydrophobic gate is formed by a triad of isoleucine residues (I641, I550, and I551) within the α6 segment (Lam et al., 2021). Upon Ca^{2+} binding, the α6 helix undergoes a hinge-like conformational change of shape around the glycine 644 (G644) residue, which

physically opens the hydrophobic gate, allowing passage of anions (De Jesus-Perez et al., 2022). A further allosteric Ca^{2+} binding site is formed by four amino acid residues on α2 and α10 which, together with a third, as yet uncharacterised binding site, may confer the synergistic voltage-Ca^{2+} dependence observed for ANO1-mediated Cl^- currents, as these sites are known to bind Ca^{2+} in a voltage-dependent manner (Le and Yang, 2020, Lim et al., 2016, Jeng et al., 2016). ANO1 activity is reciprocally regulated by Ca^{2+} and voltage: in neurons, the EC_{50} (concentration required for half-maximal activity) of ANO1 activation at hyperpolarised membrane potentials of -60 mV is 2.6 μM; however, for depolarised membrane potentials (+ 60 mV) the Ca^{2+} dependence is as low as 0.3 μM (Yang et al., 2008). Furthermore, due to the relatively inaccessible localisation of the orthosteric Ca^{2+} binding site inside the anion conduction pore, at resting sensory neuronal membrane potentials (-60 mV), ANO1 requires highly localised, micromolar Ca^{2+} signals for activation.

The consequences of ANO1 activation depend on both the intracellular and extracellular Cl- concentration, which dictate the equilibrium potential (E_{Cl}) and, subsequently, the electrochemical driving force for Cl^- flux following the opening of the ANO1 anion permeation pathway. In excitable cells including vascular smooth muscle cells, olfactory and vomeronasal sensory neurones, and nociceptive neurons of the DRG and TG, active intracellular Cl^- accumulation by the sodium (Na^+)-potassium (K^+)-Cl^- ionic co-transporter (NKCC1) mediates a positive E_{Cl} with respect to the resting membrane potential (Chipperfield and Harper, 2000, Kaneko et al., 2004, Kim et al., 2015, Price et al., 2006, Schöbel et al., 2012). Therefore, ANO1 activation induces an efflux of Cl^- down its electrochemical gradient, conferring an inward current and subsequent depolarisation of the membrane potential, likely to produce an excitatory effect (Russell, 2000). It is by this phenomenon that ANO1-mediated Ca^{2+}-activated Cl^- currents can be considered an amplification mechanism of Ca^{2+} signalling events.

1.3.3 The Role of ANO1 in Nociception

Among the wide variety of tissue types in which endogenous Ca^{2+}-activated Cl^- currents have been described, functional protein expression of ANO1 in small-diameter nociceptors has been particularly well characterised, supporting a role for ANO1 in the modulation of nociception. Yang and colleagues first confirmed immunoreactivity for ANO1 in small-diameter sensory neurons of the DRG in their seminal paper identifying ANO1 as the molecular mechanism conferring Ca^{2+}-activated Cl^- currents (Yang et al., 2008). This initial finding proposed ANO1 as the mediator of Ca^{2+}-activated Cl^- currents already theorised to confer a Ca^{2+}-dependent depolarisation to sensory neurons, which could modulate excitatory mechanisms of nociceptive signalling (Kaneko et al., 2002, Hartzell et al., 2005). More recent evidence has since confirmed ANO1 immunoreactivity

in a subpopulation of DRG and TG sensory neurons where ANO1 expression is strongly colocalised with key nociceptor biomarkers, including the transient receptor potential vanilloid receptor type 1 (TRPV1), and Substance P (SP) and isolectin B4 (IB4), markers of peptidergic and non-peptidergic nociceptors, respectively (Deba and Bessac, 2015, Takayama et al., 2015, Kanazawa and Matsumoto, 2014, Yamagata et al., 2016). This suggests that ANO1 may be involved in a broad range of pain signalling modalities, given the distinct roles of these neuronal subpopulations in thermal, chemical, and mechanical nociception.

TRPV1 is a non-selective cation-permeable ion channel abundantly expressed in small-diameter sensory neurons of the DRG and TG that functions as a polymodal nociceptive transduction receptor for noxious heat (> 42°C), acidic pH, and pungent chemicals including, most notably, capsaicin (CAP) (Caterina et al., 1997, Helliwell et al., 1998). The molecular identity of TRPV1 as the CAP receptor was confirmed using a mammalian cell expression cloning approach whereby the complementary deoxyribonucleic acid (cDNA) encoding TRPV1 was isolated from a DRG neuron messenger ribonucleic acid (mRNA)-derived cDNA library transiently transfected into HEK293 cells (Caterina et al., 1997). Interestingly, mANO1-transfected HEK293 cells have similarly demonstrated outwardly rectifying currents in response to temperatures in excess of 44°C (Cho and Oh, 2013, Cho et al., 2012), which is notable as HEK293 cells have been shown not to express endogenous responses to CAP or noxious heat (Kuwashima et al., 2021, Cho and Oh, 2013). Furthermore, Cho and colleagues demonstrated chelation of local Ca^{2+} transients with the Ca^{2+} chelator 1,2-bis(2-aminophenoxy)ethane-N,N,N',N'-tetra-acetic acid (BAPTA) failed to abolish noxious heat-evoked ANO1 Cl^- currents, suggesting ANO1 conferred an intrinsic heat sensitivity and was not indirectly activated by the noxious heat-induced release of Ca^{2+} from intracellular stores (Cho et al., 2012, Lukacs et al., 2007, Lukacs et al., 2013).

More recently, functional interaction between ANO1 and TRPV1 has been proposed as a molecular mechanism amplifying noxious heat signalling in DRG neurons. Takayama and colleagues demonstrated co-immunoprecipitation of ANO1 and TRPV1 in mANO1-mTRPV1 co-transfected HEK293 cells and of endogenous ANO1-TRPV1 complexes in the DRG, leading them to hypothesise that Ca^{2+} influx through TRPV1 was able to directly activate ANO1 due to nanodomain coupling between the two channels (Takayama et al., 2015). Indeed, CAP-induced depolarising currents in primary DRG neuronal cultures and nocifensive behavioural responses to exogenous application of CAP were reduced by the ANO1-specific antagonist T16Ainh-A01 (Takayama et al., 2015), further supporting a mechanism whereby ANO1 contributes to TRPV1-mediated nociception.

This model of functional coupling between ANO1 and TRPV1 was recently refined by Shah and colleagues, who employed proximity assays and super-resolution microscopy to visualise ANO1-TRPV1 nanodomain complexes in small-diameter DRG neurons (Shah et al., 2020). Furthermore, ANO1-TRPV1 interactions were observed within close association of the ER-resident inositol 1,4,5-trisphosphate (IP_3) receptor type 1 (IP_3R1), prompting an investigation into the role of IP_3-induced Ca^{2+} release in TRPV1-ANO1 coupling. In sensory neurons, IP_3R1 functions as a critical intracellular Ca^{2+} channel, primarily activated downstream of metabotropic G_q protein-coupled receptor (G_qPCR) signalling cascades (Hurley et al., 2023, Jin et al., 2013). Upon activation of G_qPCRs by extracellular stimuli, phospholipase Cβ (PLCβ) is stimulated, leading to the hydrolysis of phosphatidylinositol 4,5-bisphosphate (PIP2) into diacylglycerol (DAG) and IP_3, the subsequent binding of which to IP_3R1 induces the release of intracellular ER Ca^{2+} stores (Mikoshiba, 2007, Berridge, 2016). Interestingly, the PLC-δ isozyme is robustly activated by TRPV1-mediated global Ca^{2+} transients independent of the traditional G_q protein signalling cascade (Eberhard and Holz, 1988, Allen et al., 1997, Rhee and Bae, 1997), suggesting TRPV1-mediated release of IP_3-sensitive intracellular Ca^{2+} could contribute to ANO1-TRPV1 functional coupling in synergy with direct Ca^{2+} influx via TRPV1 (Lukacs et al., 2007, Lukacs et al., 2013).

An optimised dual imaging system was developed by Shah and colleagues to simultaneously measure ANO1 channel activity and TRPV1-mediated Ca^{2+} transients in nociceptive neurons *in vitro* following the application of the TRPV1 agonist CAP. Indeed, this approach evidenced a mechanism for functional ANO1-IP_3R1-TRPV1 coupling as depletion of ER Ca^{2+} stores with the sarcoplasmic reticulum (SR)/ER Ca^{2+}-ATPase (SERCA) inhibitor thapsigargin (Lytton et al., 1991) or pharmacological inhibition of IP_3R1 with xestospongin C (Castonguay and Robitaille, 2002) significantly attenuated CAP-induced TRPV1 Ca^{2+} transients and ANO1-mediated anion flux (Shah et al., 2020).

In small-diameter nociceptive neurons of the DRG, preferential coupling of ANO1 to IP_3-sensitive Ca^{2+} release has also been observed in the context of inflammatory nociceptive signalling pathways. Expression of ANO1 has been confirmed within nanodomain proximity of the bradykinin (BK) B2 G_qPCR (B2R) (Jin et al., 2013; Yang et al., 2008). In this scenario, BK stimulation of B2R initiates the canonical G_q protein-activated PLCβ signalling cascade, liberating IP_3 from the PM, which subsequently triggers the release of ER Ca2+ stores via IP_3R1 activation (Jin et al., 2013; Liu et al., 2010).

Functional coupling between ANO1 and IP_3R1, therefore, is a well-established mechanism through which ANO1 is selectively activated by localised, high-intensity Ca^{2+} signals in DRG neurons (Jin et al., 2016, Jin et al., 2013, Shah et al., 2020). This

specificity is ensured, in part, through the compartmentalisation of ANO1-IP_3R1 interactions into distinct nanodomains formed at regions of close apposition between the ER and PM, termed ER-PM membrane contact sites (MCS) (Jin et al., 2013, Chang et al., 2017). In fact, ANO1-IP_3R1 coupling is facilitated through their physical tethering via the ANO1 α2/3 loop and C-terminus. Furthermore, spatially restricted coupling between B2R and IP_3R1 is additionally essential for the BK-induced mobilisation of intracellular Ca^{2+} stores, adding another layer of necessity to nanodomain signalling complexes for the selectivity of nociception (Delmas et al., 2002). Therefore, close juxtaposition of the ER and PM is an essential characteristic for the formation of so-called junctional multiprotein signalling complexes (JMSCs), including those formed by ANO1 and IP_3R1 (Jin et al., 2013).

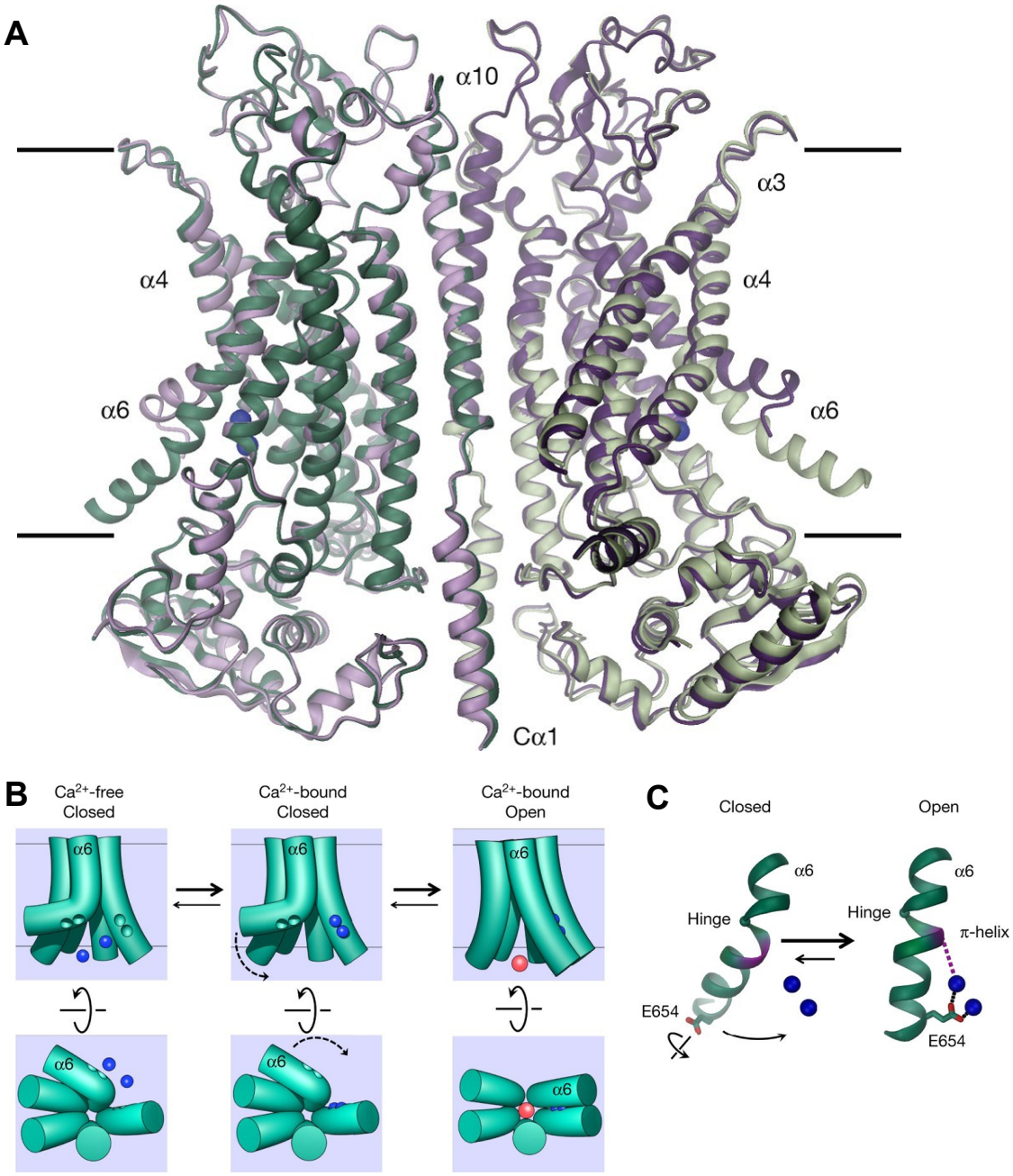

Figure 1.2: Structure-function relationship for the calcium-dependent activation mechanism of ANO1. A) Ribbon representation depicting a superposition of the Ca^{2+}-bound (green) and Ca^{2+}-free (purple) quaternary protein structures of the mANO1 homodimer. Alpha (α) helices 1, 3, 4, 6 and 10 are labelled and the orthosteric Ca^{2+} binding site is represented by the blue spheres bound at α6. **B)** Diagram depicting the two-stage Ca^{2+}-dependent activation mechanism of ANO1 as viewed from within the membrane (top panels) and from the cytoplasmic side (bottom panels). Green cylinders represent the relevant pore-lining α helices, blue spheres represent Ca^{2+} ions and red sphere represents a Cl^- ion passing through the ANO1 permeation pathway which opens as a result of the hinging conformational change of shape of α6 (shown in **C**). Adapted from Paulino et al., 2017. mANO1, murine ANO1 homologue.

1.4 Functional Organisation of Nociceptive JMSCs in DRG Neurons

JMSCs represent a robust mechanism for the compartmentalisation of Ca^{2+} signalling cascades. However, the underlying principles of formation, functional organisation and maintenance of such intracellular signalling nanodomains in excitable cells remain unresolved. To date, a small handful of 'scaffolding' proteins localised to ER-PM junctions have been identified. In mammalian ventricular cardiomyocytes and striated skeletal myocytes, the well-characterised membrane association between the PM T-tubule system and the SR is established by direct interaction of junctophilin type 1 (JPH1) or type 2 (JPH2) with the SR-expressed ryanodine receptor 1 (RyR1) and the PM-expressed L-type Ca^{2+} channel dihydropyridine receptor (DHPR); formation of this three-way complex stabilises the Ca^{2+} signalling nanodomain (Phimister et al., 2007, Golini et al., 2011). JPH type 3 (JPH3) and type 4 (JPH4) are widely expressed in neurons, and JPH4 has recently been identified as a necessary ER-PM anchor protein in the formation and maintenance of JMSCs between PM Orai1 and the ER Ca^{2+}-sensing STIM1 in DRG neurons, where JPH4 is abundantly expressed (Nishi et al., 2003, Hogea et al., 2021). Hogea and colleagues recently demonstrated attenuated BK-induced Ca^{2+} transients in DRG neurons following small interfering RNA (siRNA) knockdown of JPH4, which could be indicative of a role for JPH4 in mediating the functional interactions between B2R, ANO1 and IP_3R1 (Hogea et al., 2021).

Preliminary proteomics data obtained in the Gamper laboratory has uncovered a further novel putative ER-PM junctional scaffolding protein, which may participate in the formation and organisation of DRG ANO1-containing Ca^{2+}-signalling nanodomains. A glutathione-S-transferase (GST) fusion protein "pull-down" assay was performed utilising GST-fused full-length ANO1 (constructed in-house) as a bait construct to identify ANO1-interacting proteins (Jin et al., 2013). When whole rat DRG lysates were incubated with ANO1 GST-fused beads, mass spectrophotometric analysis of the resulting immunoprecipitants showed an approximately 7-fold increase in the concentration of the ER-resident protein Sec22B compared to the control beads without GST-fused ANO1, implicating Sec22B as an ANO1-interacting protein (Gamper and Shah, unpublished).

Sec22B is an R-soluble N-ethylmaleimide-sensitive factor attachment protein (SNAP) receptor (RSNARE) protein with a primary role in cargo-containing transport vesicle trafficking and membrane fusion at the ER-Golgi intermediate compartment, enabling efficient communication between intracellular membrane-bound organelles in all eukaryotic cell types (Adnan et al., 2019). Anterograde and retrograde vesicle transport between the ER and Golgi is achieved through functional coupling of Sec22B, expressed by coat protein-II-coated vesicles budding from the ER membrane, with target SNARE

(t-SNARE) proteins expressed on the cis Golgi membrane (Hanna et al., 2017, Adnan et al., 2019). Direct interaction of Sec22B with t-SNAREs promotes membrane fusion and the exchange of intra-vesicular components between the two organelles (Kurokawa et al., 2014). Sec22B additionally mediates a conserved non-fusogenic role in PM expansion during cell growth and development and is highly enriched in neurite growth cones of developing mammalian cortical neurones (Petkovic et al., 2014). Here, Sec22B maintains proximity of the ER and PM at MCSs via the formation of a trans-SNARE bridge with the PM-expressed Q-SNARE syntaxin 1, albeit without promoting fusion of the membranes (Petkovic et al., 2014). Trans-SNARE complex-mediated membrane fusion typically requires the interaction of an R-SNARE (such as Sec22B) with a SNAP25-like factor, enabling a zipper mechanism to pull the two lipid bilayers together, triggering complete fusion (Gao et al., 2012). While Petkovic and colleagues demonstrated coimmunoprecipitation of endogenous Sec22B and syntaxin 1 from both embryonic and adult murine brain tissue, Sec22B did not co-immunoprecipitate with growth cone-localized SNAP25, suggesting Sec22B-syntaxin 1 complexes in neurites are fusion incompetent. Of particular interest is Petkovic and colleagues' finding that Sec22B similarly coimmunoprecipitates with the single-celled-eukaryotic orthologue of syntaxin 1, Sso 1, in yeast, suggesting there is conservation of the R-SNARE proteins ER-PM tethering function across species. Given the preliminary evidence that Sec22B is a member of the ANO1 interactome (Gamper and Shah, unpublished), it is tempting to hypothesise that this non-fusogenic tethering function may translate to small-diameter nociceptive neurons of the mammalian DRG and that Sec22B may therefore be involved in the tethering of ER-PM contact sites necessary to facilitate Ca^{2+} JMSC formation between ANO1, IP_3R1 and B2R or TRPV1.

A final putative JMSC scaffolding protein of interest is the extended synaptotagmin 1 (Esyt1) protein. Esyt1 is an ER-resident protein that mediates the Ca^{2+}-dependent formation of ER-PM MCSs that are functionally distinct from the SOCE complexes maintained by JPH4 between STIM1 and Orai1 (Giordano et al., 2013). The molecular structure of Esyt1 consists of a transmembrane hairpin region at the N-terminus, which anchors the protein within the ER membrane, a synaptotagmin-like mitochondrial-lipid binding protein (SMP) domain, and five C2 domains at the C-terminus, termed C2A to C2E (Min et al., 2007b). In HEK293 cells, overexpression of Esyt1 has been shown to mediate ER-PM junction tethering at a distance between 12 and 15 nm, certainly close enough to facilitate JMSC interaction (Henry et al., 2022). The first Esyt1 C2 domain (C2A) contains a Ca^{2+} binding site which acts as a sensor for elevated cytosolic Ca^{2+} (Min et al., 2007). The binding of Ca^{2+} under high intracellular Ca^{2+} concentration ($[Ca^{2+}]_i$) conditions promotes the translocation of Esyt1 to the PM, facilitating the formation of

novel ER-PM contact sites (Chang et al., 2013, Giordano et al., 2013). In bronchial epithelial cells, a novel fluorescence-based trafficking assay has identified Esyt1 as a positive modulator of ANO1 translocation to the PM. siRNA knockdown of Esyt1 significantly decreased both PM expression of ANO1 and ANO1-mediated Ca^{2+}-activated Cl^- current density, indicative of a physiological role for Esyt1 in regulating ANO1 expression levels (Lérias et al., 2018). Whether this mechanism occurs via direct coupling between ANO1 and Esyt1 remains to be determined, although given its role as an ER-PM tethering protein, it is interesting to speculate whether Esyt1 may contribute to the formation and maintenance of ANO1-containing JMSCs at ER-PM contact sites in small-diameter sensory neurones.

1.5 Aims and Objectives

In small-diameter nociceptive neurons of the DRG, preferential coupling of ANO1 to IP_3-sensitive Ca^{2+} release from intracellular ER stores marks a novel molecular mechanism for the amplification of nociceptive signalling (Figure 1.3). This thesis aims to further characterise ANO1 signalling nanodomains in peripheral sensory neurons, including establishing a functional role for ANO1-IP_3R1 nanodomains in nociceptors of the TG and investigating putative ER-PM scaffolding proteins that may modulate the functionality of ANO1 signalling complexes in DRG nociceptors.

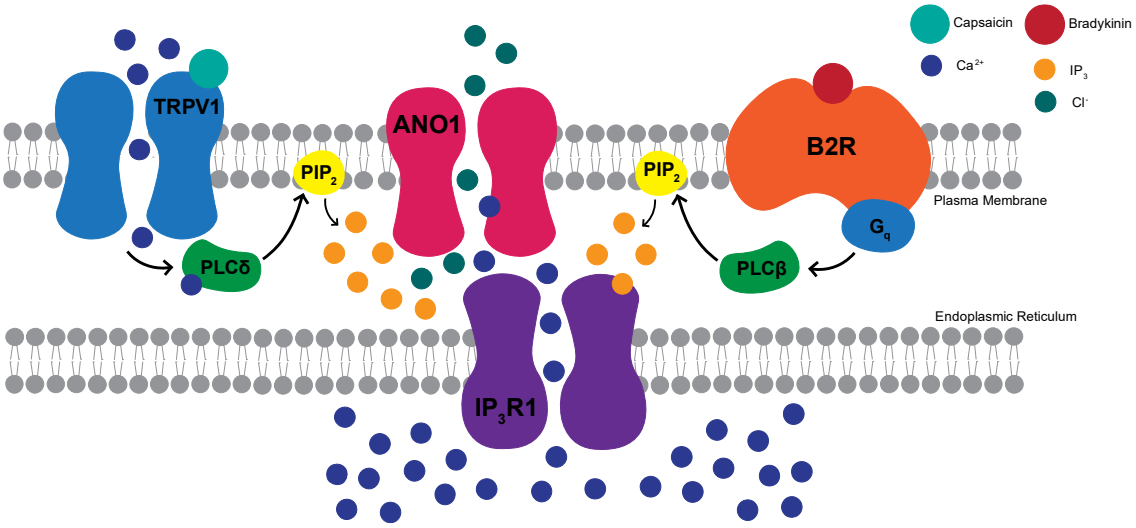

Figure 1.3: Functional coupling of ANO1 nanodomains in small-diameter DRG neurons at junctional multiprotein signaling complexes. A) Schematic depicting the functional interactions between ANO1 and the IP_3 receptor (IP_3R1) at endoplasmic reticulum-plasma membrane (ER-PM) junctional nanodomains. ANO1-IP_3R1 JMSCs are found within nanodomain proximity of the bradykinin B2 G_qPCR and the noxious heat and capsaicin receptor TRPV1. ANO1, anoctamin 1; TRPV1, transient receptor potential vanilloid receptor type 1; B2R, bradykinin receptor type 2; IP_3R1, inositol 1,4,5-trisphosphate receptor type 1; PLC, phospholipase C; PIP2, phosphatidylinositol 4,5-bisphosphate; IP_3, inositol 1,4,5-trisphosphate; Ca^{2+}, calcium cation; Cl^-, chloride anion; JMSC, junctional multiprotein signaling complex; DRG, dorsal root ganglion.

Chapter 2: Methodology

2.1 Animal Use

The use of animal tissues in the described experiments was conducted in accordance with Home Office regulation and with approval from the Faculty of Biological Sciences Research Ethics Committee and the University of Leeds' Animal Welfare and Ethical Review Body.

2.2 Tissue Dissection

Wistar rats of both sexes were terminally anaesthetised by inhalation of Isofane (100% w/w isoflurane) (988-3245, Henry Schein) and confirmation of death performed by either cervical dislocation (P3 – P7 neonatal animals used for primary neuron culture and western blot) or exsanguination followed by perfusion of 4% paraformaldehyde (PFA) (15670799, Thermo Scientific) (P21 weaned animals, subsequently post-fixed for 24 hours for immunohistochemistry experimentation). For dissection of the DRG, the vertebral column was extracted, cleaned of excess connective tissue and bisected along the sagittal plane to expose the DRGs embedded in the vertebrae on the left and right of the spine. DRGs from the cervical, thoracic and lumbar vertebral segments were extracted and placed in modified Hank's Balanced Salt Solution (HBSS) (with sodium bicarbonate, without calcium chloride and magnesium sulfate) (H9394, Sigma-Aldrich) on ice. To dissect the TG, the top of the skull was cut away to expose the brain beneath, which was subsequently removed to expose the left and right TGs embedded at the base of the skull in Meckel's cavity. The TGs were excised bilaterally after cutting the trigeminal root, mandibular branch and maxillary branch and placed into modified HBSS (as above) on ice.

Fresh dura mater tissue was obtained to lyse for western blot analysis by gently scraping the inside of the skull with forceps once removed from a neonatal animal and placed immediately into radioimmunoprecipitation assay (RIPA) lysis buffer (50 mM Tris HCl (H5123, Promega) adjusted to pH 7.4 before addition to further components, 150 mM sodium chloride (NaCl) (S/3160/63, Fisher Scientific), 1% Triton X-100 (T8787, Sigma-Aldrich), 1 % sodium deoxycholate (D6750, Sigma-Aldrich), 0.1% sodium dodecyl sulfate (SDS) (S/5200/53, Fisher Scientific), 0.5 mM ethylenediaminetetraacetic acid (EDTA) (324503, Sigma-Aldrich), supplemented with 50 µM phenylmethylsulonyl fluoride (PMSF) (P7626, Sigma-Aldrich) and cOmplete™ Mini Protease Inhibitor Cocktail (04693124001, Roche) (1 tablet/10 mL) immediately prior to use) on ice. Similarly, the liver was removed via a midline incision to expose the abdominal cavity and placed into RIPA buffer on ice before mechanical homogenisation.

2.3 Primary Neuron Culture

Autoclaved 10 mm #0 glass coverslips were placed into 6-well polystyrene cell culture plates (83.3920, Starstedt) (one coverslip per well) and pre-coated in a solution consisting of 15% 1 mg/mL poly-D-lysine (PDL) (A-003-M, Sigma-Aldrich) and 15% 1 mg/mL laminin from Engelbreth-Holm-Swarm murine sarcoma basement membrane (L2020, Sigma-Aldrich) dissolved in HyClone™ HyPure™ tissue culture-grade water (SH30529.02, Cytiva) to improve neuronal adherence. Following tissue extraction, whole DRGs and TGs were transferred to a 14 mL round-bottom tube containing an enzymatic digestion solution consisting of 20 mg Dispase II (17105041, Gibco™ ThermoFisher Scientific) and 2 mg Collagenase Type 1A from *Clostridium histolyticum* (C9891, Sigma-Aldrich) dissolved in 2 mL modified HBSS which had been sterile-filtered through a 0.22 µm filter then pre-warmed to 37°C. The ganglia were incubated for 13 minutes in a humidified 5% CO_2 atmosphere at 37°C, mechanically triturated using a P1000 pipette approximately ten times until the cell solution turned cloudy to facilitate dissociation of the tissue, then incubated for a further 3 minutes. Following enzymatic digestion, dissociated cell solutions were transferred to 8 mL ice-cold Dulbecco's Modified Eagle's Growth Medium (DMEM) with GlutaMAX™ (10566016, Gibco™ ThermoFisher Scientific) supplemented with 10% foetal bovine serum (FBS) (F7524, Sigma-Aldrich), 50 U/mL penicillin (P0781, Sigma-Aldrich) and 50 µg/mL streptomycin (P0781, Sigma-Aldrich) to terminate the enzyme activity. The dissociated DRG and TG suspensions were centrifuged at 120 *g* for 5 minutes at 4°C, and the pellets were resuspended in 10 mL ice-cold supplemented DMEM with GlutaMAX™ before repeating the centrifugation step as previously. To remove tissue debris including myelin, the DRG and TG pellets were resuspended in 1 mL supplemented DMEM with GlutaMAX™ and layered over 2 mL of a 0.22 µm filtered 15% bovine serum albumin (BSA) (A9418, Sigma-Aldrich) solution (dissolved in supplemented DMEM with GlutaMAX™), then centrifuged at 140 *g* for 10 minutes at 4°C. The final primary cell pellets were resuspended in 600 µL (DRG) or 300 µL (TG) of supplemented DMEM with GlutaMAX™ (pre-warmed to 37°C), plated onto pre-coated (as detailed above) 10 mm coverslips at a volume of 100 µL/coverslip, then incubated in a 5% CO2 humidified atmosphere at 37°C for 6 hours. After 6 hours, the wells were flooded with 37°C pre-warmed supplemented DMEM with GlutaMAX™ and returned to incubation for 72 hours before experimental use.

2.4 Immunohisto/cytochemistry

2.4.1 Dorsal Root Ganglia and Trigeminal Ganglia

Perfusion-fixed DRG and TG tissues were dissected as previously described, washed 3 times for 5 minutes in phosphate-buffered saline (PBS) (P4417, Sigma-Aldrich), dabbed

dry on filter paper, then embedded in a 10% gelatin from porcine skin (G2625, Sigma-Aldrich) solution (dissolved in distilled water). The gelatin was set at 4°C overnight before being cut into cubes containing a single DRG or TG per cube, which were then hardened in 4% PFA solution overnight at 4ºC. Hardened gelatin cubes were washed 3 times in 0.1M phosphate buffer (PB) (38.5% 0.2 M disodium hydrogen orthophosphate (771505, Sigma-Aldrich) and 11.5% sodium dihydrogen orthophosphate (71643, Sigma-Aldrich) in distilled water) and stored in 0.1 M PB at 4°C before sectioning. A Leica VT1000 S vibrating microtome (Leica Microsystems) was used to section the embedded tissue samples into 40 µm slices, which were stored in PBS at 4°C until use. Tissue slices were submerged in a 9.0 pH buffer containing 10 mM Tris Base (648310-M, Sigma-Aldrich), 1 mM EDTA and 0.05% TWEEN® 20 (P1379, Sigma-Aldrich) (TE buffer) and incubated at 85°C for 30 minutes in a digital dry bath then left to cool at room temperature for a further 30 minutes. Slices were washed 3 times for 5 minutes in PBS on a rocking table and then incubated in PBS-T-T (0.05% TWEEN® 20 and 0.25% Triton™ X-100 in PBS) supplemented with 5% donkey serum (D9663, Sigma-Aldrich) for 1 hour 30 minutes at room temperature on a rocking table. Primary antibodies were diluted in PBS containing 50 mg/mL BSA, and tissue slices were incubated in the primary antibody solutions overnight at 4°C on a rocking table. Tissue slices were washed 3 times for 5 minutes in PBS before incubation in fluorophore-conjugated secondary antibody solutions at room temperature for 2 hours and 30 minutes on a rocking table in the dark. Secondary antibodies were diluted in PBS containing 10 mg/mL BSA. Following secondary antibody incubation, tissue slices were washed a final 3 times for 5 minutes in PBS and then mounted onto glass microscope slides using Fluoroshield Aqueous Mounting Medium with DAPI (ab104139, Abcam) and #1.5 thickness high-performance glass coverslips. Mounted slides were stored at 4°C in the dark prior to imaging.

Immunocytochemistry of primary DRG and TG neuron cultures was performed similarly; cultures were maintained for three days *in vitro* prior to experimental use. For experiments requiring nociceptive stimulation, primary neuron cultures were pre-incubated with 1 µM CAP (360376, Sigma-Aldrich), 250 nM BK (05-23-0500, Calbiochem), or 1 µM calcitonin gene-related peptide (CGRP) (1161, Tocris) in a 5% CO_2 humidified atmosphere at 37°C then immediately (without washing) fixed in 4% PFA as previous. Coverslips were washed thrice in PBA for 5 minutes, and immunostaining was performed as above from incubation in PBS-T-T. For STED microscopy, coverslips were mounted using ProLong™ Gold Antifade Mountant without DAPI (P36930, Invitrogen). Immunofluorescence was imaged with either a confocal laser scanning microscopy (LSM) (ZEISS, LSM880 with Airyscan detector) or STEDycon (Abberior) as

required. Fluorophores were excited sequentially to minimise signal bleed-through from overlapping excitation-emission spectra.

2.4.2 Antibodies

Details of the primary antibodies and their respective dilutions used in all immunohisto/cytochemical, western blot and proximity ligation assay (PLA) experiments are listed in Table 2.1. Details of the secondary antibodies and their respective dilutions used in all Immunohisto/cytochemical and western blot experiments are listed in Table 2.2. Where an antibody was used for multiple applications, the dilution for each specific application is given.

Table 2.1: List of primary antibodies

Antigen	Species	Company/Cat. #	Dilution
ANO1	Rabbit Mouse	Boster Bio/pa2290 Santa Cruz/sc-377115	1:500 (Confocal and WB*)/1:200 (STED) 1:200
IP_3R1	Rabbit Mouse	Proteintech/19962-1-AP Santa Cruz/sc-271197	1:500 1:200 (Confocal)/1:100 (STED)
TRPV1	Mouse Rabbit	Proteintech/ 66983-1-Ig Abcam/ab3487	1:500 (Confocal)/1:200 (STED) 1:500
B2R	Mouse	BD Biosciences/610451	1:500
Esyt1	Mouse	Proteintech/67688-1-AP	1:500 (Confocal and WB)/1:200 (STED)
CGRP	Mouse	Santa Cruz/sc-57053	1:200
RAMP1	Mouse	Santa Cruz/sc-293438	1:500
CRLR	Rabbit	Novus Biologicals/NBP1-85643	1:500
Peripherin	Chicken	Abcam/ab39374	1:1000
NF200	Chicken	Thermo/PA110002	1:1000
STIM1	Rabbit	Proteintech/11565-1-AP	1:500
Orai1	Mouse	Abcam/ab175040	1:500
GFP	Mouse	Abcam/Ab1218	1:500
α1H	Mouse	Santa Cruz/sc-377510	1:200
GAPDH	Mouse	Proteintech/60004-1-1	1:5000
B-actin	Rabbit	Cell Signalling/4970	1:1000

*WB, western blot

Table 2.2: List of secondary antibodies

Antibody	Conjugation	Company/Cat. #	Dilution
Goat anti-Mouse	STAR RED	Abberior/STRED-1001	1:250
Goat anti-Rabbit	STAR ORANGE	Abberior/STORANGE-1002	1:250
Goat anti-Chicken	Alexa Fluor™ 488	Invitrogen/A-11039	1:1000
Donkey anti-Mouse	Alexa Fluor™ 488	Invitrogen/A-21202	1:1000
Donkey anti-Rabbit	Alexa Fluor™ Plus 647	Invitrogen/A32795	1:1000
Goat anti-Mouse	HRP*	Cell Signalling/7076	1:10 000
Goat anti-Rabbit	HRP	Cell Signalling/7074	1:10 000

*HRP, horse radish peroxidase

2.4.3 Confocal and Airyscan Image Analysis

Automated cellular segmentation of confocal and Airyscan micrographs of immunostained ganglia sections was performed using the generalist Cellpose algorithm (Stringer et al., 2021) and the resulting masks were manually quality-checked. Neurons were identified based on size and well-documented morphology, and neurons partially in the field of view were excluded from further analysis.

Theoretically, there is a linear relationship between the concentration of fluorophore present in a sample and the intensity of fluorescence that is emitted (van Slageren et al., 1973, Merchant and Periasamy, 2023). Similarly, the response of the detector is also linear (Shihan et al., 2021). Therefore, the intensity of the fluorescent signal detected is expected to be directly proportional to the concentration of fluorophore and, by extension, protein in the sample. Following these assumptions, neurons were classified as immunopositive or immunonegative based on their relative fluorescence intensity. The mean background signal was calculated based on the fluorescence intensity of neurons in a negative control with primary antibodies omitted, and this value was subtracted from the measured intensity values to give x for each cell. For each image, the overall mean fluorescence intensity (μ) and standard deviation (σ) for all identified neurons was obtained, and a Z score for each segmented region of interest (ROI) was calculated according to the following formula:

$$z = \frac{(x - \mu)}{\sigma}$$

Based on the Z score, each neuron's immunoreactivity was classified as either negative ($z < 0.5$) or positive ($z \geq 0.5$), representing a mean fluorescence intensity for each neuron less than 0.5 S.D. values above the overall mean or at least 0.5 S.D. values above the

mean value. In addition to the Z score, each neuron's somatic size was estimated as the Feret's diameter (mean distance between pairs of parallel tangents to the ROI outline) to perform a distribution analysis of protein expression against neuronal size. Distribution data was collated, and the Z score was plotted against somatic diameter for each neuron rather than mean intensity to account for variability in staining quality across experimental repeats and to normalise. All image processing and analysis was performed using FIJI (Schindelin et al., 2012), Microsoft® Excel® for Microsoft 365 MSO (Version 2408) and GraphPad Prism (Version 10.3.1 for Windows, GraphPad Software).

To investigate the colocalisation of expression of paired target proteins in perfusion-fixed ganglionic tissue sections, super-resolution Airyscan micrographs were obtained of immunofluorescence and double-positive neurons identified as described above. Pixel intensity-based colocalisation analysis of background-subtracted images was performed using the Coloc 2 plugin for FIJI to calculate Pearson's correlation coefficient (PCC) for each neuron (Bolte and Cordelieres, 2006).

2.5 Proximity Ligation Assay

PLA is an *in situ* proteomics technique which specifically labels putative protein pair interactions when the two target proteins occur within 40 nm of one another in situ (Fredriksson et al., 2002). For the described experiments, commercial Duolink® In Situ PLA® reagents were purchased from Sigma-Aldrich and used according to the manufacturer's instructions. Primary DRG and TG neuron cultures were briefly washed twice in PBS and then fixed in 4% PFA for 20 minutes on ice. Following fixation, primary cultures were washed 3 times for 5 minutes in PBS and then incubated in PBS-T-T for 45 minutes at room temperature on a rocking table to permeabilise the cells in preparation for the assay. At this point, an ImmEdge® Hydrophobic Barrier Pen (H-4000, Vector Laboratories) was used to delimit a reaction area surrounding each 10 mm coverslip to facilitate the formation of a meniscus of the PLA reagents. Primary cultures were incubated in Duolink® In Situ Blocking Solution (DUO82014) for 1 hour in a humidified atmosphere at 37°C prior to incubation with primary antibody overnight at 4°C. Primary antibodies were diluted in Duolink® In Situ Antibody Diluent (DUO82015) to the concentrations in Table 1.1. Primary cultures were washed 3 times for 5 minutes at room temperature in Duolink® In Situ Wash Buffer A (DUO82049) (0.01 M Tris, 0.15 M NaCl and 0.05% TWEEN 20; pH 7.4) then incubated for 1 hour in a humidified atmosphere at 37°C in an oligonucleotide conjugated secondary antibody solution containing Duolink® In Situ PLA® Probe Anti-Rabbit PLUS (DUO92002) and Anti-Mouse MINUS (DUO92004) (dependent on the primary antibodies used) diluted to a 1:200 concentration in Duolink® In Situ Antibody Diluent. A further wash step was performed

as before using Wash Buffer A, and then primary cultures were incubated for 30 minutes in a humidified atmosphere at 37°C in a ligation solution consisting of 20% Duolink® 5X Ligation Stock (DUO92014) and 2.5% 1 U/µL ligase (DUO92014) in HyClone™ HyPure™ tissue culture-grade water. Following ligation, primary cultures were washed as previously in Wash Buffer A prior to a final incubation period in an amplification solution consisting of 20% Duolink® 5X Green Amplification Stock (DUO92014) and 1.25% 10U/µL polymerase (DUO92014) in HyClone™ HyPure™ tissue culture-grade water for 100 minutes in a humidified environment at 37°C. Primary cultures were washed twice for 10 minutes in Duolink® In Situ Wash Buffer B (DUO82048) (0.2 M Tris, 0.1 M NaCl; pH 7.5) and once for 1 minute in 0.01X Wash Buffer B before mounting on glass microscope slides using Duolink® In Situ Mounting Medium with DAPI (DUO82040). Mounted slides were stored in the dark at -20°C prior to confocal fluorescent LSM imaging (ZEISS, LSM880). Z-stack images were obtained and quantitatively analysed using FIJI according to the protocol established by Lopez-Cano, Fernandez-Duenas and Ciruela (2019). Neurons were identified based on their morphological appearance in corresponding brightfield images obtained prior to fluorescent imaging of the PLA signal. PLA signal was normalised as the number of puncta per unit diameter (calculated as the Feret's diameter in FIJI) to control for heterogeneity in the sensory neuron populations studied.

2.6 Molecular Biology

Freshly excised tissue (DRG, TG, dura mater, liver) was incubated in 200 µL RIPA buffer supplemented with cOmplete™ Mini Protease Inhibitor Cocktail (as above) for 30 minutes on ice prior to mechanical homogenisation. Homogenised tissue samples were centrifuged at 22 000 *g* for 10 minutes at 4°C, and the resulting supernatant was decanted and stored at -20°C prior to analysis.

2.6.1 Protein Concentration

Total protein concentration of tissue lysate samples was estimated using a colourimetric assay based on the Bradford method (Bradford, 1976) to ensure equal amounts of protein for each lysate were subsequently analysed through electrophoresis. Bio-Rad Protein Assay Dye Reagent Concentrate (500-0006, Bio-Rad) was diluted with UltraPure water according to the manufacturer's instructions in a 1:4 ratio prior to use. Following dilution, 700 µL of dye was combined with 2 µL of lysate sample in a disposable 1.5 mL semi-micro cuvette (Z628026, BRAND®) (which has a standard 10 mm light path), and the absorbance measured at 595 nm (A_{595}) using a Jenway™ 6305 spectrophotometer. Bio-Rad Protein Assay Dye Reagent is based on the Coomassie Brilliant Blue G-250 dye, which undergoes a shift in its absorbance maximum from 465 nm to 595 nm upon

binding to basic and aromatic amino acids, therefore, can be used to quantify the concentration of protein in solution based on the A_{595} (Reisner et al., 1975, Sedmak and Grossberg, 1977, Spector, 1978). The total protein concentration for each lysate sample was calculated based on the linear range for a standard curve prepared from known concentrations of BSA (500-0002, Bio-Rad) between 0.2 and 0.9 mg/mL (Kyriakopoulou, 2019). From the protein concentration (c) calculated for each lysate sample, the volume (v) required to analyse 50 µg of protein per well in subsequent electrophoresis was calculated as

$$v = 50/c$$

2.6.2 Sodium Dodecyl Sulphate-Polyacrylamide Gel Electrophoresis (SDS-PAGE)

The required volume of lysate sample was combined with 4x Laemmli Sample Buffer (161-0747, Bio-Rad) in a 3:1 ratio and incubated at 95°C in a digital dry bath for 5 minutes to denature the protein sample. Denatured lysate samples containing 50 µg of protein were loaded into the wells of a 4-20% Mini-PROTEAN® TGX™ Precast polyacrylamide gel (4561094, Bio-Rad), which was secured in a Mini-PROTEAN® Tetra Companion Running Module (1658038, Bio-Rad) for the Mini-PROTEAN® Tetra Vertical Electrophoresis Cell (1658004, Bio-Rad). Samples were run alongside 10 µL of Precision Plus Protein™ All Blue Prestained Protein Standards (1610373, Bio-Rad), which contains a mixture of ten recombinant proteins sized between 10 and 250 kDa. The buffer tank was filled with an appropriate volume of Tris/Glycine/SDS running buffer (25 mM Tris-Base, 192 mM glycine (220910010, Thermo Scientific Chemicals), 0.1% SDS in distilled water, adjusted to pH 8.3) and the electrophoresis cell connected to a PowerPac™ High-Current Power Supply (1645052, Bio-Rad). Electrophoresis of denatured lysate samples was performed at 120V, 3A and 300W for 1 hour and 10 minutes to separate proteins according to their molecular weight.

2.6.3 Western Blot

Following SDS-PAGE, polyacrylamide gels were removed and soaked in Tris/Glycine transfer buffer (25 mM Tris, 192 mM glycine in distilled water, adjusted to pH 8.3). Semi-dry western blotting was performed according to the manufacturer's instructions using the Trans-Blot® Turbo™ Mini 0.2 µm PVDF Transfer Pack (1704156, Bio-Rad) and Trans-Blot® Turbo™ Transfer System (1704150, Bio-Rad). Gels were placed onto polyvinylidene difluoride (PVDF) membranes included in the Trans-Blot® Turbo™ Transfer Pack and sandwiched between the top and bottom ion reservoir stacks and top (cathode) and bottom (anode) cassette electrodes. The transfer was performed at 1.0A and 25V for 30 minutes. Following transfer, the PVDF membrane was trimmed to size according to the expected molecular weights for target proteins and incubated in blocking

buffer (40 mM Tris-HCl, 10 mM Tris-Base, 150 mM NaCl, 1 mM EDTA, 1% TWEEN® 20, 5% skim milk powder (LP0033B, Oxoid) in distilled water) for 2 hours at room temperature on a rocking table. Primary antibody solutions were prepared in blocking buffer to the dilutions specified in Table 2.1, and membranes were incubated overnight at 4°C on a rocking table before washing three times for five minutes in wash buffer (40 mM Tris-HCl, 10 mM Tris-Base, 150 mM NaCl, 1 mM EDTA, 1% TWEEN® 20 in distilled water). Horseradish peroxidase (HRP) conjugated secondary antibody solutions were prepared in blocking buffer to the dilutions specified in Table 2.2, and membranes were incubated for 2 hours at room temperature on a rocking table before washing three times for 10 minutes. Antibody binding to the membrane was visualised using the Super Signal™ West Pico PLUS Chemiluminescent Substrate kit (34580, Thermo Scientific™) according to the manufacturer's instructions. Equal parts of Super Signal™ West Pico PLUS Luminol Enhancer Solution were combined with Super Signal™ West Pico PLUS Stable Peroxide Solution and applied to membranes for 1 minute. HRP oxidises luminol in the presence of peroxide. This reaction produces a chemiluminescent signal that can be visualised, therefore identifying regions of the PVDF membrane where primary-secondary antibody complexes are bound (Yang et al., 2015). Visualisation of the chemiluminescent signal was achieved with the iBright FL1500 Imaging System (A4115, Invitrogen™) using an exposure length between 2 and 30 seconds, dependent on the target protein (ANO1, Esyt1, GAPDH or β-actin).

2.7 Stimulated Emission Depletion (STED) Microscopy

Immunocytochemistry of primary cultured DRG neurons was performed as previously described. Mounted slides were stored at 25°C for 48 hours to allow the mounting medium to fully cure prior to imaging. Two-colour STED imaging was acquired on a ZEISS Axio-Observer Z1 with Abberior STEDYCON attachment using a 775 nm depletion laser for both the STAR RED and STAR ORANGE fluorophores and a 100x/1.4 numerical aperture (NA) oil immersion objective. The excitation wavelengths used for STAR RED and STAR ORANGE were 640 nm and 561 nm, respectively. Optical sectioning was performed at a Z pixel size of 140 nm using a piezoelectric objective positioner and Z stacks were obtained of the full depth of focus for each neuron imaged. Only neurons displaying positive peripherin immunoreactivity and developed arborisation were imaged to ensure a population of healthy, small-diameter neurons was sampled.

2.7.1 Image Processing and Nearest Neighbour Distance Analysis

Raw STED images were deconvolved in Huygens Professional (Version 23.10, Scientific Volume Imaging, Netherlands) using the Standard Deconvolution Express profile prior to further processing in FIJI. A ring-shaped ROI extending into the cytoplasmic

compartment 500 nm perpendicular to the PM was used to capture only protein expression likely to be contained to ER-PM contact sites. To obtain Cartesian coordinates (x, y, z) of localised immunoreactive intensities (puncta), deconvolved STED data was processed using the Phansalkar local threshold algorithm (Phansalkar et al., 2011), and puncta were identified according to the 3D Objects Counter in FIJI (Bolte and Cordelieres, 2006). The MosaicIA plugin for FIJI was used to calculate the nearest neighbour distance (NND) between puncta pairs based on the obtained coordinate values (Shivanandan et al., 2013) and further statistical analysis was performed on these data using GraphPad Prism 10 for Windows 64-bit (Version 10.1.1, GraphPad).

2.8 In Vitro Calcium Imaging

Primary TG neuron cultures were maintained for three days in vitro prior to loading with 2 μM of the ratiometric Ca^{2+} indicator dye fura-2 acetoxymethyl ester (Fura-2 AM) (F1221, Invitrogen) in the presence of 0.01% pluronic F-127 (P2443, Sigma-Aldrich) in standard extracellular solution (EC) (160 mM NaCl, 2.5 mM KCl (P9333, Sigma-Aldrich), 1 mM $MgCl_2$ (M2670, Sigma-Aldrich), 2 mM $CaCl_2$ (C5080, Sigma-Aldrich), 10 mM 4-(2-hydroxyethyl)piperazine-1-ethane-sulfonic acid (HEPES) (BP310-1, Fisher Bioreagents) and 10 mM D-(+)-glucose (G8270, Sigma-Aldrich)) for 30 minutes in a 5% CO_2 humidified incubator at 37°C. Following Fura-2 AM loading, coverslips were washed in standard EC and transferred to a circular perfusion chamber stage insert. The chamber was perfused with room temperature solution at an approximate rate of 2 mL/min by a gravity-driven perfusion system. Fura-2 AM-loaded neurons were identified using the 380 nm excitation wavelength and delimited as ROIs. In vitro imaging experiments were performed using an inverted Nikon TE-2000 microscope with a 20x objective. The imaging setup included a Polychrome V monochromator, IMAGO charge-coupled device camera and the Live Acquisition software (Version 2.2.0, FEI). Fura-2 AM imaging was performed using excitation wavelengths of 340 nm and 380 nm, and emission was filtered using the UV-2A filter cube (Nikon). The fluorescent signal for each wavelength was captured every 2 seconds, and the exposure was adjusted to 150 ms for both 340 and 380 nm to provide an optimal signal-to-noise ratio. To measure Fura-2 AM Ca^{2+} response to CGRP in TG neurons, the following imaging protocol was followed during continuous live imaging: perfusion of standard EC for 1 minute, perfusion of 1 μM CGRP solution (prepared in standard EC) for 2 minutes, subsequent 'washout' perfusion of standard EC for 2 minutes and a final perfusion of 50 mM K^+ EC solution (112.5 mM NaCl, 50 mM KCl, 1 mM $MgCl_2$, 2 mM $CaCl_2$, 10 mM HEPES, 10 mM D-(+)-glucose) for 3 minutes. To investigate neuronal Ca^{2+} response to CGRP in the absence of extracellular Ca^{2+}, a 'Ca^{2+}-free' EC solution was produced with an increased NaCl

concentration (165 mM) to compensate for Cl^- removed by exclusion of $CaCl_2$ from the standard EC solution recipe and used to prepare the CGRP solution.

Data analysis was performed in Microsoft® Excel®. Fluorescence intensity signals were background corrected and the ratio between the signal at 340 nm and 380 nm was calculated for each 2-second timepoint. Fura-2 AM ratios were subsequently normalised to the ratio at t = 0 seconds (R/R_0) and plotted against time. Neurons were positively identified based on their Ca^{2+} response to 50 mM K^+ as elevated extracellular K^+ is commonly used to depolarise the neuronal membrane, which induces Ca^{2+} influx via the $Ca_v1.2$ and $Ca_v1.3$ L-type voltage-gated Ca^{2+} channels (VGCCs) (Rienecker et al., 2020, Lipscombe et al., 2004). To determine which neurons demonstrated a significant increase in $[Ca^{2+}]_i$ following perfusion of 1 µM α-CGRP, a threshold R/R_0 value was determined at 5% of the maximal response to K^+.

2.9 CGRP Release Assay

2.9.1 Sample Collection

To quantify the release of neuropeptide CGRP from trigeminal sensory neurons in primary culture and from a TG ex vivo preparation, a series of enzyme-linked immunosorbent assays (ELISA) were performed. Primary TG neuron cultures were prepared as previously described, and the final cell pellet was resuspended in 300 µL, which was evenly plated over three 10 mm #0 coverslips pre-coated with PDL and laminin in a Costar® Ultra-Low Attachment 24-well plate (CLS3473, Corning®). Cultures were maintained for three days before experimental use. For the ex vivo tissue preparation, the TG were dissected into HBSS on ice and transferred to an Ultra-Low Attachment 24-well plate (one ganglion per well) containing 350 µL 0.22 µm filter-sterilised EC. Tissue samples were incubated at 37°C in a 5% CO_2, humidified incubator for 20 minutes, and the EC was replaced every 5 minutes to ensure adequate oxygenation as previously described (Rasmussen et al., 2022). Prior to treatment, cultures and ex vivo tissue samples were washed three times in 0.22 µm filter-sterilised EC. The appropriate wells were pre-treated for 30 minutes with 1 µM Ani9 (selective ANO1 inhibitor molecule (Seo et al., 2016)) (6076, Tocris) made up in standard EC. Treatment solutions were made up in 0.22 µm filter-sterilised EC supplemented with Protease Inhibitor Cocktail (1 µL/mL) and cOmplete™ Mini Protease Inhibitor Cocktail (1 tablet/10 mL). The treatment solutions were 1) Control (standard EC), 2) 1 µM CAP and 3) 1 µM CAP with 1 µM Ani9. Following the Ani9 pre-treatment, wells were aspirated (without touching the ex vivo tissue preparation or cover glass) and replaced with 350 µL treatment solution. Tissue samples and primary cultures were incubated in treatment solution for 30 minutes at 37°C in a 5% CO_2, humidified incubator. The total volume of

treatment solution containing secreted neuropeptide was collected for subsequent assay and transferred to Protein LoBind® 1.5 mL microcentrifuge tubes (0030108116, Eppendorf). Samples were centrifuged at 1000 *g* for 20 minutes at 4°C, and the resulting supernatant was transferred to new Protein LoBind® 1.5 mL microcentrifuge tubes and stored at - 80°C for less than 24 hours prior to analysis by ELISA.

Once the sample solution was removed for processing, it was replaced with 350 µL ice-cold EC. Following treatment, whole TG ganglia were blotted dry using filter paper and weighed in order to subsequently normalise the concentration of CGRP released (quantified with ELISA) to the dry weight of the whole ganglia to control for total tissue protein content. For primary TG neuron cultures, following a single EC wash, 500 µL RIPA buffer (supplemented with Protease Inhibitor Cocktail, cOmplete™ Mini Protease Inhibitor Cocktail and PMSF as previous) was added and cultures were incubated for 2 minutes at room temperature on a rocking table. Fully lysed cell culture samples were transferred to Protein LoBind® 1.5 mL microcentrifuge tubes and centrifuged at 22 000 *g* for 5 minutes at 4°C. The supernatant was collected for subsequent analysis of total protein concentration with a Micro Bicinchoninic Acid (MicroBCA) protein concentration assay.

2.9.2 MicroBCA Protein Concentration Assay

A commercially available MicroBCA Assay kit (23235, Thermo Scientific) was used to quantify the total protein concentration per well according to the manufacturer's protocol. BSA standards were prepared through serial dilution starting from a 200 µg/mL stock solution. Dilutions of concentrations 100, 40, 20, 10, 5, 2.5, 1, 0.5 and 0 µg/mL were prepared using RIPA buffer as the diluent in order to plot a standard curve against which the protein concentration of samples could be interpolated. Lysate protein samples and standards were assayed in triplicate; therefore, 150 µL of sample or standard was pipetted into each of three wells of a CytoOne® 96-well polystyrene microplate (CC7672-7596, Starlab). MicroBCA working solution was prepared according to the manufacturer's instructions as a 25:24:1 ratio of Reagent MA, Reagent MB and Reagent MC, respectively, and 150 µL added to each well containing sample or standard. The well plate was sealed with Sealing Tape for 96-Well Plates (15036, Thermo Scientific) and mixed for 30 seconds on a rocking table at room temperature prior to incubation for 2 hours in a 37°C, 5% CO_2 humidified incubator. Following incubation, the microplate was cooled to room temperature and the absorbance at 562 nm (A_{562}) was measured using a FLUOstar® Omega multi-plate reader (BMG Labtech). The background absorbance was quantified as the mean of the A_{562} of the 0 µg/mL standard (RIPA buffer diluent). The background absorbance value was subtracted from the absorbance

readings for each unknown sample and standard replicate prior to calculating the mean A_{562} values. A standard curve was prepared by plotting the mean background-subtracted A_{562} values for the standards against their known concentrations in µg/mL and fit with a best-fit second-order polynomial equation using GraphPad Prism 10 for Windows 64-bit (Version 10.1.1, GraphPad Software, Boston, Massachusetts, USA). The concentrations of the unknown samples were therefore interpolated based on this equation, and the mean values were used as a measure of total protein concentration against which to normalise the concentration of CGRP released according to each treatment.

2.9.3 ELISA

A sandwich ELISA was used to quantify the concentration of CGRP released from TG neurons in response to noxious stimulation alone and in the presence of an ANO1 inhibitor. Samples were assayed in triplicate using a commercially available ELISA kit utilising a monoclonal primary antibody against rat CGRP (A05482, Bertin Bioreagent), which has previously been used successfully in the Gamper laboratory to quantify CGRP release from primary cultured TG neurons (Pettinger et al., 2013). All reagents were brought to room temperature prior to use and the samples were thawed from -80 °C on ice. ELISA buffer (A07000, Bertin Bioreagent) was reconstituted with 50 mL of HyClone™ HyPure™ tissue culture-grade UltraPure water according to the manufacturer's instructions. The rat CGRP standard (A06482, Bertin Bioreagent) was reconstituted with 1 mL of ELISA buffer to produce Standard 1 (S1) of known concentration 500 pg/mL. Serial dilution was used to prepare standards 2 through 8 of concentrations 250, 125, 62.5, 31.25, 15.53, 7.81 and 3.91 pg/mL using ELISA buffer. A Quality Control (QC) of known concentration 75 pg/mL (A10482, Bertin Bioreagent) and the CGRP Tracer solution were similarly reconstituted in 1 mL and 10 mL of ELISA buffer, respectively. The ELISA Wash Buffer (A17000, Bertin Bioreagent) was prepared by diluting 1 mL of concentrated stock solution in 400 mL of HyClone™ HyPure™ tissue culture-grade UltraPure water to which 200 µL of Tween® 20 (A12000, Bertin Bioreagent) was added.

The ELISA microplate was washed with 300 µL Wash Buffer five times, and excess solution was blotted away by inversion of the plate onto filter paper. To measure in triplicate, 100 µL for each sample, standard (S1 – S8) and the QC was pipetted into three microplate wells. In addition, 100 µL of ELISA Buffer was added to three wells to measure background absorbance caused by non-specific binding of the CGRP antibody. As an additional control, three wells were designated as Blank wells to which Tracer was not included, and for all other wells containing sample, standard, QC or ELISA Buffer, 100

µL Tracer was added. The microplate was sealed and incubated for 20 hours on a rocking table at 4°C.

Following incubation, wells were emptied by inversion and washed six times with 300 µL of Wash Buffer before blotting dry as previously. Ellman's Reagent (A09000_49+1, Bertin Bioreagent) was prepared 5 minutes prior to the development of the microplate by reconstitution with 49 mL of HyClone™ HyPure™ tissue culture-grade UltraPure water and 1 mL of concentrated Wash Buffer. The ELISA microplate was developed by adding 200 µL Ellman's Reagent and incubated at room temperature for 30 minutes, protected from light. Absorbance was measured at 405 nm (A_{405}) using a FLUOstar® Omega multi-plate reader. The mean A_{405} of the Blank wells was calculated and subtracted from each A_{405} measurement to correct for background absorbance. A standard curve was obtained by plotting the mean background-corrected A_{405} calculated for each standard S1 to S8 against their known concentration and fitting a second-order polynomial equation using GraphPad Prism. The unknown sample concentrations were subsequently interpolated from this equation.

2.9.4 Immunofluorescent Assay

Quantitative immunohistochemistry has also been successfully used to demonstrate CAP-induced differences in the expression levels of CGRP in the trigeminal system (Zhou et al., 2016, Spekker et al., 2021), therefore, an immunofluorescent CGRP expression assay was developed as an alternative to ELISA. Primary TG neuron cultures were prepared as described in Section 2.3 and maintained in vitro for three days prior to identical treatment as described for ELISA. Following treatment, primary TG cultures were washed thrice with standard EC and fixed in 4% PFA on ice for 20 minutes. Immunocytochemistry and subsequent image analysis was performed as described in Section 2.4 using primary antibodies against ANO1 and CGRP. Neurons were identified based on their morphological appearance in corresponding brightfield images obtained prior to fluorescent imaging of immunoreactive signal

2.10 General Statistics

Unless otherwise stated, this thesis presents data as mean ± standard error of the mean (S.E.M.), and datasets consist of at least three biological replicates (tissue obtained from three biologically individual animals). Considering data was collected from heterogeneous cell populations (both the DRG and TG consist of a varied neuron population with respect to both size and modality (Petruska et al., 2000)) it was not deemed representative to pool measurements and calculate a mean value per biological replicate; instead, measurements from cells across all biological replicates were pooled and statistical analysis performed on an 'overall' mean value to better capture the

inherent variability of primary sensory neurons. Where relevant, data was also plotted against somatic diameter to visualise differences due to neuron size and fit with a linear best-fit equation subject to regression analysis (R^2). All statistical analysis was performed using GraphPad Prism 10. The distribution of datasets was assessed for normality using the Shapiro-Wilk test to determine if further parametric or non-parametric statistical testing was appropriate. Between groups comparisons were made using either an unpaired t-test or Mann-Whitney test as appropriate for normally distributed or non-normally distributed data sets consisting of two groups. For datasets of three or more groups, statistical comparisons were made using either a two-way ANOVA and Holm-Sidak's post hoc test for normally distributed data or a Kruskall-Wallis with Dunn's multiple comparisons tests for datasets determined not to be normally distributed.

Chapter 3: Proximity Microscopy Approaches to Investigate ANO1 Signalling Complex Dynamics in Dorsal Root Ganglion Nociceptors

3.1 Introduction

3.1.1 ANO1-Containing Multiprotein Signalling Complexes in the Dorsal Root Ganglion

The impressive array of intracellular signalling pathways reliant on Ca^{2+} as a ubiquitous secondary messenger highlights the importance within somatosensory neurons for precise spatial and temporal restriction of individual Ca^{2+} signals. Changes in $[Ca^{2+}]_i$ regulate a variety of processes from membrane excitability and neurotransmitter release to gene transcription; thus, Ca^{2+} signalling must remain highly distinctive to ensure the specificity of those signals (Berridge, 2006, Berridge, 1998). One mechanism by which the selective localisation of Ca^{2+} signals is achieved is through the compartmentalisation of specific signalling pathways into distinct nanodomains, such as JMSCs. Examples of such localised nanodomains can be found in synaptic active zones as well as at junctions between the PM and SR or ER, where functional coupling of the interacting proteins is maintained via the close, non-fusogenic apposition of organelle membranes (Delmas and Brown, 2002, Dickson and Hille, 2019). In small-diameter nociceptive neurons of the DRG, ANO1-IP_3R1 JMSCs are localised to ER-PM MCSs within nanodomain proximity of B2R and TRPV1, constituting a molecular mechanism for the amplification of both BK- and CAP-induced nociception (Jin et al., 2016, Jin et al., 2013, Liu et al., 2010, Shah et al., 2020).

3.1.2 Evidence for Dynamic Modulation of ER-PM Junctions in the DRG

Common between BK- and CAP-induced ANO1 activation is the principle of close apposition between the ER and PM as essential to facilitate functional coupling between ANO1 and IP_3-mediated release of intracellular Ca^{2+} stores. Indeed, the direct interaction between ANO1 and IP_3R1 (ANO1 is physically tethered to IP_3R1 via its C-terminus and transmembrane 2-3 loop (Jin et al., 2013)) implies a proximity within the close nanometre scale. However, in resting sensory neurons, PM-adjacent regions of the ER may be up to 30 nm apart (Phillips and Voeltz, 2016). Therefore, the dynamic stimulus-dependent modulation of ER-PM proximity describes an important characteristic providing further control over the dynamic range of ANO1-mediated nociception. Indeed, multiple independent lines of investigation support a generalised mechanism whereby the ER undergoes translocation towards the PM in response to intracellular Ca^{2+} store depletion, facilitating the nanodomain proximity between ER-resident and PM-resident JMSC proteins necessary for their functional interaction. Commonly studied is the dynamic interaction between the constituents of the Ca^{2+}-release activated Ca^{2+} (CRAC) channel:

the ER-anchored STIM1 and its PM-resident binding partner, Orai1 (Hogan, 2015). Ultrastructural analysis of HeLa cells revealed a significant increase in the percentage of PM length sharing sub-15 nm apposition with regions of the ER in response to 10-minute stimulation with the Ca^{2+}-ATPase inhibitor thapsigargin, used to deplete intracellular Ca^{2+} stores (Orci et al., 2009). It is thought that the luminal domain of STIM1 undergoes a conformation rearrangement and dimerisation in response to depleted $[Ca^{2+}]_i$, promoting its translocation towards the PM and direct binding of Orai1 to initiate Ca^{2+} influx and refilling of intracellular stores through the formation of new ER-PM junctions: this mechanism is known as store-operated Ca^{2+} entry (SOCE) (Shen et al., 2011, Stathopulos et al., 2006).

Recently, STIM1-Orai1 JMSCs have been shown to be dynamically regulated by the endogenous inflammatory mediator BK in nociceptive DRG neurons. Furthermore, evidence supports the role of Ca^{2+}-sensitive ER-PM contact site tethering proteins such as JPH4 in facilitating the formation of CRAC channel JMSCs (Hogea et al., 2021). Further unpublished observations from the Gamper laboratory support BK-induced translocation of the ER towards the PM: in primary cultured DRG neurons loaded with the ER-selective fluorescent marker ER-Tracker Green, total internal reflection fluorescent (TIRF) microscopy measured a significant increase in fluorescent intensity at the PM surface, suggestive of stimulus-dependent fluctuation in the proximity of the ER to the PM (Shah, 2017). Similar results have been obtained by other groups utilising the luminal ER marker, ER-oxGFP (oxidising environment-optimised green fluorescent protein), to monitor ER translocation under TIRF (Giordano et al., 2013, Saheki et al., 2016a).

3.1.3 Using Proximity Ligation Assay to Investigate Protein-Protein Interactions in Sensory Neuroscience

PLA is a highly sensitive proteomics method enabling the detection and sub-cellular localisation of protein-protein interactions *in situ* when the target proteins are expressed within a ~40 nm proximity (Söderberg et al., 2006, Söderberg et al., 2008, Weibrecht et al., 2010). Observation of a positive PLA signal relies on the formation of a PLA detection complex via the ligation of two complementary oligonucleotide proximity probes (PLUS and MINUS), each conjugated to a secondary antibody raised against the protein target-specific primary antibody. The hybridisation of these PLA oligonucleotides, mediated by DNA ligase, only occurs if the complementary probe pair share at least 40 nm proximity; therefore, it depends on the *in situ* localisation of the target proteins determining the proximity of the primary antibody-antigen complexes. The circular DNA detection complex acts as a template for rolling circle amplification (RCA), catalysed by Phi29 DNA

polymerase enzyme, to produce the rolling circle product (RCP), an approximately 100 kb DNA bundle less than 1 μm in diameter. The RCP is visualised by fluorescent tagging at repeat sequences within the amplified DNA (Söderberg et al., 2008). A positive PLA signal manifests as individual fluorescent puncta with a diameter between 0.5 and 1 μm, which can be resolved by confocal microscopy and quantified as a discrete measure of protein-protein interaction (PPI) (Figure 3.2) (Shah et al., 2020, Jarvius et al., 2006).

PLA circumvents several relevant limitations associated with traditional PPI methodologies based on protein complementation, including the year two-hybrid system (Y2H) and fluorescent resonance energy transfer (FRET) approaches. The Y2H protein complementation assay relies on the reconstitution of a functional transcription factor protein from inactive subunits fused to each putative PPI pair. In the event of PPI, oligomerisation of the interacting protein partners facilitates the reconstitution of the reporter transcription factor, driving the expression of a reporter gene and allowing PPI to be quantified (Brückner et al., 2009). FRET-based proximity assays involve the expression of paired fluorophores with overlapping excitation-emission spectra (a donor and an acceptor fluorophore) conjugated to putative PPI pairs; therefore, resonance energy transfer can take place such that the emission wavelength of the donor fluorophore is capable of exciting the acceptor fluorophore, only when the two proteins share a proximity of up to 10 nm (Ward and Milligan, 2014). Both Y2H and FRET-based PPI assays require the use of homologous expression systems overexpressing the proteins of interest, which is a particular limitation as this gives no useful indication as to whether these proteins interact similarly in a native environment or what physiological role their interaction may play in a heterogeneous cell population. Furthermore, mass overproduction of exogenously expressed proteins may result in false positive signals identifying low-affinity interactions that are not present between endogenous proteins. Conversely, PLA allows the detection of native PPIs *in situ and*, therefore, can be considered a more robust methodology to confirm physiologically relevant multi-protein complex formation.

The commercially available Duolink® In Situ PLA kit has been historically advantageous in studying JMSCs and their contribution to nociception in peripheral sensory neurons. The functional coupling between ANO1 and IP_3R1-mediated localised Ca^{2+} signals in DRG neurons was first inferred through the detection of a PLA signal between ANO1 and IP_3R1 that was not present between ANO1 and VGCC-mediators of global Ca^{2+} transients (Jin et al., 2016, Jin et al., 2013). While original investigations into functional ANO1-IP_3R1 interactions focused on BK-induced Ca^{2+} release, later investigations confirming ANO1's role as a general nociceptive amplifier similarly used PLA to establish nanodomain proximity between ANO1, IP_3R1 and the noxious thermosensor TRPV1

(Shah et al., 2020). Chapter 5 of this thesis additionally presents PLA as a valuable tool for investigating putative ANO1 interactions in the TG, the cranial analogue to the DRG.

3.1.4 Super-Resolution Stimulated Emission Depletion Microscopy: Imaging Protein-Protein Interactions Beyond the Diffraction Limit

Efficient and successful protein-protein interaction relies upon the co-localisation and compartmentalisation of essential interacting molecules into their distinct signalling nanodomains within a cell (Batada et al., 2004). Multiplexed immunohistochemistry and immunocytochemistry are standard antibody-based techniques used to visualise the sub-cellular localisation of proteins of interest via the formation of highly specific antibody-antigen complexes, which can be probed with fluorophore-conjugated secondary antibodies and imaged using fluorescence confocal microscopy. Commonly, co-localisation of fluorophore signal as assessed by various quantitative colocalisation algorithms measuring the correlation in intensity and expression pattern is accepted as evidence of PPI (Petrescu et al., 2003, Agnati et al., 2005, Parmryd et al., 2003).

However, while colocalisation would posit an interaction between protein pairs, the resolution limit (minimum distance at which two distinct points can be distinguished as separate) of confocal microscopy (≈ 250 nm) is such that apparent spatial overlap between two fluorophore markers does not necessarily constitute close protein juxtaposition (MacDonald et al., 2015). This limitation is due to a fundamental physical property of light known as diffraction, which describes the spreading out of photons when a point source of light, such as a fluorophore, is focused (Abbe, 1873). The concentric ring-like diffraction pattern of such point light sources is known as the Airy disc, and its intensity profile in the lateral axis can be plotted as a point spread function (PSF), the resolution of which can be defined as the full width at half maximum (FWHM) (Figure 3.3A) (Schmolze et al., 2011, Airy, 1835). Therefore, the diffraction limit can be overcome by reducing the size of the PSF.

An elegant solution to overcoming this diffraction barrier to achieve super-resolution imaging employs the principle of stimulated emission using a depletion laser (Hell and Wichmann, 1994). Here, stimulated emission refers to the optical process through which a fluorophore becomes de-excited to its ground state by an incident photon; with respect to STED microscopy, this is achieved with a doughnut-shaped depletion laser with a zero-intensity point which selectively de-activates an area surrounding the excitation laser to minimise the region from which emission is detected to the centre of the ‘doughnut’, therefore, effectively narrowing the point spread function (Figure 3.3B) (Dunst and Tomancak, 2019). Theoretically, STED microscopy is diffraction-*unlimited* as the effective achievable resolution is proportional to the inverse square root of the

saturation factor of the depletion laser; therefore, by increasing depletion laser intensity, the FWHM of the PSF is reduced (Harke et al., 2008).

Two-colour STED microscopy has been used to investigate the localisation of synaptic proteins syntaxin 1 and synaptophysin in cultured hippocampal neurons prepared from neonatal rats. The super-resolution achieved (25 – 35 nm) was sufficient to reveal clustering of the proteins confined to different regions of the synapse, providing ultrastructural information not available through conventional confocal microscopy (Meyer et al., 2008). In addition to sub-cellular localisation down to the molecular scale, STED microscopy is particularly suited to colocalisation studies when both fluorophores undergo stimulated emission via the same depletion doughnut simultaneously, ensuring perfect alignment (Göttfert et al., 2013). Dual-colour STED microscopy imaging of individual hippocampal synapses at the single fluorophore level has been used to reveal unique colocalisation between different neurotransmitter vesicular transporter proteins expressed at single synaptic vesicles, lending credibility to theorised 'co-release' of different neurotransmitters from the same vesicle pool (Upmanyu et al., 2022). Together, these reports from the literature suggest STED microscopy may be a powerful and accessible approach to investigating colocalisation between JMSC proteins in peripheral sensory neurons in a physiologically meaningful manner.

3.1.5 Research Objectives and Hypotheses

It is likely that in DRG sensory neurons, the ER undergoes a stimulus-dependent remodelling, which may similarly be necessary for the functional interaction between ANO1 and IP_3R1, as confirmed for STIM1 and Orai1. The first section of this thesis chapter will examine the use of a proteomics approach (PLA) to study the dynamic interactions between JMSC proteins, while the second section will investigate the use of super-resolution STED microscopy to characterise protein-protein interactions in small-diameter DRG neurons.

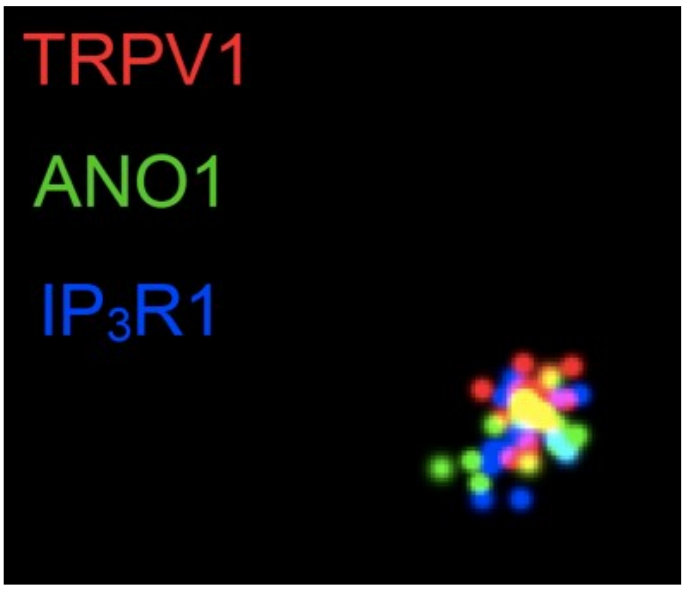

Figure 3.1: Three-colour STORM revealed ANO1-TRPV1-IP_3R1 complex formation in DRG neurons. Representative STORM image of clustering between TRPV1 (red), ANO1 (green) and IP_3R1 (blue) demonstrates protein-protein interactions at putative junctional multiprotein signalling nanodomains in fixed DRG neurons (Adapted from Shah, 2017). Scale bar = 200 nm. STORM, stochastic optical reconstruction microscopy; TRPV1, transient receptor potential vanilloid type 1 receptor; ANO1, anoctamin 1; IP_3R1, inositol triphosphate receptor type 1.

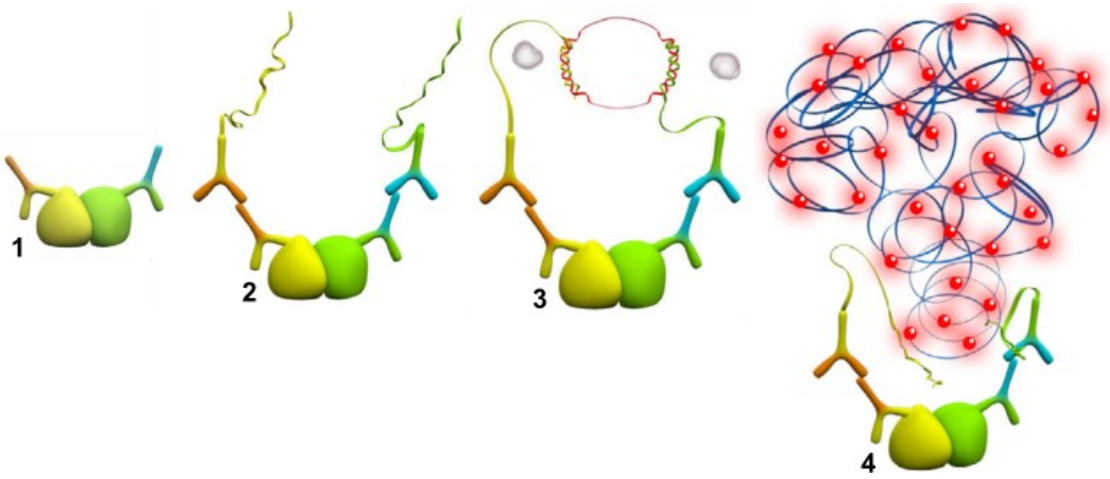

Figure 3.2: Schematic of the reaction theory underlying PLA. 1) Binding of selective primary antibodies against two target proteins with ≤ 40 nm proximity is subsequently detected by two complementary oligonucleotide proximity probes (PLUS and MINUS) conjugated to secondary antibodies raised against the protein-specific primary antibodies **(2)**. **3)** Hybridisation between the PLUS and MINUS oligonucleotides catalysed by DNA ligase forms a circular DNA strand which is amplified by a rolling circle mechanism catalysed by Phi29 DNA polymerase. **4)** The resulting DNA bundle is visualized by inclusion of fluorophore-tagged complementary oligonucleotide probes at specific repeat sequences within the rolling circle product. PLA signal manifests as individual fluorescent puncta with a diameter between 0.5 and 1 µm, which is readily resolved using confocal microscopy. Adapted from Marck, 2017. PLA, proximity ligation assay.

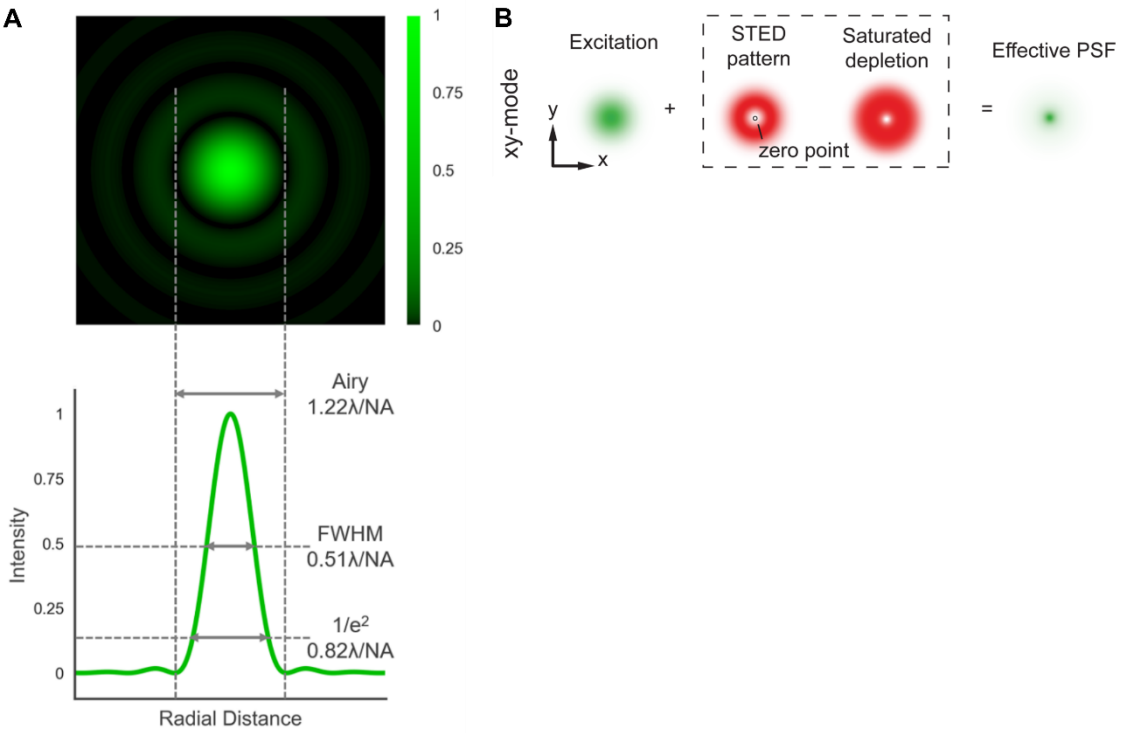

Figure 3.3: Theoretical principles underlying Stimulated Emission Depletion (STED) microscopy. A) Diagram showing a theoretical Airy Disc diffraction pattern for a point source of light such as a single fluorophore and associated Point Spread Function as a profile of intensity across the Airy Disc. The diameter of the Airy disc is taken as the distance between the first minima of the diffraction pattern and is defined as 1.22λ/NA, where λ is the excitation wavelength in nm and NA is the numerical aperture of the objective lens used. The Full Width at Half Maximum (FWHM) is the generally accepted measure of the lateral spatial resolution limit and can be defined as a theoretical minimum equal to 0.51λ/NA. Spot size may also be measured as the width of the Airy Disc at the $1/e^2$ intensity which is equal to 0.82λ/NA. Adapted from Edinburgh Instruments, 2024. **B)** Diagram showing the theory underlying STED super-resolution microscopy. Excited fluorophores undergo stimulated emission through the use of a doughnut-shaped high-power depletion laser with a zero-intensity point at the centre, therefore, minimising the diameter of the effective point spread function as surrounding emission is de-excited. Adapted from Huang et al, 2009.

3.2 Results

3.2.1 Evaluating Proximity Ligation Assay as an Approach to Study Protein-Protein Interactions in Sensory Neurons

Although PLA has been previously used in the Gamper laboratory to demonstrate nanodomain proximity between ANO1, IP_3R1 and TRPV1 (Jin et al., 2013, Shah et al., 2020), these experiments were performed in non-stimulated neurons. Therefore, a 'time-resolved' approach to PLA was developed and optimised to investigate dynamic interactions between JMSC proteins in the DRG in response to noxious stimulation.

A series of positive and negative controls were performed in primary cultured DRG neurons to confirm the ability of PLA to accurately distinguish nanodomain proximity between paired proteins (Figure 3.4). PLA detects proximity between target proteins within ~40 nm. Therefore, a simple positive control to demonstrate the efficacy of the reaction is to target proteins that are known to interact in the cell type of study. To confirm the efficacy of PLA in primary cultured DRG nociceptive neurons, PLA between the CRAC channel proteins STIM1 and Orai1 was performed utilising primary antibodies previously validated for their use in PLA (Hogea et al., 2021). As expected, a robust punctate PLA signal was observed, confirming nanodomain proximity between the interactors (Figure 3.4A). A second robust positive control for PLA can be visualising a single target protein using two primary antibodies raised in separate species. For this, the ER-PM junctional tethering protein Esyt1 (Kang et al., 2019b) was probed using anti-rabbit and anti-mouse primary antibodies and corresponding PLUS and MINUS oligonucleotide-conjugated secondary antibody probes. Considering both primary antibodies bind distinct epitopes of the same target protein, a positive PLA signal is expected, confirming at least 40 nm proximity between the PLUS and MINUS probes. Indeed, a strong punctate signal was observed, confirming the reliability of PLA to detect proximity between the secondary oligonucleotide probes when bound to target primary antibodies (Figure 3.4A).

A series of negative controls were also performed to confirm the specificity of PLA and identify any non-specific proximity signals that may be due to non-specific primary or secondary antibody binding. PLA was performed using previously validated primary antibodies against the α1H subunit of the T-type VGCC ($Ca_v3.2$) and ANO1 (Figure 3.4B). Although both ANO1 and $Ca_v3.2$ are abundantly expressed at the PM of medium-diameter DRG sensory neurons (Talley et al., 1999), ANO1 does not functionally couple to global $Ca_v3.2$-mediated Ca^{2+} transients; therefore, nanodomain proximity between ANO1 and $Ca_v3.2$ is not expected to occur (Jin et al., 2016, Jin et al., 2013, Liu et al., 2010). Indeed, no discernible puncta were observed, suggesting ANO1 and $Ca_v3.2$

expression is segregated to distinct signalling domains at least 40 nm apart in DRG neurons and, therefore, bound secondary oligonucleotide probes are incapable of mediating proximity ligation. A further technical negative control for PLA includes omitting the primary antibodies, thus identifying non-specific binding of oligonucleotide probes. No puncta were detected when PLA was performed in the absence of primary antibodies, confirming the specificity of binding of the secondary antibody probes in DRG neurons (Figure 3.4B). The combination of these positive and negative controls demonstrated PLA as a suitable technique for investigating protein-protein interactions in primary cultured peripheral sensory neurons.

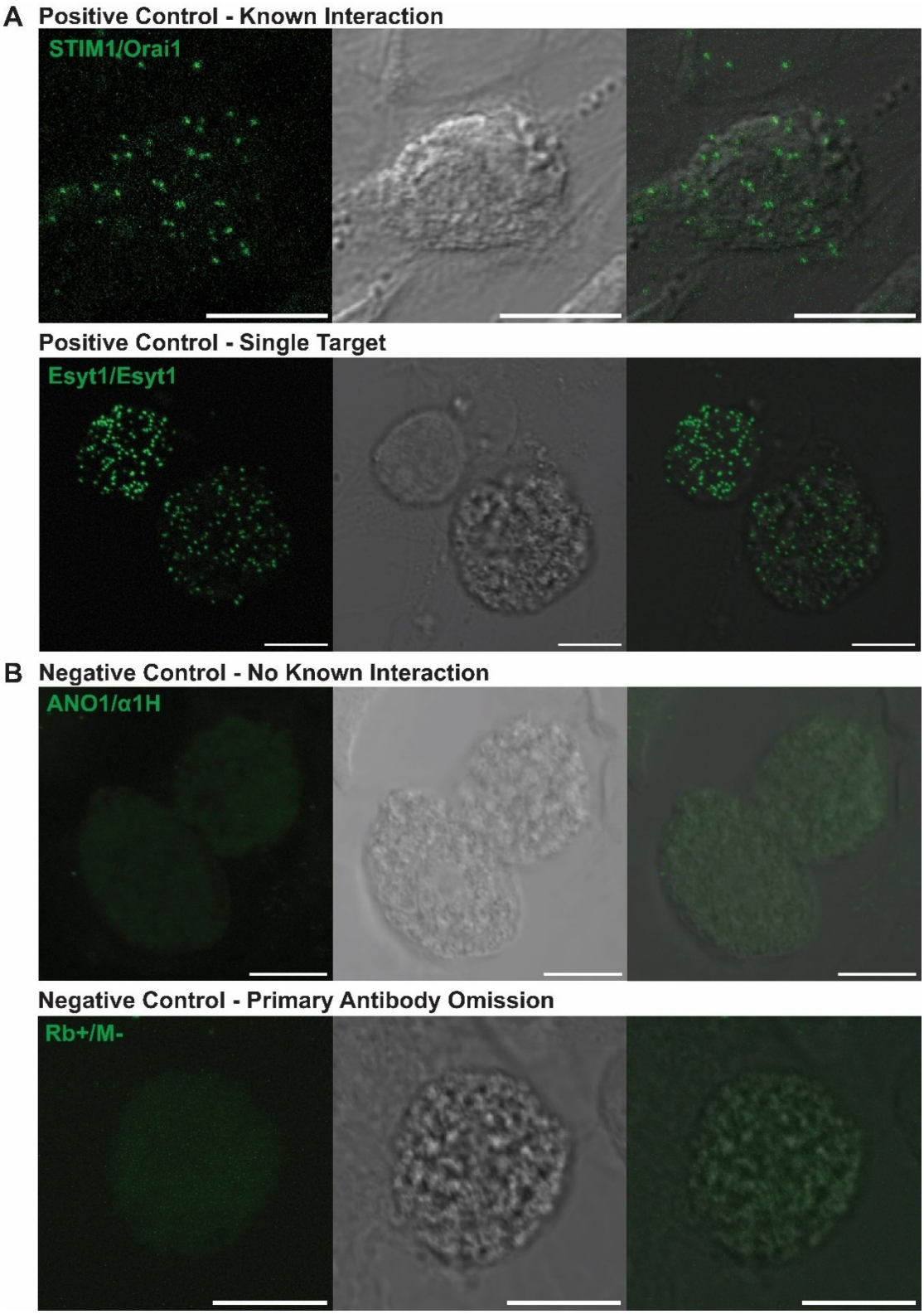

Figure 3.4: Controls to verify the use of PLA to detect nanodomain proximity between target proteins in primary rat dorsal root ganglion neuron cultures. A) Positive controls for PLA include probing for a known protein-protein interaction in the target cell type (top row) or using two primary antibodies against the same target protein (bottom row). A positive PLA signal is observed as fluorescent puncta between 0.5 and 1 µm in size (Jarvius et al., 2006). **B)** Negative controls for PLA include probing for two proteins not known to interact in the target cell type (top row) or performing PLA as standard other than omitting the primary antibodies to control for non-specific binding and ligation of the oligonucleotide-conjugated secondary antibody probes. Scale bars = 10 µm. PLA, proximity ligation assay; STIM1, stromal interaction molecule 1; Esyt1, extended synaptotagmin 1; ANO1, anoctamin 1; α1H, $Ca_v3.2$ T-type voltage-gated calcium channel; Rb+, Rabbit PLUS PLA oligonucleotide probe; M-, Mouse MINUS PLA oligonucleotide probe.

3.2.2 'Time-Resolved' PLA Reveals Stimulus-Dependent Formation of ANO1-IP_3R1 Junctional Multiprotein Signalling Complexes in Dorsal Root Ganglion Nociceptive Neurons

Functional coupling between ANO1 and IP_3R1 is a well-established mechanism conferring amplification of inflammatory signalling in small-diameter nociceptive neurons of the DRG (Jin et al., 2016, Jin et al., 2013). Although nanodomain proximity between ANO1, IP_3R1 and B2R in DRG sensory neurons at rest (prior to stimulation) has been confirmed using PLA and co-immunoprecipitation studies, patch clamp electrophysiology approaches were used to verify direct interaction between ANO1 and IP_3R1 via the ANO1 α2-3 loop and C-terminus following stimulation of the proinflammatory protease-activated receptor 2 (PAR-2). Direct evidence of ANO1-IP_3R1 complexing in response to the inflammatory mediator BK has not been published. Therefore, to first confirm continued nanodomain proximity between ANO1 and IP_3R1 during noxious stimulation as a proof of principle experiment, PLA was performed in primary cultured DRG neurons exposed to 250 nM BK for 1 minute prior to immediate fixation in 4% PFA without washout.

In neurons at rest, puncta denoting a positive PLA signal between ANO1 and IP_3R1 were detected in 43 out of 83 neurons (N = 3), representing 51.8% of the cultured DRG neuron population (Figure 3.5A). The mean somatic diameter of control neurons with confirmed nanodomain proximity between ANO1 and IP_3R1 was 18.1 ± 0.906 μm, consistent with previous reports confirming ANO1-IP_3R1 functional coupling in small-diameter nociceptive neurons (Jin et al., 2016, Jin et al., 2013, Shah et al., 2020). When DRG cultures were stimulated with 250 nM BK, the proportion of neurons positive for PLA between ANO1 and IP_3R1 significantly increased to 86.6% (58 out of 67, N = 3) ($p < 0.0001$, Fisher's exact test) (Figure 3.5B). The rat DRG consists of a heterogeneous population of sensory neurons typically consisting of neurons with somatic diameters between 10 and 55 μm (Bosco et al., 2010). Mathematically, a neuron with a larger diameter will have a greater PM surface area and may possess a more extensive ER architecture; therefore, larger-diameter neurons will express a greater volume of target proteins, increasing the chance for PLA to detect individual nanodomain complexes compared to a smaller-diameter neuron.

To control for the range of neuronal sizes, the number of PLA puncta per neuron was therefore normalised to somatic diameter (puncta/diameter in μm). Interestingly, stimulation with 250 nM BK not only significantly increased the proportion of neurons displaying positive PLA signal between ANO1 and IP_3R1, but the normalised mean number of puncta also significantly increased from 0.228 ± 0.0292 to 0.573 ± 0.0428 (p

< 0.0001, Mann-Whitney test) (Figure 3.5C). In DRG neurons, BK acts at the G_q protein-coupled B2R, therefore, initiating an intracellular signalling cascade that results in the release of IP_3-sensitive ER Ca^{2+} stores (Liu et al., 2010). In order to investigate whether the BK-induced increase in PLA signal between ANO1 and IP_3R1 could be due to the release of intracellular Ca^{2+}, the experiment was repeated in Ca^{2+}-free extracellular conditions. Under this experimental setup, any Ca^{2+} transient occurring in the neuron must be due to release of intracellular stores, rather than influx of extracellular Ca^{2+}. Remarkably, 99.5% of DRG neurons (182 out of 183, N = 3) displayed a robust punctate PLA signal between ANO1 and IP_3R1 following 250 nM BK stimulation in Ca^{2+}-free conditions, representing a significantly greater proportion of cells than both the control neurons ($p < 0.0001$, Fisher's exact test) and those treated with BK under normal extracellular Ca^{2+} concentrations ($p < 0.0001$, Fisher's exact test) (Figure 3.5D). Similarly, the mean normalised puncta increased significantly in neurons exposed to BK in Ca^{2+}-free conditions (0.860 ± 0.0310), compared to the control neurons ($p < 0.0001$, Mann-Whitney test) (Figure 3.5E). Together, these data suggest that not only does BK promote an increase in proximity between ANO1 and IP_3R1 but that this dynamic rearrangement is not reliant on extracellular Ca^{2+} influx.

Although PLA measures putative protein-protein interaction in fixed samples, a 'time-resolved' approach to fixation was developed to capture the dynamics of interaction between ANO1 and IP_3R1 in response to increasing duration of stimulation with BK. Primary DRG cultures were individually exposed to 250 nM BK under normal extracellular Ca^{2+} concentrations for 10, 20, 30, 40, 50, 60, 120, 180 and 300 seconds prior to immediate fixation in 4% PFA without washout. Punctate PLA signal was detected in small-diameter DRG neurons at all time points (Figure 3.6A); however, quantifying the mean number of puncta per neuron revealed a distinct time course in the nanodomain proximity between ANO1 and IP_3R1. Compared to the control group, the mean PLA signal per neuron was only significantly elevated between 40 and 180 seconds of exposure to BK ($p < 0.0001$, Kruskall-Wallis with Dunn's multiple comparisons tests) (Figure 3.6B). Plotting the mean number of puncta per neuron against time revealed that initially, upon BK stimulation, there was a slight reduction in PLA signal between ANO1 and IP_3R1, albeit not significant, followed by a sharp increase, which peaked at 50 seconds before a gradual decline back to baseline levels (Figure 3.6C). Most intriguingly, the kinetics of this response appeared to closely match the kinetics of BK-induced translocation of the IP_3/PIP2 signalling probe PLCδ-PH when overexpressed in cultured DRG neurons and of BK-induced Fura-2 AM Ca^{2+} transients (Liu et al., 2010) suggesting that ANO1-IP_3R1 coupling dynamics may occur on a similar timescale to BK-evoked release of IP_3-sensitive ER Ca^{2+} stores, and further, that this

coupling is perhaps dependent on intracellular Ca^{2+} release. Together, these data support a scenario whereby functional coupling between ANO1 and IP_3R1 is a dynamically regulated response to noxious stimulation. This mechanism likely provides an important level of control over ANO1-mediated amplification of noxious stimulation. It raises important questions regarding how the interaction between ANO1 and IP_3R1 may become dis-regulated during peripheral sensitisation or the pathogenesis of chronic pain conditions.

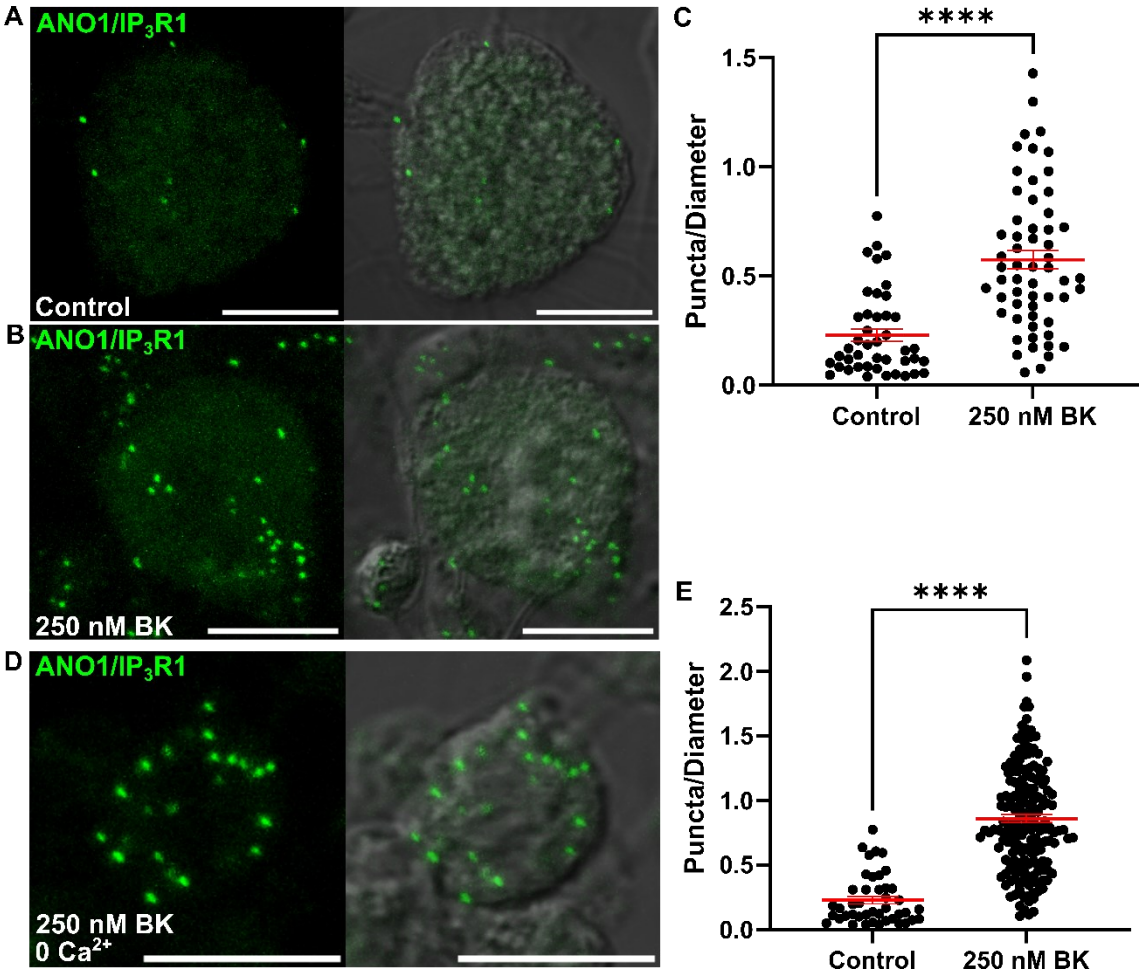

Figure 3.5: PLA confirms dynamic nanodomain proximity between ANO1 and IP_3R1 in small-diameter DRG neurons. Representative confocal micrographs depicting robust punctate PLA signal between the calcium-activated chloride channel ANO1 and the ER-localised IP_3-sensitive calcium channel IP_3R1 in primary neuron cultures prepared from neonatal (P3-7) rat DRGs. Cultures were fixed in 4% PFA at rest **(A)** or immediately following 60-second exposure to the inflammatory mediatory bradykinin (250 nM) **(B)**. **C)** The number of PLA puncta per neuron was normalised to respective somatic diameter to control for a heterogeneous population. Stimulation with 250 nM BK significantly increased the mean number of puncta per neuron suggesting increased nanodomain proximity between ANO1 and IP_3R1. **D)** Representative confocal micrograph of PLA signal between ANO1 and IP_3R1 following 60-second stimulation with 250 nM BK in a Ca^{2+}-free extracellular environment. **E)** Stimulation of DRG neurons with 250 nM BK in the absence of extracellular Ca^{2+} significantly increased the mean number of PLA puncta per neuron (normalised to respective somatic diameter), suggesting dynamic regulation of the nanodomain proximity between ANO1 and IP_3R1 is dependent on the release of intracellular Ca^{2+} stores. Error bars represent mean ± SEM. Scale bars = 10 µm. ****$p < 0.0001$, Mann-Whitney test. PLA, proximity ligation assay; BK, bradykinin; ANO1, anoctamin 1; IP_3R1, inositol triphosphate receptor type 1.

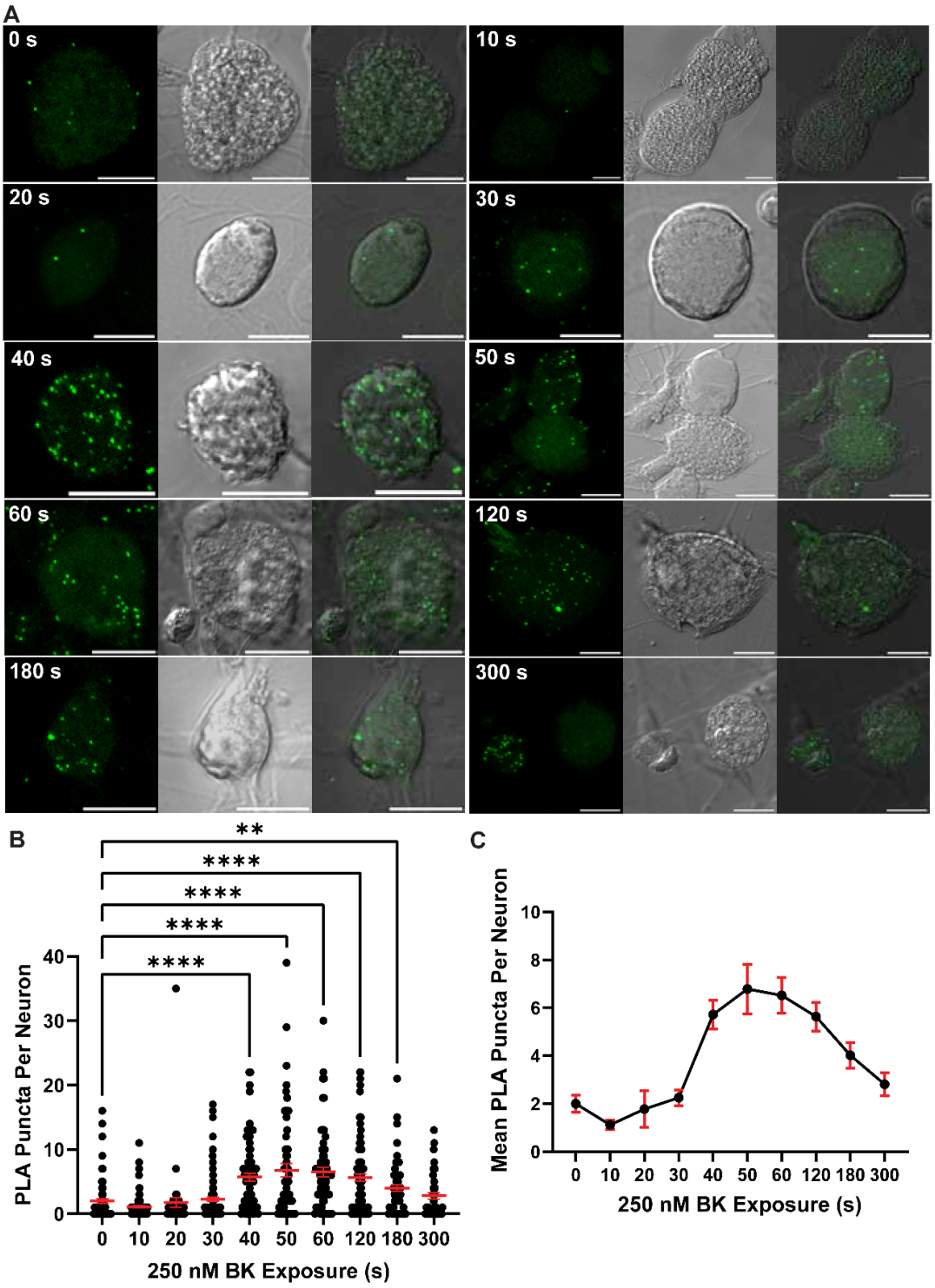

Figure 3.6: Time-resolved PLA reveals BK-induced nanodomain proximity between ANO1 and IP_3R1 in primary cultured DRG neurons. A) Individual primary DRG cultures were exposed to 250 nM BK for progressively increasing periods (10, 20, 30, 40, 50, 60, 120, 180 and 300 seconds) prior to immediate fixation in 4% PFA. PLA performed between ANO1 and IP_3R1 revealed robust punctate signal at all time points as shown in maximum intensity projections of confocal Z stacks. **B)** The mean number of PLA puncta per neuron was significantly greater than the baseline from 40 seconds to 180 seconds of stimulation with 250 nM BK (Kruskall-Wallis with Dunn's multiple comparisons tests). **C)** Plotting the mean number of puncta per neuron against length of BK exposure revealed kinetics of ANO1-IP_3R1 interaction similar to that observed for BK-induced translocation of the IP_3/PIP2 sensor PLCδ-PH (insert) (Liu et al., 2010). Error bars represent mean ± SEM. Scale bars = 10 μm. **p < 0.01, ****p < 0.0001; Kruskall-Wallis with Dunn's multiple comparisons tests. PLA, proximity ligation assay; BK, bradykinin; ANO1, anoctamin 1; IP_3R1, inositol triphosphate receptor type 1.

3.2.3 Proximity Ligation Assay Reveals Differential Stimulus-Dependent Nanodomain Signalling Complex Formation Between ANO1-TRPV1 in Dorsal Root Ganglion Nociceptive Neurons

In small-diameter sensory neurons from the DRG, the functional interaction between ANO1 and IP_3R1 is considered a fundamental mechanism in amplifying both BK-induced inflammatory nociception and CAP-evoked noxious signalling. This occurs via coupling to B2R and TRPV1, respectively, at junctional multi-protein signalling complexes (JMSCs) that form at MCSs between the ER and PM (Jin et al., 2013, Shah et al., 2020). Understanding the interplay between these processes is crucial to decoding the complexities of nociception. Although well-established, experiments confirming the role of ANO1 in these two signalling cascades have been performed independently of one another. Furthermore, limited experimental work has been carried out to investigate the putative role of ANO1-IP_3R1 coupling in peripheral sensory neurons under physiological conditions, including examining the response of peripheral nerve terminals to noxious environmental stimuli. However, evidence from *in vitro* and *in vivo* models of neuropathic pain confirms a significant interplay between TRPV1 and B2R-mediated signalling cascades in the context of peripheral sensitisation (Sugiura et al., 2002).

Peripheral sensitisation is primarily characterised by a reduction in the activation threshold (allodynia) and an increase in the responsiveness of nociceptors to external stimuli (hyperalgesia) following tissue injury (Basbaum et al., 2009). The neuro-inflammatory response to injury is triggered by the infiltration of immune cells, which release various pro-inflammatory mediators, including BK, into the extracellular space. At peripheral nerve terminals expressing B2R, activation by BK initiates the G_q protein-mediated signalling cascade involving the activation of PLC, which hydrolyses PIP2 into IP_3 and DAG. In addition to the previously discussed mechanisms of IP_3-mediated release of intracellular Ca^{2+} stores, DAG mediates an important role in contributing to BK-induced thermal and chemical hypersensitivity via TRPV1. DAG is known to activate protein kinase C (PKC), which, in turn, has been shown to phosphorylate TRPV1, reducing its thermal activation threshold to ambient temperature (Premkumar and Ahern, 2000, Bhave et al., 2003, Numazaki et al., 2002). An equivalent mechanism has also been shown to potentiate TRPV1 activation by CAP in primary cultured DRG neurons (Vellani et al., 2001). Alternatively, BK-mediated activation of PLC contributes to a depletion of PM-bound PIP2; PIP2 may act as an inhibitory modulator of TRPV1. Therefore, its depletion disinhibits TRPV1, further amplifying TRPV1-mediated nociceptive signalling, although this mechanism is contested within the literature (Rohacs, 2015). Irrespective of the underlying mechanism, *in vivo* evidence supports

TRPV1 contribution to BK-evoked nocifensive behaviour; injection of BK to the plantar surface of the forepaw was shown to evoke a significantly attenuated nocifensive behavioural response (paw licking) in TRPV1-knock out mice compared to wild type, suggesting TRPV1 activation may be a critical mediator of BK-induced nociception in peripheral neurons (Katanosaka et al., 2008).

This reciprocity between B2R and TRPV1 signalling cascades raises an important question concerning the proposed activity-dependent interactions between ANO1 and IP_3R1 in the DRG: does ANO1 display preferential coupling to either B2R- or TRPV1-mediated IP_3-sensitive Ca^{2+} release? Furthermore, how might this combination of functionally coupled proteins be arranged? Do ANO1-B2R and ANO1-TRPV1 nanodomains exist as separate and distinct entities, or are all 3 PM receptors more likely to be localised to larger 'super-complexes'?

PLA has previously been used to demonstrate nanodomain proximity between ANO1, IP_3R1, and B2R and ANO1, IP_3R1, and TRPV1 in nociceptive DRG neurons; however, colocalisation between B2R and TRPV1 has not yet been assessed. Primary neuron cultures prepared from dissociated neonatal rat DRGs were maintained *in vitro* for 3 days prior to fixation with 4% PFA. PLA was performed using previously validated anti-B2R and anti-TRPV1 primary antibodies (Jin et al., 2013, Shah et al., 2020). A robust punctate signal was observed in non-stimulated neurons, which indicates at least 40 nm proximity between B2R and TRPV1 (Figure 3.7). This finding supported a hypothesised 'super-complex' describing a scenario where ANO1, B2R and TRPV1 are all co-localised within nanodomain proximity at the same ER-PM junctions, which may undergo stimulus-dependent rearrangement to gain proximity with IP_3R1. Furthermore, this supports prior STORM data demonstrating that ANO1-TRPV1 and ANO1-TRPV1-IP_3R1 superclusters are more abundantly expressed in DRG neurons than independent ANO1 immunoreactivity, which was rarely observed expressed alone (Shah et al., 2020).

To test this hypothesis, independent DRG neuron cultures (N = 3) were stimulated for 5 minutes with either 250 nM BK BK, 1 µM CAP, or both BK and CAP simultaneously before immediate fixation in 4% PFA without recovery. To investigate how ANO1 nanodomains may be differentially regulated, PLA between ANO1 and TRPV1 was quantified for each of the three experimental conditions and in control cells. TRPV1 was selected for this initial study over B2R due to its wealth of interacting partners, which may or may not be additionally associated with ANO1 (Gamper and Shah, 2022). Furthermore, prior evidence from super-resolution STORM imaging has suggested DRG neurons express ANO1-TRPV1 complexes that are not co-localised to IP_3R1, although

these experiments were conducted in non-stimulated neurons; therefore, whether this proportion of complexes would gain proximity to IP_3R1 upon stimulation is not certain (Shah et al., 2020). Consequently, it was relevant to investigate how ANO1-TRPV1 nanodomains behave in response to G_qPCR activation (via BK at B2R), considering that the release of IP_3-sensitive Ca^{2+} stores will likely promote ANO1 nanodomain formation.

PLA signal between ANO1 and TRPV1 was detected in control neurons, those stimulated with 1 μM CAP, 250 nM BK, and those dually stimulated with both CAP and BK of the same doses (Figure 3.8A-D). PLA-positive neurons were defined as those with at least 1 detectable fluorescent punctum found within the boundary of the cell identified in the corresponding brightfield image. The mean somatic diameter of DRG neurons positive for PLA between ANO1 and TRPV1 did not significantly differ between the experimental conditions (including the control) ($p = 0.0835$, Kruskall-Wallis test). Still, it confirmed that ANO1-TRPV1 coupling is restricted to small-diameter, putative nociceptive neurons. The mean somatic diameters were 13.3 ± 0.323, 11.8 ± 0.460, 13.1 ± 0.280 and 12.9 ± 0.225 μm for control neurons, CAP-stimulated, BK-stimulated and dually stimulated neurons, respectively (Figure 3.8E). The percentage of the analysed neuronal population positive for PLA signal between ANO1 and TRPV1 was compared between the four experimental conditions (Figure 3.8F). Interestingly, treatment with either 1 μM CAP (95.1% PLA-positive) or 250 nM BK alone (94.0% PLA-positive), but not together, significantly increased the percentage of neurons positive for PLA between ANO1 and TRPV1 compared to the control (84.8%) ($p = 0.0186$ and $p = 0.0005$, respectively; Fisher's exact test). There was no significant difference in the percentage of the PLA-positive neuronal population between the control and the dual-stimulation groups (84.6%) ($p > 0.999$; Fisher's exact test). Similarly, there was no significant difference between the CAP and BK conditions ($p > 0.999$; Fisher's exact test).

The number of puncta per neuron was quantified and normalised to the respective somatic diameter as previously described to compare experimental conditions (Figure 3.8G). The baseline mean number of PLA puncta per unit diameter for control neurons was 0.626 ± 0.0358. Unsurprisingly, treatment with 1 μM CAP significantly increased this value to 1.19 ± 0.123 ($p = 0.0025$ compared to the control; Kruskall-Wallis with Dunn's multiple comparisons test), suggesting a general increase in proximity between ANO1 and TRPV1 in response to CAP activation of TRPV1. Treatment with 250 nM BK alone did not significantly affect the mean number of puncta (normalised to diameter) compared to the control (0.686 ± 0.0340; $p > 1.00$ compared to the control; Kruskall-Wallis with Dunn's multiple comparisons test), suggesting no BK-evoked change in proximity between ANO1 and TRPV1. However, when DRG neurons were

simultaneously stimulated with 1 μM CAP and 250 nM BK, the mean normalised puncta per neuron between ANO1 and TRPV1 was reduced to 0.374 ± 0.0153. This represented a significant reduction compared not only to the control ($p < 0.0001$) but also to those neurons stimulated with CAP ($p < 0.0001$) or BK ($p < 0.0001$) alone. This unexpected result suggests that while neuronal activation by CAP alone increased proximity between ANO1 and TRPV1, when neurons are co-activated by both CAP and BK simultaneously, proximity between ANO1 and TRPV1 is reduced by a mechanism not evoked by BK stimulation alone. Initially, this suggests the number of active ANO1 channels expressed at ER-PM junctions may be a rate-limiting factor to TRPV1-ANO1 functional coupling and perhaps ANO1 engages in preferential coupling to BK-induced Ca^{2+} release over interaction with TRPV1. Clearly, further experimental work is required to elucidate this complex interplay between nociceptive signalling mechanisms.

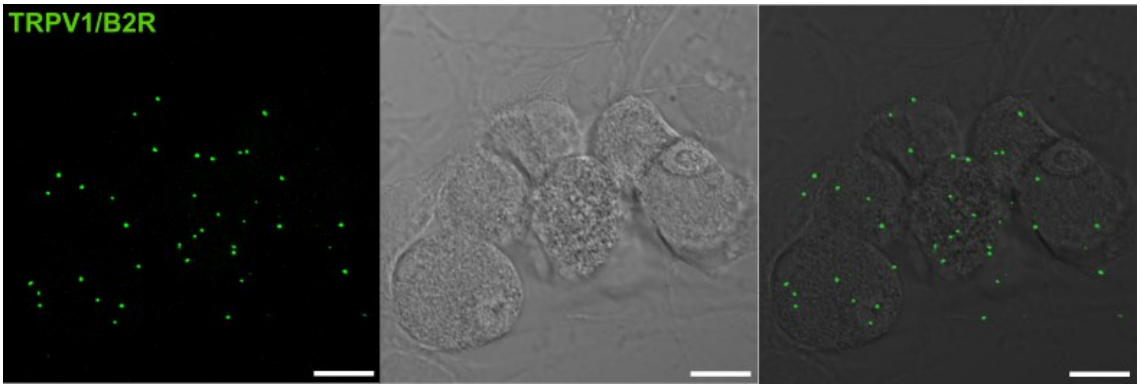

Figure 3.7: PLA supports nanodomain proximity between TRPV1 and B2R in small-diameter DRG neurons. Representative maximum intensity projection of confocal Z stack depicting positive PLA signal between TRPV1 and B2R in primary cultured DRG neurons (left panel). Middle panel depicts corresponding brightfield image of cultured neuron morphology and right panel represents an overlay of the PLA signal with brightfield. Scale bars = 10 µm. PLA, proximity ligation assay; DRG, dorsal root ganglion; TRPV1, transient receptor potential vanilloid type 1 receptor; B2R, bradykinin type 2 receptor.

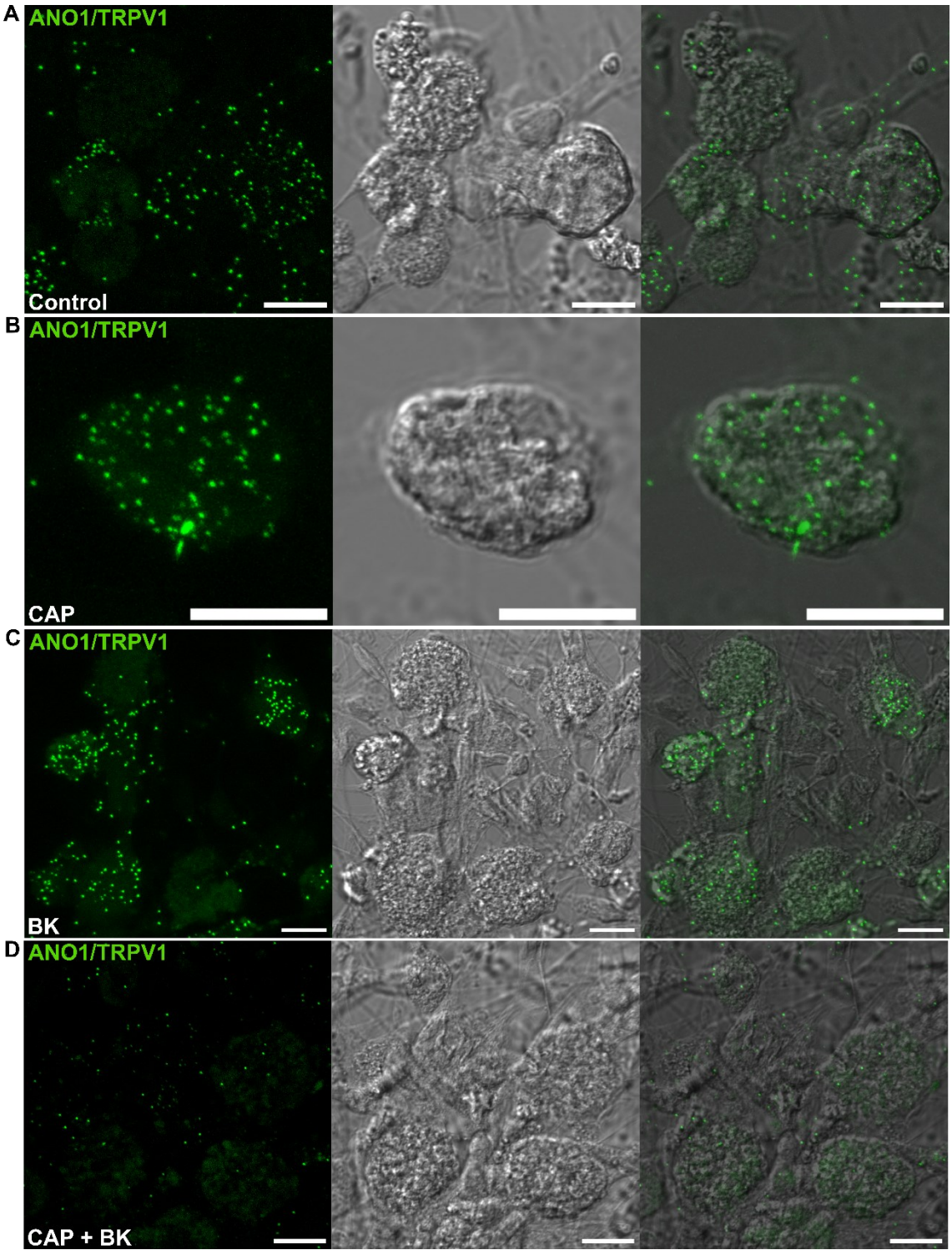

Figure 3.8: PLA reveals dynamic stimulus-dependent modulation of ANO1-TRPV1 nanodomain proximity in small-diameter DRG neurons. Continued on next page.

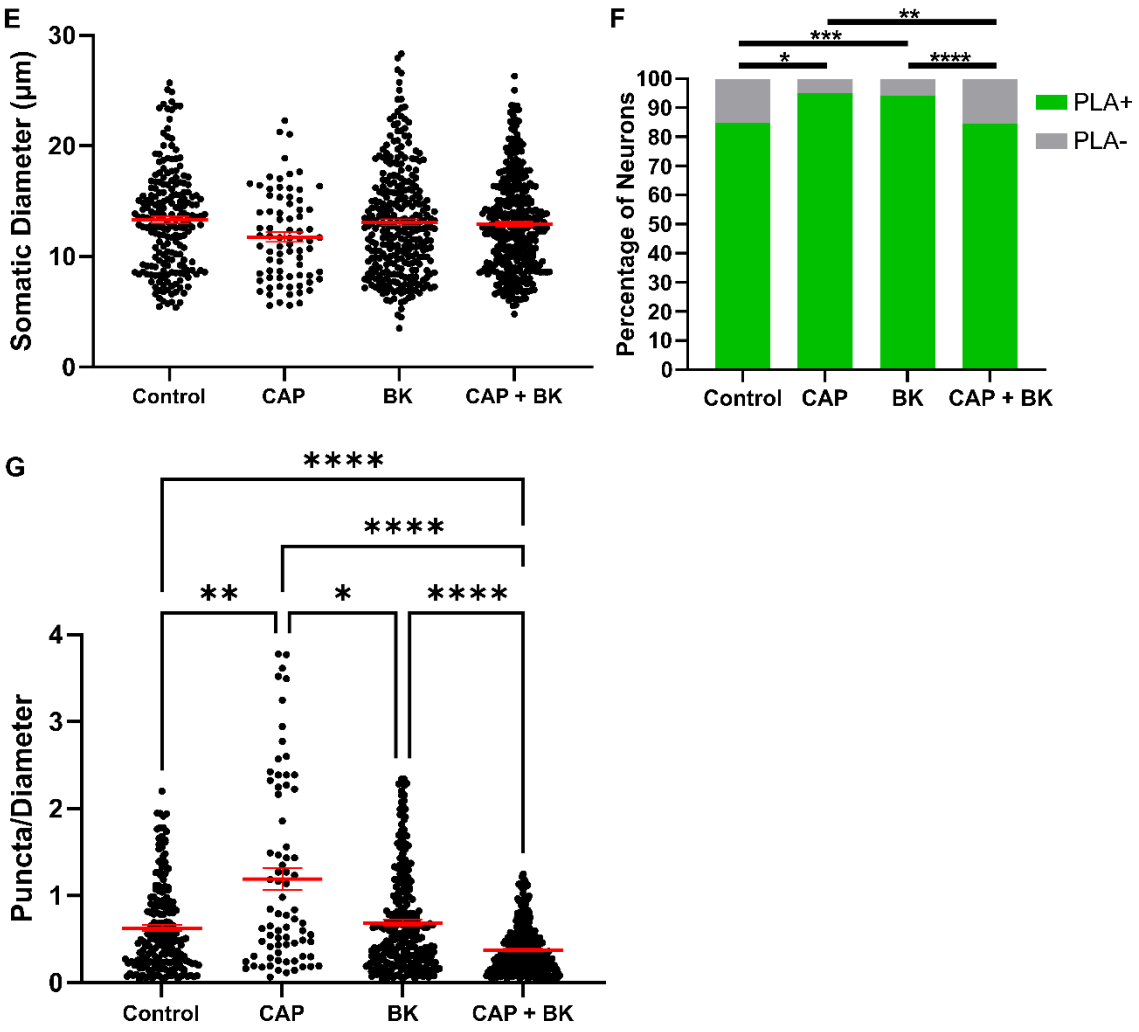

Figure 3.8: PLA reveals dynamic stimulus-dependent modulation of ANO1-TRPV1 nanodomain proximity in small-diameter DRG neurons. Representative maximum intensity projections of confocal Z stacks depicting PLA signal between ANO1 and TRPV1 in neonatal rat DRG neurons (N = 3, all conditions). Primary neurons were cultured *in vitro* for 3 days prior to treatment with standard growth media **(A)**, 1 µM CAP **(B)**, 250 nM BK **(C)**, or 1 µM CAP and 250 nM BK simultaneously **(D)** followed by immediate fixation without washout to capture dynamic protein-protein interactions *in situ*. **E)** No significant difference in the mean somatic diameter of the sampled neuron population that were PLA-positive between the control (n = 200), CAP-treated (n = 77), BK-treated (n = 300) and neurons treated with both CAP and BK (n = 367) ($p = 0.0835$, Kruskall-Wallis test). **F)** Noxious stimulation of primary DRG cultures significantly altered the proportion of the total neuron population sampled that was positive for PLA between ANO1 and TRPV1 (Fisher's exact tests were performed between the following: Control vs CAP, Control vs BK, Control vs CAP + BK, CAP vs BK, CAP vs CAP + BK and BK vs CAP + BK). **G)** For PLA-positive neurons, the number of PLA puncta per neuron was normalised to the respective diameter and means compared between each of the experimental conditions ($p < 0.0001$; Kruskall-Wallis test with Dunn's multiple comparisons tests). *$p < 0.05$, **$p < 0.01$, ***$p < 0.001$, ****$p < 0.0001$. PLA, proximity ligation assay; ANO1, anoctamin 1; TRPV1, transient receptor potential vanilloid type 1 receptor; DRG, dorsal root ganglion; CAP, capsaicin; BK< bradykinin.

3.2.4 Evaluating Stimulated Emission Depletion Microscopy as an Approach to Study Protein-Protein Interactions in Sensory Neurons

While certainly a valuable approach to investigating protein-protein interaction in fixed cells, PLA only detects discrete instances of at least 40 nm proximity between two target proteins. Therefore, PLA cannot be used to quantify the proportion of the available population of the target proteins within the neuron that are interacting or the actual proximity between putatively interacting proteins and must be complemented with additional experimental techniques. As an approach to characterise the total membrane-bound ANO1 and TRPV1 channel population on an individual neuron scale, super-resolution STED microscopy was considered for its ability to localise immunoreactivity at the single-molecule level (Upmanyu et al., 2022).

To confirm whether STED would provide sufficient spatial resolution to localise JMSC interactions in DRG neurons, it was first essential to quantify the effective resolution achievable by the microscopy setup available. Preliminary immunocytochemistry experiments to optimise imaging conditions were performed utilising the same anti-ANO1 and anti-TRPV1 primary antibodies used for PLA and secondary antibodies conjugated to specialised STED fluorophores (STAR RED and STAR ORANGE, Abberior) (Figure 3.9). The imaging parameters used for visualisation of ANO1 and TRPV1 immunoreactivity in 4% PFA-fixed primary cultured DRG neurons are given in Table 3.1.

Table 3.1: STED microscopy imaging parameters for anti-ANO1 and anti-TRPV1 immunoreactivity, and associated control experiments.

	Excitation laser λ (nm)/power (%)	STED laser λ (nm)/power (%)	Pixel size (nm)	Pixel dwell time (µs)
ANO1	561/100	775/100	20	10
TRPV1	640/10	775/100	20	10

To calculate the relative increase in resolving power achieved with a combination of STED imaging and post-processing over conventional confocal imaging, two-colour fluorescent nanoparticles (120 nm diameter) were imaged with identical parameters as were used to visualise ANO1 and TRPV1 immunoreactivity and the resulting images deconvolved in Huygens Professional with an acuity of 13.8 (standard profile) (Figure 3.10A). The FWHM of the linear intensity profiles of a representative sample of nanoparticles was calculated to demonstrate the resolution advantages achieved with STED imaging (Figure 3.10B). Improvement in resolution was calculated as a ratio of the FWHM measured by confocal imaging compared to the FWHM measured by STED imaging with deconvolution post-processing. Deconvolution of STED images obtained of

120 nm diameter fluorescent nanoparticles resulted in a mean 4.52 ± 0.824-fold improvement in the lateral (XY) resolution using a 640 nm excitation laser (n = 28 nanoparticles) and a mean 3.11 ± 0.969-fold improvement using the 561 nm excitation laser (n = 28 nanoparticles), demonstrating the power of super-resolution microscopy over confocal for visualising protein-protein interactions (Figure 3.10C). To accurately measure the effective resolution achieved with STED, fluorescent nanoparticles with a diameter of 40 nm (smaller than the theoretically achievable resolution of 50 nm) were imaged and the FWHM of Gaussian-fitted linear intensity profiles calculated (Figure 3.11A, B). The mean FWHM calculated for deconvolved STED images of 40 nm nanoparticles was 43.5 ± 12.1 nm, indicating that the resolving power of this imaging approach was likely sufficient to differentiate fluorescent puncta at least 40 nm apart and verify PLA data (Figure 3.11C).

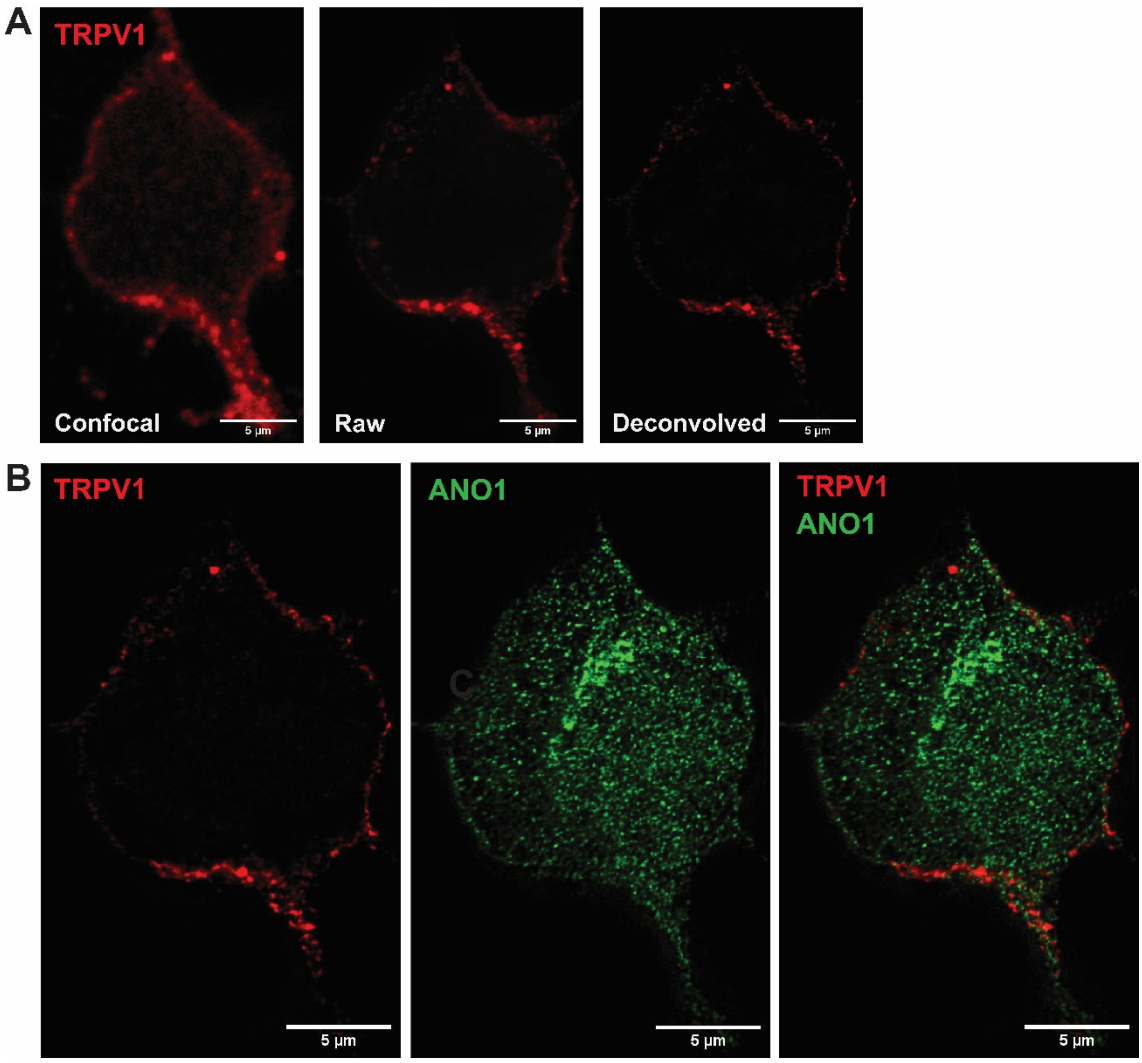

Figure 3.9: Deconvolution of STED microscopy images enables punctate resolution of protein immunoreactivity in primary cultured DRG neurons. Small-diameter DRG neurons maintained *in vitro* for 3 days were fixed in 4% PFA and immunostained with primary antibodies against ANO1 and TRPV1 and secondary antibodies conjugated to STAR ORANGE and STAR RED STED-capable fluorophores. **A)** Deconvolution of raw STED microscopy images visibly improved resolution of punctate, membrane-bound TRPV1 immunoreactivity. **B)** Representative deconvolved STED microscopy images showcasing punctate ANO1 and TRPV1 immunoreactivity in small-diameter DRG neurons. STED, stimulated emission depletion; ANO1, anoctamin 1; TRPV1, transient receptor potential vanilloid type 1 receptor.

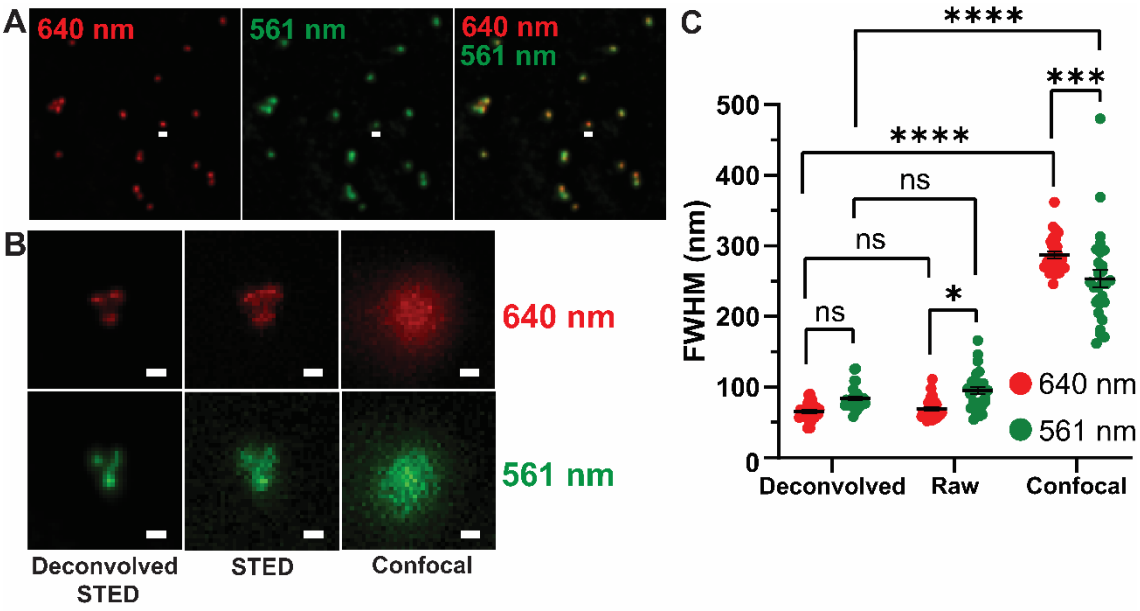

Figure 3.10: Deconvolution of STED data provides at least a three-fold improvement in resolution over standard confocal microscopy. A) Representative STED microscopy of 120 nm two-colour fluorescent nanoparticles imaged under identical settings optimised for TRPV1 (640 nm) and ANO1 (561 nm) immunoreactivity in primary cultured small-diameter DRG neurons. **B)** Nanoparticles were imaged in both confocal and STED microscopy setups and raw STED images were post-processed using the Huygens Professional Standard deconvolution algorithm. **C)** Resolution was quantified as the FWHM of Gaussian-fit linear intensity profiles of a representative sample of nanoparticles (n = 28). There was no significant difference in resolution achieved with the 640 and 561 nm excitation wavelengths once raw STED images were deconvolved but deconvolution of STED images afforded a significant 3-fold improvement in resolution compared to confocal imaging (two-way ANOVA with Sidak's multiple comparisons tests). Error bars represent mean ± SEM. Scale bars = 100 nm. *p < 0.05, ***p < 0.001, ****p < 0.0001. FWHM, full-width at half-maximum; STED, stimulated emission depletion.

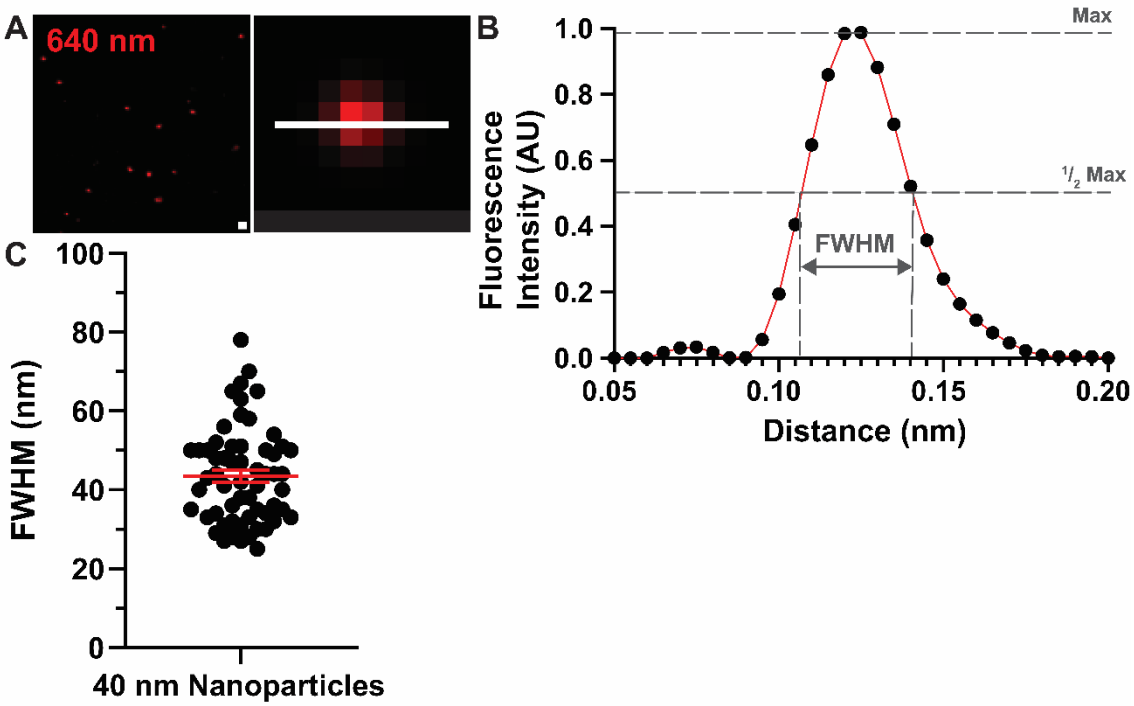

Figure 3.11: Nanoscale STED resolution is comparable to PLA. A) Fluorescent nanoparticles 40 nm in diameter were imaged under an identical STED microscopy setup as optimised for TRPV1 immunoreactivity in small-diameter DRG neurons. Right panel shows an individual 40 nm nanoparticle with 100 nm scale bar overlayed. To quantify the effective resolution achieved with combined STED microscopy and deconvolution post-processing of images, the FWHM of Gaussian-fit linear intensity profiles of a representative sample of 40 nm nanoparticles was measured. **B)** Example Gaussian fit (red) of the linear intensity profile (measured in Huygens Professional) of a single 40 nm nanoparticles with annotations to demonstrate how FWHM is calculated. **C)** The mean FWHM calculated from a sample of 100 nanoparticles was 43.5 ± 12.1 (SD) suggesting STED microscopy is able to image fluorescent puncta within a similar resolution as PLA (40 nm proximity detection). Error bars represent mean ± SEM. Scale bars = 100 nm. FWHM, full-width at half-maximum; STED, stimulated emission depletion; PLA, proximity ligation assay; AU, arbitrary units.

3.2.5 Stimulated Emission Depletion Imaging Captures Protein-Protein Interaction in Sensory Neurons

Deconvolution of STED microscopy in fixed primary cultured DRG neurons revealed punctate patterns of expression for both anti-ANO1 and anti-TRPV1 immunoreactivity, suggesting it was likely STED could be used as an approach to investigate proximity on a single molecule (protein-antibody complex) level (Figure 3.9). To quantify proximity between putative interacting protein pairs, a NND analysis approach was taken. Deconvolved STED images of target protein immunoreactivity were segmented based on the expression pattern of membrane-bound immunoreactivity to obtain a 500 nm-wide 'ring-shaped ROI which captured the PM and regions of cortical ER likely to form ER-PM junctions. Individual puncta were identified based on an automated local thresholding algorithm in FIJI and Cartesian coordinates for each punctum were calculated to localise the centroid in the x, y and z dimensions. The NND was measured as the distance in nm for each punctum to the centroid of the closest punctum in the opposing channel.

To determine whether this analysis approach was able to detect protein-protein interactions at ER-PM contact sites, STED was performed on primary cultured DRG neurons immunostained against the CRAC channel subunits STIM1 and Orai1. As a negative control, neurons were immunostained against ANO1 and the α1H subunit of the T-Type Ca^{2+} channel $Ca_v3.2$, which were shown by PLA to not share nanodomain proximity. To control for neuron size, DRG cultures were also co-stained against the small-diameter neuron marker peripherin and only those cells immunopositive for peripherin were imaged for NND analysis (Ferri et al., 1990). Punctate expression patterns were observed throughout the neuron for all proteins and regions of co-localisation were observed between STIM1 and Orai1, but not between ANO1 and α1H (Figure 3.12A, B). Typically, a greater number of Orai1-positive puncta were detected compared to STIM1-positive puncta; therefore, mean proximity between CRAC proteins was quantified for each neuron (n = 9, N = 3) based on the nearest Orai1 neighbour distance to STIM1 puncta (mean STIM1 to Orai1 distance). Similarly, a greater number of A1H-positive puncta were detected compared to ANO1-positive puncta so the mean ANO1 to A1H distance for each neuron (n = 6, N = 3) was quantified as a negative control. The overall mean nearest Orai1 neighbour distance to STIM1 localisations was 240 ± 20.5 nm, which was significantly smaller than the mean nearest ANO1 neighbour to α1H distance, which was 499 ± 44.7 nm (p = 0.0006, Mann-Whitney test) (Figure 3.12C).

Frequency distribution histograms were plotted for all STIM1-Orai (Figure 3.12D) and ANO1-α1H (Figure 3.12E) NNDs ≤ 500 nm and fit with a single-Gaussian distribution to better visualise the distinction between co-localised and non-co-localised protein pairs. Although a small percentage of NNDs within each condition exceeded 500 nm, the x-axis scale was clipped to 500 nm for clarity of presentation. The single-Gaussian distribution, however, was calculated using all data (Supplementary Figure 3.1). The distribution of proximities between interacting proteins is expected to follow a normal (Gaussian) distribution pattern whereas for non-interacting proteins, their distribution throughout the cell relative to one another is more likely to be random, and therefore, the NNDs will not fit a normal distribution. STIM1-Orai1 interactions showed a nearest neighbour distribution with a peak of 186.6 nm and peak width (± 1 S.D. value) between 78.2 and 295 nm. The distribution was well fit with a single-Gaussian equation and the R^2 value (indicating goodness of fit) was 0.912. Contrary, the distribution of ANO1-α1H NNDs was less well-fit with a Gaussian distribution (R^2 = 0.766) (Figure 3.12E); the distribution peak was also greater than that observed for STIM1-Orai1 at 245 nm and the peak width was wider ranging from 118 to 371 nm.

Although this initially supported NND analysis as a suitable approach to distinguish between protein pairs expected to be intimately associated from those that are not, the density of localisations was likely to be a major contributing factor to the mean NND calculations. Density of immunoreactive puncta was calculated for STIM1, Orai1, ANO1 and α1H as the total number of puncta detected per neuron divided by the area in μm of the 500 nm doughnut ROI for a single slice of the z stack. These calculations were therefore made under the assumption that both protein expression and immunostaining were consistent through the cell and should not be taken as an absolute quantification of the density of membrane-localised protein expression.

Overall, there was no significant difference between the mean density of STIM1-, ANO1- and α1H-immunoreactive puncta (7.12 ± 1.35, 6.18 ± 2.03 and 8.03 ± 1.88 puncta per μm^2, respectively), however, the mean density of Orai1 localisations (21.1 ± 4.61 puncta per μm^2) was significantly greater ($p = 0.004$, ordinary one-way ANOVA), which may have contributed to the overall closer proximity between STIM1-Orai1 pairs quantified in the NND analysis (Figure 3.12F). Putative interacting partner proteins are expected to co-localise within nanodomain proximity, regardless of the overall density of protein expression across the membrane; therefore, it made sense to compare the proportion of nearest neighbour pairs that were localised within sufficient proximity to interact with one another to give an overview of the likelihood of protein association or functional coupling within a cell. A proximity threshold of 100 nm was chosen based on the mean diameter

of ANO1-immunoreactive puncta (n = 30) calculated across three representative deconvolved STED microscopy images. The mean FWHM was 67.1 ± 14.4 (S.D.) nm, therefore, the threshold was set based on this value plus a linkage error of 30 nm for binding of the primary and secondary antibodies to their respective antigens (Maidorn et al., 2016), resulting in a mean size of 97.1 nm, which was subsequently rounded to 100 nm for ease of calculations. The mean percentage of STIM1-Orai1 nearest neighbours within 100 nm was 15.7 ± 1.88 %, which represented a significantly greater proportion of putatively interacting proteins than was observed for ANO1-α1H nearest neighbours, of which only 6.18 ± 1.92 % were within 100 nm ($p = 0.0047$, unpaired t-test). (Figure 3.12G).

As a necessary negative control, fixed DRG cultures were incubated with secondary fluorophore-conjugated antibodies only to control for non-specific immunosignal. Peripherin-positive small-diameter DRG neurons were imaged under identical STED parameters and images post-processed by identical deconvolution and puncta detection algorithms. No identifiable puncta were detected in either the 640 or 561 nm excitation wavelengths, confirming target protein specificity of puncta localisation for both secondary antibodies used in the present study (Figure 3.13).

Together, these data suggest that STED microscopy is capable of identifying protein pairs that are expected to be intimately associated in fixed DRG neurons. To further investigate stimulus-dependent proximity between ANO1 and TRPV1, STED microscopy was used as a complementary approach to PLA to localise ANO1 and TRPV1 immunoreactivity in DRG neurons fixed immediately following stimulation with 1 μM CAP, 250 nM BK, or both agonists simultaneously for 1 minute.

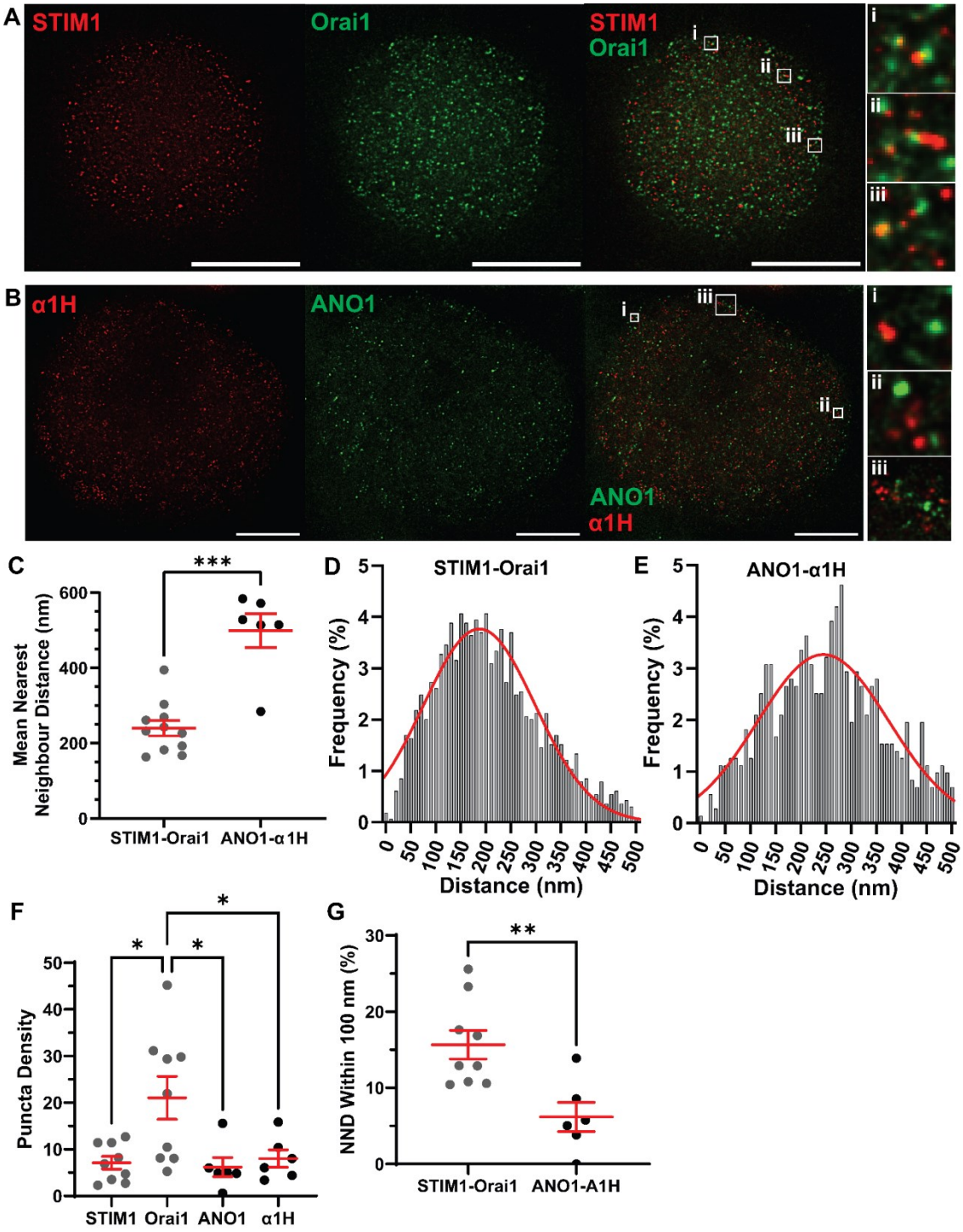

Figure 3.12: Colocalisation analysis of deconvolved STED data can distinguish between known interacting and non-interacting protein pairs. Continued on next page.

Figure 3.12: Colocalisation analysis of deconvolved STED data can distinguish between known interacting and non-interacting protein pairs. Primary DRG neuron cultures (N = 3, both conditions) were prepared from neonatal rats and maintained for 3 days *in vitro* prior to immunostaining against the known JMSC proteins STIM1 and Orai1 **(A)** or against ANO1 and the α1H subunit of the T-Type $Ca_v3.2$ calcium channel **(B)**, which are not reported to interact. STED microscopy was performed and z stacks post-processed (deconvolution) using Huygens Professional. i, ii and iii depict representative regions of closest association between either of the protein pairs. **C)** Immunopositive puncta were identified and localised according to their Cartesian coordinates to perform nearest neighbour distance (NND) analysis between STIM1 and Orai1, and ANO1 and α1H pairs. The mean NND was calculated for each sampled neuron (STIM1-Orai1, n = 11; ANO1- α1H, n = 6) and statistically compared (Mann-Whitney test). NNDs between STIM1 and Orai1 **(D)** and between ANO1 and α1H **(E)** for all neurons sampled were pooled and frequency distribution histograms plotted and fit with a single-Gaussian distribution curve. Note that the full datasets here have been clipped to 500 nm for clarity of presentation. **F)** The total number of detected immunopositive puncta for each neuron was normalised to the somatic diameter to quantify and compare puncta density. The mean density of Orai1-positive puncta detected by STED microscopy was found to be significantly greater than that for STIM1-, ANO1- and α1H-positive puncta (one-way ANOVA). **G)** The mean percentage of STIM1 puncta with an Orai1 nearest neighbour within 100 nm was significantly greater than the mean percentage of ANO1 puncta with an α1H nearest neighbour within 100 nm (unpaired t-test). Scale bars = 10 μm. Error bars represent mean ± S.D. *p < 0.05, **p < 0.01, ***p < 0.001. STED, stimulated emission depletion; STIM1, stromal interaction molecule type 1; ANO1, anoctamin 1; NND, nearest neighbour distance.

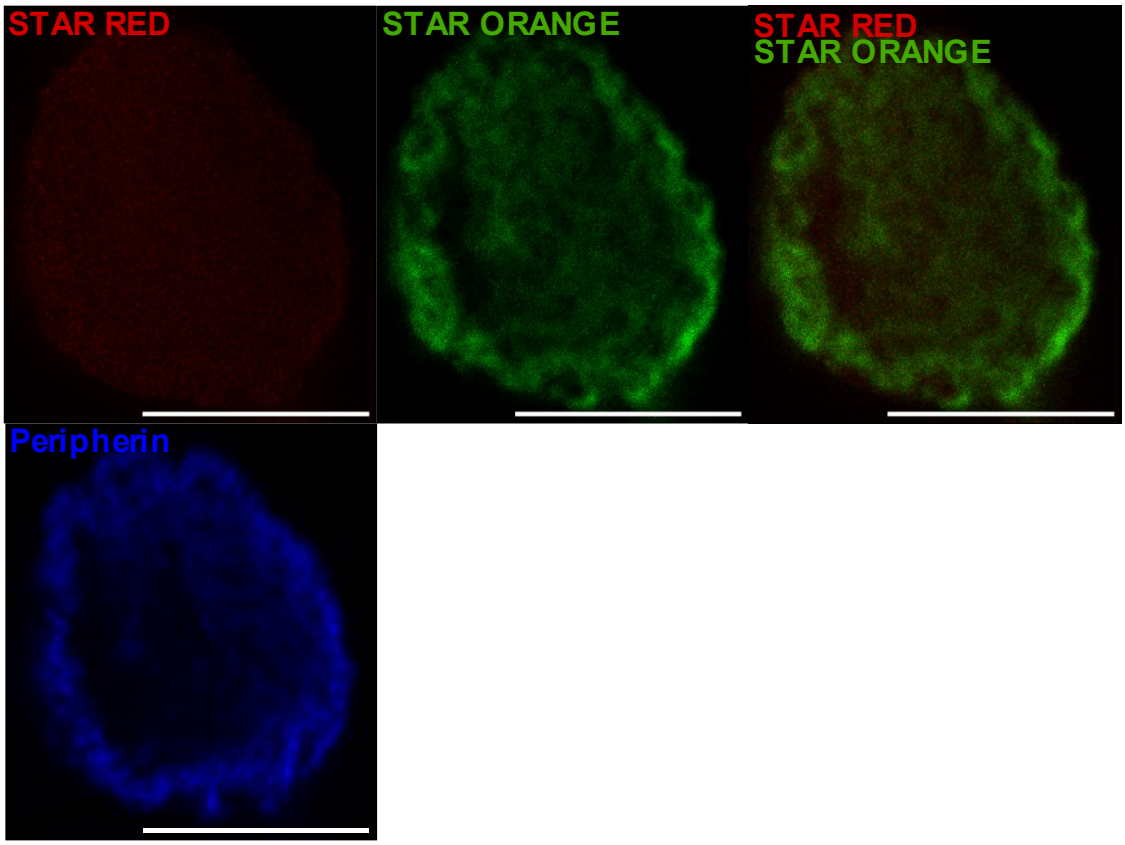

Figure 3.13: Secondary antibody-only negative control for STED microscopy of immunocytochemistry in cultured DRG neurons. PFA-fixed primary DRG neuron cultures were incubated with STAR RED and STAR ORANGE secondary STED antibodies in the absence of primary antibodies. No detectable punctate staining pattern was observed for either secondary antibody in peripherin-positive DRG neurons. Scale bars = 10 µm.

3.2.6 Stimulated Emission Depletion Microscopy Confirms Stimulus-Dependent Translocation of ANO1

Primary DRG neuron cultures were treated for 1 minute with either 1 μM CAP, 250 nM BK, or both CAP and BK simultaneously and immediately fixed in 4% PFA without recovery washout. Cultures were co-immunostained against ANO1 and TRPV1, with peripherin to positively identify small-diameter, putative nociceptive neurons. STED images obtained for ANO1 and TRPV1 immunoreactivity were post-processed as previously described and revealed robust punctate staining patterns for both proteins across all experimental conditions (Figure 3.14 A – D). TRPV1 immunoreactivity was consistently localised primarily to the PM, while ANO1 immunoreactivity was distributed throughout the cytoplasm in addition to membrane localisation. For this reason, ROIs were segmented as described in Chapter 2 based on the outer limits of TRPV1-like immunoreactivity.

To control for variability in the quality of immunostaining between replicates and for density of localisations, the number of ANO1-positive and TRPV1-positive puncta detected per cell was plotted against the respective mean NND for the control neuron population (Figure 3.14E, F). Although for both ANO1- and TRPV1- there was a general negative correlation between these values (ANO1, slope = -0.0675; TRPV1, slope = -0.0431), linear regression analysis revealed this was not significant for either ANO1 puncta (R^2 = 0.175) or TRPV1 puncta (R^2 = 0.263), suggesting differing densities of localisations were not a factor that needed to be controlled for. This can be explained by the observation that localisations detected by the thresholding algorithm tended to cluster to similar regions of the membrane ROI rather than display an even distribution, therefore, a lesser number of puncta did not necessarily correspond to greater distances between nearest neighbours.

To investigate activity-dependent modulation of ANO1-TRPV1 nanoscale proximity frequency distribution histograms were plotted for the pooled datasets of all ANO1-TRPV1 (N = 3) (Figure 3.15) and, conversely, all TRPV1-ANO1 (N = 3) (Figure 3.16) NNDs for each of the experimental conditions (Control: A, 1 μM CAP: B, 250 nM BK: C, and 1 μM CAP with 250 nM BK: D). All histograms were fit with a single-Gaussian distribution to allow for comparisons between both the distribution peak distance and width as measures of the mean NND and variability within the datasets. The normal distributions between each experimental condition measuring the nearest ANO1 neighbour to each TRPV1 localisation (TRPV1 – ANO1 NND) were broadly similar. The respective distribution peaks for control neurons and neurons treated with CAP, BK or

both CAP and BK, respectively, were at 287 ± 149 nm, 301 ± 150 nm, 316 ± 166 nm and 337 ± 171 nm (peak ± S.D.). Subsequently, there was limited variability in the peak widths, representing ± 1 S.D. value from the mean, resulting in considerable overlap of distributions (Figure 3.17A). Conversely, the frequency distributions between each experimental condition measuring the nearest TRPV1 neighbour to each ANO1 localisation (ANO1-TRPV1 NND) appeared considerably different (Figure 3.17B). The distribution peak for control neurons was 355 nm with a peak width between 124 and 587 nm, which was notably smaller than that for neurons simultaneously stimulated with both 1 µM CAP and 250 nM BK, where the distribution peak was 515 nm with a peak width between 149 and 881 nm. The respectively distribution peaks for neurons treated with either CAP or BK alone were 398 ± 241 nm and 415 ± 273 nm, respectively. Thus far, these data indicate a substantial stimulus-dependent rearrangement of the distribution of ANO1 and TRPV1 localisations relative to one another at the PM and in particular it is interesting that the major differences are noted between experimental conditions measuring the nearest TRPV1 neighbour to ANO1 puncta. This may be further indicative of a preferential coupling of ANO1 to BK-induced Ca^{2+} signals over those that are CAP-induced.

Frequency distribution histograms consider the states of individual ANO1- and TRPV1-positive localisations, pooled across the entire dataset, therefore, can give an indication of the likelihood of proximity between these two proteins as independent entities but does not consider the broader physiological state on each individual neuron as a member of the heterogeneous population of the DRG. As a better representation of the effect of noxious stimulation on ANO1-TRPV1 proximity on a cellular level, the mean NND between ANO1 and TRPV1, and between TRPV1 and ANO1, was calculated for each neuron and compared between experimental states. Overall, the mean ANO1-TRPV1 NND in control neurons (n = 12, N = 3) was 585 ± 56.5 nm, and this value was not significantly altered as a result of treatment with either CAP or BK alone, or both simultaneously (p = 0.0923, Kruskll-Wallis test) (Figure 3.18A). The mean ANO1-TRPV1 NND for neurons stimulated with CAP (n =13, N = 3) was 544 ± 38.9 nm, representing a slight reduction compared to the control. For neurons stimulated with BK (n = 14, N = 3) and with CAP and BK (n = 10, N = 3), the mean ANO1-TRPV1 NNDs were increased compared to the control to 670 ± 56.0 nm and 715 ± 58.9 nm, respectively.

Generally, the mean TRPV1-ANO1 NNDs were smaller than the mean ANO1-TRPV1 distances for the same neuron samples, however, this is likely the result of thresholding segmenting a greater number of ANO1-positive localisations in the same ROI than TRPV1-positive localisations so overall, there is greater chance an ANO1 puncta is in

closer proximity to a TRPV1 puncta than vice versa. Therefore, it is necessary to consider the effect of the experimental treatment for ANO1-TRPV1 and TRPV1-ANO1 NNDs separately. For control neurons, the mean TRPV1-ANO1 distance was 367 ± 22.0 nm, and similarly, this was not significantly changed as a result of noxious stimulation ($p = 0.425$, Kruskall-Wallis test) (Figure 3.18B). For neurons exposed to CAP, BK and both simultaneously, the respective mean TRPV1-ANO1 NNDs were increased to 381 ± 25.0 nm, 411 ± 33.4 nm and 464 ± 52.3 nm. Although these data are not indicative of an effect of differential noxious stimulation on proximity between ANO1 and TRPV1, perhaps most relevant to consider is stimulus-evoked differences in the proportion of the PM-localised ANO1 and TRPV1 protein population within nanodomain proximity, particularly considering ANO1 and TRPV1 are not exclusive interacting partners.

Therefore, for both ANO1 and TRPV1 the percentage of the total protein population, as detected by STED microscopy, with a corresponding nearest TRPV1 or ANO1 neighbour, respectively, within 100 nm was calculated for each neuron and compared between experimental conditions (Figure 3.18C, D). Interestingly, treatment with CAP alone did not significantly alter the mean percentages of either ANO1-TRPV1 (1.91 ± 0.239 %, $p = 0.301$, one-way ANOVA with Holm-Sidak's multiple comparisons test) or TRPV1-ANO1 NNDs (3.58 ± 0.385 %, $p = 0.541$, one-way ANOVA with Holm-Sidak's multiple comparisons test) within 100 nm compared to the respective control values (2.58 ± 0.368 % and 4.25 ± 0.419 %). However, stimulation with 250 nM BK *did* significantly reduce the mean percentage of ANO1-TRPV1 pairs within 100 nm to 1.54 ± 0.179 % ($p = 0.0407$, one-way ANOVA with Holm-Sidak's multiple comparisons test) but did not significantly change, compared to the control, the mean proportion of TRPV1-ANO1 NNDs, which was 2.95 ± 0.368 % ($p = 0.0981$, one-way ANOVA with Holm-Sidak's multiple comparisons test). Most notably, simultaneous stimulation with both CAP and BK significantly reduced the mean proportion of both ANO1 and TRPV1 populations with a corresponding neighbouring protein within 100 nm compared to the respective controls. The mean percentage of ANO1-TRPV1 NNDs equal to or less than 100 nm following dual-stimulation was 1.41 ± 0.302 % ($p = 0.0377$, one-way ANOVA with Holm-Sidak's multiple comparisons test) and for TRPV1-ANO1 NNDs was 2.60 ± 0.399 % ($p = 0.0441$, one-way ANOVA with Holm-Sidak's multiple comparisons test).

Together, these data present novel evidence towards elucidating mechanisms of activity-dependent dynamic rearrangement of ANO1 protein interactions in small-diameter neurons of the DRG and support the use of STED super-resolution microscopy as a valuable technique to perform meaningful protein localisation analyses in fixed samples.

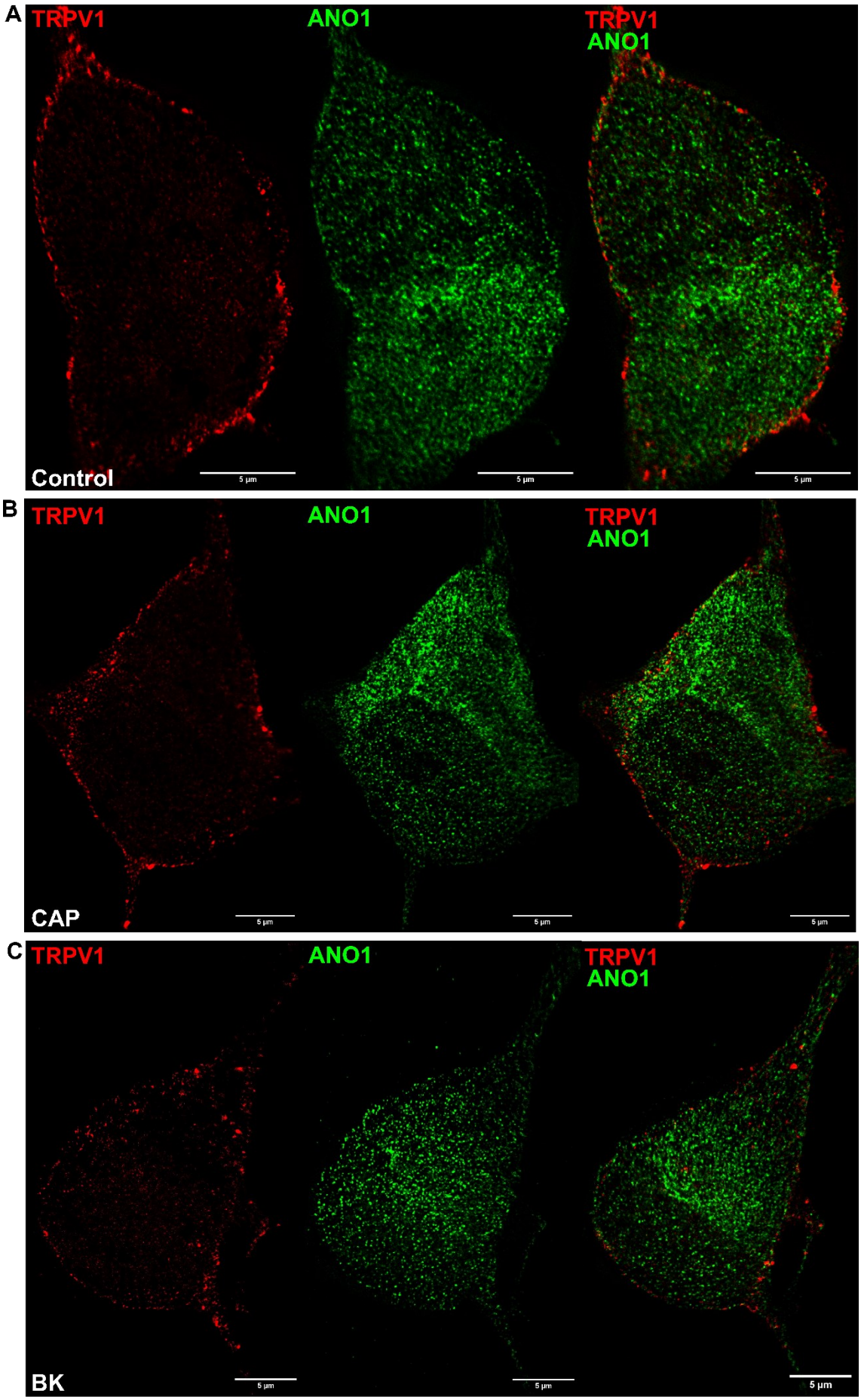

Figure 3.14: STED microscopy enables punctate localisation of ANO1 and TRPV1 immunoreactivity in DRG neurons *in vitro.* Continued on next page.

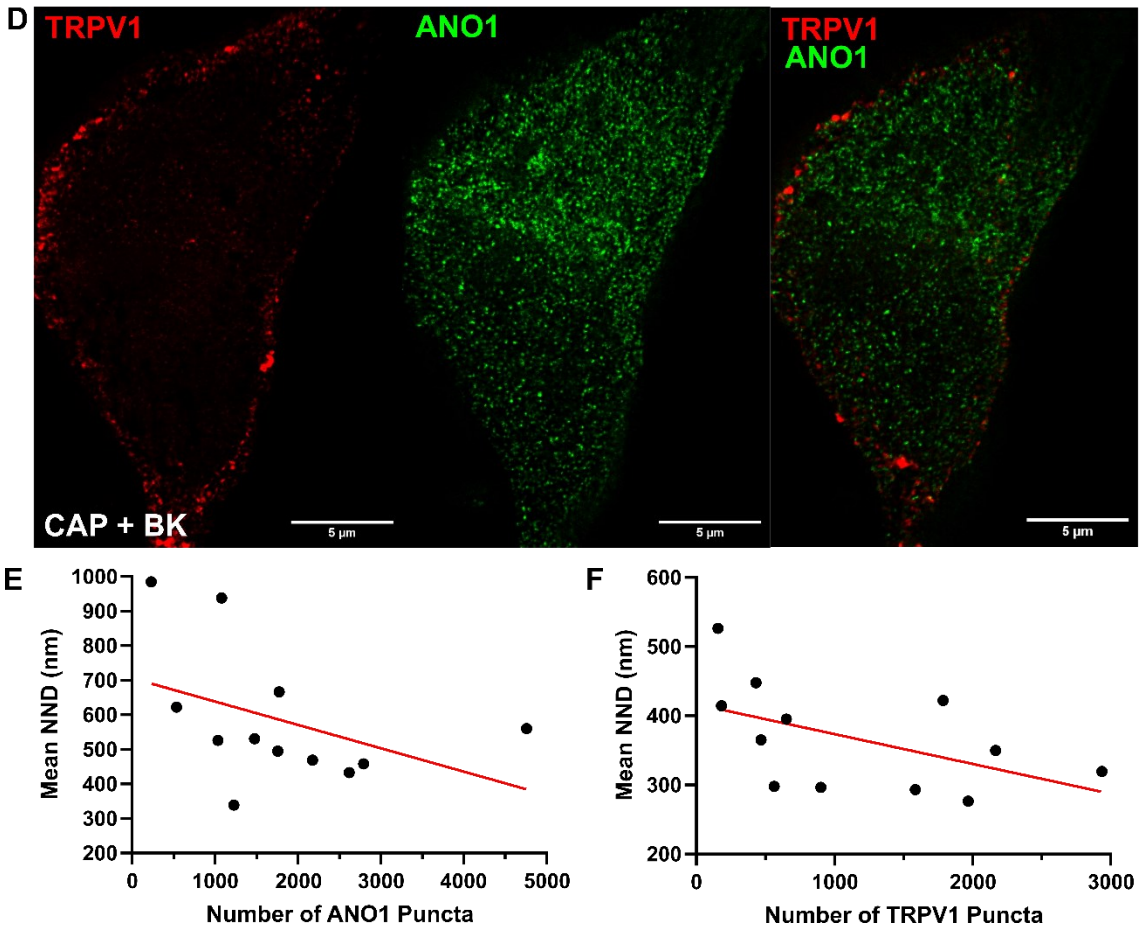

Figure 3.14: STED microscopy enables punctate localisation of ANO1 and TRPV1 immunoreactivity in DRG neurons *in vitro.* Small-diameter DRG neurons (identified by positive peripherin immunoreactivity – not shown) maintained *in vitro* for 3 days were fixed in 4% PFA and immunostained with primary antibodies against ANO1 and TRPV1 and secondary antibodies conjugated to STAR ORANGE and STAR RED STED-capable fluorophores (N = 3, all conditions). Prior to fixation neurons were incubated in standard growth media **(A)**, or growth media containing 1 µM CAP **(B)**, 250 nM BK **(C)** or both 1 µM CAP with 250 nM BK **(D)** to investigate the effect of differential noxious stimulation on the relative localisation of ANO1 and TRPV1-positive immunoreactivity through the plasma membrane. Deconvolution of STED microscopy z stacks revealed punctate staining patterns for both ANO1 and TRPV1 at the plasma membrane. Figure shows a representative deconvolved single STED z stack section for each experimental condition depicting ANO1 and TRPV1 immunoreactivity. Scale bars = 5 µm. For each of the sample of control neurons (n = 12), the mean ANO1 - TRPV1 **(E)** and mean TRPV1 – ANO1 **(F)** nearest neighbour distance was plotted against the respective number of ANO1 or TRPV1 punctate localisations and fitted with a linear best-fit equation for regression analysis, which found no significant correlation between either the number of detected ANO1-positive puncta (R^2 = 0.175) or TRPV1-positive puncta (R^2 = 0.263) and the calculated nearest neighbour distance. ANO1, anoctamin 1; TRPV1, transient receptor potential vanilloid type 1 receptor; NND, nearest neighbour distance; STED, stimulated emission depletion.

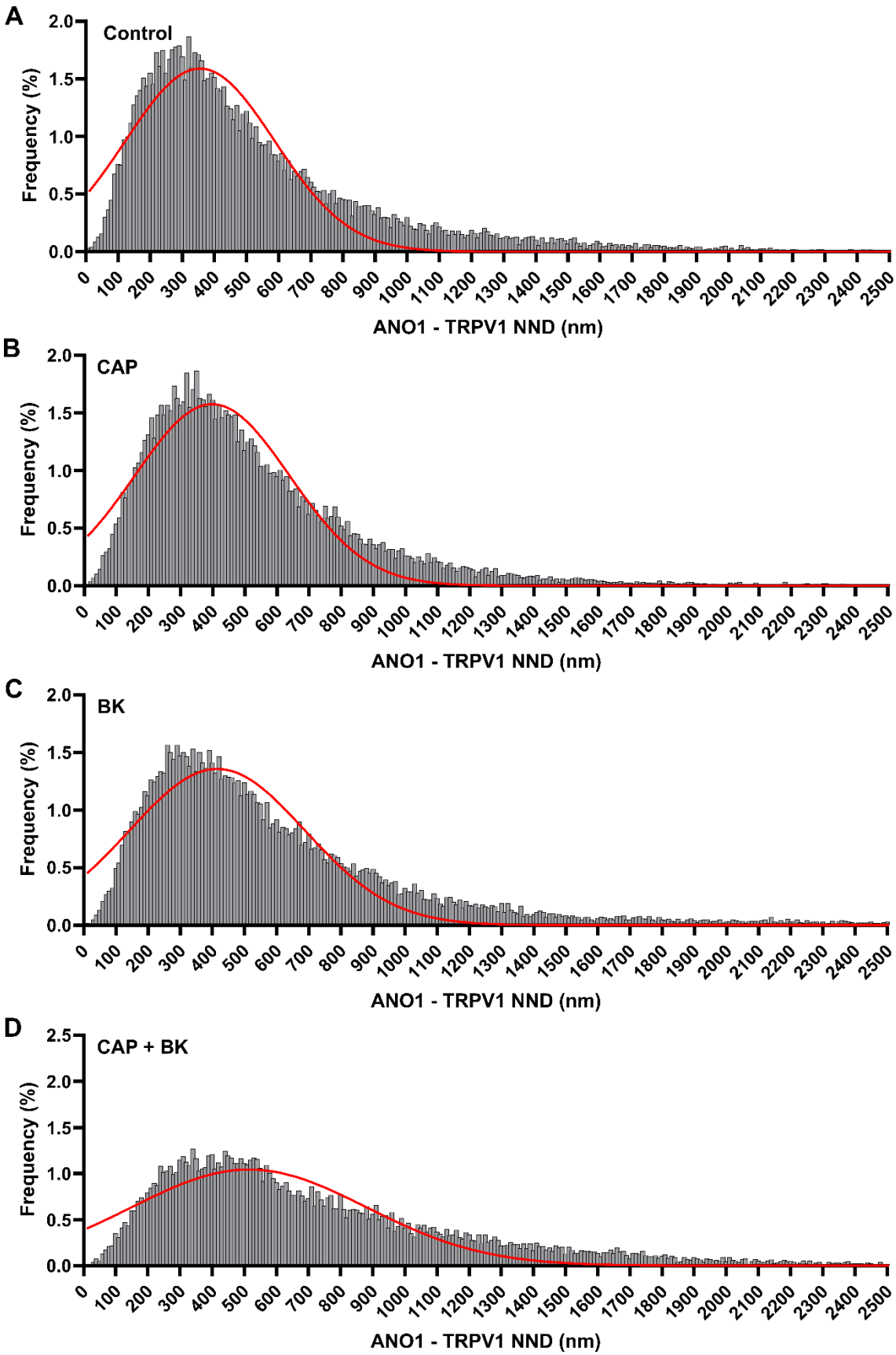

Figure 3.15: Frequency distribution histograms for ANO1–TRPV1 NNDs in DRG neurons. All nearest neighbour distances were pooled from the total sampled DRG neuron population treated with standard growth media (A) (n = 12), 1 μM CAP (B) (n = 13), 250 nM BK (C) (n = 14) or 1 μM CAP and 250 nM BK simultaneously (D) (n = 10). Histograms were fit with a single-Gaussian distribution curve to allow for comparison of the peak (mean) and peak width between experimental conditions. Note that the full datasets here have been clipped to 2500 nm for clarity of presentation. ANO1, anoctamin 1; TRPV1, transient receptor potential vanilloid type 1 receptor; NND, nearest neighbour distance.

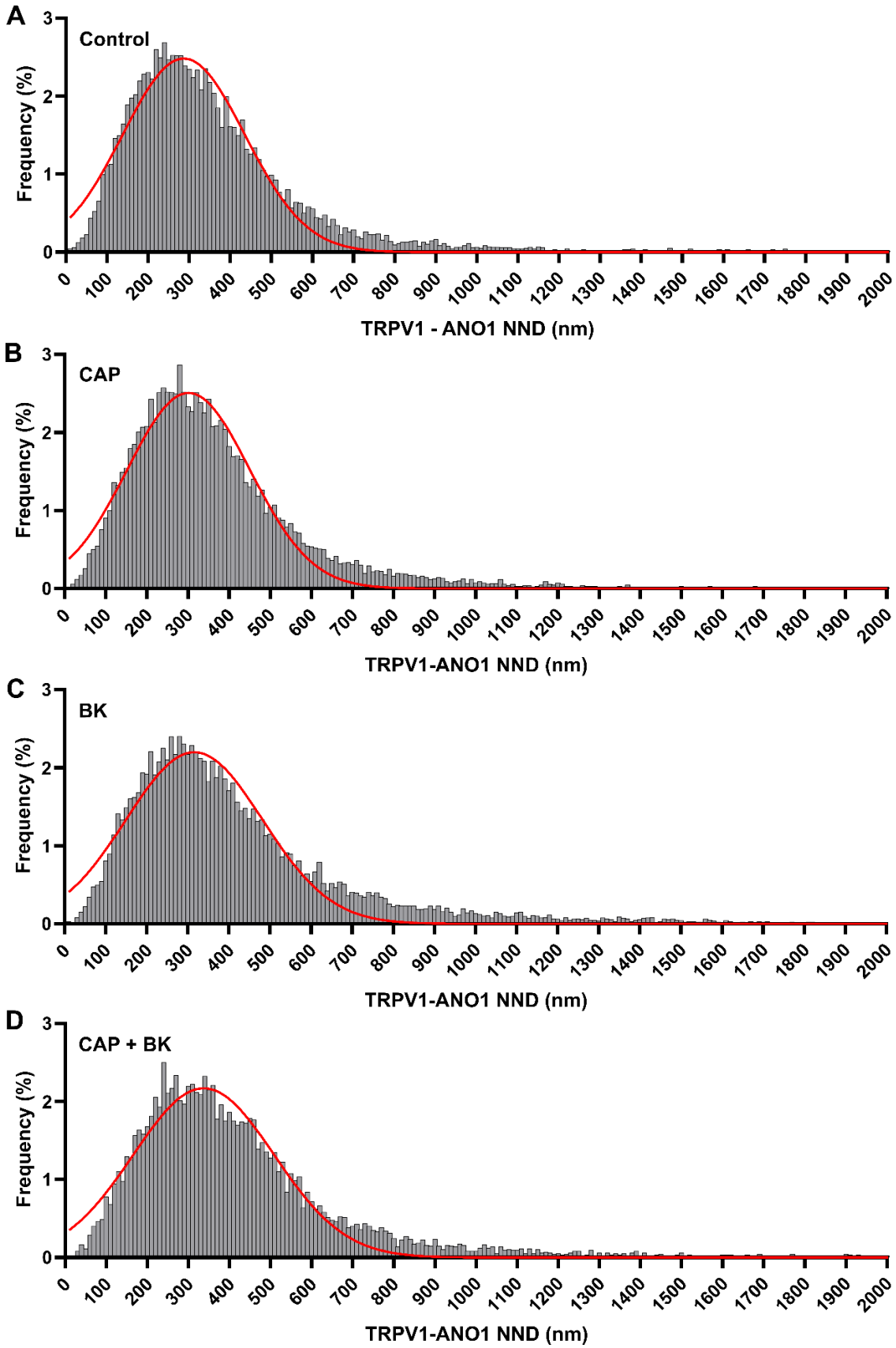

Figure 3.16: Frequency distribution histograms for TRPV1–ANO1 NNDs in DRG neurons. All nearest neighbour distances were pooled from the total sampled DRG neuron population treated with standard growth media (A) (n = 12), 1 μM CAP (B) (n = 13), 250 nM BK (C) (n = 14) or 1 μM CAP and 250 nM BK simultaneously (D) (n = 10). Histograms were fit with a single-Gaussian distribution curve to allow for comparison of the peak (mean) and peak width between experimental conditions. Note that the full datasets here have been clipped to 2000 nm for clarity of presentation. ANO1, anoctamin 1; TRPV1, transient receptor potential vanilloid type 1 receptor; NND, nearest neighbour distance.

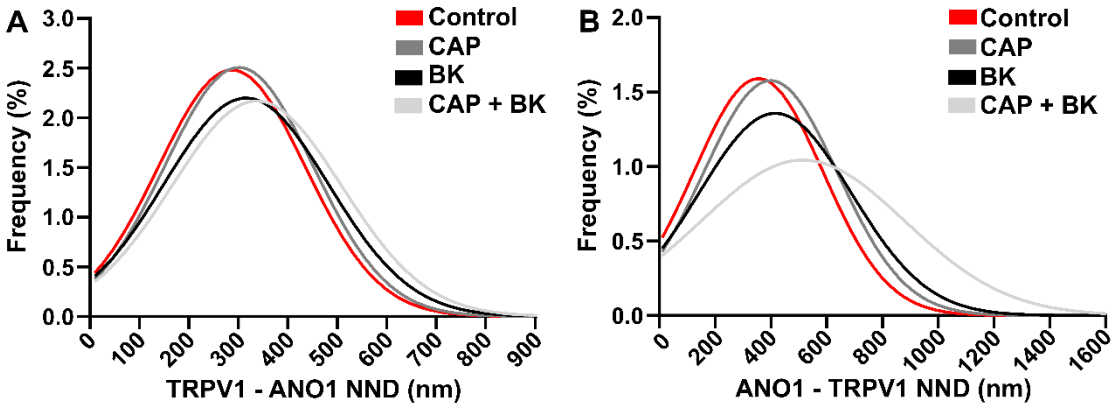

Figure 3.17: Noxious stimulation changes the Gaussian frequency distribution of ANO1–TRPV1 nearest neighbour distances in rat DRG neurons. Figure depicts an overlay of the single-Gaussian fits of frequency distribution histograms for pooled nearest neighbour distances between TRPV1 and ANO1 **(A)** and conversely between ANO1 and TRPV1 **(B)**. Primary DRG neuron cultures (N = 3, all conditions) were incubated with standard growth media (Control – red) (n = 12 neurons), 1 µM CAP (dark grey) (n = 13 neurons), 250 nM BK (black) (n = 14 neurons) or simultaneously 1 µM CAP and 250 nM BK (light grey) (n = 10 neurons) prior to PFA fixation, immunostaining against ANO1 and TRPV1, and subsequent STED microscopy to localise punctate immunoreactivity. Note that the full datasets here have been clipped to 900 **(A)** and 1600 **(B)** nm for clarity of presentation. ANO1, anoctamin 1; TRPV1, transient receptor potential vanilloid type 1 receptor; DRG, dorsal root ganglion; NND, nearest neighbour distance; STED, stimulated emission depletion; CAP, capsaicin; BK, bradykinin.

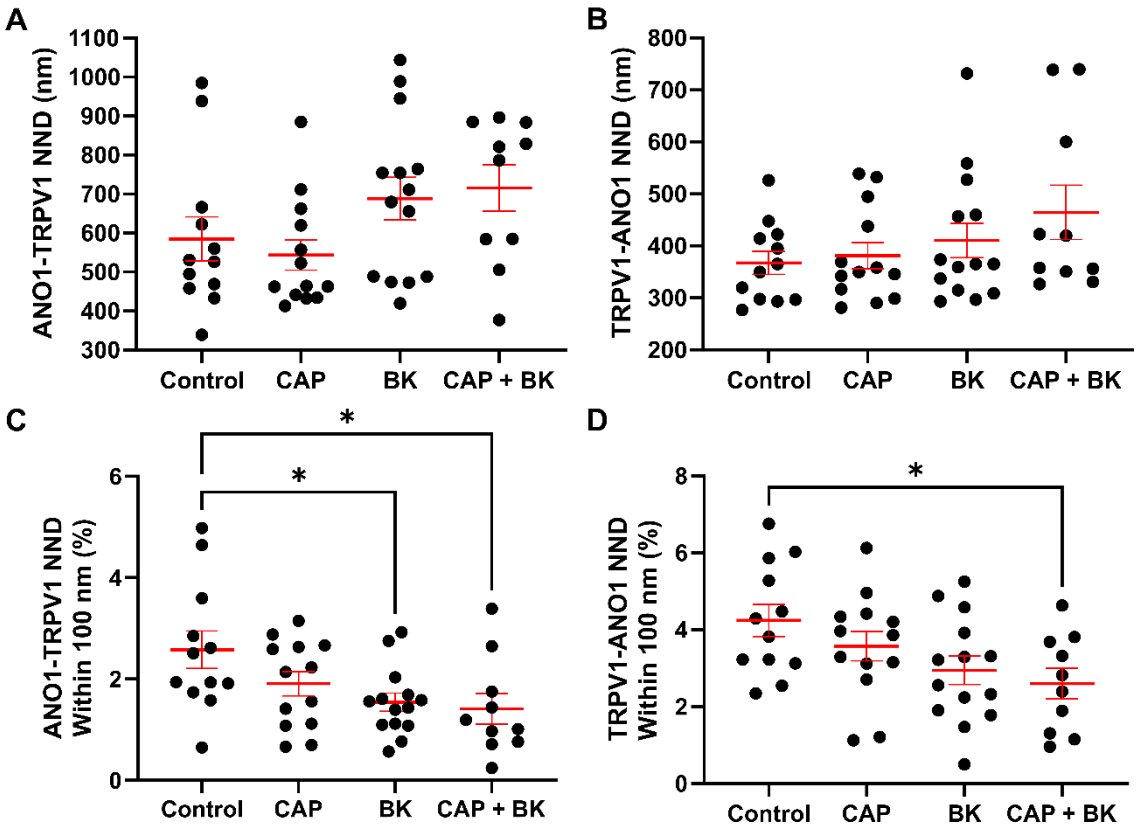

Figure 3.18: Nearest neighbour analysis describes a reduction in ANO1-TRPV1 coupling in response to certain noxious stimulation. A) Difference in the mean nearest TRPV1 neighbour to ANO1 distance between experimental conditions approached significance, showing a general trend that stimulation with CAP alone slightly reduced the mean distance (suggestive of ANO1 translocation towards TRPV1) while stimulation with BK alone or CAP and BK simultaneously increased the mean (suggesting a trend of loss of proximity between ANO1 and TRPV1) ($p = 0.0923$, Kruskll-Wallis test). **B)** No significant difference in the mean nearest ANO1 neighbour to TRPV1 distance between experimental conditions ($p = 0.425$, Kruskall-Wallis test). **C)** The mean percentage of total ANO1-immunoreactive puncta with a nearest TRPV1 neighbour within 100 nm significantly reduced in response to treatment with BK or CAP and BK, but no change was observed for CAP treatment. **D)** Only simultaneous treatment with both CAP and BK significantly changed the mean percentage of total TRPV1 immunoreactive puncta with an ANO1 nearest neighbour. Error bars represent mean ± SD. *$p < 0.05$ (one-way ANOVA with Holm-Sidak's multiple comparisons test). ANO1, anoctamin 1; TRPV1, transient receptor potential vanilloid type 1 receptor; CAP, capsaicin; BK, bradykinin; NND, nearest neighbour distance.

3.3 Discussion

In small-diameter nociceptive neurons of the DRG, selective localisation of Ca^{2+} signalling is achieved through the compartmentalisation of intracellular signalling pathways to distinct nanodomains, including the formation of JMSCs at regions of close apposition between the ER and PM (Delmas and Brown, 2002). To provide further control over the range and specificity of such signalling mechanisms, it is likely the formation and maintenance of JMSCs, including those between the PM-bound CaCC ANO1 and the ER-bound IP_3R1, is dynamically regulated. Despite evidence in support of activity-dependent translocation of the ER towards the PM (Orci et al., 2009), the dynamic regulation of ANO1-containing JMSCs in response to noxious stimulation in the DRG is unproven. This chapter demonstrates for the first time the activity-dependent formation of JMSCs between ANO1 and IP_3R1 and provides extensive evidence in support of a stimulus-specific dynamic rearrangement of ANO1 signalling complexes in primary DRG neurons *in vitro.* A combination of PLA and STED microscopy were used to probe nanoscale proximity between ANO1 and known interacting partners IP_3R1, at JMSCs between the ER and PM, and TRPV1, at the PM, and the data present herein supports a hypothesised mechanism of preferential coupling of ANO1 to BK-induced Ca^{2+} signals over those that are CAP-induced.

3.3.1 Proximity Ligation Assay Reveals the Activity-Dependent Formation of Novel Junctional Multiprotein Signalling Complexes in Small-Diameter Dorsal Root Ganglion Neurons

Activation of ANO1 by highly localised, high concentration IP_3-sensitive Ca^{2+} release from the ER is dependent upon nanodomain proximity between ANO1 and IP_3R1 at JMSCs in peripheral nociceptors (Jin et al., 2016, Jin et al., 2013). While PLA has been used previously to demonstrate proximity within 40 nm between ANO1 and IP_3R1 in DRG neurons at rest, it has been uncertain whether these interactions were static or under dynamic stimulus-dependent control. Considerable evidence supports the activity-dependent formation of *de novo* ER-PM contact sites in neurons (Mao et al., 2023, Hogea et al., 2021, Vullhorst et al., 2023). Therefore, it is logical to propose that increased proximity between the membranes coincides with increased proximity and formation of new signalling nanodomain complexes. Indeed, for the first time, this thesis presents evidence for noxious stimuli-induced formation of new ANO1-IP_3R1 functional couplings in DRG neurons.

PLA can be considered a discrete indicator of protein-protein interaction: either the target proteins are expressed within 40 nm of each other, in which case a PLA signal is resolved, or they are not. Therefore, each punctum can be considered an instance of

nanodomain proximity between the target proteins. As such, an increased number of puncta represents the formation of new nanodomain proximities, if not direct interactions. When primary DRG neuron cultures were exposed to 250 nM BK for 1 minute, the proportion of neurons displaying a positive PLA signal significantly increased compared to the control, supporting a mechanism of stimulus-evoked formation of novel ANO1-IP_3R1 nanodomains, although not necessarily the formation of new ER-PM contact sites. It may be the case that ANO1 and IP_3R1 are already expressed at existing ER-PM junctions in DRG neurons at rest, albeit at a greater distance apart than 40 nm, and re-localise to within 40 nm of each other in response to noxious stimuli-induced signalling events. Indeed, quantifying the PLA signal between ANO1 and IP_3R1 in DRG neurons exposed to BK for progressively increasing time periods revealed a fascinating and distinct time course for ANO1-IP_3R1 JMSC interaction, the kinetics of which appeared to closely match those observed for BK-induced mobilisation of PIP2 and subsequent release of intracellular Ca^{2+} stores (Liu et al., 2010). This makes sense in a physiological context as it would be necessary that prolonged exposure to an inflammatory stimulus requires a stronger nociceptive signal; therefore, with the recruitment of further ANO1-IP_3R1 functional couplings, a larger proportion of the viable population of ANO1 expressed at the PM is activated by stimulus-evoked release of intracellular Ca^{2+} stores resulting in increased Cl^- efflux, subsequent depolarisation and likelihood of firing an action potential serving to increase nociception to the CNS.

Therefore, it would be of scientific interest to investigate a potential dose-response effect of BK on ANO1-IP_3R1 nanodomain formation and to further speculate on how potential dysregulation of ANO1-IP_3R1 nanodomain formation may represent a novel pathophysiological mechanism underlying the development of chronic pain. Further, to unequivocally demonstrate that *de novo* ANO1-IP_3R1 nanodomains are formed in response to the release of intracellular Ca^{2+} stores, it would be necessary to repeat such PLA experiments following the depletion of ER Ca^{2+} stores with an agent such as the Ca^{2+}-ATPase inhibitor, thapsigargin. Under these conditions, application of BK would not evoke significant release of intracellular Ca^{2+} stores, therefore, we hypothesise that while the rate of ANO1-IP_3R1 interaction may be attenuated, it is unlikely to be abolished considering PLA signal is detected in DRG neurons prior to BK exposure and after the expected lifetime of BK-induced Ca^{2+} release, although this was not experimentally tested.

Most interestingly, this data also reveals an apparent dynamic range in the strength of ANO1-IP_3R1 interactions, considering PLA signal was detected in at least some DRG neurons at all timepoints of BK application and was only significantly increased above the baseline after at least 40 seconds. This suggests that to an extent, some ANO1-

IP_3R1 JMSCs are present at ER-PM contact sites that are not responsive to BK-induced Ca^{2+} release. It may be the case, therefore, that there is in fact two 'varieties' of ANO1-IP_3R1 JMSC which are differentially controlled, a Ca^{2+}-dependent and a Ca^{2+}-independent sub-population, which accounts for both the dynamic noxious stimuli-induced increase in PLA signal and for the baseline level of interaction. Potential mechanisms governing the control over each of these populations could be due to the independent or combined roles of multiple proteins mediating a 'tethering' function between the ER and PM, although this will be discussed in further detail in the following chapter and Chapter 7.

To conclude this section, these results undoubtedly reveal a degree of re-localisation of either ANO1, IP_3R1, or both within closer proximity likely to facilitate functional coupling and activation of ANO1 by IP_3-mediated Ca^{2+} release from the ER.

3.3.2 Theorising on the Organisation of ANO1 Signalling Nanodomains in Nociceptive Dorsal Root Ganglion Neurons

In small-diameter DRG neurons, ANO1-IP_3R1 JMSCs have been shown to couple independently to both B2R and TRPV1, mediating nociceptive amplification of BK and CAP-induced nociceptive signalling, respectively (Shah et al., 2020, Jin et al., 2013, Liu et al., 2010). This raises an important question of how ANO1-B2R interactions are balanced against ANO1-TRPV1 interactions, particularly in a physiological context where DRG neurons are likely to be simultaneously exposed to multiple noxious stimuli. Two alternate hypotheses have been proposed to model multimeric protein interactions in sensory neurons: that proteins which functionally interact with a variety of signalling partners, such as ANO1 or TRPV1, do so in an independent manner, or that larger 'super-complexes' comprised of multiple interacting partners are clustered into signalling microdomains (Gamper and Shah, 2022). The data presented in this thesis supports the view that ANO1, together with IP_3R1, TRPV1 and B2R, likely cluster together at ER-PM junctions in a 'super-complex' that undergoes dynamic activity-dependent rearrangement in response to differential noxious stimulation (Figure 3.19).

A combination of PLA and STED microscopy was utilised to probe ANO1 multi-protein signalling complexes in nanoscale resolution in fixed primary DRG neurons. While inherently, PLA imparts an effective 'resolution' of 40 nm for protein-protein proximity and the resolution achieved through STED imaging coupled with deconvolution was similarly around 40 nm. This is likely sufficient to resolve ANO1 interactions on the single-molecule scale; published high-resolution single-particle cryo-electron microscopy of Ca^{2+}-bound ANO1 protein purified from mouse predict the maximum diameter of its dimeric structure to be approximately 11 nm parallel to the PM (Paulino et al., 2017).

Additionally, single particle electron microscopy investigating the 3D structure of purified, tetrameric rat TRPV1 has estimated the functional protein's size to 15 nm tall perpendicular to the PM and the transmembrane region 6 nm wide parallel to the PM (Moiseenkova-Bell et al., 2008). Therefore, combining the expected linkage error of 30 nm per protein for binding of a primary and secondary antibody, the maximum size of a single ANO1-TRPV1 interaction could be estimated to be at most 77 nm in diameter parallel to the PM. Nearest neighbour analysis of STED localisations was an effective approach to visualising a general trend of proximity in DRG neurons, while PLA could quantify the number of discrete instances of nanodomain interaction between ANO1 and TRPV1.

Similar to ANO1-IP_3R1 JMSCs, the PLA data presented herein supports activity-dependent formation of ANO1 interactions. Stimulation of primary DRG cultures with the TRPV1 agonist CAP was sufficient to significantly increase the proportion of the neuronal population positive for PLA between ANO1 and TRPV1 and further, significantly increased the mean number of PLA puncta per neuron for those neurons displaying proximity between ANO1 and TRPV1. This suggests that, as observed between ANO1 and IP_3R1, a proportion of the total ANO1 population is already expressed within nanodomain proximity of TRPV1 in neurons at rest, but new ANO1-TRPV1 nanodomains are formed in response to noxious stimulation. Not only CAP was capable of increasing the proportion of DRG neurons positive for ANO1-TRPV1 nanodomain proximity; unexpectedly, stimulation with BK alone also increased the proportion of the total neuron population positive for PLA signal between ANO1 and TRPV1.

Together this data indicates a new hypothesis that upon noxious stimulation there may be increased trafficking of ANO1 towards regions of the PM where TRPV1 and B2R reside. This would account for the paradoxical increase in proportion of neurons displaying PLA signal between ANO1 and TRPV1 following exposure to BK, an agonist at B2R. Considering ANO1 is known to couple to both B2R and TRPV1, it makes sense that either BK or CAP treatment would be sufficient to promote its trafficking towards ER-PM junctions. Indeed, nociceptive ion channels including TRPV1 are reported to undergo activity-dependent trafficking to the PM as a mechanism of nociceptor sensitization in DRG neurons (Morenilla-Palao et al., 2004) so it is not unreasonable to consider ANO1 expression may be similarly regulated. It is further likely all three membrane proteins are co-expressed at the same nanodomains considering PLA signal was detected in neurons at rest between TRPV1 and B2R also. Interestingly, however, dual stimulation with both CAP and BK simultaneously did not significantly change the percentage of neurons displaying ANO1-TRPV1 PLA signal compared to the control; this does not necessarily imply an increased ANO1 trafficking, but perhaps represents a preferential coupling of

ANO1 to BK-induced Ca^{2+} signals, in which case newly formed ANO1-IP_3R1 JMSCs complex with B2R over TRPV1, resulting in ANO1 losing proximity with TRPV1 due to the activity-dependent rearrangement of an ER-PM junction super-complex (Figure 3.19). This hypothesis is supported by the observation that dual stimulation with CAP and BK significantly reduced the mean number of PLA puncta per neuron compared to the control, indicating a reduction in the number of ANO1-TRPV1 nanodomains despite the presence of CAP.

Nearest neighbour analysis of STED microscopy of immunostaining against ANO1 and TRPV1 in DRG neurons differentially stimulated with CAP, BK, or both agonists simultaneously, further supports a hypothesis of preferential coupling of ANO1 to BK-induced nociceptive signalling nanodomains over those that are CAP-induced. When the percentage of ANO1-TRPV1 and TRPV1-ANO1 NNDs within 100 nm was compared between experimental conditions it was observed that the mean percentage of ANO1-TRPV1 distances within 100 nm was significantly reduced in neurons exposed to BK compared to control neurons. This indicates that in response to BK, a smaller proportion of the total population of ANO1 molecules is found within 100 nm of a TRPV1 channel compared to neurons at rest, suggesting a translocation of at least 0.493 % (representing the minimum likely percentage of ANO1-TRPV1 pairs within 100 nm at rest minus the maximum likely percentage of ANO1-TRPV1 pairs with 100 nm following BK exposure) of the total ANO1 population away from TRPV1. Contrastingly, BK stimulation alone did not induce a significant change in the proportion of total TRPV1 molecules with a nearest ANO1 neighbour within 100 nm. This may suggest a likelihood of at least two distinct populations of ANO1 which differentially couple to either TRPV1 or B2R, rather than a single population that translocates between the two, dependent on the stimulus, and in that case, the overall effect observed following simultaneous treatment CAP and BK would represent a sum of the activity of two separate ANO1 populations.

Here it is vital to consider, however, that through the nature of the experimental design, only CAP-sensitivity could be selected for as there was no way to positively identify BK-responsive neurons whilst only immunostaining against ANO1 and TRPV1. This likely biases the results towards ANO1 functional coupling to CAP-evoked signalling pathways as all neurons sampled will express TRPV1, and therefore be CAP-sensitive, but not all neurons sampled may also express B2R, thus rendering their BK sensitivity unknown. While imaging a larger sample size may partially mitigate the impact of including non-BK responsive cells in the data set, this technicality means it may be likely only a small number of neurons would have been double-positive. The possible inclusion of B2R-negative neurons in the analysed dataset likely accounts for the large spread of data observed and in particular, may be reflected in the apparent clustering of BK-stimulated

neurons into sub-populations concerning their mean ANO1-TRPV1 NND (Figure 3.18A). To gain a fuller understanding of how ANO1 may display preferential coupling to different signalling nanodomains it would be of interest to repeat this series of PLA and STED experiments with ANO1 and B2R.

The proposed mechanism of preferential coupling of ANO1 to B2R-mediated Ca^{2+} release over that which is TRPV1-mediated could be explained in terms of activity levels of each of the PLC isoforms that B2R and TRPV1 activate. As a traditional G_qPCR, B2R activation primarily recruits the PLCβ1 isoform (Choi et al., 2010), while Ca^{2+} influx directly via the non-selective cation channel TRPV1 activates the PLCδ4 isoform (Lukacs et al., 2013). While the efficacy of each of these isoforms to mobilise intracellular Ca^{2+} stores has not been directly compared in the literature, PLCβ1 is reported to be expressed in greater concentrations in putative nociceptive DRG neuron populations compared to PLCδ4 (Usoskin et al., 2015), therefore, it is logical to assume a higher proportion of ANO1 is functionally coupled to PLCβ-activating B2R.

It is important to note also that ANO1 and TRPV1 and not exclusive binding partners, therefore, not all TRPV1 molecules will interact with ANO1 as TRPV1 multimerises in a great number of protein-protein associations (Gamper and Shah, 2022). This is reflected in the nearest neighbour analysis: it makes sense that there is no significant stimulus-dependent change in the distance from each TRPV1 channel expressed at the PM to the nearest neighbouring ANO1 as the proportion of TRPV1 channels that putatively interact with ANO1 is a smaller percentage of the total TRPV1 population, as measured by cluster analysis of STORM localisations in primary DRG neurons (approximately 46%) (Shah, 2017, Shah et al., 2020). This is further confirmed in the current dataset by the low percentage of total NNDs between TRPV1 and ANO1 that are within 100 nm even when neurons are stimulated with a TRPV1 agonist, CAP, which has been shown to activate ANO1. Interestingly, cluster analysis of triple-colour STORM localisations for ANO1, TRPV1 and IP_3R1 has revealed a small percentage (≈2%) of ANO1-TRPV1 associations are formed in absence of IP_3R1 (Shah et al., 2020). While this point towards ANO1-TRPV1 coupling in regions of the PM not in close apposition to the ER, and therefore, not forming part of JMSCs, previous studies investigating ANO1 nanodomains were restricted to DRG neurons at rest, equivalent to the control condition in the present study. Therefore, while no significant increase in degree of proximity between ANO1 and TRPV1 was measured by nearest neighbour analysis of STED data, PLA experiments did suggest increased instances of proximity between ANO1 and TRPV1 with CAP and also activity-dependent dynamic nature of ANO1-IP_3R1 JMSCs. It may be the case that stimulating DRG neurons with CAP would result in a larger proportion of triple-labelled clusters representing ANO1-IP_3R1-TRPV1 complexes in Shah and colleagues' STORM

experimental setup and indeed, it would be of interest to repeat the 'time-resolved' PLA experiment between ANO1 and IP_3R1 following stimulation of CAP to ascertain whether activation of TRPV1 is similarly capable of promoting the formation of novel ANO1-containing JMSCs.

3.3.3 Conclusion

The data presented in this thesis chapter demonstrates for the first time that ANO1 nociceptive signalling nanodomains in the DRG are dynamically and differentially regulated in an activity-dependent manner. Combining approaches to visualise ANO1-TRPV1 proximity at nanoscale resolution suggests that ANO1 may show preferential coupling to B2R, as nanodomain proximity between ANO1 and TRPV1 was lost following simultaneous stimulation with the TRPV1 agonist CAP and the B2R agonist BK. Furthermore, modulation of ANO1-IP_3R1 JMSCs may be under control of both a Ca^{2+}-dependent and Ca^{2+}-independent mechanism. The following chapter will evaluate a putative molecular mechanism underlying the dynamic regulation of Ca^{2+}-dependent ANO1-IP_3R1 signalling nanodomains in small-diameter DRG neurons, although, it is clear significant further work will be required to fully describe the new complexities underlying ANO1's role as a dynamically regulated amplifier of nociceptive signalling in sensory neurons.

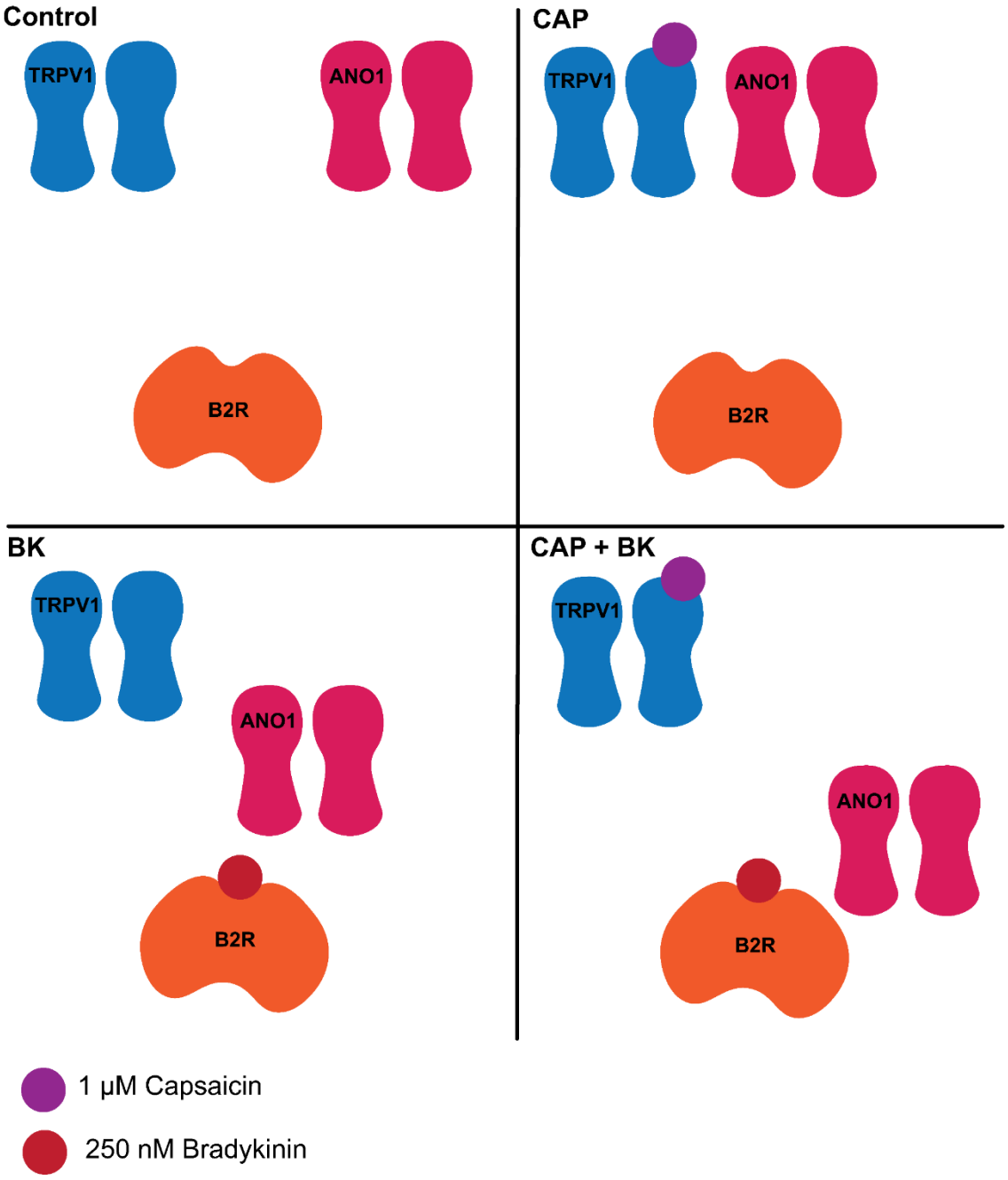

Figure 3.19: Schematic depicting the hypothesised stimulus-dependent rearrangement of putative ANO1-TRPV1-B2R 'supercomplexes' in nociceptive neurons. ANO1, anoctamin 1; B2R, bradykinin receptor type 2; TRPV1, transient receptor potential vanilloid type 1 receptor; CAP, capsaicin; BK, bradykinin.

Chapter 4: Extended Synaptotagmin 1 as a Putative Scaffolding Protein Associated with ANO1-IP_3R1 Junctional Multiprotein Signalling Complexes in Dorsal Root Ganglion Neurons

4.1 Introduction

Experimental evidence presented in Chapter 3 revealed a novel mechanism of BK-induced nanodomain proximity between ANO1 and IP_3R1 in small-diameter nociceptive neurons of the DRG. This was hypothesised to be the result of a Ca^{2+}-dependent translocation of the ER towards the PM, which may either promote formation of *de novo* JMSCs or simply facilitate closer interaction among existing complexes. Indeed, ER-PM contact site structure and function is thought to be closely regulated by intracellular Ca^{2+} signalling dynamics. In mammalian cell lines, depletion of ER Ca^{2+} stores has been shown to promote expansion of ER-PM contact sites following the redistribution of STIM1 to regions of ER in close apposition to the PM (Wu et al., 2006, Poteser et al., 2016, Orci et al., 2009). However, the molecular mechanisms by which ER-PM contact sites may be dynamically regulated in DRG sensory neurons are not yet fully understood. MCS scaffolding proteins such as JPH4 have been proposed to mediate JMSC formation between STIM1 and Orai1, facilitating SOCE upon ER Ca^{2+} store depletion (Hogea et al., 2021), but such a mechanism has not yet been investigated for ANO1-IP_3R1 JMSCs.

Recently, interest has turned towards Esyt1 as a candidate neuronal ER-PM scaffolding protein. Esyt1 is an evolutionarily conserved ER-resident protein that mediates a Ca^{2+}-dependent lipid transfer between the ER and PM and modulation of ER-PM contact sites through its function as a dynamic tether (Fernández-Busnadiego et al., 2015b). The Esyt1 C2A and C2C domains have been shown to act as a sensor for elevated cytosolic Ca^{2+} signals, including SOCE following store depletion, which subsequently promotes translocation of Esyt1 towards the PM, facilitating the formation of novel ER-PM contact sites to which STIM1 is recruited (Giordano et al., 2013, Min et al., 2007a, Saheki et al., 2016b). Binding of Ca^{2+} to the C2C domain is essential for Esyt1-mediated membrane tethering as genetic deletion of the C2C domain was sufficient to abolish Ca^{2+}-dependent translocation of Esyt1 towards the PM (Chang et al., 2013, Bian et al., 2018). Interestingly, the C2C and C2E domains possess a relatively low Ca^{2+} sensitivity, suggesting the need for a highly localised micromolar source of Ca^{2+}, similar to that observed for functional coupling between ANO1 and IP_3R1 (Idevall-Hagren et al., 2015). Though whether Esyt1 may be activated by release of intracellular Ca^{2+} stores in sensory neurons remains to be seen. Giordano and colleagues demonstrated that stimulation of G_q-coupled muscarinic receptors transfected in HeLa cells was sufficient to promote Esyt1 translocation to the PM (Giordano et al., 2013). However, these experiments were

conducted in the presence of extracellular Ca^{2+}, therefore ER store depletion would have been coupled to STIM1-Orai1-mediated SOCE. When repeated in the absence of extracellular Ca^{2+}, therefore inhibiting SOCE, G_q signalling-evoked release of ER Ca^{2+} stores failed to recruit Esyt1 to the PM, suggesting there may be a necessity for Ca^{2+} influx from the extracellular space for Esyt1-mediated ER-PM tethering (Idevall-Hagren et al., 2015). Nonetheless, Esyt1-mediated ER-PM junctions were demonstrated to be functionally distinct from those formed by STIM1-Orai1 interactions as genetic knockdown of Esyt1 had no effect on SOCE in HeLa cells and Esyt1-mediated contact sites displayed a characteristic electron dense layer between the ER and PM not observed under conditions expected to induce CRAC channel formation (Giordano et al., 2013, Fernández-Busnadiego, 2016, Fernández-Busnadiego et al., 2015a, Woo et al., 2020).

Intriguingly, in some cell types Esyt1 has been reported to functionally interact with ANO1. In airway epithelial cells ANO1 mediates Ca^{2+}-dependent Cl^- secretion necessary for the osmotic homeostasis of the extracellular environment to promote efficient mucociliary clearance (Ousingsawat et al., 2009, Rock et al., 2009). In one study, cell surface expression of ANO1 in bronchial epithelial cells was shown to be positively modulated by Esyt1. Small interfering ribonucleic acid (siRNA) knockdown of Esyt1 significantly decreased both PM expression of ANO1 and ANO1-mediated Cl^- current density, indicative of a physiological role for Esyt1 in regulating ANO1 functionality (Lérias et al., 2018). The molecular mechanism underlying Esyt1 modulation of ANO1 trafficking to the PM or whether such a mechanism is conserved across ANO1-expressing cell types is yet to be determined. Given its known role as an ER-PM tethering protein, it is tempting to speculate that Esyt1 may contribute to the formation and maintenance of ANO1-IP_3R1 JMSCs in peripheral nociceptors in a manner that involves recruitment of ANO1 to ER-PM junctions. Esyt1 has also been shown to promote PM localisation and activity of the transient receptor potential canonical 3 (TRPC3) Ca^{2+} channel (Liu, 2019). In the DRG, TRPC3 activation is coupled to IP_3-induced Ca^{2+} release and TRPC3-mediated Ca^{2+} influx contributes to SOCE in primary nociceptive neurons (Alkhani et al., 2014). Therefore, it may be the case that Esyt1 is similarly localised to ER-PM junctions and functionally interacts with JMSCs in the DRG.

4.1.1 Research Objectives and Hypotheses

The inherent Ca^{2+} sensitivity of Esyt1 presents an intriguing mechanism whereby the formation of ER-PM junctions may be under dynamic, Ca^{2+} signal-dependent regulation which could facilitate formation of JMSC interactions including those between ANO1 and IP_3R1. This thesis sought to evaluate a hypothesised role for Esyt1 as an ER-PM

junctional tether in small-diameter DRG neurons using a combination of super-resolution microscopy techniques including array detector microscopy, PLA and STED microscopy to investigate proximity between Esyt1 and ANO1-IP_3R1 JMSCs.

4.2 Results

4.2.1 Esyt1 is Expressed in a Heterogeneous Population of DRG Neurons

To ascertain a role for Esyt1 as a scaffolding protein in the peripheral somatosensory system, it was first essential to characterise protein expression of Esyt1 in the DRG. Primary rat DRG cultures were maintained in vitro for three days then lysed in RIPA buffer. Lysates were separated according to molecular weight via gel electrophoresis, transferred to a PVDF membrane (western blotting) and incubated with a primary anti-Esyt1 mouse antibody previously verified to recognise rat Esyt1 transfected in cell lines (see Chapter 2, Section 2.4.4) (Figure 4.1A). Immunostaining against the 'housekeeping' gene β-actin was included as a positive control for successful protein denaturing and transfer and robust β-actin immunoreactivity was observed at the expected molecular weight of 42 kDa. Esyt1 immunoreactivity was observed a single band with size between 100 and 150 kDa, consistent with the expected molecular weight of 123 kDa (Ashraf and Gerke, 2022). Specificity of the primary antibody to detect Esyt1 immunoreactivity was confirmed through western blot of lysate obtained from HEK293 cells transfected to overexpress recombinant Esyt1, which produced a clean immunoreactive band of the expected molecular weight (data not shown, unpublished observation courtesy of S. Shah).

Western blot analysis of lysates prepared from primary DRG culture is not able to distinguish cell type-specific expression. Therefore, to better localise Esyt1 expression in the DRG, immunostaining was performed in 4% PFA perfusion-fixed DRG sections and 4% PFA-fixed primary DRG cultures. Strong Esyt1 immunoreactivity was observed primarily in neurons (identified based on well-characterised morphology) with little to no immunofluorescence detected in surrounding satellite glial cells (SGCs) and Esyt1 expression was observed throughout the cytosolic compartment (Figure 4.1B). In primary DRG cultures, Esyt1 expression was entirely excluded from SGCs and other non-neuronal cells and present only in neurons (Figure 4.1B, right panel).

In the DRG, peripheral sensory neurons can be broadly classified as small-diameter unmyelinated C-fibre types (10 – 35 μm), medium-diameter thinly-myelinated Aδ-fibre types (35 – 50 μm) or large-diameter myelinated Aβ/α type (50+ μm) with C/Aδ types functioning primarily as nociceptors and thermoreceptors, while larger fibers being mostly low-threshold mechanoreceptors and proprioceptors (Aβ/α) (Le Pichon and Chesler, 2014). Furthermore, small-diameter and large-diameter subpopulations can be distinguished based on their differential expression of commonly used peripheral neuron size markers, peripherin, which typically labels non-myelinated C-fibre neurons (small-diameter), and neurofilament 200 kDa (NF200), which typically labels myelinated A-fibre

neurons (large-diameter) (Sleigh et al., 2017, Ferri et al., 1990). To further characterise Esyt1 expression in the DRG based on expected neuron modality, somatic diameter distribution analysis was performed on a representative sample of confocal micrographs depicting Esyt1 immunoreactivity in 4% PFA perfusion fixed rat DRG sections (N = 4). Sections were immunostained against Esyt1 with either peripherin (Figure 4.1C) or NF200 (Figure 4.1D) to further distinguish neuronal populations. Positive immunoreactivity was determined based on meeting a threshold 'Z score' set based on the mean fluorescence intensity calculated for all neurons in each biological replicate as described in Section 2.4.2.

Esyt1 immunoreactivity was detected in both peripherin-positive and NF200-positive neurons, suggesting Esyt1 expression may be present throughout the neuron and not confined to the soma (Figure 4.1D). In total, 542 of 1778 DRG neurons analysed were determined to be significantly immunoreactive for Esyt1, representing 30.5% of the population. The mean somatic diameter of Esyt1 immunoreactive neurons was 29.8 ± 0.401 μM, although this was significantly greater than that of non-immunoreactive neurons (27.7 ± 0.267 μM) ($p = 0.0019$, Mann-Whitney test). The mean somatic diameter of peripherin-positive neurons (27.8 ± 0.355 μM) was significantly smaller than the mean somatic diameter of NF200-positive neurons (31.6 ± 0.975 μM) ($p = 0.0002$, Kruskall-Wallis with Dunn's multiple comparisons test), consistent with the prior literature and confirming the ability of these two markers to distinguish between different neuronal populations. The Esyt1-positive neuron population has a mean somatic diameter both significantly greater than that of peripherin-positive neurons ($p = 0.0346$, Kruskall-Wallis with Dunn's multiple comparisons test) and significantly smaller than that of NF200-positive neurons ($p = 0.0211$, Kruskall-Wallis with Dunn's multiple comparisons test), suggesting that Esyt1 expression was not biased towards neurons of a particular size class. Indeed, Esyt1-positive neurons in DRG sections ranged in diameter from 6.17 μM up to 72.0 μM (Figure 4.1E).

Interestingly, of the total neuronal population that was either peripherin-positive (n = 354) or NF200-positive (n = 75), a significantly greater proportion of NF200-positive neurons were also immunoreactive for Esyt1 (92.0 %) compared to the proportion of peripherin-positive neurons that co-expressed Esyt1 (61.9 %) ($p < 0.0001$, Fisher's exact test) (Figure 4.1F). However, it is important to note here that the much smaller sample size of NF200-positive neurons used for these calculations was not due to a lesser proportion of the whole DRG neuron population expressing NF200 but simply due to an overall reduced sample size analysed and in fact of the total populations sampled for NF200 (n = 311) and peripherin (n = 1468) immunoreactivity, there was no significant difference in the percentage of neurons classified as immunoreactive for NF200 (24.1 %) as for

peripherin (24.1 %) ($p > 0.999$, Fisher's exact test). For the total neuronal population classified as Esyt1-positive, 77.9% had a somatic diameter of 35 μM or less, supportive of a functional role in small-diameter nociceptive neurons; however, of the total DRG neuron population sampled, the mean somatic diameter was 28.3 ± 0.224 μm and 80.3 % had a somatic diameter of 35 μM or less, so perhaps this distribution for Esyt1 expression is not unexpected.

To further confirm antibody specificity and control for non-specific binding of the fluorophore-conjugated secondary antibodies used throughout this study, immunohistochemistry in 4% PFA perfusion-fixed DRG sections was repeated as previous with the exception of excluding any primary antibodies used. Confocal microscopy performed under the same experimental parameters with regard to excitation laser power and gain detected no non-specific immunofluorescent signal, confirming specificity for the secondary antibodies (Figure 4.2).

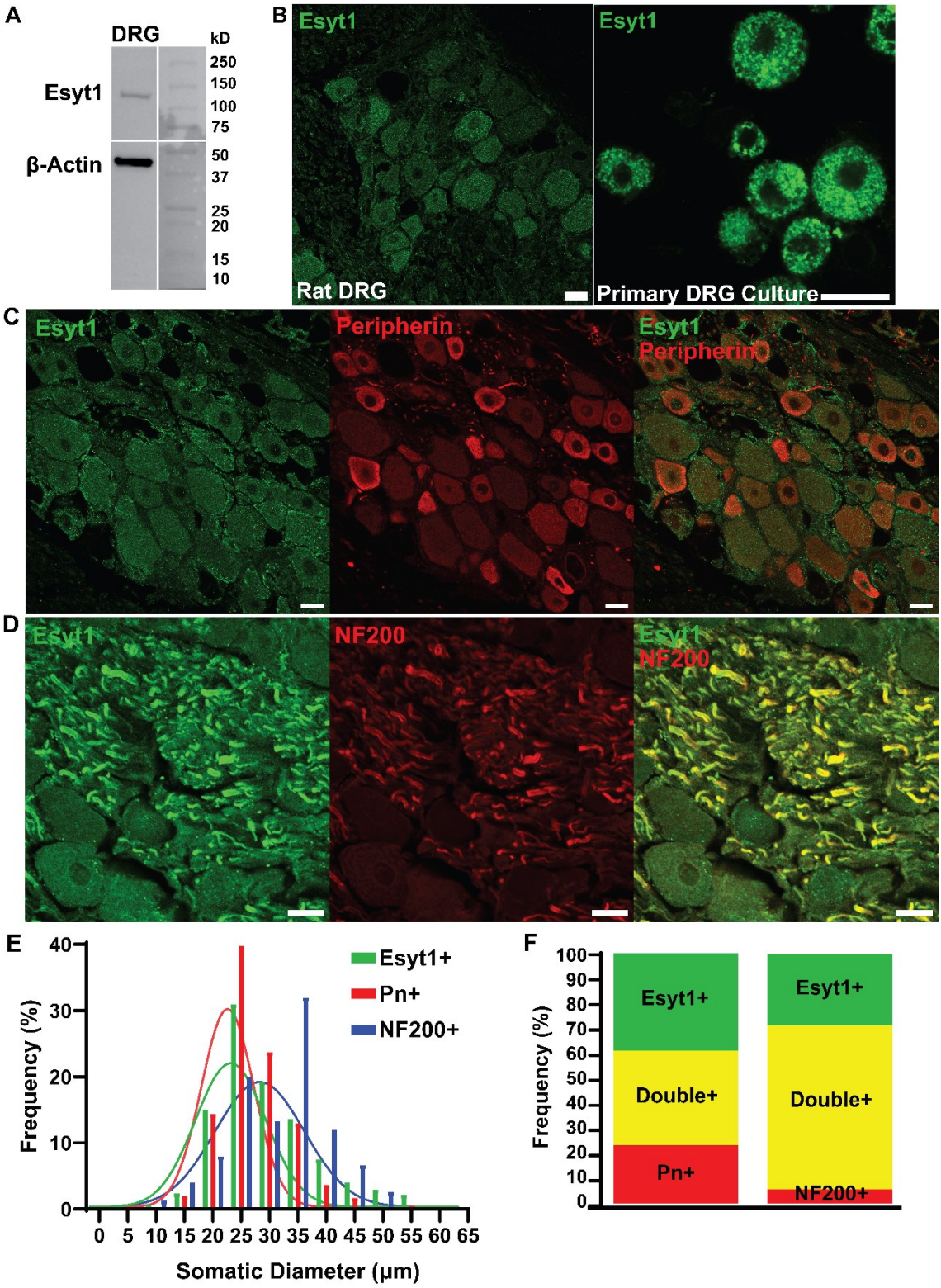

Figure 4.1: Esyt1 protein expression in the dorsal root ganglion. Continued on next page.

Figure 4.1: Esyt1 protein expression in the dorsal root ganglion.
A) Western blot of electrophoresed primary DRG culture lysate demonstrating immunoreactivity for Esyt1 (band between 100 and 150 kDa) and the 'housekeeping' protein β-actin (band between 37 and 50 kDa). **B)** Representative confocal micrographs depicting Esyt1 protein immunoreactivity in neurons from vibratome sections of 4% PFA perfusion-fixed weaned rat DRG (left panel) and 4% PFA-fixed primary neuron culture prepared from dissociated neonatal rat DRG tissue (right panel). **C)** Representative (N = 3) confocal micrographs depicting co-expression of Esyt1 in DRG neurons immunoreactive for the small-diameter peripheral C-fibre neuronal marker peripherin. **D)** Confocal micrograph depicting co-expression of Esyt1 in putative A-fibres immunoreactive for the medium-to-large-diameter peripheral neuron marker NF200. **E)** Frequency distribution histograms for the somatic diameters of DRG neurons significantly immunoreactive for Esyt1 (green), peripherin (red), and NF200 (blue). Histograms were fit with a single-Gaussian distribution curve to allow for comparisons between the peak (mean) and width (± 1 S.D.) for each protein's expression pattern. Positive immunoreactivity was determined by comparing the mean fluorescence intensity for each neuron against the overall mean calculated from all neurons sampled in each biological replicate (N = 3). **F)** The percentage of the total DRG neuron population immunoreactive for Esyt1 (Esyt1+), peripherin (peripherin+) or NF200 (NF200+) alone was compared against the percentage of neurons co-expressing Esyt1 and peripherin (Double+) (left) or Esyt1 and NF200 (Double+) (right). A significantly greater proportion of NF200-positive neurons were also immunoreactive for Esyt1 (92.0 %) compared to the proportion of peripherin-positive neurons that co-expressed Esyt1 (61.9 %) ($p < 0.0001$, Fisher's exact test). Scale bars = 10 µm. Esyt1, extended synaptotagmin 1; DRG, dorsal root ganglion; NF200, neurofilament 200; PFA, paraformaldehyde.

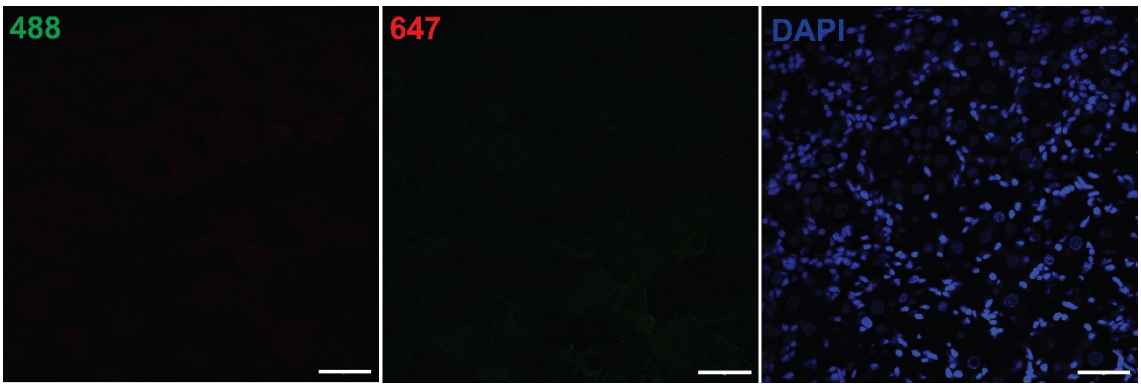

Figure 4.2: Secondary antibody-only negative controls for immunohistochemistry of DRG neurons. PFA perfusion-fixed DRG sections were immunostained in the absence of primary antibodies using the Alexa Fluor™ 488- and Alexa Fluor™ 647-conjugated secondary antibodies utilised throughout this thesis. No detectable non-specific immunofluorescence was observed for either secondary antibody in DRG tissue sections. The far-right panel depicts the corresponding DAPI counterstain for the section where the nuclei of neurons are visible as larger, dim round regions of fluorescence and the brighter, smaller oval regions of staining represent nuclei of supporting satellite glial cells. Scale bars = 10 μm. DRG, dorsal root ganglion; PFA, paraformaldehyde; DAPI, 4',6-diamidino-2-phenylindole.

4.2.2 Colocalisation Analysis Reveals Esyt1-ANO1 Colocalisation in Small-Diameter DRG Neurons

Having confirmed Esyt1 protein expression in small-diameter DRG neurons, interest turned to whether this expression is closely associated with ANO1-IP_3R1 signalling nanodomains, which would posit a functional interaction between Esyt1 and JMSCs during nociception. Immunohistochemistry was performed in 4% PFA-fixed DRG sections against Esyt1 with either ANO1 or IP_3R1 to assess for co-expression in the same neuronal sub-populations. Traditional confocal microscopy detected Esyt1-like immunoreactivity in neurons that were also immunoreactive for ANO1 (Figure 4.3A) and IP_3R1 (Figure 4.3B). However, considering JMSC interactions occur in the nanoscale, diffraction-limited confocal microscopy is underpowered to detect true colocalisation of signalling complexes. Having established the usefulness of super-resolution microscopy approaches to investigating protein-protein interaction in sensory neurons in Chapter 3, a similar approach was utilised here with the addition of array detector microscopy (Airyscan).

The ZEISS Airyscan detector provides an up to 1.7x increase in spatial resolution in the x, y and z dimensions with a 4-8x improvement in signal-to-noise (SNR) ratio compared to traditional confocal laser scanning microscopy (LSM) (Huff, 2015), therefore providing an accessible super-resolution approach to study protein colocalisation. Colocalisation analysis provides a quantitative measure of either the co-occurrence (overlap) of fluorophore signals or the correlation of their intensities for each pixel within an identified ROI (Adler and Parmryd, 2010, Adler and Parmryd, 2013). Correlation analysis based on the PCC produces a scatter plot of the intensity of each pixel in the first channel against its corresponding intensity in the second channel (Bolte and Cordelieres, 2006). Linear regression analysis of the resulting plot provides a correlation coefficient between -1 and 1 where the plot's gradient represents the rate of fluorophore association within the ROI with a PCC of 1 representing perfect colocalization, -1 representing perfect exclusion and 0 representing no correlation between pixel intensities (Bolte and Cordelieres, 2006). PCC was chosen over other colocalisation algorithms as the signal-to-noise ratio has limited effect on its ability to differentiate colocalised pixels from non-colocalised pixels therefore it remains useful even in the case of high background signal (Krauß et al., 2015).

Colocalisation analysis was performed for Airyscan images obtained of 4% PFA perfusion-fixed DRG sections immunostained against Esyt1 with ANO1 (N = 3) and Esyt1 with IP_3R1 (N = 3) and PCC values were calculated for all neurons determined to be double immunopositive (n = 43 Esyt1+/ANO1+ neurons and n = 41 Esyt1+/IP_3R1+ neurons). Neurons demonstrating significant immunoreactivity for both Esyt1 and ANO1

had somatic diameters between 15.2 and 37.2 µm with a mean of 24.2 ± 0.821 µm, which was significantly smaller than the mean somatic diameter of neurons immunoreactive for both Esyt1 and IP_3R1 (34.4 ± 1.35 µm, range: 21.9 to 58.0 µm) ($p < 0.0001$, unpaired t-test) (Figure 4.3C, D). This likely reflects the preferential distribution of ANO1 to small-diameter nociceptors (Liu et al., 2010) whereas IP_3R1 does not show such an expression pattern (Dent et al., 1996).

Colocalisation analysis suggested a significantly greater degree of colocalisation between ANO1 and Esyt1 immunoreactivity than between IP_3R1 and Esyt1 immunoreactivity. The mean PCC value between ANO1-like and Esyt1-like immunosignal was determined to be 0.432 ± 0.0353, indicative of a weak positive correlation. This was significantly larger than the mean PCC between IP_3R1-like and Esyt1-like immunosignal, however, which was only 0.0656 ± 0.0332, suggesting no correlation between Esyt1 and IP_3R1 immunoreactivity ($p < 0.0001$, Mann-Whitney test). To investigate whether Esyt1 colocalisation with either ANO1 or IP_3R1 differed dependent on neuronal size, the somatic diameter of double-positive neurons was plotted against the PCC for each respective neuron. Linear regression analysis of colocalisation between Esyt1 and ANO1 revealed a best-fit slope of -0.00528 ± 0.00666, indicating a slight negative correlation which may allude to a stronger degree of colocalisation between Esyt1 and ANO1 immunoreactivity in smaller-diameter neurons, however, this correlation was not deemed significantly non-zero ($p = 0.432$, $R^2 = 0.0151$), therefore indicating Esyt1-ANO1 colocalisation was similar across the range of neuronal sizes sampled (Figure 4.3E). Similarly, linear regression analysis of colocalisation between Esyt1 and IP_3R1 immunoreactivity revealed a best-fit slope of 0.00178 ± 0.00393, which was also not significantly non-zero ($p = 0.653$, $R^2 = 0.00524$), indicating no correlation between degree of colocalisation and somatic diameter for Esyt1-IP_3R1 double-positive neurons (Figure 4.3F).

In conclusion, colocalisation analysis did not identify a significant correlation between the expression patterns of Esyt1-like immunoreactivity with that of ANO1 or IP_3R1 in DRG neurons. However, Airyscan typically achieves a lateral resolution of approximately 120 nm (Wu and Hammer, 2021), which is insufficient to visualise true nanodomain proximity between interacting proteins. Therefore, more powerful super-resolution approaches were required to probe potential interaction between Esyt1 and ANO1 in small-diameter DRG neurons.

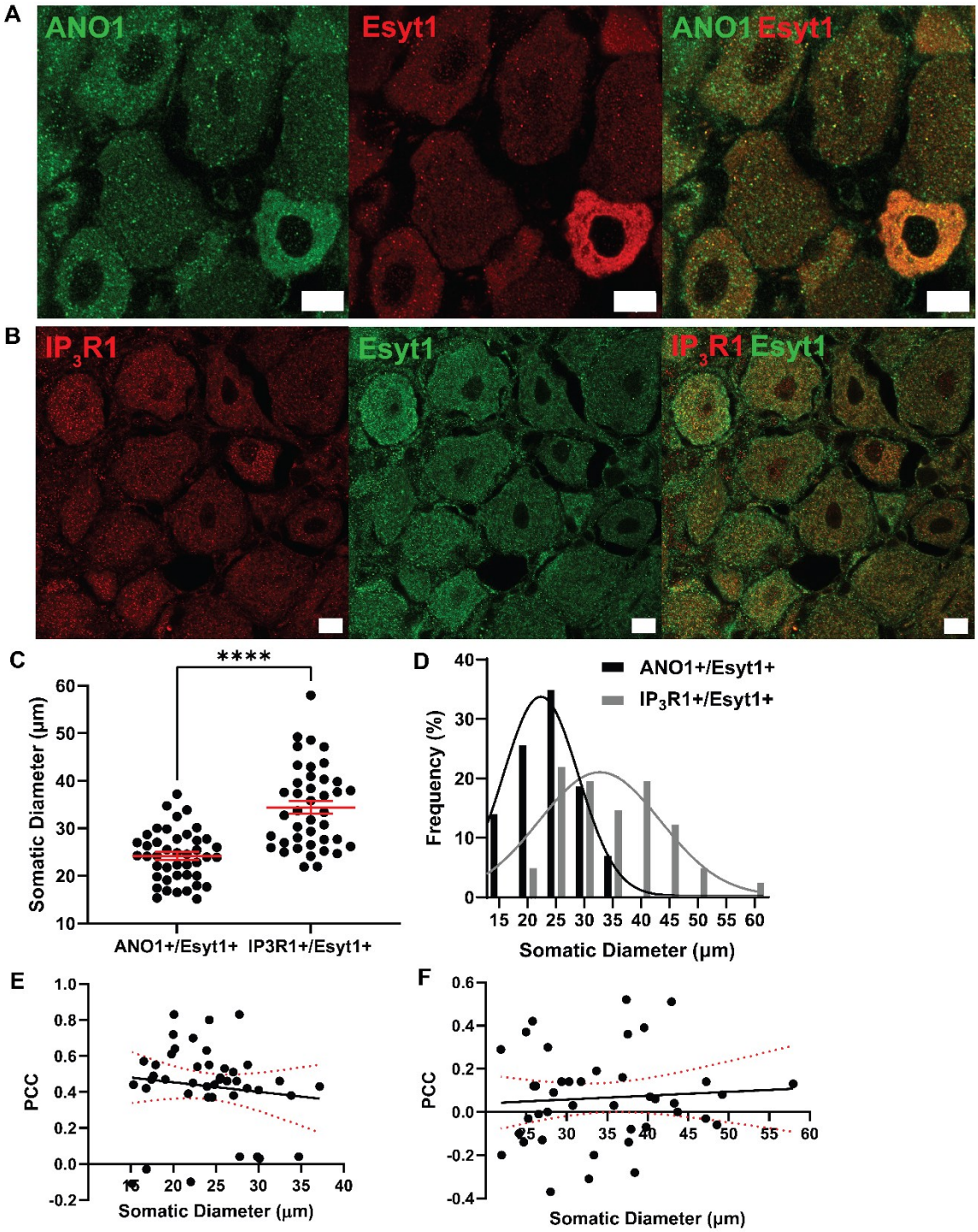

Figure 4.3: Super-resolution array detector microscopy reveals significant colocalisation between Esyt1 and ANO1 in a sub-population of small-diameter DRG neurons. Continued on next page.

Figure 4.3: Super-resolution array detector microscopy reveals significant colocalisation between Esyt1 and ANO1 in a sub-population of small-diameter DRG neurons. Representative (N = 3) Airyscan micrographs depicting co-expression of Esyt1 and ANO1 **(A)** and Esyt1 and IP_3R1 **(B)** immunoreactivity in small-diameter neurons in a 4% PFA perfusion-fixed DRG sections. **C)** The mean somatic diameter of DRG neurons immunopositive for both Esyt1 and ANO1 was significantly smaller than that for neurons co-expressing Esyt1 and IP_3R1 ($p < 0.0001$, Mann-Whitney test). **D)** Frequency distribution histograms for the somatic diameters of DRG neurons immunopositive for both Esyt1 and ANO1, and Esyt1 and IP_3R1 were fit with a single-Gaussian distribution curve to visualise differences in the mean diameter between two distinct sub-populations. Colocalisation between Esyt1 and ANO1 **(E)** and Esyt1 and IP_3R1 **(F)** in double-immunopositive DRG neurons was quantified using Pearson's correlation coefficient and plotted against the respective somatic diameter. No significant correlation was observed between colocalisation and somatic diameter suggesting Esyt1 colocalisation with ANO1-IP_3R1 signalling complexes is not preferentially restricted to DRG sensory neurons of any size and therefore, sensory modality. However, the mean PCC between Esyt1 and ANO1 was significantly greater than the mean PCC between Esyt1 and IP_3R1 ($p < 0.0001$, Mann-Whitney test). Error bars represent the mean ± SEM **(C)** or the 95% confidence interval for linear regression best-fit **(E** and **F).** **** $p < 0.0001$. Scale bars = 10 µm. DRG, dorsal root ganglion; Esyt1, extended synaptotagmin 1; ANO1, anoctamin 1; IP_3R1, inositol triphosphate receptor type 1; PCC, Pearson's correlation coefficient; ANO1+, ANO1-immunopositive; Esyt1+, Esyt1-immunopositive; IP_3R1+, IP_3R1-immunopositive.

4.2.3 PLA Reveals a Stimulus-Dependent Dynamic Rearrangement of Putative ANO1-IP_3R1-Esyt1 Signalling Complexes *In Vitro*

PLA provides a more precise measure of protein colocalisation than traditional immunohistology-based colocalisation analysis and was therefore used to investigate the putative nanodomain association of Esyt1 with ANO1-IP_3R1 JMSCs in DRG neurons.

PLA performed in untreated 4% PFA-fixed primary DRG neuron cultures (N = 3) revealed a robust punctate signal between Esyt1 with both ANO1 (Figure 4.4A) and IP_3R1 (Figure 4.4B). A positive PLA signal was once again defined as any neuron displaying at least one fluorescent punctum. PLA between Esyt1 and ANO1 was observed in a total of 68 neurons ranging in diameter from 8.87 to 40.6 µm, and the mean somatic diameter for this neuronal population was 22.2 ± 0.789 µm. The mean number of puncta per neuron was 1.76 ± 0.183, suggesting a relatively low incidence of nanodomain proximity between Esyt1 and ANO1 in DRG neurons at rest. To control for the heterogeneous size range of DRG neurons, the number of puncta per neuron was normalised as puncta/diameter and the resulting value was plotted against the respective diameter for each cell (Figure 4.4C). Linear regression analysis of the best-fit slope (slope = 0.0000905) revealed no significant correlation between the number of PLA puncta and the somatic diameter. Contrastingly, analysis of PLA between Esyt1 and IP_3R1 in DRG neurons at rest (N = 3, n = 75) revealed the mean number of puncta per neuron (normalised to diameter) to be significantly greater than that for PLA between Esyt1 and ANO1 ($p < 0.0001$, Mann-Whitney test) (Figure 4.4D). A greater incidence of nanodomain proximity between Esyt1 and IP_3R1 is logical, considering both are localised to the ER However, it is also important to recognise that different antibody pairs may differ in their ability to form a PLA signal due to their particular binding orientation and the relative locations of antigen residues on the respective target proteins. PLA signal between Esyt1 and IP_3R1 was detected in neurons ranging in diameter from 7.67 to 29.5 µm, and the mean somatic diameter of PLA-positive neurons was 17.6 ± 0.573 µm, which was significantly lower ($p < 0.0001$, Mann-Whitney test) than the mean diameter of DRG neurons identified to be positively immunoreactive for both Esyt1 and IP_3R1 (refer to Figure 4.3C and D) This may suggest that while Esyt1 and IP_3R1 are both expressed by medium-to-large-diameter DRG neurons, in these neurons their expression is not closely associated, which could reflect a preferential role for Esyt1 coupling to JMSCs in nociceptive neurons. The number of puncta per neuron was normalised to somatic diameter and plotted as previously; however, linear regression analysis of the best-fit slope (slope = -0.0144 ± 0.00780) revealed no significant correlation between somatic diameter and PLA signal between Esyt1 and IP_3R1 ($p = 0.0693$) (Figure 4.4E).

In the previous chapter, a time-resolved PLA approach was developed to demonstrate dynamic, stimulus-evoked nanodomain proximity between ANO1 and IP_3R1 and TRPV1. Therefore, to investigate whether Esyt1's association with ANO1 and IP_3R1 changes as a result of noxious stimulation, a similar approach was taken. Primary DRG cultures (N = 3) were individually exposed to 250 nM BK under normal extracellular Ca^{2+} concentrations for 10, 20, 30, 40, 50, 60, 120, 180 and 300 seconds prior to immediate fixation in 4% PFA without washout. Punctate PLA signal between both Esyt1 and ANO1 (Figure 4.5 and 4.7A), and Esyt1 and IP_3R1 (Figure 4.6 and 4.7C) was detected in small-diameter DRG neurons at all time points except for 180 seconds for Esyt1 and ANO1 (due to technical issues with culture preparation data for this time point was incomplete). Interestingly, PLA signal between Esyt1 and IP_3R1 was observed to be highly localised to the PM, whereas the signal between Esyt1 and ANO1 was distributed throughout the neuronal soma. Plotting the mean number of puncta per neuron (normalised to diameter) for each time point revealed that prolonged stimulation with the inflammatory mediator BK significantly altered the degree of nanodomain proximity between both Esyt1 and ANO1 (Figure 4.7B) and Esyt1 with IP_3R1 (Figure 4.7D). Stimulation with 250 nM BK for all periods tested significantly increased the mean PLA signal between Esyt1 and ANO1 compared to the control ($p < 0.0001$, Kruskall-Wallis with Dunn's multiple comparisons test). However, the mean number of puncta per neuron fluctuated considerably with increasing duration of BK stimulation and did not suggest an obvious pattern to this dynamic interaction between Esyt1 and ANO1. The peak PLA signal was observed in neurons exposed to 250 nM BK for 120 seconds where the mean number of puncta per neuron (normalised to diameter) was 1.30 ± 0.0924. It is relevant to note here that this value was highly significantly greater than the mean number of puncta per neuron for neurons stimulated with BK for both 60 seconds (0.620 ± 0.0560, $p < 0.0001$) and 300 seconds (0.562 ± 0.0622, $p < 0.0001$) so marks an unexpected secondary spike in nanodomain proximity between Esyt1 and ANO1. To make a qualitative observation, it is interesting to note that the localisation of PLA signal between Esyt1 and ANO1 appeared most closely associated with the PM in neurons stimulated with BK for 40 and 50 seconds, which may be a relevant parallel to the peak interaction between ANO1 and IP_3R1 observed in Chapter 3. Combining observations of puncta localisation and fluctuations in the mean PLA signal suggests a complex, multi-faceted interaction between Esyt1 and ANO1 in small-diameter DRG neurons which will require additional experimental approaches to fully elucidate.

Similarly, plotting the mean number of puncta per neuron (normalised to diameter) against the duration of BK exposure for PLA between Esyt1 and IP_3R1 revealed an interesting fluctuation in the degree of 40 nm proximity. Interestingly, the mean PLA

signal in neurons stimulated with BK for 10 seconds (1.40 ± 0.0755 puncta per unit diameter) was significantly increased compared to that of the control neurons (0.973 ± 0.0967) ($p < 0.0001$, Kruskall-Wallis with Dunn's multiple comparisons test). However, for neurons stimulated with BK for 20, 30, 40 and 50 seconds, the mean number of puncta per neuron was not significantly different than the control group. A secondary peak in the mean PLA signal between Esyt1 and IP_3R1 was observed in neurons stimulated with BK for 60 and 120 seconds. However, in neurons stimulated with BK for 180 and 300 seconds, the mean number of puncta per neuron was significantly *less* than that of control neurons (0.370 ± 0.0412, $p = 0.0012$ and 0.441± 0.0390, $p = 0.0033$, respectively, Kruskall-Wallis with Dunn's multiple comparisons test). Again, it is relevant to make the qualitative observation that for neurons stimulated with BK for both 60 and 120 seconds, representing the apparent peak in nanodomain proximity between Esyt1 and IP_3R1, the pattern of punctate PLA signal shows greater distribution throughout the neuron rather than the specific localisation towards the PM observed in neurons stimulated with BK for a shorter duration, or indeed, the control neurons.

Overall, these data reflect a complex and dynamic rearrangement of Esyt1 with respect to ANO1-IP_3R1 JMSCs in small-diameter DRG neurons and whether Esyt1 may interact with either ANO1 or IP_3R1 independently of ER-PM contact sites remains to be determined.

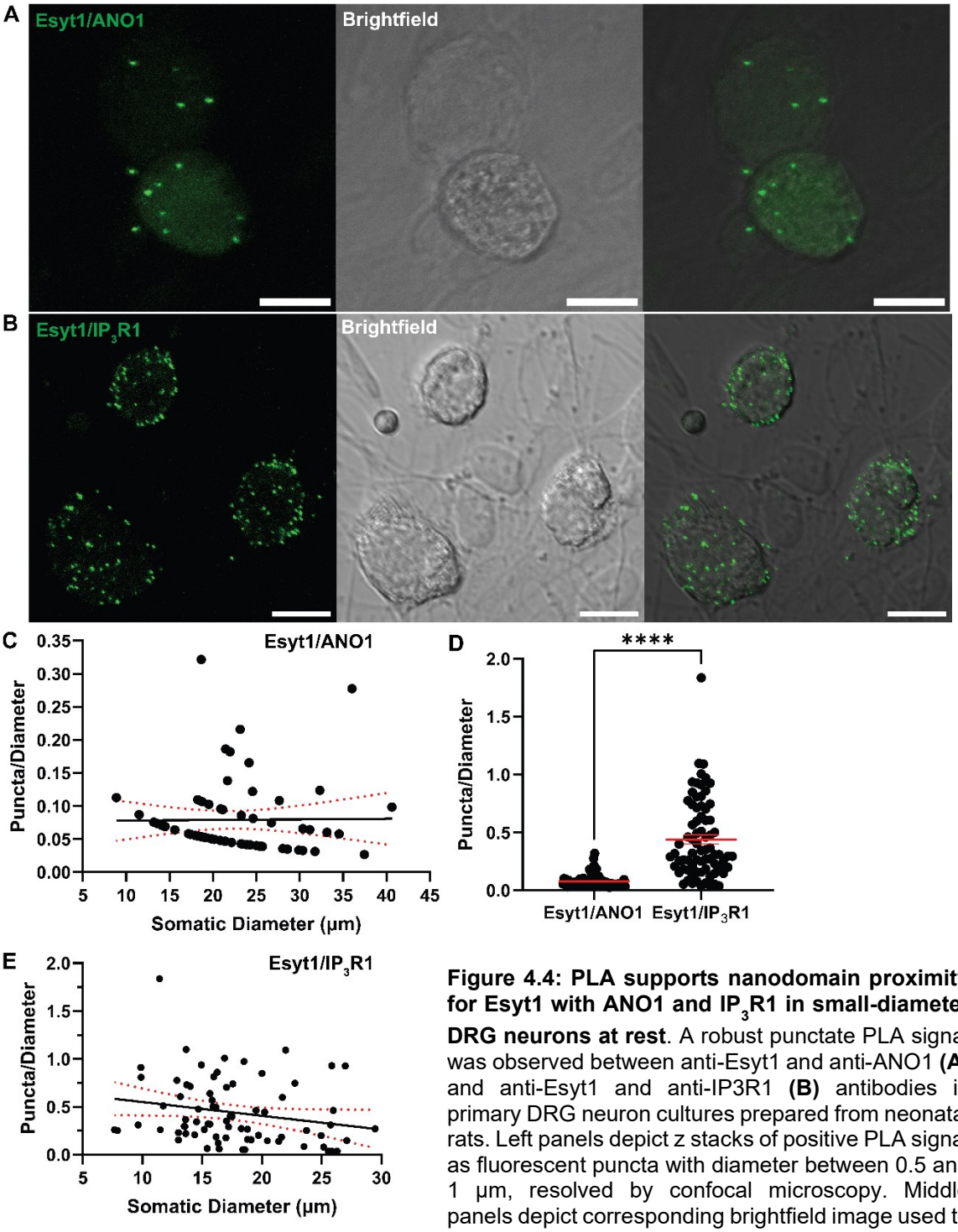

Figure 4.4: PLA supports nanodomain proximity for Esyt1 with ANO1 and IP_3R1 in small-diameter DRG neurons at rest. A robust punctate PLA signal was observed between anti-Esyt1 and anti-ANO1 **(A)** and anti-Esyt1 and anti-IP3R1 **(B)** antibodies in primary DRG neuron cultures prepared from neonatal rats. Left panels depict z stacks of positive PLA signal as fluorescent puncta with diameter between 0.5 and 1 μm, resolved by confocal microscopy. Middle panels depict corresponding brightfield image used to identify DRG neurons based on their morphological appearance in culture. Right panels represent an overlay of the brightfield and fluorescent PLA signal to localise puncta to particular sub-cellular compartments. Number of puncta was normalised to somatic diameter for each neuron and plotted against its respective diameter to perform linear regression analysis for PLA between Esyt1 and ANO1 **(C)** and Esyt1 and IP_3R1 (**E).** No significant correlation was observed for either condition between somatic diameter and the normalised PLA signal suggesting the degree of proximity between Esyt1 and ANO1-IP_3R1 nanodomains did not differ as a result of neuronal size, and therefore, modality. **D)** The mean PLA signal between Esyt1 and IP_3R1 was significantly greater than between Esyt1 and ANO1 in DRG neurons at rest ($p < 0.0001$, Mann-Whitney test). Error bars represent the mean ± SEM **(D)** or the 95% confidence interval for linear regression best-fit **(C** and **E).** **** $p < 0.0001$. Scale bars = 10 μm. PLA, proximity ligation assay; Esyt1, extended synaptotagmin 1; ANO1, anoctamin 1; IP_3R1, inositol triphosphate receptor type 1.

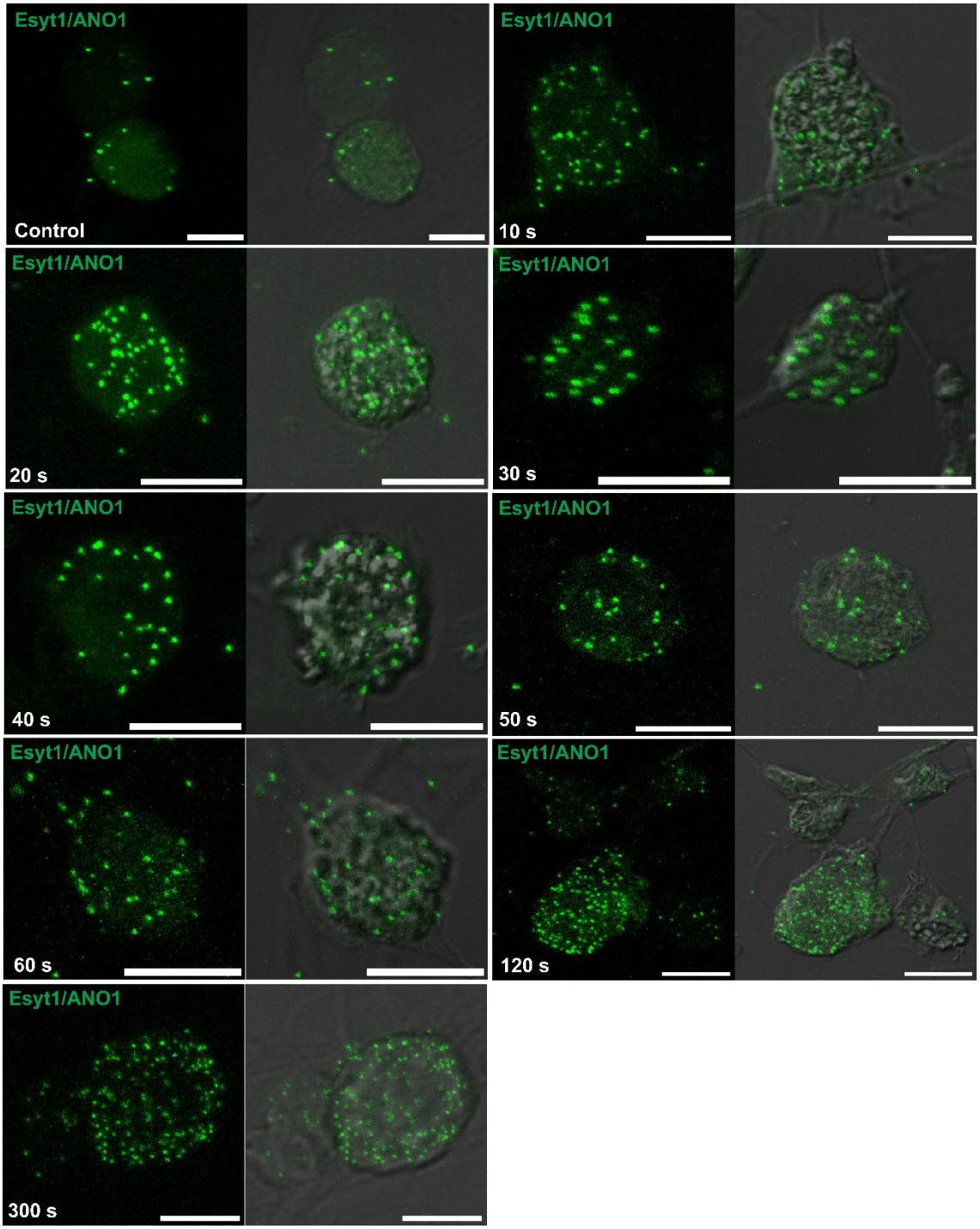

Figure 4.5: Time-resolved PLA between Esyt1 and ANO1 in primary cultured DRG neurons. Representative maximum intensity projections of confocal z stacks depicting robust punctate PLA signal between anti-Esyt1 and anti-ANO1 primary antibodies in primary cultured DRG neurons exposed to 250 nM BK for progressively increasing durations of time (10, 20, 30, 40, 50, 60, 120 and 300 seconds) prior to immediate fixation in 4% PFA without washout. Left panels depict PLA signal as fluorescent puncta with diameter between 0.5 and 1 µm, resolved by confocal microscopy. Right panels depict an overlay of PLA signal with corresponding brightfield images to identify DRG neurons based on their morphological appearance in culture. Scale bars = 10 µm. PLA, proximity ligation assay; Esyt1, extended synaptotagmin 1; ANO1, anoctamin 1; DRG, dorsal root ganglion; PFA, paraformaldehyde; BK, bradykinin.

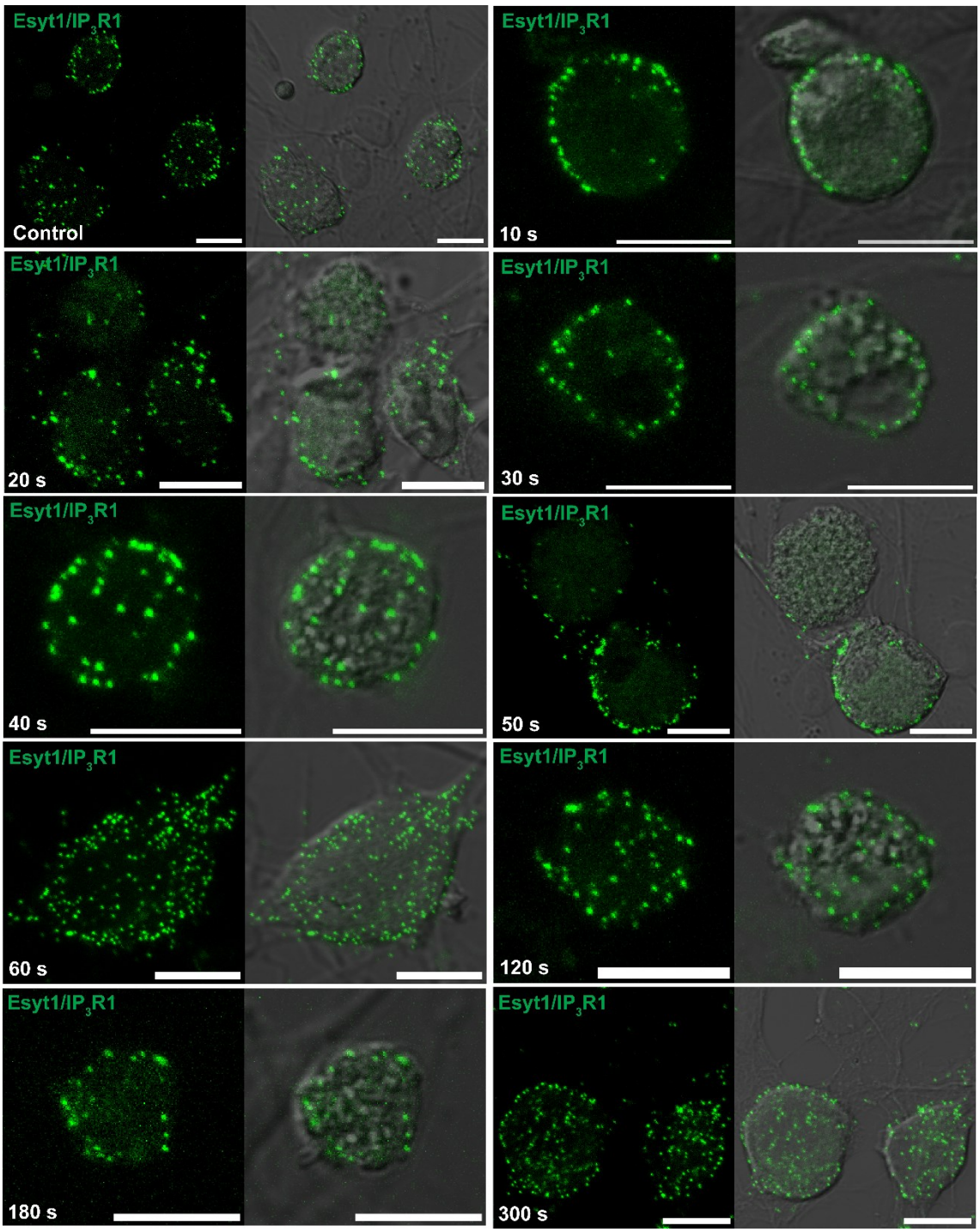

Figure 4.6: Time-resolved PLA between Esyt1 and IP_3R1 in primary cultured DRG neurons. Representative maximum intensity projections of confocal z stacks depicting robust punctate PLA signal between anti-Esyt1 and anti-IP_3R1 primary antibodies in primary cultured DRG neurons exposed to 250 nM BK for progressively increasing durations of time (10, 20, 30, 40, 50, 60, 120, 180 and 300 seconds) prior to immediate fixation in 4% PFA without washout. Left panels depict PLA signal as fluorescent puncta with diameter between 0.5 and 1 µm, resolved by confocal microscopy. Right panels depict an overlay of PLA signal with corresponding brightfield images to identify DRG neurons based on their morphological appearance in culture. Scale bars = 10 µm. PLA, proximity ligation assay; Esyt1, extended synaptotagmin 1; IP_3R1, inositol triphosphate receptor type 1; DRG, dorsal root ganglion; PFA, paraformaldehyde; BK, bradykinin.

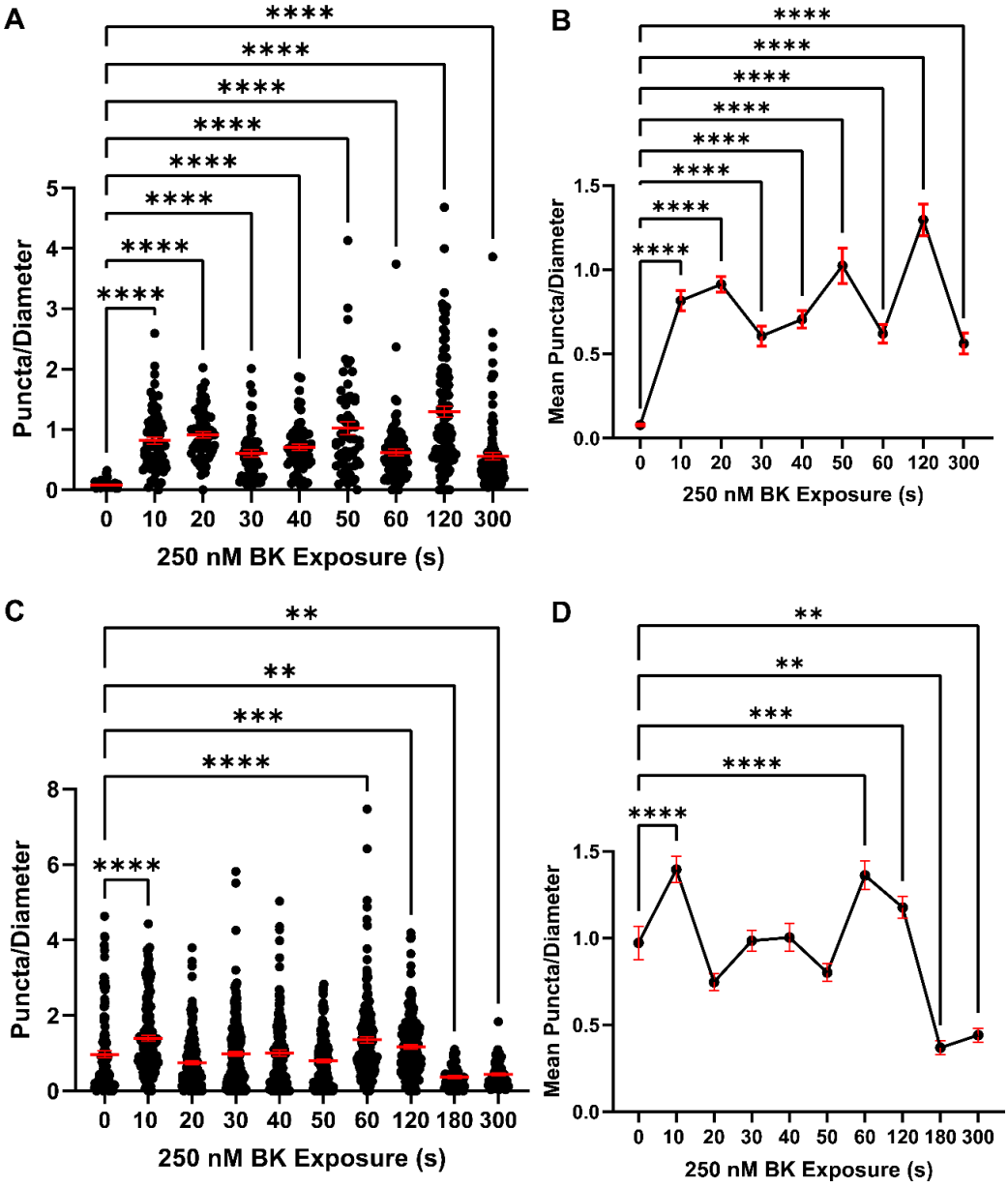

Figure 4.7 Time-resolved PLA reveals activity-dependent modulation of nanodomain proximity between Esyt1 with ANO1 and IP_3R1 in small-diameter DRG neurons. Primary DRG neuron cultures were treated with 250 nM BK for progressively increasing durations of time (10, 20, 30, 40, 50, 60, 120, 180 and 300 seconds) prior to immediate fixation with 4% PFA without washout. PLA signal between anti-Esyt1 and anti-ANO1 **(A, B)** and anti-Esyt1 and anti-IP_3R1 **(C, D)** primary antibodies was quantified as the number of fluorescent puncta per neuron normalised to the neuron's somatic diameter to control for the heterogeneous size distribution of DRG neurons. Stimulation with BK significantly increased the mean PLA signal between Esyt1 and ANO1 compared to the control (rest) neurons at all time points ($p < 0.0001$, Kruskall-Wallis with Dunn's multiple comparisons test) **(A).** Plotting the mean number of puncta per unit diameter against the duration of BK stimulation **(B)** revealed a time course with three distinct peaks at 10-20 seconds, 50 seconds and 120 seconds, which may represent a multi-faceted functional role for Esyt1-ANO1 coupling in the DRG. **C** and **D)** The mean PLA signal between Esyt1 and IP_3R1 was significantly increased compared to the control in DRG neurons stimulated with BK for 10 seconds ($p < 0.0001$), 60 seconds ($p < 0.0001$) and 120 seconds ($p < 0.001$). However, it was significantly reduced compared to control neurons in neurons stimulated with BK for 180 ($p < 0.01$) and 300 seconds ($p < 0.01$) (Kruskall-Wallis with Dunn's multiple comparisons test). Error bars represent mean ± SEM. ** $p < 0.01$, *** $p < 0.001$, *** $p < 0.0001$. PLA, proximity ligation assay; Esyt1, extended synaptotagmin 1; ANO1, anoctamin 1; IP_3R1, inositol triphosphate receptor type 1; DRG, dorsal root ganglion; BK, bradykinin; PFA, paraformaldehyde.

4.2.4 Multiple Noxious Stimuli Induce Nanodomain Proximity Between Esyt1 and ANO1

PLA data presented in Chapter 3 revealed that ANO1 nanodomain proximity between both IP_3R1 and TRPV1 is dynamically modulated by multiple noxious stimuli, the inflammatory mediator BK and the TRPV1 agonist CAP. Having previously shown BK-induced nanodomain proximity between Esyt1 with ANO1 and IP_3R1, it was pertinent to assess whether stimulation of DRG neurons with CAP could also elicit a dynamic response with respect to the PLA signal.

Primary DRG cultures (N = 3, all conditions) were treated with either 250 nM BK or 1 μM CAP for five minutes and PLA performed against anti-Esyt1 and anti-ANO1 (Figure 4.8 A-C) or anti-IP_3R1 primary antibody pairs (Figure 4.9A-C). As before, stimulation with 250 nM BK significantly increased the mean PLA signal (measured as the number of puncta per neuron normalised to somatic diameter) between Esyt1 and ANO1 compared to control neurons ($p < 0.0001$, Kruskal-Wallis with Dunn's multiple comparisons test). Stimulation with 1 μM CAP also significantly increased the mean normalised number of puncta to 0.382 ± 0.337, representing a nearly 5-fold increase over the control ($p < 0.0001$, Kruskal-Wallis with Dunn's multiple comparisons test). Interestingly, however, the efficacy of CAP to induce nanodomain proximity between Esyt1 and ANO1 appeared to be less than that of BK, as the mean PLA signal between Esyt1 and ANO1 following CAP stimulation was significantly smaller than that for BK ($p = 0.0231$, Kruskal-Wallis with Dunn's multiple comparisons test) (Figure 4.8D). The mean number of puncta per neuron was plotted against somatic diameter for PLA-positive DRG neurons stimulated with BK (Figure 4.8E) and CAP (Figure 4.8F). Linear regression analysis revealed no significant correlation between neuronal size and number of puncta for either BK- (slope = 0.0126 ± 0.00924, $R^2 = 0.0192$, $p = 0.175$) or CAP-treated (slope = 0.00357 ± 0.00540, $R^2 = 0.00314$, $p = 0.509$) neurons. There was no significant difference between the mean diameter of PLA-positive neurons in the BK condition (21.8 ± 0.684 μM) compared to that for PLA-positive neurons in the CAP condition (20.4 ± 0.528 μM) ($p = 0.178$, Mann-Whitney test).

Contrastingly, although stimulation with 250 nM BK for five minutes significantly reduced the mean PLA signal between Esyt1 and IP_3R1 compared control DRG neurons ($p = 0.0008$, Kruskall-Wallis with Dunn's multiple comparisons test), stimulation with 1 μM CAP had no significant effect on the mean number of puncta per neuron ($p = 0.943$, Kruskall-Wallis with Dunn's multiple comparisons test) suggesting noxious stimulation with CAP did not positively or negatively influence nanodomain proximity between Esyt1 and IP_3R1 (Figure 4.9D). As before, the normalised PLA signal was plotted against somatic diameter for PLA-positive DRG neurons treated with BK (Figure 4.9E) and CAP

(Figure 4.9F) to investigate a correlation between Esyt1-IP_3R1 nanodomain proximity and neuron size, however, no significant negative or positive correlation was observed for either noxious treatment (BK: slope = -0.0144 ± 0.00780, R^2 = 0.0445, p = 0.0693; CAP: slope = 0.0141, R^2 = 0.00831, p = 0.533). Together, these PLA data support a functional role for Esyt1 involvement in BK-evoked, but perhaps not CAP-evoked dynamic ANO1-IP_3R1 JMSC interactions in small-diameter nociceptive neurons of the DRG. This raises interesting questions concerning whether CAP is capable of eliciting dynamic modulation of ANO1-IP_3R1 proximity in sensory neurons, which will be further explored in Chapter 5. However, further investigation concerning noxious-stimulation evoked proximity of Esyt1 with ANO1 and IP_3R1 focused only on the response of neurons to BK.

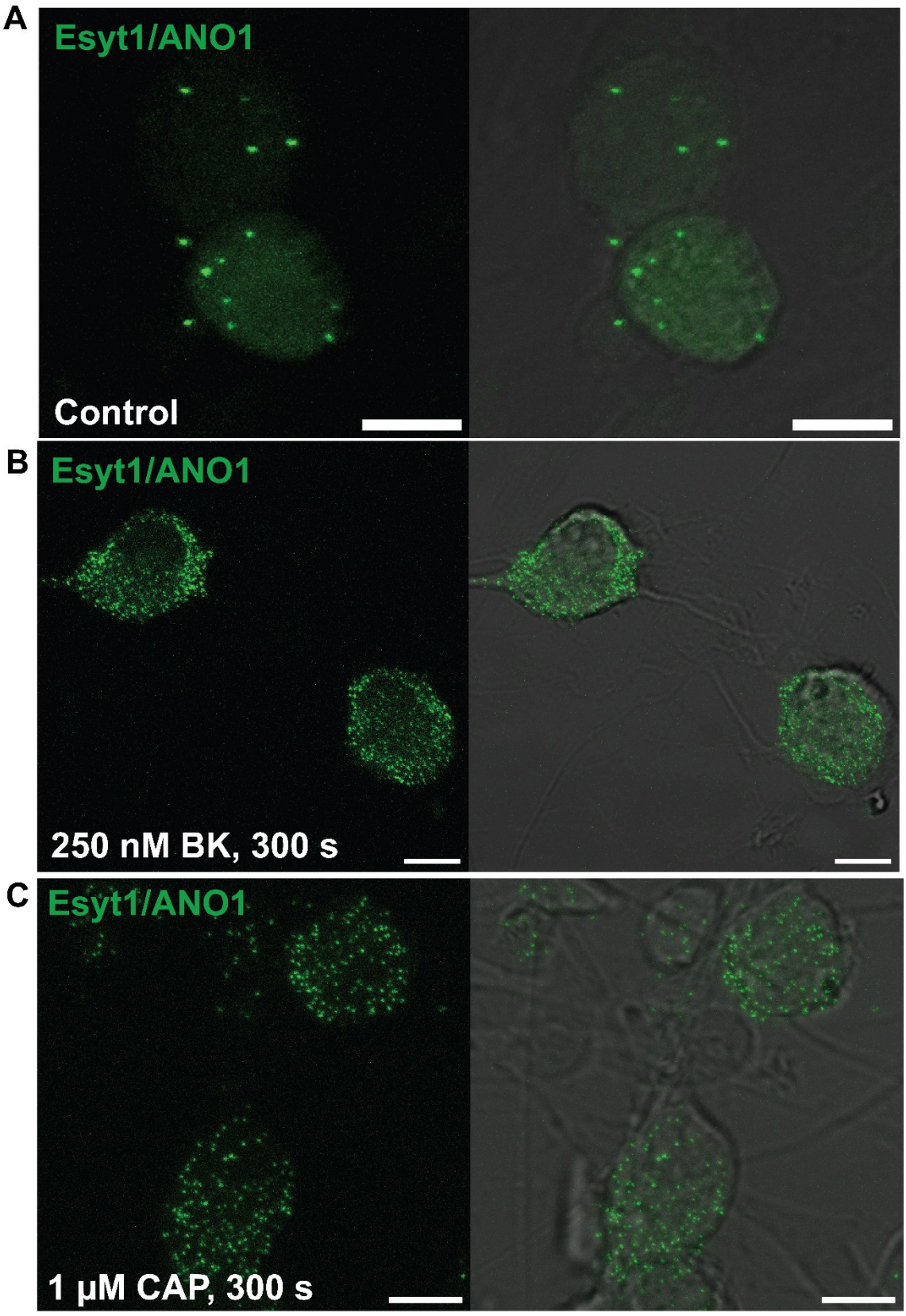

Figure 4.8: Nanodomain proximity between Esyt1 and ANO1 is dynamically modulated by multiple noxious stimuli. Continued on next page.

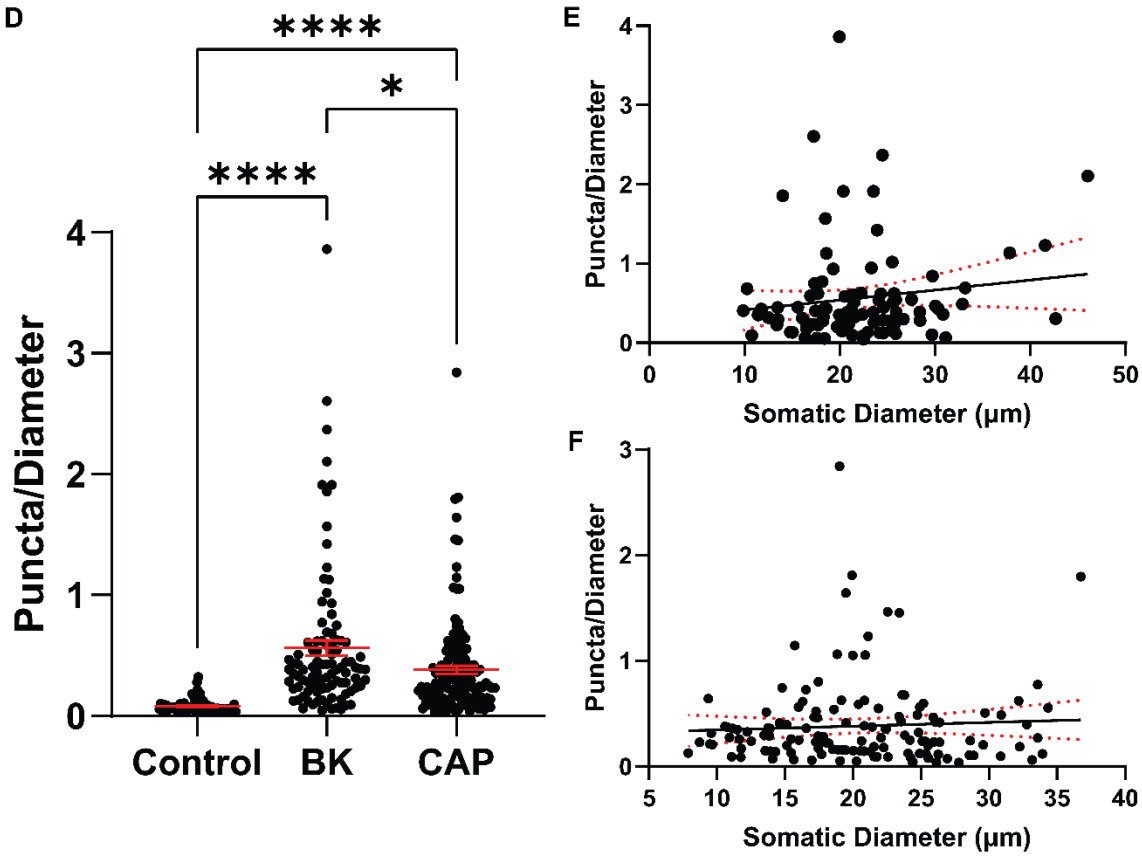

Figure 4.8: Nanodomain proximity between Esyt1 and ANO1 is dynamically modulated by multiple noxious stimuli. Representative maximum intensity projections of confocal z stacks depicting robust punctate PLA signal between anti-Esyt1 and anti-ANO1 primary antibodies in primary cultured DRG neurons fixed at rest **(A)** and following stimulation with either 250 nM BK **(B)** or 1 µM CAP **(C)** for five minutes. **D)** PLA signal was quantified as number of puncta per neuron normalised to the somatic diameter. The mean PLA signal between Esyt1 and ANO1 in DRG neurons stimulated with 1 µM CAP was significantly greater than that observed in control neurons ($p < 0.0001$). However, the mean PLA signal in DRG neurons stimulated with 250 nM BK was significantly greater than both the control ($p < 0.0001$) and CAP-stimulated neurons ($p = 0.231$, Kruskall-Willis with Dunn's multiple comparisons test), indicating BK-evoked nociception has greater efficacy in recruiting Esyt1-ANO1 nanodomains than CAP-induced signalling. PLA signal was plotted against somatic diameter for neurons displaying PLA between Esyt1 and ANO1 following treatment with BK **(E)** or CAP **(F)**, although linear regression analysis of these scatter plots did not reveal a significant correlation between the number of puncta per neuron and the neuronal diameter, suggesting the degree of activity-dependent Esyt1-ANO1 nanodomain proximity did not differ as a result of neuron size. Error bars represent mean ± SD **(D)** or the 95% confidence intervals of the linear regression best-fit **(E** and **F)**. Scale bars = 10 µm. Esyt1, extended synaptotagmin 1; ANO1, anoctamin 1; PLA, proximity ligation assay; DRG, dorsal root ganglion; BK, bradykinin; CAP, capsaicin.

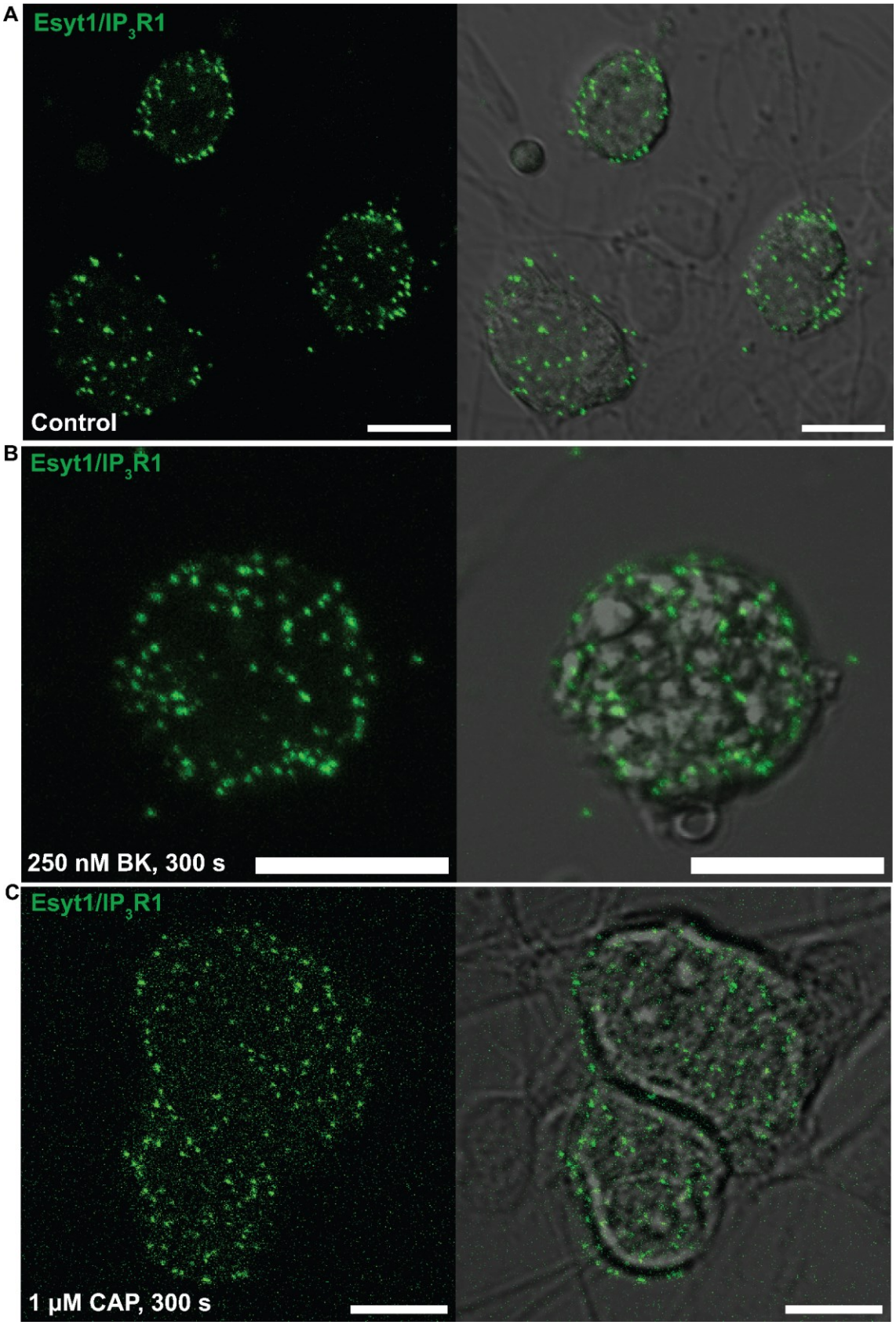

Figure 4.9: Nanodomain proximity between Esyt1 and IP_3R1 is sensitive to BK-evoked but not CAP-evoked nociception in small-diameter DRG neurons. Continued on next page.

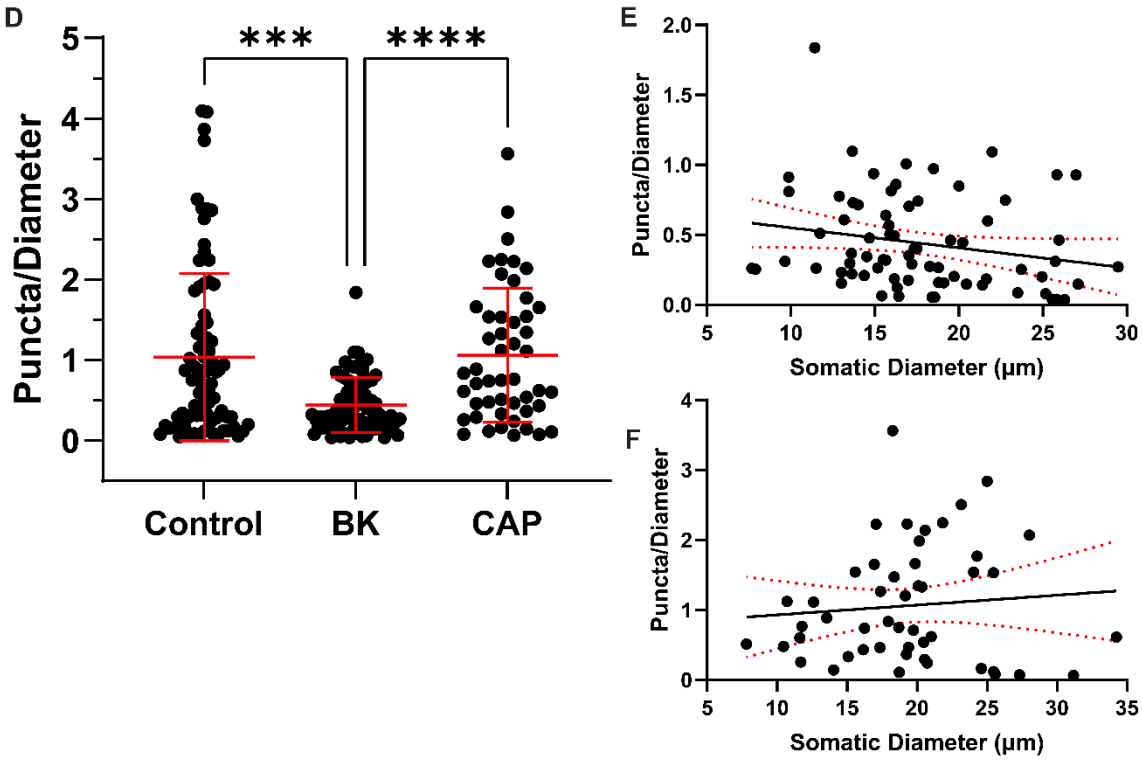

Figure 4.9: Nanodomain proximity between Esyt1 and IP_3R1 is sensitive to BK-evoked but not CAP-evoked nociception in small-diameter DRG neurons. A) Representative maximum intensity projections of confocal z stacks depicting robust punctate PLA signal between anti-Esyt1 and anti-IP_3R1 primary antibodies in primary cultured DRG neurons fixed at rest **(A)** and following stimulation with either 250 nM BK **(B)** or 1 µM CAP **(C)** for five minutes. **D)** PLA signal was quantified as number of puncta per neuron normalised to the somatic diameter. The mean PLA signal between Esyt1 and IP_3R1 in DRG neurons stimulated with 250 nM BK was significantly less than that observed in control neurons ($p < 0.001$). However, the mean PLA signal was not significantly different from control neurons in neurons treated with 1 µM CAP, further supporting a hypothesis that Esyt1 association with ANO1-IP_3R1 nanodomains is dynamically regulated by BK- but not CAP-evoked nociceptive signalling pathways. PLA signal was plotted against somatic diameter for neurons displaying PLA between Esyt1 and IP_3R1 following treatment with BK **(E)** or CAP **(F)**. However, linear regression analysis of these scatter plots did not reveal a significant correlation between the number of puncta per neuron and the neuronal diameter. Error bars represent mean ± SD **(D)** or the 95% confidence intervals of the linear regression best fit **(E** and **F)**. Scale bars = 10 µm. Esyt1, extended synaptotagmin 1; ANO1, anoctamin 1; IP_3R1, inositol triphosphate receptor type 1; PLA, proximity ligation assay; DRG, dorsal root ganglion; BK, bradykinin; CAP, capsaicin.

4.2.3 STED Confirms Activity-Dependent Proximity Between ANO1 and Esyt1

In Chapter 3, quantitative super-resolution STED microscopy was shown to be a valuable approach to investigating nanodomain proximity between ANO1 and TRPV1; therefore, to complement PLA data presented previously, STED microscopy was also used to further quantify proximity between Esyt1 with ANO1 and IP_3R1 in primary cultured DRG neurons at rest and fixed in an 'active' state following stimulation with BK.

To increase likelihood of imaging a population of small-diameter, putative nociceptors, DRG cultures were additionally immunostained against the small-diameter sensory neuron marker peripherin and only those neurons triple immunoreactive for peripherin, Esyt1 and either ANO1 or IP_3R1 were imaged with STED. Deconvolution of STED microscopy of fixed primary cultured DRG neurons co-immunostained against Esyt1 with ANO1 (Figure 4.10A) or IP_3R1 (Figure 4.10C) revealed punctate patterns of expression for all three proteins throughout the soma which could be localised in order to quantify the NND between puncta pairs. Distinct regions of close association between Esyt1-like and ANO1-like (Figure 4.10E) and between Esyt1-like and IP_3R1-like (Figure 4.10F) immunoreactivity were apparent, localised to the PM of small-diameter neurons at rest. Notably, stimulation of DRG neurons with 250 nM BK produced an evident translocation of Esyt1-positive puncta towards the PM in small-diameter neurons (Figure 4.10B and D) and regions of colocalisation between Esyt1 and ANO1 (Figure 4.10E) and Esyt1 and IP_3R1 (Figure 4.10F) persisted at the PM, putatively localised to ER-PM contact sites. Interestingly, DRG neurons stimulated with BK additionally demonstrated a greater concentration of IP_3R1 localised to an intracellular compartment, presumably the ER (Figure 4.10D). Whether this observation reflects a BK-induced translocation of IP_3R1 present at cortical ER regions towards non-cortical ER or an upregulation of IP_3R1 throughout the ER in response to noxious challenge is unknown.

To investigate activity-dependent modulation of proposed functional coupling between Esyt1 with ANO1-IP_3R1 JMSCs, frequency distribution histograms were plotted for the pooled datasets of all NNDs calculated for each staining condition in control neurons (top panels) and those treated with 250 nM BK (bottom panels) (Figure 4.11A-D). To ensure analysis of the relevant ER-PM junction-localised population of ANO1, IP_3R1 and Esyt1, thresholded punctate immunofluorescence was delimited to a 500 nm-deep ring-shaped ROI extending perpendicular from the outer perimeter of the neuron (see Chapter 2 for details). All histograms were well fit with a single-Gaussian distribution to allow for comparisons between the distribution peak and width (mean ± 1 S.D. value) as measures of the mean NND and variability within the datasets. These values are summarised in Table 4.1. Overall, the frequency distributions for each category of NND were largely similar between the control and BK-treated neurons, although interestingly, noxious

stimulation with BK tended to slightly reduce the mean nearest Esyt1 neighbour distance to both ANO1 and IP_3R1, while the mean nearest ANO1 or IP_3R1 neighbour distance to Esyt1 was somewhat increased in each case, particularly concerning the mean Esyt1 – ANO1 NND. This may reflect multiple functional populations of Esyt1 that could interact at ER-PM JMSCs distinct from those that are formed between ANO1 and IP_3R1, such as the SOCE CRAC channel complex between STIM1 and Orai1. Interestingly, in HEK293 and A2058 cell lines, Esyt1 has been proposed to functionally re-organise STIM1-mediated ER-PM junctions in response to intracellular Ca^{2+} store depletion, facilitating SOCE (Kang et al., 2019a), although IP_3R1, and therefore potentially ANO1, may also localise to ER-PM contact sites mediated by STIM1-Orai1 JMSCs (Sampieri et al., 2018). In general, NND analysis of STED microscopy identified the majority of ANO1 and IP_3R1 molecules have a nearest Esyt1 neighbour within approximately 170 nm regardless of the activation state of the neuron. However, it is important to note that for these experiments, DRG cultures were stimulated with BK for 5 minutes prior to fixation so are unlikely to have captured putative protein-protein interactions in their closest proximities.

Table 4.1: Gaussian fit of frequency distribution histograms describes the pooled NND datasets for DRG neurons immunostained against Esyt1, ANO1 and IP_3R1 and imaged using STED microscopy

	Mean ± SD		Width (nm)	
	Control	**BK (250 nM)**	**Control**	**BK (250 nM)**
ANO1 – Esyt1	98.8 ± 62.4	95.0 ± 71.6	36.4 – 161 (125)	23.4 – 167 (144)
Esyt1 – ANO1	105 ± 70.1	117 ± 81.5	34.6 – 175 (140)	35.2 – 198 (163)
IP_3R1 – Esyt1	96.5 ± 70.4	95.4 ± 65.5	26.1 – 167 (141)	29.9 – 161 (131)
Esyt1 – IP_3R1	92.5 ± 64.3	94.1 ± 67.0	28.2 – 157 (129)	27.0 – 161 (134)

Functional coupling between proteins at ER-PM contact sites can be assumed by their consistent colocalisation within nanodomain proximities, and such close associations were observed between Esyt1 with ANO1 and IP_3R1 with STED microscopy. Therefore, to quantify the colocalisation of these proteins in a manner that could be meaningfully compared to the outcome of previous PLA experiments, the proportion of nearest ANO1 and IP_3R1 neighbours identified within 40 nm of an Esyt1 immunoreactive localisation (and vice versa) was compared between control neurons and those stimulated with BK. In peripherin-positive DRG neurons at rest, the mean percentage of the immunoreactive ANO1 protein population with a nearest Esyt1-immunoreactive neighbour within 40 nm

was 10.6 ± 1.31 % and, in concurrence with the prior PLA data, BK treatment significantly increased this proportion to 14.9 ± 1.56 %, supporting a nociception-induced gain of proximity between ANO1 and Esyt1 ($p = 0.0479$, unpaired, two-tailed t-test) (Figure 4.12A). Interestingly, however, the converse was not observed. There was no significant difference in the percentage of the total Esyt1-immunoreactive population with a nearest ANO1 neighbour within 40 nm between the control and BK-treated neurons ($p = 0.184$, unpaired, two-tailed t-test) (Figure 4.12B). This may further support the hypothesis of multiple distinct Esyt1 populations as ANO1 and Esyt1 do not appear to be exclusive interacting partners, but for those Esyt1 molecules that *are* in close association with ANO1, stimulation with BK promotes greater nanodomain proximity.

Although a considerable percentage of the IP_3R1-immunoreactive population did share 40-nm proximity with a nearest Esyt1-neighbour distance in DRG neurons at rest (11.1 ± 1.37 %), this proportion did not significantly change as a result of BK stimulation (12.3 ± 0.785 %) ($p = 0.399$, unpaired, two-tailed t-test) (Figure 4.12C). Similarly, the percentage of the Esyt1-immunoreactive protein population with a nearest IP_3R1 neighbour within 40 nm was not significantly altered following treatment with BK (control: 11.5 ± 0.810 %, BK: 10.0 ± 0.920 %) ($p = 0.312$, unpaired two-tailed t-test) (Figure 4.12D). Therefore, while quantitative analysis of these STED data was inconclusive concerning whether nanodomain proximity between IP_3R1 and Esyt1 is subject to nociception-dependent modulation, it remains relevant that a non-zero proportion of the immunoreactive population is co-localised within sufficient proximity to facilitate functional interaction within the same nanodomain signalling complex. Together, this STED data indeed demonstrates close apposition of Esyt1 with ANO1 and IP_3R1 in the vicinity of the PM, where ER-PM contact sites will be located.

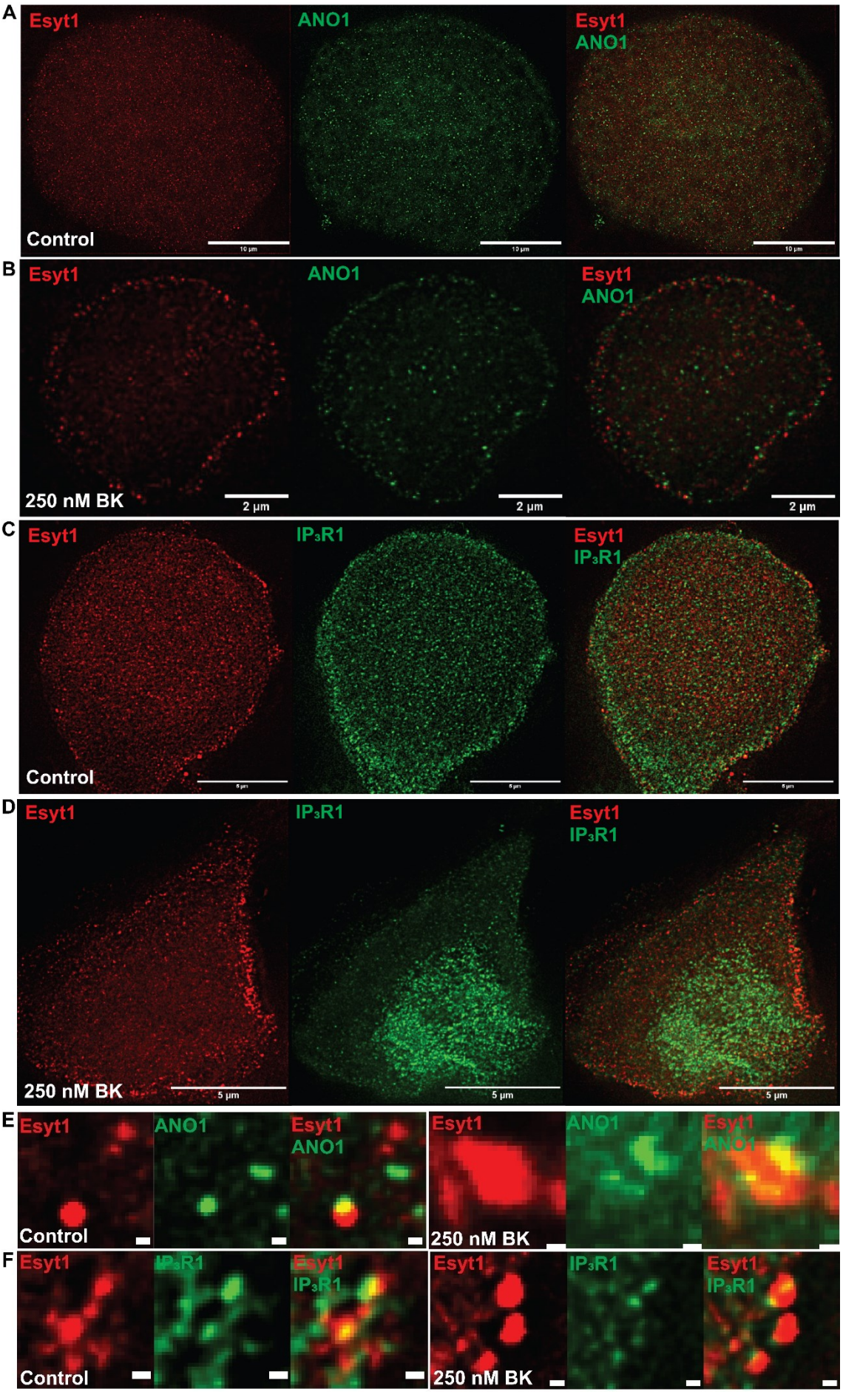
A
Esyt1
ANO1
Esyt1
ANO1
Control
10 µm
B
Esyt1
ANO1
Esyt1
ANO1
250 nM BK
2 µm
C
Esyt1
IP3R1
Esyt1
IP3R1
Control
D
Esyt1
IP3R1
Esyt1
IP3R1
250 nM BK
5 µm
E
Esyt1
ANO1
Esyt1
ANO1
Control
250 nM BK
F
Esyt1
IP3R1
Esyt1
IP3R1
Control
250 nM BK

Figure 4.10: Super-resolution STED microscopy reveals nanodomain colocalisation between Esyt1 with ANO1 and IP_3R1 in small-diameter peripherin-immunoreactive DRG neurons. Small-diameter DRG neurons (identified by positive peripherin immunoreactivity – not shown) were maintained in vitro for three days, PFA fixed and co-immunostained with primary antibodies against Esyt1 with either ANO1 **(A and B)** or IP_3R1 **(C and D)** and secondary antibodies conjugated to STAR RED and STAR ORANGE STED-capable fluorophores. Prior to fixation neurons were incubated in either standard growth media (control) **(A and C)** or growth media containing 250 nM BK **(B and D)** in investigate the effect of noxious stimulation on the relative localisations of Esyt1, ANO1 and IP_3R1-positive immunoreactivity adjacent to the plasma membrane. Deconvolution of STED microscopy z stacks revealed punctate staining patterns for the three target proteins in both control and BK-treated DRG neurons and BK treatment induced an apparent translocation of Esyt1-immunoreactivity towards the outer plasma membrane. **A-D** depicts representative deconvolved single STED z stack section for each experimental condition. **E)** Examples of close association between Esyt1 and ANO1 immunoreactivity at the outer membrane in small-diameter DRG neurons from the control (left) and BK-treated (right) sampled population. Similarly, **F)** depicts examples of close association between Esyt1 and IP_3R1 immunoreactivity in control (left) and BK-treated (right) DRG neurons. Scale bars labelled in figure panels. Esyt1, extended synaptotagmin 1; ANO1, anoctamin 1; IP_3R1, inositol triphosphate receptor type 1; DRG, dorsal root ganglion; STED, stimulated emission depletion; PFA, paraformaldehyde; BK, bradykinin.

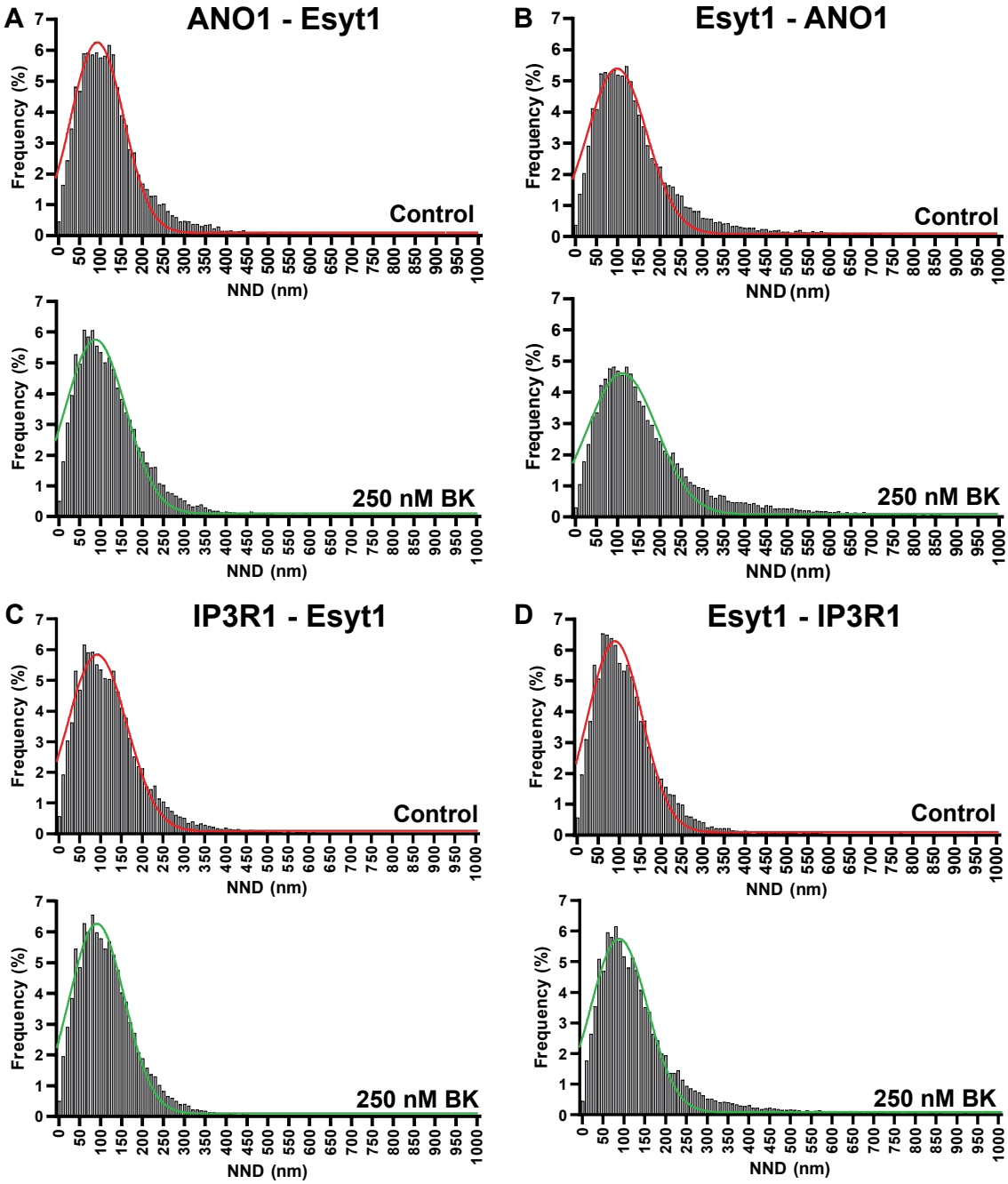

Figure 4.11: Frequency distribution histograms for nearest neighbour distances between Esyt1 with ANO1 and IP_3R1 in DRG neurons. Small-diameter, peripherin-positive DRG neurons were immunostained against Esyt1 with either ANO1 or IP_3R1 and punctate immunoreactivity was localised using STED microscopy and subsequent deconvolution in order to quantify proximity between nearest neighbour pairs. All nearest neighbour distances were pooled from the total sampled DRG neuron populations (N = 5, all conditions) and frequency distribution histograms were fit with a single-Gaussian distribution curve to allow for comparisons of the peak (mean) and peak width (± 1 S.D. value) for each experimental condition. Figure depicts the distribution of the nearest ANO1 to Esyt1 **(A)**, Esyt1 to ANO1 **(B)**, IP_3R1 to Esyt1 **(C)** and Esyt1 to IP_3R1 **(D)** NNDs in control (top panel) and BK-treated (bottom panel) DRG neuron populations. Note that the full datasets here have been clipped to 1000 nm for clarity of presentation. Esyt1, extended synaptotagmin 1; ANO1, anoctamin 1; IP_3R1, inositol triphosphate receptor type 1; DRG, dorsal root ganglion; NND, nearest neighbour distance; STED, stimulated emission depletion; BK, bradykinin.

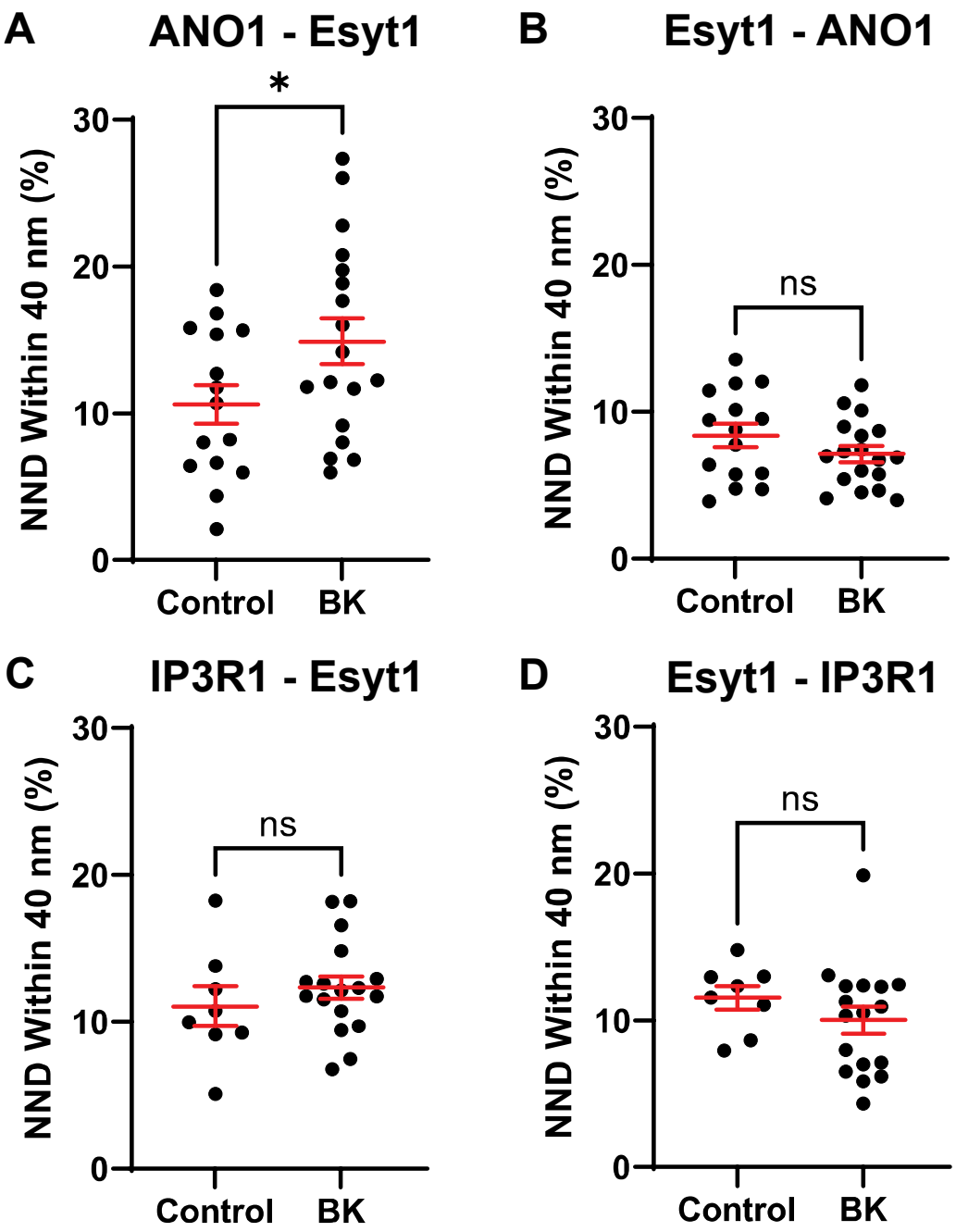

Figure 4.12: Bradykinin-induced gain of nanodomain proximity between Esyt1 and ANO1 indicative of functional coupling. The mean percentage of ANO1 to Esyt1 (A), Esyt1 to ANO1 (B), IP_3R1 to Esyt1 (C) and Esyt1 to IP_3R1 (D) nearest neighbour distances within 40 nm nanodomain proximity was compared between the control DRG neuron population and those that were treated with the inflammatory mediator BK (250 nM) for five minutes prior to fixation, immunostaining and STED imaging. Stimulation with BK significantly increased the mean proportion of ANO1 to Esyt1 NNDs within 40 nm ($p = 0.0479$, unpaired two-tailed t-test). Error bars represent mean ± SEM. *$p < 0.05$. Esyt1, extended synaptotagmin 1; ANO1, anoctamin 1; IP_3R1, inositol triphosphate receptor type 1; DRG, dorsal root ganglion; NND, nearest neighbour distance; STED, stimulated emission depletion; BK, bradykinin.

4.3 Discussion

The previous chapter of this thesis presented novel evidence that nanodomain signalling complexes between ANO1 and IP_3R1 in small-diameter DRG nociceptors are not static interactions but instead are dynamically modulated in a manner consistent with translocation of the ER towards the PM. Similar expansion of ER-PM contact sites has been reported for other cell types (Wu et al., 2006, Poteser et al., 2016, Orci et al., 2009). The organisation and maintenance of nociceptive ER-PM junctions is an intriguing question for sensory neuroscience and elucidating the molecular mechanisms by which ANO1-IP_3R1 nanodomain proximity is dynamically regulated may uncover novel therapeutic targets for the disruption of JMSCs which may attenuate nociception in cases of chronic pain, for example. Esyt1 was proposed as a putative ER-PM scaffolding protein governing ANO1-IP_3R1 JMSCs in the DRG due to its inherent Ca^{2+} sensitivity, presenting a mechanism by which nociceptive Ca^{2+} signals may induce ER-PM junction formation, and for its known interactions with ANO1 in other cell types, confirming the possibility for functional coupling between Esyt1 and ANO1. Together the data presented in this chapter support a functional interaction between Esyt1 and ANO1, and further suggests a complex, activity-dependent rearrangement of proteins localised to ER-PM junctions in small-diameter DRG neurons.

4.3.1 Super-resolution Imaging Confirms Nanodomain Proximity Between Esyt1 with ANO1 and IP_3R1

A combination of antibody-based, super-resolution imaging approaches were used to characterise Esyt1 expression in nociceptive neurons of the DRG and quantify its proximity to ANO1 and IP_3R1. Indeed, both PLA and STED microscopy demonstrated co-localisation of a fraction of Esyt1 molecules within 40 nm of both ANO1 and IP_3R1, supporting the likelihood of their functional interaction. As triple immunostaining was not performed, it cannot be said with certainty that nanodomain proximities between ANO1 and Esyt1 will also be within nanodomain proximity of IP_3R1. However, previous cluster analysis of STORM imaging for ANO1 and IP_3R1 immunoreactivity in primary cultured DRG neurons found only a small percentage of ANO1-positive clusters were independent of an IP_3R1-positive cluster (Shah, 2017, Shah et al., 2020). Therefore, dynamic regulation of ANO1-Esyt1 nanodomains, as confirmed by both PLA and NND analysis of STED data, likely reflects a functional role for Esyt1 modulation of ANO1-IP_3R1 JMSCs. Interestingly, the same could not be said for IP_3R1 clusters as a much larger percentage were identified not in close association with ANO1 (Shah, 2017, Shah et al., 2020). Therefore, it is possible separate Esyt1-IP_3R1 nanodomains exist independent of ANO1, and NND analysis further suggested ANO1 and Esyt1 are unlikely to be exclusive binding partners. For those Esyt1 molecules that are closely associated

with ANO1, stimulation with BK promotes greater nanodomain proximity. There are multiple viable explanations for this: it may be that either ANO1 or Esyt1 (or both) are undergoing a translocation towards ER-PM contact sites and forming de novo JMSC interactions, or that established interacting pairs are tightening in their proximity, possibly due to activity-dependent movement of the ER towards the PM. Of course, that is also not to say that both mechanisms are not co-occurring in response to nociception.

4.3.2 Limitations Associated with Antibody-based Localisation Approaches

Why did quantitative analysis of STED microscopy not reveal the same activity-dependent re-arrangement for IP_3R1 and Esyt1 as was observed with PLA? It may be that PLA is more sensitive to nanodomain proximity between target proteins than NND analysis of immunofluorescent puncta. As an 'all-or-nothing' technique, PLA identifies true nanodomain proximities, that is, proteins are either within the 40 nm sensitivity range, and thus produce a PLA signal, or they are not. Meanwhile, the NND analysis of STED data is likely to miss the 'real' nearest neighbour due to the limitations of the antibodies' ability to bind its target proteins. At highly protein-dense membrane regions, including ER-PM contact sites, macromolecular crowding negatively influences the physical accessibility of soluble ligands, including primary and secondary antibodies, to their respective targets (Arnold et al., 2023). Therefore, the total immunofluorescent signal detected by STED by no means represents the total expression of the respective protein at the membrane. Thus, quantifying the percentage of NNDs within 40 nm is likely to be an under-representation of the true number of nanodomain signalling complexes functioning at ER-PM junctions *in vivo.* PLA on the other hand more reliably identifies protein pairs within 40 nm of one another and does so irrespective of either unlabelled nanodomain pairs or proteins expressed at a greater distance than 40 nm. Further, background noise is likely to impart a higher influence on STED data analysis than for PLA. Demonstrating a significant increase of this close association in response to a particular physiological stimulus with PLA, therefore, likely reflects a physiologically relevant interaction between ANO1 and Esyt1. Regardless, that high-resolution STED microscopy *did* identify regions of nanodomain-level colocalisation between Esyt1 with ANO1 and IP_3R1 both in neurons at rest and following BK stimulation is significant in itself and does support a hypothesised role for Esyt1 in mediating ANO1-IP_3R1 JMSC functionality in small-diameter nociception neurons of the DRG.

Alternatives to traditional primary-secondary antibody complex identification of target antigens exist including the use of fluorophore-conjugated primary antibodies or nanobodies (single-domain antigen-binding proteins that may be as small as 15 kDa) (de Beer and Giepmans, 2020), although with respect to STED the increased signal-to-noise ratio afforded by binding of multiple secondary antibodies to a single primary antibody is

a particular advantage. Therefore, alternative super-resolution techniques may be better suited to circumvent the problem of molecular crowding associated with studying protein-protein interactions in dense membrane regions such as at ER-PM junctions, albeit these are typically less readily available or user-friendly than the Abberior STEDycon setup utilised for the present study. For example, expansion microscopy (ExM) enables physical molecular decrowding through the embedding of biological specimens in a hydrogel that undergoes an up-to ten-fold isotropic expansion with preservation of antigens in situ (Chen et al., 2015, Truckenbrodt et al., 2018). Post-expansion immunostaining ensures greater accessibility of target epitopes to primary antibodies, coupling super-resolution imaging capabilities with enhanced antigen detection for protein-protein interactions previously inaccessible through traditional immunostaining protocols (Valdes et al., 2024).

4.3.3 Conclusions

The data presented herein further complements evidence discussed in Chapter 3 for the dynamic, activity-dependent modulation of ANO1 nanodomains in small-diameter DRG neurons. A combination of super-resolution microscopy and PLA were used to demonstrate for the first time the nanodomain proximity between ANO1, IP_3R1 and the putative ER-PM tethering protein Esyt1, supporting a hypothesised role for Esyt1 as a potential molecular mechanism mediating ANO1-IP_3R1 JMSC organisation and functionality in DRG neurons (Figure 4.13). Of particular relevance, Esyt1 co-localisation with both ANO1 and IP_3R1 was shown to be dynamically modulated by noxious stimulation, adding further complexity to the newfound phenomenon of dynamic ANO1 nanodomain interactions. While further experimental work is undoubtedly required to fully elucidate its functionality at nociceptive ER-PM contact sites, the evidence here establishes Esyt1 as an intriguing addition to the nociceptive signalling interactome in the DRG.

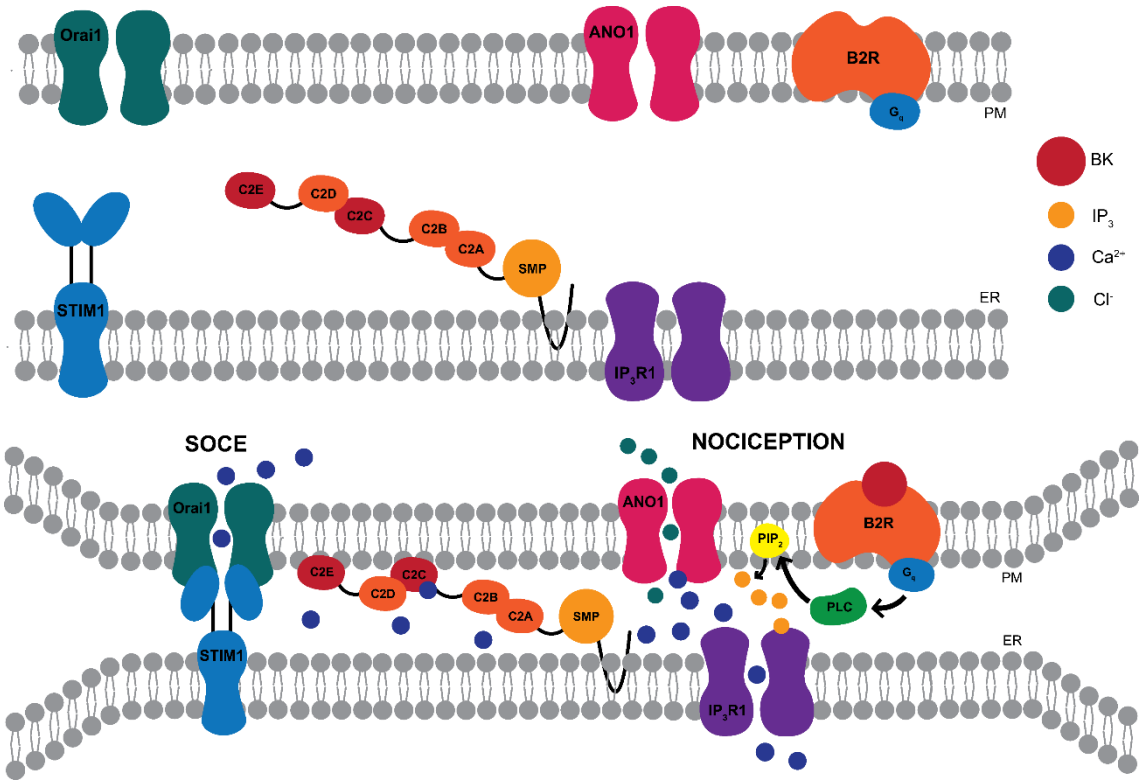

Figure 4.13: Schematic depicting the hypothesised mechanism of action for Esyt1-mediated ER-PM tethering in nociceptive DRG neurons.
The Esyt1 C2A and C2C domains function as a sensor for elevated cytosolic Ca^{2+} signals, including SOCE following store depletion, which subsequently promotes a conformational translocation of Esyt1 towards the PM, facilitating the formation of novel ER-PM contact sites to which STIM1 is recruited. Esyt1-mediated ER-PM tethering is independent from STIM1-Orai1 JMSCs involved in SOCE. Evidence from super-resolution STED microscopy and PLA confirms an activity-dependent gain of nanodomain proximity between Esyt1 and nociceptive ANO1-IP_3R1 functional JMSCs supporting a putative role for Esyt1 as a novel ER-PM tethering protein involved in inflammatory nociception in small-diameter DRG neurons.
SOCE, store-operated Ca^{2+} entry; STIM1, stromal interaction molecule 1; ANO1, anoctamin 1; IP_3R1, inositol triphosphate receptor type 1; SMP, synaptotagmin-like mitochondrial-lipid binding protein; B2R, bradykinin receptor type 2; PLC, phospholipase C; PIP2, phosphatidylinositol 4,5-bisphosphate; BK, bradykinin; PM, plasma membrane; ER, endoplasmic reticulum; IP_3, inositol triphosphate; Ca^{2+}, calcium cation; Cl^-, chloride anion; DRG, dorsal root ganglion.

Chapter 5: Expression and Function of ANO1 in Trigeminal Ganglion Neurons

5.1 Introduction

To date, previous investigations into the mechanisms of ANO1 activation in the PNS have been limited to primary DRG sensory neurons (Jin et al., 2013, Shah et al., 2020). However, as the cranial analogue to the DRG, such mechanisms describing ANO1-mediated nociceptive amplification are likely to be conserved in small-diameter nociceptive neurons of the TG, although this is yet to be experimentally confirmed.

5.1.1 Transcriptomic Evidence for ANO1 Expression in the Trigeminal Ganglion

Whereas the DRG is responsible for the primary sensory innervation of the body, the TG are paired structures which provide sensory innervation to the intra- and extracranial structures of the head and neck. Despite arising from distinct embryological origins, DRG and TG neurons display close-to-identical gene expression. Ribounucleic acid (RNA) sequencing (RNA-Seq) investigations have provided comprehensive transcriptomic data for somatosensory ganglia, allowing for the statistical comparison of differentially expressed genes between the TG and DRG across various species. Multiple independent transcriptomics analyses concur that in rodents, the DRG and TG demonstrate at least a 98% similarity in their gene expression profiles overall (Kogelman et al., 2017, Lopes et al., 2017a, Manteniotis et al., 2013) and that expression levels of ANO1 are broadly similar between the two tissue types (Figure 5.1A, B). Comparable expression levels of ANO1 mRNA transcripts between murine TG and DRG has also been confirmed using reverse transcription-polymerase chain reaction (RT-PCR) (Schöbel et al., 2012) (Figure 5.1C).

However, there is strong evidence to suggest transcriptional and translational efficiencies are not well correlated and abundant mRNA expression is not an accurate predictor of functional protein expression unless sequencing is performed on ribosome-bound mRNA (Fortelny et al., 2017, Ingolia, 2016). Furthermore, for RNA-Seq experiments performed on complete ganglia samples, distinctions between neuronal sub-populations or between neurons and supporting glial cells cannot be made. The TRAP technique of RNA-Seq enables pulldown of actively translating ribosomes bound to mRNA via tagging of ribosomal proteins within a genetically defined cellular population, providing a more accurate measure of active gene expression (Doyle et al., 2008, Heiman et al., 2008).

TRAP sequencing has been performed in matched TG and DRG samples obtained from a Nav1.8^{Cre} mouse line to investigate the mRNA expression profiles of specific

nociceptive neuron populations. Comprehensive transcriptomic analysis of these small-diameter neuron-enriched samples did not identify ANO1 as one of the 372 or 348 mRNAs significantly enriched in the TG or DRG, respectively (relative to the other tissue type), suggesting comparable expression levels between the two sensory ganglia (Megat et al., 2019b). On the other hand, despite the well-established role for ANO1 in nociception in the DRG (Jin et al., 2013, Shah et al., 2020, Takayama et al., 2015, Kim et al., 2024), single-cell RNA-Seq commonly does not identify ANO1 mRNA transcription in small-diameter C fibre neurons of the DRG (Usoskin et al., 2015, Bhuiyan et al., 2024). There are multiple biological processes beyond transcription alone that account for variability in protein expression including the rate of ribosomal translation, the rate of transcript and protein turnover, and post-transcription modulation (Liu et al., 2016, McManus et al., 2015). In particular, the molecular half-life for protein degradation may be up to 5-6-fold longer than that for corresponding mRNA, therefore, low transcription but high protein expression is plausible (Schwanhäusser et al., 2011). The extent to which protein expression can be accurately predicted based on mRNA transcript levels is highly contentious (Prabahar et al., 2024, Maier et al., 2009, Liu et al., 2016), but it is likely transcription levels are insufficient to predict protein expression and functionality.

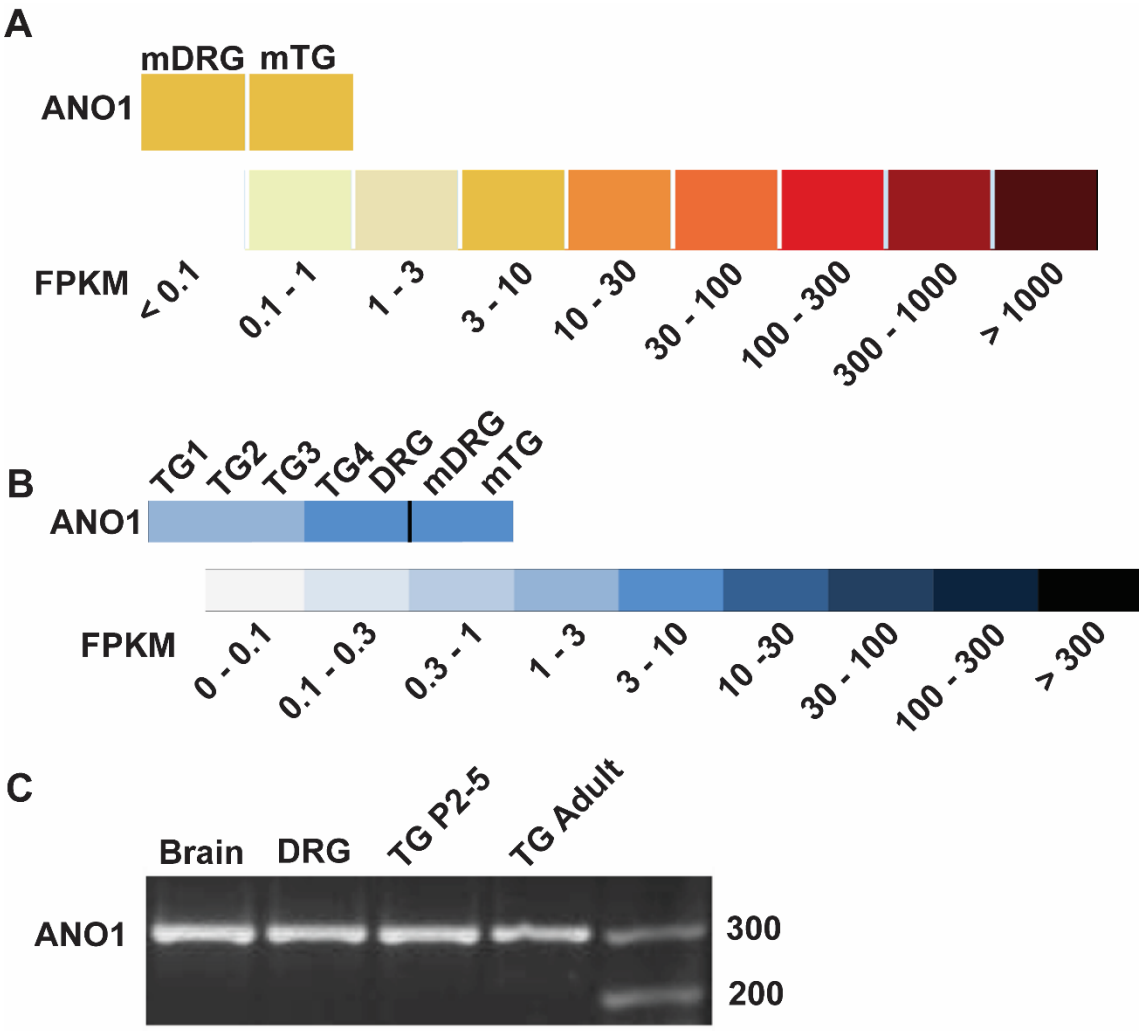

Figure 5.1: Transcription of ANO1 mRNA is comparable between the DRG and TG as measured by RNA-Seq and RT-PCR. Heat maps comparing expression levels of ANO1 mRNA transcripts in murine DRG and TG tissue samples (**A:** Adapted from (Schöbel et al., 2012) and human and murine DRG and TG tissue samples (**B:** Adapted from Flegel et al., 2015). In both mDRG and mTG tissue, ANO1 mRNA transcript levels are typically found to be expressed around 3 – 10 FPKM. **C)** RT-PCR for ANO1 mRNA transcript expression in murine brain, DRG, postnatal and adult TG tissue samples (Adapted from Schöbel et al., 2012). RNA-Seq, RNA sequencing; RT-PCR, real-time polymerase chain reaction; FPKM, fragments per kilobase of exon per million fragments mapped; DRG, dorsal root ganglion; TG, trigeminal ganglion; mDRG, murine DRG; mTG, murine TG.

5.1.2 Evidence for Calcium-Activated Chloride Channel Functionality in the Trigeminal Ganglion

Given the substantial evidence supporting a functional role for ANO1 as a nociceptive amplifier in small-diameter neurons of the DRG (Jin et al., 2013, Shah et al., 2020, Takayama et al., 2015), ANO1 is likely expressed analogously in the nociceptive population of TG sensory neurons. Indeed, evidence supports Ca^{2+}-activated Cl^- current functionality in the CAP-responsive (nociceptive) subpopulation of TG neurons. In wild-type TG neurons, the mean intracellular Cl^- concentration ($[Cl^-]_i$) has been measured to be 34.1 ± 6.9 mM, suggesting active accumulation of Cl^- inside neurons (Schöbel et al., 2012). Indeed, in wild-type TG neurons pretreated with the NKCC1 antagonist bumetanide (50 µM), and in TG neurons obtained from $NKCC1^{-/-}$ homozygous knockout mice, this mean $[Cl^-]_i$ was significantly reduced ($p < 0.001$) to 10.9 ± 1.2 mM and 13.2 ± 1.1 mM, respectively (Schöbel et al., 2012) indicating that, similar to what is observed in DRG sensory neurons, active accumulation of Cl^- inside TG neurons is mediated by NKCC1, which has been shown to be co-expressed in 44.7% of TRPV1-positive TG neurons (Price et al., 2006). Furthermore, this $[Cl^-]_i$ was shown to be sufficient to mediate a Cl^- efflux following the activation of anion-permeable ion channels as the calculated mean Cl^- reversal potential (ECl) (-37.6 mV) was more positive than the mean resting membrane potential (-53.9 ± 1.8 mV) (Schöbel et al., 2012).

TG neurons functionally express purinergic G_q-protein-coupled P2Y receptors (Ruan and Burnstock, 2003, Ceruti et al., 2008). Application of 100 µM ATP (which is sufficient to induce Ca^{2+} transients in approximately 90% of rodent TG neurons (Spehr et al., 2004)) caused a mean 74.2% decrease in $[Cl^-]_i$, indicative of Ca^{2+}-activated Cl^- efflux (Schöbel et al., 2012). Efflux of Cl^- from primary sensory neurons serves to depolarise the neuronal membrane potential, increasing the likelihood of action potential firing, particularly following the opening of L-type VGCCs, allowing further Ca^{2+} influx. Indeed, the mean amplitude of Ca^{2+} transients induced by the application of 3.3 µM CAP in the presence of reduced extracellular $[Cl^-]$ (to amplify the outward driving force for Cl^- efflux) was significantly increased by 35% (Schöbel et al., 2012). Conversely, co-application of CAP with the non-selective CaCC inhibitors 4,4′ Di-isothiocyanatostilbene-2,2′ -disulfonic acid (DIDS) (100 µM) or niflumic acid (NFA) (500 µM) significantly decreased the amplitude of Ca^{2+} transients by 73.7% and 51.3%, respectively, compared to the control (Schöbel et al., 2012). Collectively, this evidence supports a putative role for a CaCC-mediated Cl^--dependent amplification mechanism of membrane depolarisation following CAP exposure in TG neurons; however, Schobel et al. did not fully deduce the molecular mechanism underlying this amplification.

5.1.3 Immunohistochemical Evidence for ANO1 Protein Expression in the Trigeminal Ganglion

Classically, ANO1 activation occurs downstream of G_qPCR activation, such as activation of B_2R by the inflammatory mediator BK in nociceptive DRG neurons, which has not been confirmed in the TG (although CaCC have been recorded in TG sensory neurons, the molecular mediator of these currents has not been investigated (Schöbel et al., 2012, Bader et al., 1987). However, there *is* limited evidence to support functional ANO1-TRPV1 interaction in the TG as in the DRG (Shah et al., 2020, Takayama and Tominaga, 2024, Takayama et al., 2015). A high degree of ANO1 and TRPV1 protein co-expression has been observed in small-to-medium-diameter neurones present in the mandibular division (innervating the anterior two-thirds of the tongue) of the TG of wild-type naive Wistar rats; of the 13.7% of mandibular TG neurons immunopositive for ANO1, a majority 76.2% of that population was also immunopositive for TRPV1 (Kanazawa and Matsumoto, 2014). In mice, a much higher percentage of trigeminal mandibular division neurons (approximately 45%) was found to be immunopositive for ANO1 (Suzuki et al., 2016). In contrast, in the DRG, approximately 80% of TRPV1-positive neurons are also immunoreactive for ANO1 (Takayama et al., 2015).

Therefore, while expression of ANO1 in the TG and CaCC functionality is supported, the contribution of ANO1 to TG nociceptive signalling demands further elucidation, particularly concerning the potential contribution of ANO1 to trigeminal-specific signalling pathways, for example, the pathophysiological mechanisms of headache and migraine.

5.1.4 Trigeminal Nociceptive Signalling Mechanisms: The Role of CGRP

CGRP is a highly expressed neuropeptide intimately associated with mechanisms of nociception within the trigeminovascular system (Schou et al., 2017). Classical immunohistochemical studies have estimated that its expression occurs in up to 40% of TG neurons (Tajti et al., 1999). In the TG, there is a distinct differential expression of the CGRP peptide and its canonical receptor (Messlinger et al., 2020, Edvinsson et al., 2020). Activation of trigeminal afferent fibres causes the release of CGRP from dense core vesicles present at the axon terminal of small-diameter non-myelinated C-fibre neurons (Haanes and Edvinsson, 2019), while at thinly myelinated Aδ-fibre dendrites, CGRP binds heteromeric calcitonin receptor-like receptor/receptor activity modifying protein (CRLR/RAMP) receptor complexes, primarily consisting of CRLR with the RAMP1 isoform (Edvinsson et al., 2020). Activation of CRLR/RAMP1 receptors initiates downstream G_s-, G_i and G_q-linked signalling pathways to modulate downstream targets influencing neuronal excitability - sending nociceptive signals to the CNS - and inducing the release of vasodilatory factors such as nitric oxide (Haanes and Edvinsson, 2019).

This differential expression separates TG neurons into either CGRP-secreting or CGRP-responding subpopulations (Lennerz et al., 2008).

Extensive evidence supports CGRP in the development and maintenance of peripheral neuronal sensitisation and vasodilation, conditions considered important factors underlying the pathophysiology of migraine and headache (Schou et al., 2017, Haanes and Edvinsson, 2019, Hoffmann et al., 2019, Retsky et al., 2023). While the pathophysiological relevance of CGRP to trigeminal pain disorders is well studied, further molecular mechanisms modulating the CGRP signalling pathway remain uncovered.

5.1.4 Hypothesised Mechanisms for ANO1 Modulation of CGRP Signalling in the Trigeminal Ganglion

Given that CGRP's mechanisms of action increase TG neuronal excitability, it follows that further mechanisms either sensitising TG Aδ-fibres, or potentiating CGRP release from C-fibres could contribute to exacerbating CGRP-mediated head pain. In the TG, TRPV1 immunoreactivity has been detected in approximately 70% of CGRP-positive neurons, while ANO1 has been shown to co-express with TRPV1 in nearly 60% of TRPV1-positive neurons (Price and Flores, 2007, Kanazawa and Matsumoto, 2014). Intriguingly, both ANO1 and TRPV1 mRNA transcription has demonstrated upregulation in response to high-dose estradiol treatment in rats, which corresponded with significant potentiation of CAP-evoked nocifensive behaviour responses (Yamagata et al., 2016). This suggests putative ANO1-TRPV1 interactions in the TG may contribute to the modulation of CGRP release from C-fibres or otherwise be involved in peripheral sensitization associated with multiple trigeminal pain disorders. However, it would also be interesting to investigate a potential interaction between ANO1 and the protein components of the CGRP receptor, RAMP or CRLR, particularly considering RAMP1/CRLR heterodimers are known to couple to G_q protein signalling pathways in addition to G_s proteins (Weston et al., 2016).

5.1.5 Research Objectives and Hypotheses

In DRG sensory neurons, the CaCC ANO1 confers an amplification mechanism of nociceptive signalling via functional coupling to ER-resident IP_3R1 at JMSCs. Building on evidence for ANO1 expression and CaCC functionality in the trigeminal system, this thesis primarily hopes to characterise functional ANO1-containing JMSCs in nociceptive TG neurons and to evaluate the contribution of ANO1 modulation to CGRP signalling in the TG. Given the similarities between DRG and TG nociception, it was hypothesised that ANO1 confers an equivalent mechanism of nociceptive signalling via functional coupling to IP_3R1 at JMSCs in small-diameter nociceptive TG neurons and may

contribute an amplification of CGRP signalling via coupling to the canonical CGRP receptor complex, CRLR/RAMP1.

5.2 Results

5.2.1 ANO1 is Expressed in the Trigeminal Ganglion and Trigeminal Afferent Fibres

To verify RNA sequencing experiments and provide further evidence of translational protein expression for ANO1 in sensory TG neurons, immunohistochemistry was performed as previously described. Immunohistochemistry enables the detection and subcellular localisation of protein expression based on the high specificity and affinity of an antibody for a specific protein antigen.

Robust ANO1 immunoreactivity was detected primarily in the neuronal soma in both transverse sections obtained from PFA perfusion-fixed TGs from weaned rats (P21 days) (Figure 5.2Ai) and in primary TG neuronal cultures prepared from neonatal rats (P4-10 days) fixed with 4% PFA at 3 days in vitro (Figure 5.2Aii). The anti-ANO1 rabbit polyclonal antibody used for Immunohisto/cytochemistry throughout this thesis also performed well in trigeminal tissue perfusion-fixed with a 1:1 mixture of acetone and methanol; strong ANO1 immunoreactivity was apparent in neurons visible in acetone-methanol fixed TG sections (Figure 5.2Aiii). ANO1 immunoreactivity was also evident in transverse sections of PFA-fixed afferent fibres distal to the trigeminal V1-3 divisions where ANO1 expression appeared to co-localise with some C-fibre marker peripherin-positive nerve fibres (Figure 5.2B).

To further verify ANO1 immunoreactivity in the trigeminal system, whole TG and dura mater lysates obtained from primary rat tissue were separated according to protein molecular weight via gel electrophoresis, transferred to a nitrocellulose membrane (western blotting) and incubated with primary anti-ANO1 antibody (as described in Chapter 2, Section 2.6). Lysate obtained from fresh liver tissue was run as a positive control for ANO1 protein expression as ANO1 has been shown to be robustly expressed in both hepatocytes and biliary epithelial cells (BECs) (Uhlén et al., 2015, Dutta et al., 2011). In all cases, immunostaining against the ‘housekeeping’ gene glyceraldehyde 3-phosphate dehydrogenase (GAPDH) was included as an additional control for successful protein transfer and in each sample robust GAPDH immunoreactivity was observed in a single band at the expected size of 36 kDa (Barber et al., 2005) (Figure 5.2C). In the positive control ANO1 immunoreactivity was observed as a single band sized between 100 and 150 kDa, consistent with the expected molecular weight of the monomeric form of the ANO1 protein: 114 kDa (Yang et al., 2008). ANO1 immunoreactivity was present in Western blots of both TG and dural lysates, albeit displaying protein fragments of varying size. Two bands were present in the dural lysate samples: between 100 and 150 kDa, at the same molecular weight as observed in the liver samples, and between 75 and 100 kDa. Only one band was observed in the TG

lysate, 75 kDa in molecular weight (Figure 5.2C), marking an unexpected result that may be explained by alternative splicing of the ANO1 gene; this will be further explored in the following Discussion (Section 5.3).

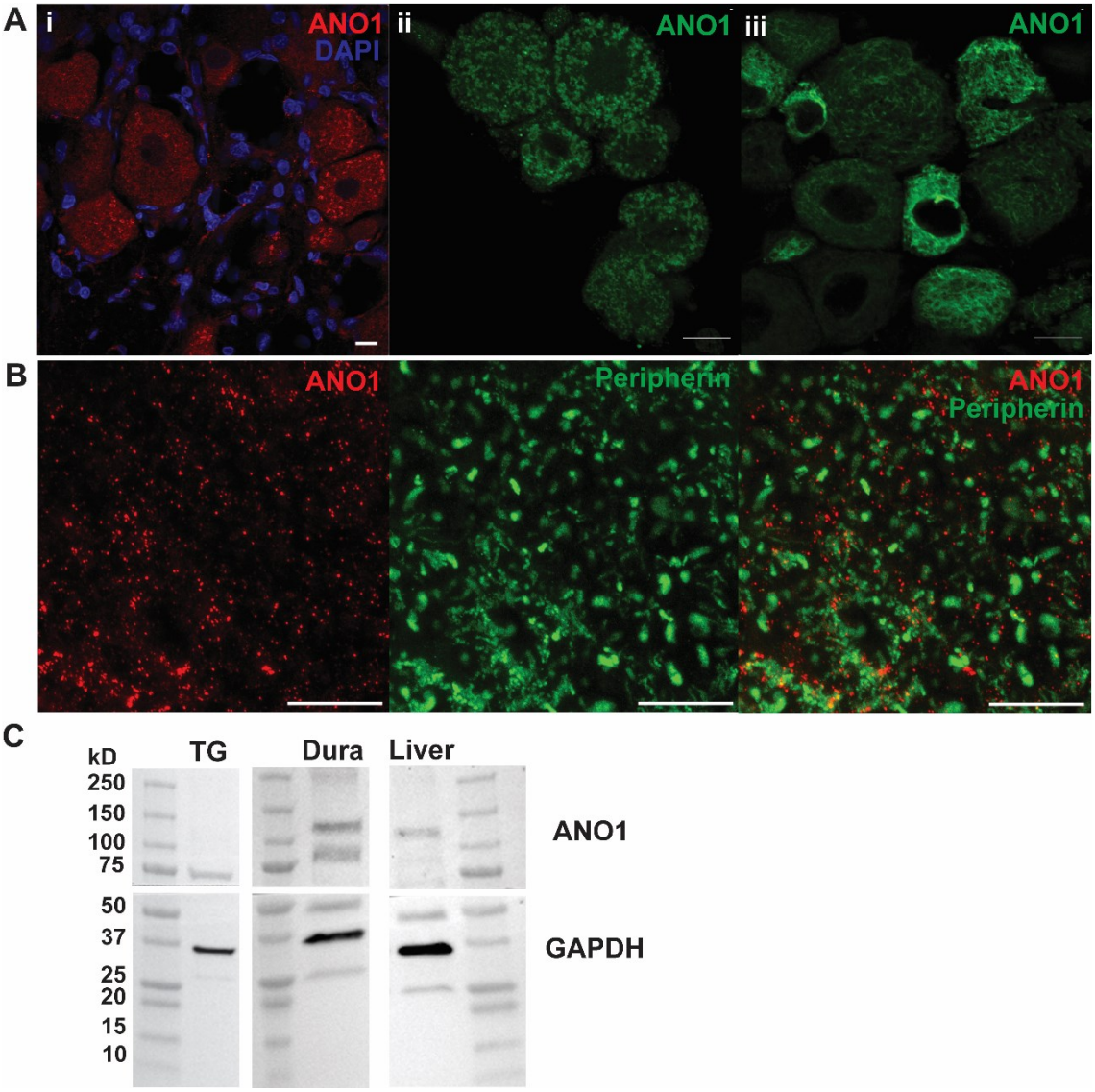

Figure 5.2: ANO1 protein immunoreactivity in the trigeminal ganglion and trigeminally innervated tissues. A) Representative confocal micrographs (N = 3) demonstrating robust ANO1 protein expression in neurons from transverse sections of adult rat TG perfusion-fixed in 4% PFA (i) and acetone/methanol fixative (iii) and primary culture obtained from neonatal rat TG (P3-7) fixed in 4% PFA following 3 days *in vitro* incubation (ii). **B)** Confocal micrographs displaying punctate ANO1 protein expression (red) co-localising with a protein marker for nociceptive neuron fibres, peripherin (green), in a cross-section of afferent nerve fibres distal to the trigeminal ganglion (perfusion-fixed in 4% PFA). **C)** Representative (N = 3) western blots of electrophoresed whole TG, dura mater and liver lysates obtained from fresh tissue (neonatal rat, P3-7), demonstrating ANO1 and GAPDH immunoreactivity. DAPI, 4',6-diamidino-2-phenylinodole; ANO1, anoctamin 1; GAPDH, glyceraldehyde-3-phosphate dehydrogenase. Scale bars = 10 μm.

5.2.2 Size Distribution Analysis Suggests Heterogeneous ANO1 Expression in Trigeminal Ganglion Neurons

A well-established principle in peripheral somatosensory neuroscience is the general classification of neuronal modality as a function of its size. Briefly, sensory neurons in both the DRG and TG are recognised as either small-diameter unmyelinated C-fibre types (10 – 35 μm), medium-diameter thinly-myelinated Aδ-fibre types (35 – 50 μm) or large-diameter myelinated Aβ/α type (50+ μm) functioning primarily as nociceptors and thermoreceptors (C/Aδ) or as low-threshold mechanoreceptors and proprioceptors (Aβ/α) (Le Pichon and Chesler, 2014). Neuronal size distribution analysis of protein expression can, therefore, be a helpful indicator of protein function in somatosensory ganglia.

Analysis of representative confocal micrographs of 4% PFA-fixed rat TG sections obtained from 3 animals identified the overall mean somatic diameter of ANO1 immunoreactive neurons (ANO1+) (n = 94 cells) to be 26.1 ± 0.876 μm, which was found to be significantly smaller than that of ANO1-negative (ANO1-) neurons (n = 262 cells) (28.4 ± 0.542 μm) ($p = 0.0152$, Mann-Whitney test). Previous investigations have estimated that 90% of rat TG neurons are small-to-medium C- and Aδ-fibres, which typically have diameters less than 35 μm; however, neuronal diameters in the TG can range from 10 to 55 μm (Lennerz et al., 2008, Ambalavanar and Morris, 1992). Observations from the present study are mainly similar. 82.0% of all TG neurons measured and 86.2% of ANO1+ neurons had a somatic diameter of 35 μm or less. Of the 292 neurons measured with a somatic diameter of less than 35 μm, 81 were ANO1+, representing 27.7% of the putative nociceptive population.

To further characterise ANO1 expression in the trigeminal system, transverse sections of afferent trigeminal nerve fibres distal to the TG were immunostained against ANO1 and the commonly used neuronal size markers NF200, which typically labels myelinated A-fibre neurons (large-diameter), and peripherin, which typically labels non-myelinated C-fibre neurons (small-diameter) (Sleigh et al., 2017, Ferri et al., 1990) (Figure 5.3A). The mean diameter of trigeminal afferent fibres immunopositive for ANO1, NF200 and peripherin was calculated as an average of the FWHM distance from 3 intensity line plots taken perpendicular to the direction of each fibre. As expected, the mean fibre diameter for NF200+ fibres (1.66 ± 0.122 μm) was significantly greater than that for peripherin+ fibres (0.994 ± 0.0853 μm) ($p < 0.0001$; Kruskall-Wallis with Dunn's multiple comparisons tests) (Figure 5.3B). However, while the mean fibre diameter of ANO1+ trigeminal fibres (1.53 ± 0.0697 μm) was not significantly different from that for NF200+ fibres ($p > 0.9999$; Kruskall-Wallis with Dunn's multiple comparisons tests), ANO1+ fibres were, on average,

significantly larger in diameter the peripherin+ fibres ($p = 0.0002$; Kruskall-Wallis with Dunn's multiple comparisons tests) (Figure 5.3B).

Thus far, these data demonstrate ANO1 protein expression in TG neurons and trigeminal afferent fibres, including in trigeminally innervated tissues such as the dura mater.

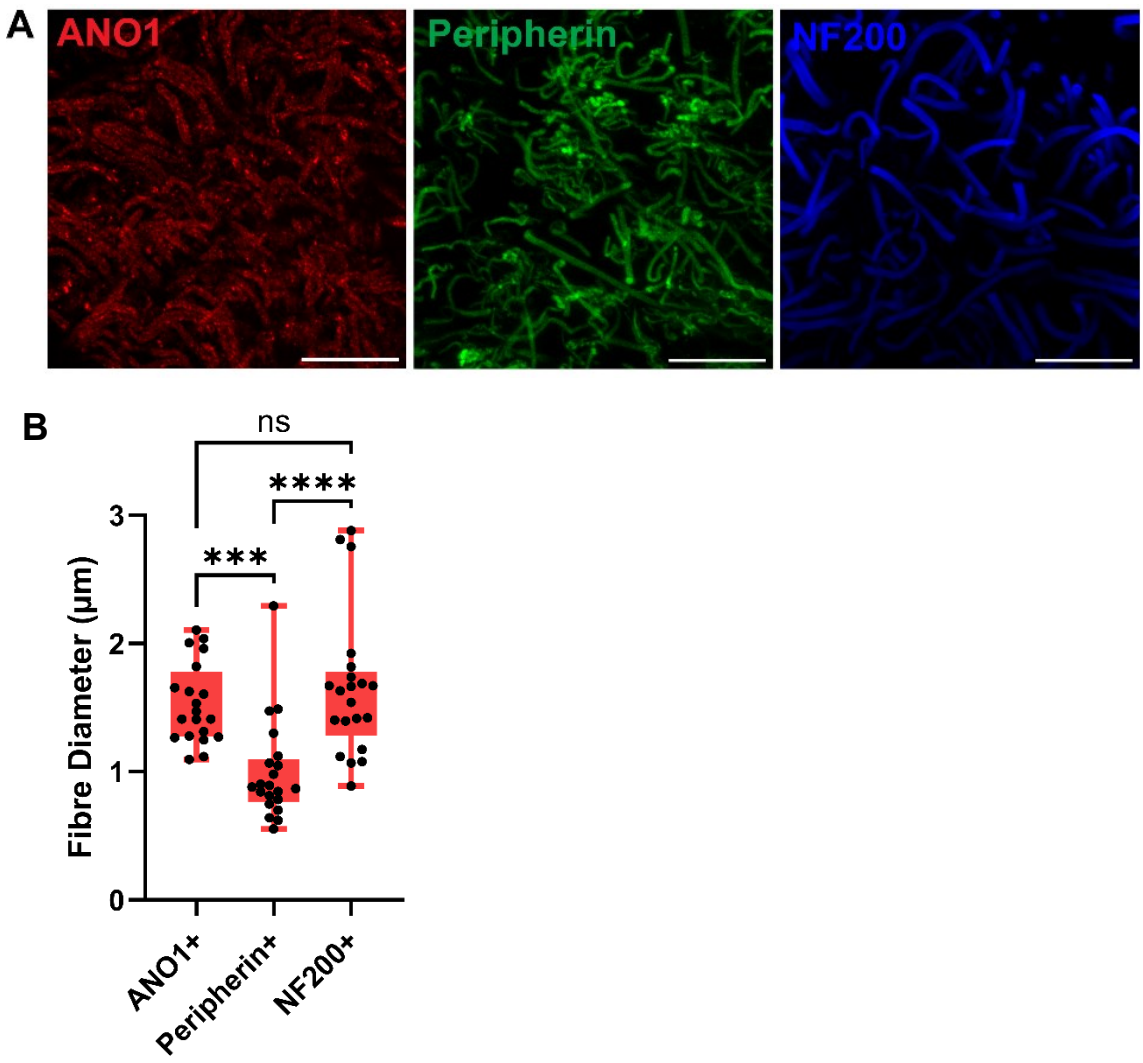

Figure 5.3: ANO1 is expressed in trigeminal afferent nerve fibres closer in size to NF200-positive fibres than peripherin-positive fibres. A) Representative confocal micrographs of PFA perfusion-fixed trigeminal afferent fibres sectioned distal to the trigeminal ganglion and immunostained against ANO1 and the nerve fibre size markers peripherin (small-diameter C fibres) and NF200 (medium-to-large diameter A fibres). **B)** Box plots demonstrating the range of mean fibre diameters for ANO1+ (n = 20), peripherin+ (n = 21) and NF200+ (n = 21) trigeminal afferent fibres measured from confocal micrographs of immunostained PFA-fixed tissue sections obtained from 3 independent biological replicates. Solid red box represents the first to third quartile of the dataset and error bars represent the minimum and maximum values measured. Scale bars = 10 µm. ***p < 0.001; ****p < 0.0001, Kruskall-Wallis with Dunn's multiple comparisons test. ANO1, anoctamin 1; NF200, neurofilament 200.

5.2.3 ANO1 Immunoreactivity Colocalises with Expression of IP_3R1 and TRPV1 in Trigeminal Ganglion Neurons

ANO1 has been consistently localised to ER-PM junctions in DRG nociceptors where it demonstrates nanodomain proximity with IP_3R1 and TRPV1 immunoreactivity, therefore, it was necessary to investigate whether such colocalisation was also present in small-diameter TG neurones.

Immunohistochemistry performed in 4% PFA-fixed primary TG cultures revealed strong ANO1 immunoreactivity in neurons that were also immunopositive for IP_3R1 (Figure 5.4A) or TRPV1 (Figure 5.4B). However, while colocalisation would posit an interaction between protein pairs, the resolution limit (minimum distance at which two points can be distinguished as separate) of optical confocal microscopy (≈ 200 nm) is such that the apparent spatial colocalisation of two fluorophore markers does not necessarily constitute close protein juxtaposition: JMSC protein interactions, such as those that occur between ANO1 and IP_3R1, or ANO1 and TRPV1, exist in the low nanometre domain (~ 15 nm), far smaller than the effective resolution of the LSM880 confocal microscope used for immunohistochemistry imaging (Jin et al., 2013, Cox and Sheppard, 2004). Therefore, it was pertinent to utilise super-resolution Airyscan microscopy techniques to bypass the diffraction limit and confirm the presence of ANO1-IP_3R1 and ANO1-TRPV1 nanodomain localisations.

Colocalisation analysis was performed for Airyscan images obtained of 4% PFA perfusion-fixed TG sections immunostained against ANO1 with either IP_3R1 or TRPV1, and PCCs were calculated for all neurons determined to be double immunopositive. Neurons demonstrating significant immunoreactivity for both ANO1 and IP_3R1 had somatic diameters between 10.3 and 47.0 µm with a mean of 24.7 ± 8.21 µm. The mean PCC was determined to be 0.501 ± 0.166 (n = 74 neurons), suggesting a positive correlation. Neurons immunopositive for both ANO1 and TRPV1 ranged in somatic diameter from 16.8 to 55.0 µm with a mean diameter of 33.6 ± 8.83 µm (n = 60 neurons) and the mean PCC calculated was 0.617 ± 0.353, also indicative of a positive correlation. In the TG, TRPV1 expression is primarily confined to small and medium-diameter neurons while results of the present study suggest ANO1 expression may be distributed throughout TG neurons of all sizes. To investigate whether ANO1 colocalisation with IP_3R1 and TRPV1 differed depending on neuronal size, the somatic diameter of double-positive neurons was plotted against the PCC for each respective neuron. Linear regression analysis of colocalisation between ANO1 and TRPV1 revealed a best-fit slope of 0.00726 ± 0.00516, which was not deemed significantly non-zero ($p = 0.164$) (Figure 5.4D). Conversely, plotting the diameter of ANO1-IP_3R1 immunopositive neurons against

their measured PCC revealed a significantly negative correlation with a best-fit slope of -0.00842 ± 0.00217 ($p = 0.0002$) (Figure 5.4C). This indicated significantly greater colocalisation between ANO1 and IP_3R1 immunoreactivity in smaller-diameter TG neurons compared to larger-diameter neurons, although there was no significant effect of neuronal size on colocalisation between ANO1 and TRPV1 immunoreactivity.

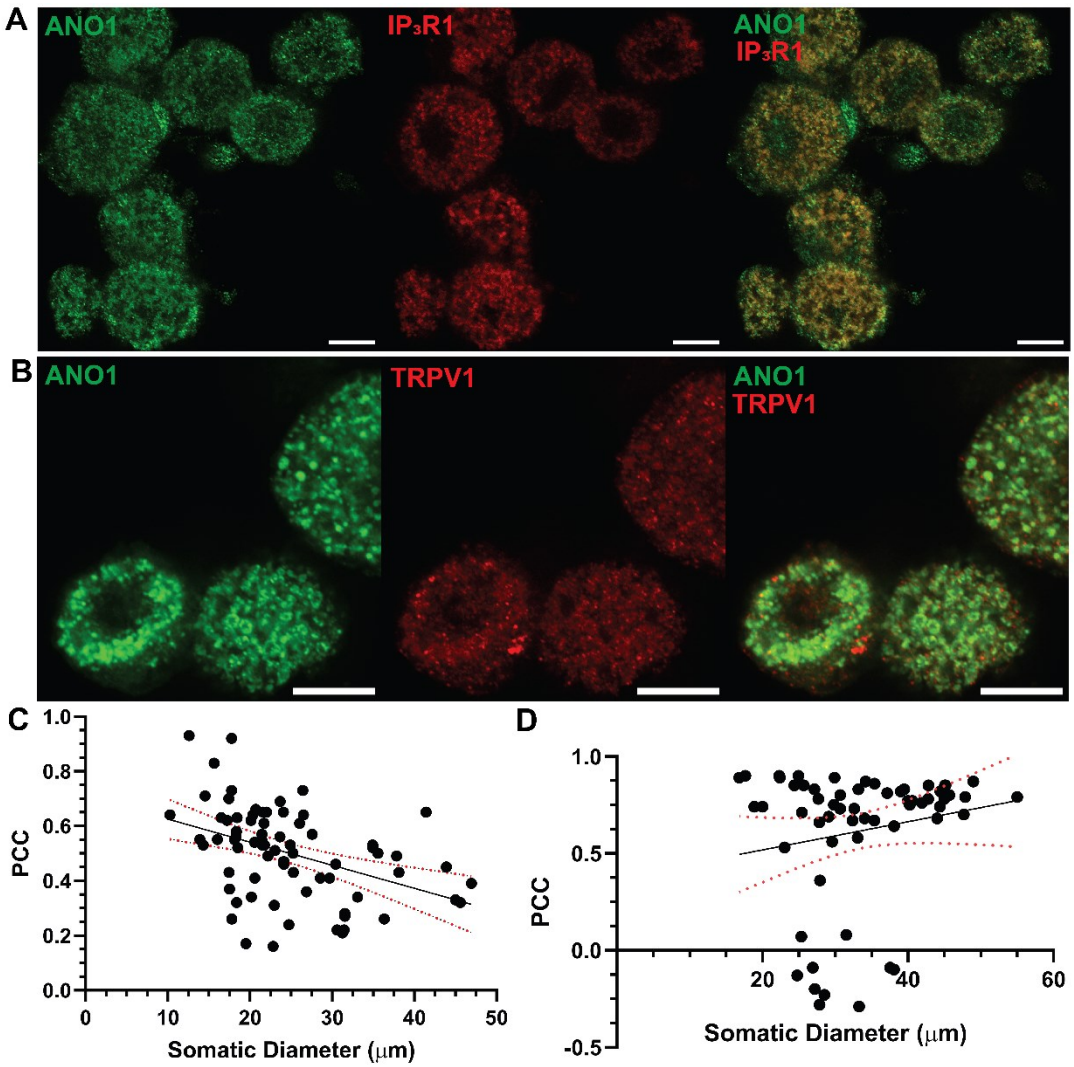

Figure 5.4 Colocalisation of ANO1 with IP_3R1 but not TRPV1 is significantly greater in smaller-diameter TG neurons than larger neurons. Representative Airyscan of PFA fixed primary TG neuron preparation from neonatal (P1-7) rats co-immunostained against ANO1 with IP_3R1 **(A)** and TRPV1 **(B)**. Colocalisation between ANO1 and IP_3R1 **(C)** or TRPV1 **(D)** immunoreactivity in neurons from PFA-fixed TG sections was quantified using Pearson's correlation coefficient (PCC) and plotted against somatic diameter. Linear regression analysis revealed a significant negative correlation between ANO1-IP_3R1 colocalisation and neuronal diameter ($p = 0.0002$) but no correlation for ANO1-TRPV1 colocalisation ($p = 0.164$). Error bars (red dotted lines) represent the 95% confidence intervals of the linear regression best-fit. Scale bars = 10 µm. ANO1, anoctamin 1; TRPV1, transient receptor potential vanilloid receptor type 1.

5.2.4 Proximity Ligation Assay Confirms Nanodomain Proximity Between IP_3R1 and TRPV1 with ANO1 in the Trigeminal Ganglion

Analysis of PLA performed in untreated 4% PFA-fixed primary TG neuronal cultures (N = 5) between ANO1 and IP_3R1 showed a robust punctate signal in 93 neurons ranging in somatic diameter from 14.2 µm to 35.6 µm (mean = 23.7 ± 5.18 µm). However, the majority (66.7%) of neurons positive for PLA signal had somatic diameters between 15 and 25 µm (Figure 5.5A, B). To control for the range of neuron sizes, the number of PLA puncta per neuron was normalised as puncta/diameter and the resulting value was plotted against the respective diameter for each cell (Figure 5.5B); however, linear regression analysis of the resulting plot did not reveal a significant correlation between the normalised PLA signal and neuronal diameter ($p = 0.720$).

CAP elicits a dose-dependent elevation in $[Ca^{2+}]_i$ in approximately 85% of neonatal TG neurons in culture (Belinskaia et al., 2022). Similarly, immunohistochemical studies have confirmed expression of the CAP-responsive Ca^{2+} channel TRPV1 in a comparable percentage of the TG neuron population (Bae et al., 2004). To investigate a hypothesised role for ANO1-IP_3R1 functional coupling downstream of TRPV1 activation, similar to that observed in DRG sensory neurons (Shah et al., 2020), primary TG neuron cultures prepared from neonatal rats (N = 3) were treated with 1 µM CAP for 5 minutes and immediately fixed in 4% PFA without washout.

As with the control group, a strong PLA signal between ANO1 and IP_3R1 was observed in 38 trigeminal neurons ranging in diameter from 10.4 to 25.4 µm (mean = 16.5 ± 3.74 µm) and the mean number of puncta per neuron was 14.8 ± 9.97 (Figure 5.5A). To control for neuron size, the number of puncta per neuron was normalised to its diameter. However, linear regression analysis confirmed there was no significant correlation between this value and neuronal size ($p = 0.164$) (Figure 5.5C). When the mean number of puncta per unit diameter was compared between the control TG neurons (0.775 ± 0.0919) and those treated with 1 µM CAP (0.873 ± 0.0816), it was found that exposure to CAP significantly increased the normalised PLA signal between ANO1 and IP_3R1 in small-diameter TG neurons ($p = 0.0150$, Mann-Whitney test) (Figure 5.5D).

In DRG sensory neurons, functional ANO1-IP_3R1 coupling is found within nanodomain proximity of TRPV1 at so-called JMSCs that form at contact sites between the PM and ER (Shah et al., 2020). Ca^{2+} influx via TRPV1 following activation by noxious heat (>42°C) or vanilloid compounds, such as CAP, is sufficient to activate the Ca^{2+}-sensitive PLCδ isoform, contributing to IP_3-induced release of intracellular Ca^{2+} stores independent of prior G_q protein activation, and subsequent activation of ANO1 (Lukacs et al., 2013, Shah et al., 2020). Building on the colocalisation analyses demonstrating

close co-expression of ANO1 and TRPV1 in TG neurons, PLA experiments were performed to investigate nanodomain proximity for the protein pair in primary neonate rat TG neurons.

Primary TG neuron preparations (N = 3) were cultured in standard growth media (see Methods for details) for 3 days prior to fixation in 4% PFA immediately or following incubation with 1 μM CAP for 5 minutes at 37ºC. For both the control (n = 77 neurons) and treated (n = 45 neurons) conditions, a very strong PLA signal was observed between ANO1 and TRPV1 (Figure 5.6A). The mean somatic diameter of TG neurons at rest (untreated), which were positive for ANO1-TRPV1 PLA puncta, was 21.3 ± 0.641 μm, which was significantly greater than the mean diameter of PLA-positive neurons treated with CAP (16.7 ± 0.721 μm) ($p < 0.0001$, Mann-Whitney test). However, treatment with 1 μM CAP significantly increased both the mean number of puncta per neuron, from 10.3 ± 1.11 to 36.7 ± 5.38 ($p < 0.0001$, Mann-Whitney test), but also the mean value of puncta normalised to somatic diameter (0.480 ± 0.0518 to 1.97 ± 0.190, $p < 0.0001$, Mann-Whitney test), to control for the effect of differing mean neuronal population diameters (Figure 5.6D).

For each of the PLA-positive control and CAP-treated neurons, the normalised number of puncta was plotted against the respective somatic diameter, and linear regression analyses were performed to investigate the effect of neuronal size on the degree of interaction between ANO1 and TRPV1. While in the control group, there was not a significantly non-zero correlation between PLA signal and somatic diameter (slope = 0.00136, $p = 0.884$) (Figure 5.6B), in neurons treated with 1 μM CAP, linear regression analysis revealed a significant positive correlation (slope = 0.169, $p < 0.0001$) indicating a trend towards a greater number of PLA puncta in neurons of larger somatic diameter, between a range in diameters from 9.23 to 30.5 μm (Figure 5.6C).

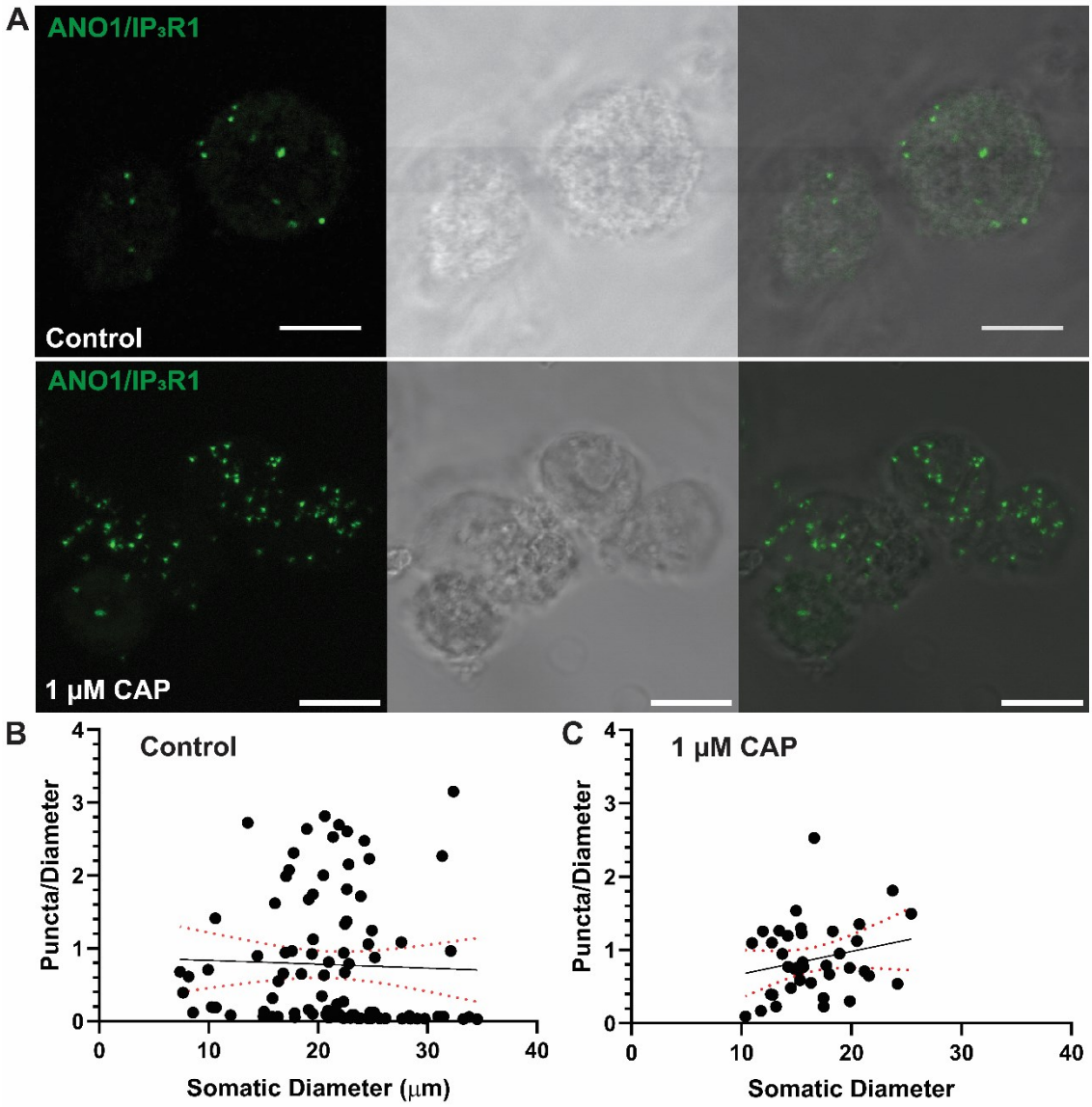

Figure 5.5 PLA supports nanodomain proximity between ANO1 and IP_3R1 in TG neurons. A) Robust punctate PLA signal observed between anti-ANO1 and anti-IP_3R1 antibodies in 4% PFA fixed primary trigeminal ganglion neuronal cultures prepared from neonatal (P1-7) rats. Cells were fixed before (top panels) or after (bottom panels) treatment with 1 µM capsaicin. Left panel = PLA, middle panel = brightfield, right panel = overlay. Number of puncta was normalised to somatic diameter for each cell and plotted against its respective diameter to perform linear regression analysis for control neurons **(B)** and neurons treated with 1 µM of the TRPV1 agonist, CAP **(C). D)** Exposure to 1 µM CAP significantly increased the mean number of puncta per neuron for PLA between ANO1 and IP_3R1 ($p = 0150$, Mann-Whitney test). Error bars (red dotted lines) represent the 95% confidence intervals of the linear regression best-fit (B and C) or the mean ± SD (D). Scale bars = 10 µm. *$p < 0.05$. CAP, capsaicin; ANO1, anoctamin 1; IP_3R1, inositol triphosphate receptor type 1; PLA, proximity ligation assay.

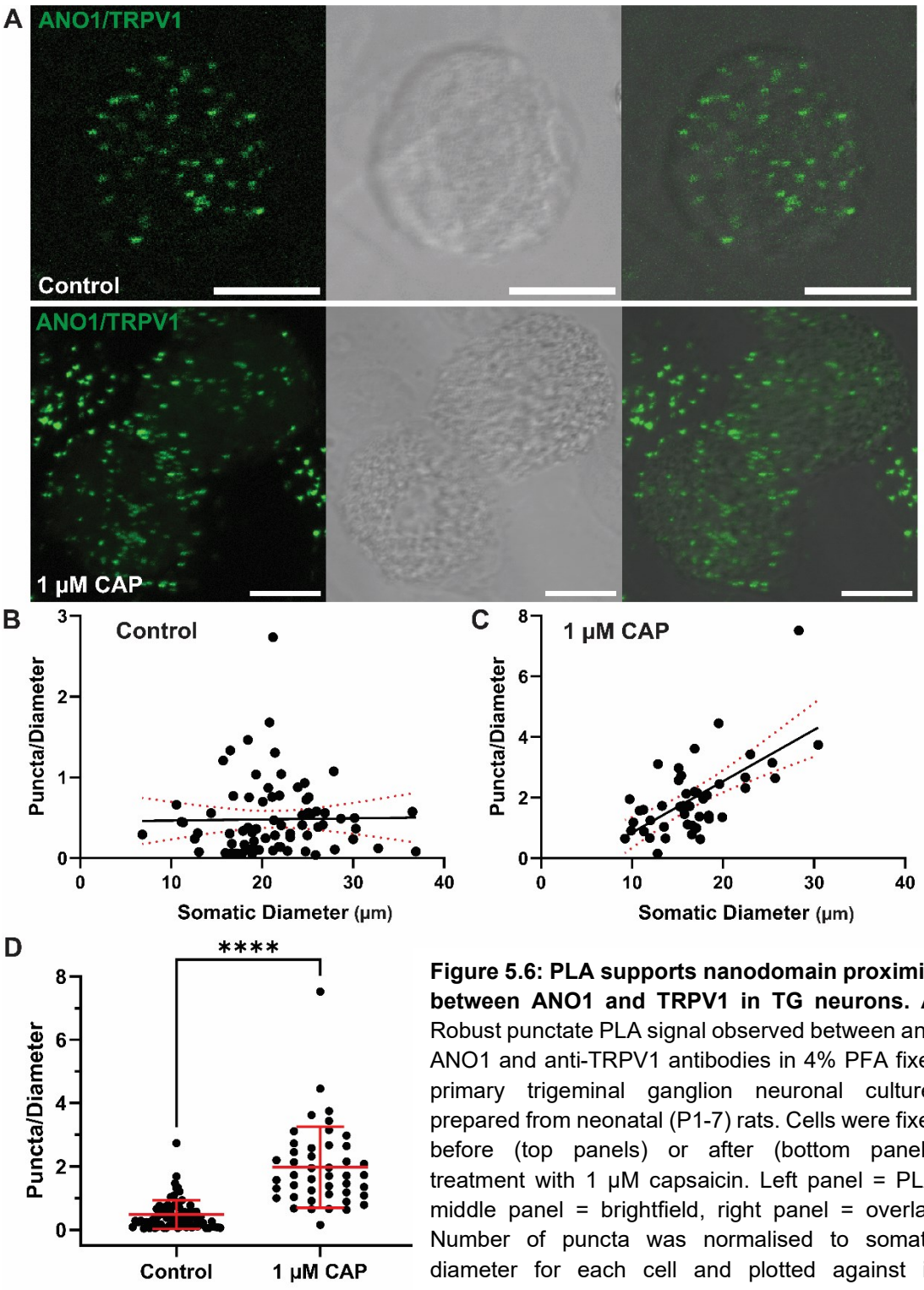

Figure 5.6: PLA supports nanodomain proximity between ANO1 and TRPV1 in TG neurons. A) Robust punctate PLA signal observed between anti-ANO1 and anti-TRPV1 antibodies in 4% PFA fixed primary trigeminal ganglion neuronal cultures prepared from neonatal (P1-7) rats. Cells were fixed before (top panels) or after (bottom panels) treatment with 1 µM capsaicin. Left panel = PLA, middle panel = brightfield, right panel = overlay. Number of puncta was normalised to somatic diameter for each cell and plotted against its respective diameter to perform linear regression analysis for control neurons **(B)** and neurons treated with 1 µM of the TRPV1 agonist, CAP **(C). D)** Exposure to 1 µM CAP significantly increased the mean number of puncta per neuron for PLA between ANO1 and TRPV1 ($p < 0.0001$, Mann-Whitney test). Error bars (red dotted lines) represent the 95% confidence intervals of the linear regression best-fit (B and C) or the mean ± SD (D). Scale bars = 10 µm. ****$p < 0.0001$. CAP, capsaicin; ANO1, anoctamin 1; TRPV1, transient receptor potential vanilloid receptor 1; PLA, proximity ligation assay.

5.2.5 ANO1-IP_3R1 Nanodomains are Colocalised with the Canonical CGRP Receptor Proteins RAMP1 and CLR

In the TG, differential expression patterns of the major signalling neuropeptide CGRP and its canonical GPCR separates sensory neurons into either CGRP-releasing (peptidergic) or CGRP-responding sub-populations of differing diameters (Haanes and Edvinsson, 2019, Lennerz et al., 2008, Edvinsson et al., 2020). Data presented in this thesis supports expression of CaCC ANO1 in both small-diameter C fibre and medium-diameter Aδ fibre neurons, raising multiple scenarios through which ANO1 activation may modulate mechanisms underlying CGRP signalling in CGRP-releasing small-diameter or CGRP-responding medium-diameter neurons.

To investigate potential ANO1 coupling to the canonical CGRP receptor in rat TG sensory neurons, immunohistochemistry for ANO1 and the CGRP receptor component RAMP1 was performed in both 4% PFA perfusion-fixed transverse adult (P21+) TG sections (Figure 5.7A) and primary TG neuronal cultures prepared from neonatal rats (Figure 5.7B). The mean somatic diameter of TG neurons immunopositive for both ANO1 and RAMP1 (N = 4 animals) was 31.8 ± 6.87 µm. Although double-positive neurons ranged in diameter from 15.7 to 47.9 µm, of the 106 neurons characterised, 72 had a somatic diameter equal to or less than 35 µm, representing 66.7% of a majority small-diameter putative nociceptive population. Quantitative colocalisation analysis (PCC) of representative Airyscans of ANO1/RAMP1 immunostaining in TG sections revealed an overall mean PCC of 0.439 ± 0.100 and PCC did not significantly differ as a result of neuronal diameter, as indicated by linear regression analysis of the PCC for each double-positive neuron plotted against its respective somatic diameter (slope = -0.00109, p = 0.448) (Figure 5.7C).

Considering RAMP1 is a component of the G_q-coupled CGRP receptor known to activate IP_3R1 downstream, it was hypothesized that following activation of RAMP1-containing receptors by CGRP, ANO1 may be recruited to RAMP1-IP_3R1 signalling domains in TG Aδ neurons and would therefore be present within the nanodomain proximity detectable by PLA (40 nm). Indeed, PLA performed between ANO1 and RAMP1 in primary TG culture revealed robust punctate signals in neurons with somatic diameters ranging from 8.77 to 32.1 µm (N = 7 animals, n = 67 neurons) (Figure 5.8A). The mean somatic diameter of this population was 19.5 ± 4.99 µm. For neurons cultured in standard growth media, the mean number of PLA puncta per neuron was 6.06 ± 8.88; however, stimulation of primary TG cultures with 1 µM α-CGRP for 1 hour at 37ºC significantly increased the mean number of puncta between ANO1 and RAMP1 to 12.0 ± 1.60 per neuron (N = 3, n = 41 neurons) (p = 0.0002, Mann-Whitney test) (Figure 5.8B). To

account for sampling of a heterogenous population of neurons, the number of PLA puncta was normalised to each neurons' respective somatic diameter, however, there was still a significant difference between the control and CGRP groups (0.327 ± 0.0522 puncta per unit diameter vs 0.637 ± 0.0719, p = 0.0001, Mann-Whitney test). The normalised puncta data was plotted against the diameter for each neuron for both the control and CGRP-treated groups for linear regression analysis. No significant correlation was observed between PLA signal and neuron size for either the control group (slope = -0.0124, p = 0.243) (Figure 5.8C) nor the CGRP-treated neurons (slope = 0.0291, p = 0.120) (Figure 5.8D).

In the trigeminal system, RAMP1 is typically expressed in Aδ sensory neurons and fibres (Edvinsson et al., 2019, Eftekhari et al., 2013). Although not significant, the positive correlation observed in CGRP-treated neurons between increasing somatic diameter and increasing PLA signal would be consistent with the expected size range for RAMP1-expressing, CGRP-responding, Aδ-type diameter neurons. Indeed, when the mean number of PLA puncta was compared between control and CGRP-treated neurons separated by somatic diameter (10 – 15 µm, 15 – 20 µm, 20 – 25 µm and 25 – 30 µm), a significant difference was only observed for neurons with somatic diameters between 20 and 25 µm (p = 0.0033), and between 25 and 30 µm (p = 0.0232) (Kruskall-Wallis with Dunn's multiple comparisons tests) (Figure 5.8E). There was no significant change in the mean number of PLA puncta following CGRP stimulation in neurons with smaller diameters (10 - 15 and 15 - 20 µm), supporting a role for ANO1 coupling to CGRP receptor activation in Aδ fibres over C fibres.

The canonical G protein-coupled CGRP receptor is comprised of multiple peptide components: RAMP1 and CRLR (Simms et al., 2019). Serving as a positive control for PLA and as confirmation for expression of the canonical CGRP receptor in TG neurons *in vitro,* PLA was performed between anti-RAMP1 and anti-CRLR antibodies in PFA-fixed primary TG cultures prepared from neonatal rats (Figure 5.9A). Indeed, a robust punctate signal was observed in neurons ranging in somatic diameter between 9.65 and 40.6 µm (n = 159, N = 3), where the mean diameter for this subpopulation was 20.1 ± 0.418. The number of puncta per neuron was normalised to somatic diameter and plotted for linear regression analysis, which revealed a slight positive correlation (slope = 0.0161), although this was not significant (p = 0.171) (Figure 5.9B).

PLA experiments were performed for ANO1-CRLR and IP_3R1-CRLR antibody pairs to provide further evidence in support of a functional interaction between ANO1-IP_3R1 coupling at ER-PM junctions and CGRP signalling mechanisms. Positive PLA signal was observed in PFA-fixed primary TG neuronal cultures prepared from neonatal rats for both

ANO1 and CRLR (n = 112, N = 3) (Figure 5.10A) and IP_3R1 and CRLR (n = 99, N = 3) pairs (Figure 5.11A). The mean somatic diameter of TG neurons displaying 40 nm proximity between ANO1 and CRLR was 19.6 ± 0.473 μm, although puncta were observed in neurons ranging in size from 8.79 to 31.6 μm. A larger range in diameter of TG neurons positive for PLA between IP_3R1 and CRLR (from 8.61 to 41.1 μm), although the mean somatic diameter (20.7 ± 0.630 μm) was not significantly different from those neurons displaying ANO1-CRLR proximity ($p = 0.284$, Mann-Whitney test). The number of puncta per neuron for both populations was normalised to diameter as before and plotted prior to linear regression analysis to investigate a potential correlation between PLA signal and neuronal diameter. A positive trend was observed for both ANO1-CRLR (Figure 5.9B) and IP_3R1-CRLR (Figure 5.10B) PLA pairs, and both populations demonstrated a significant correlation (ANO1-CRLR: slope = 0.0455, $p = 0.0006$; IP_3R1-CRLR: slope = 0.0163, $p = 0.0185$), indicative of ANO1-IP_3R1 proximity to the CGRP receptor in medium-diameter, putative Aδ neurons.

Most interestingly, while treatment with 1 μM α-CGRP had significantly increased the mean PLA signal between ANO1 and RAMP1 in TG neurons, the mean number of puncta per neuron seen in PLA experiments between ANO1 and CRLR significantly decreased following CGRP exposure from to ($p < 0.0001$, Mann-Whitney test) (Figure 5.10C). Similarly, a significant reduction in PLA signal between IP_3R1 and CRLR was seen between the control (10.3 ± 1.04 puncta per neuron) and α-CGRP-treated groups (2.83 ± 0.231 puncta per neuron) (Figure 5.11), indicating significant rearrangements within the putative nanodomain complexes upon RAMP1-CRLR receptor activation.

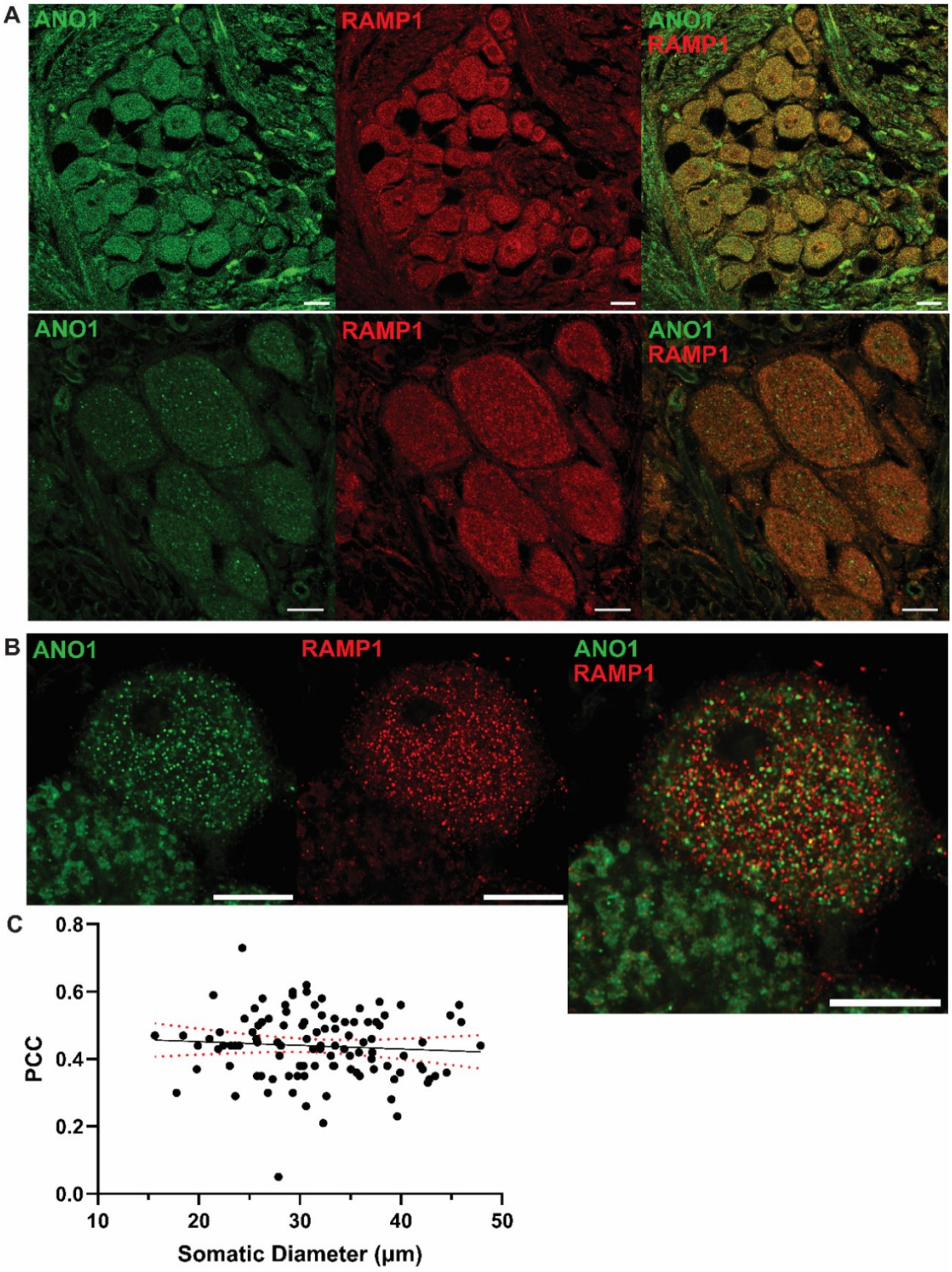

Figure 5.7: ANO1 and RAMP1 are similarly colocalised in small and medium-diameter TG neurons. Representative Airyscans of PFA-fixed whole adult TG sections **(A)** and primary TG neuron preparation from neonatal rats (P1-7) **(B)** showing high degree of co-expression of ANO1 and the canonical CGRP receptor subunit RAMP1 in a large range of neuron sizes. **C)** Colocalisation between ANO1 and RAMP1 immunoreactivity in neurons from PFA-fixed TG sections was quantified using Pearson's correlation coefficient (PCC) and plotted against somatic diameter. Linear regression analysis revealed there was not a significant correlation between ANO1-RAMP1 colocalisation and neuronal diameter ($p = 0.448$). Error bars (red dotted lines) represent the 95% confidence intervals of the linear regression best-fit. Scale bars = 10 µm. RAMP1, receptor activity modifying protein 1; ANO1, anoctamin 1.

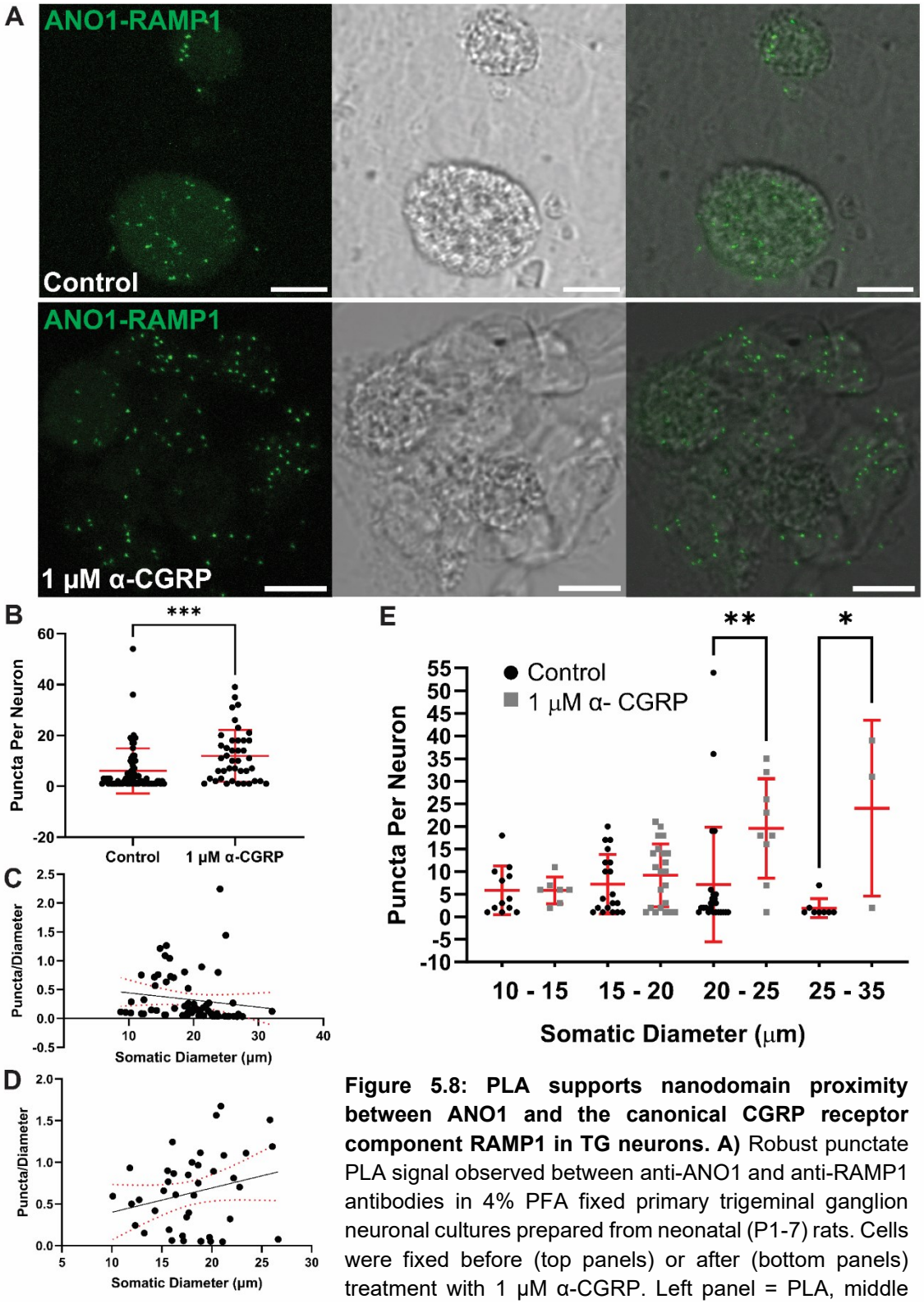

Figure 5.8: PLA supports nanodomain proximity between ANO1 and the canonical CGRP receptor component RAMP1 in TG neurons. A) Robust punctate PLA signal observed between anti-ANO1 and anti-RAMP1 antibodies in 4% PFA fixed primary trigeminal ganglion neuronal cultures prepared from neonatal (P1-7) rats. Cells were fixed before (top panels) or after (bottom panels) treatment with 1 µM α-CGRP. Left panel = PLA, middle panel = brightfield, right panel = overlay. **B)** Exposure to 1 µM α-CGRP significantly increased the mean number of puncta per neuron for PLA between ANO1 and RAMP1 ($p < 0.0001$, Mann-Whitney test). Number of puncta was normalised to somatic diameter for each cell and plotted against its respective diameter to perform linear regression analysis for control neurons **(C)** and neurons treated with 1 µM α-CGRP **(D)**. Error bars (red dotted lines) represent the 95% confidence intervals of the linear regression best-fit **(D)** or the mean ± SD **(B, C** and **E)**. *$p < 0.05$; **$p < 0.01$; ***$p < 0.001$. Scale bars = 10 µm. CGRP, calcitonin gene-related peptide; ANO1, anoctamin 1; RAMP1, receptor activity modifying protein 1; PLA, proximity ligation assay.

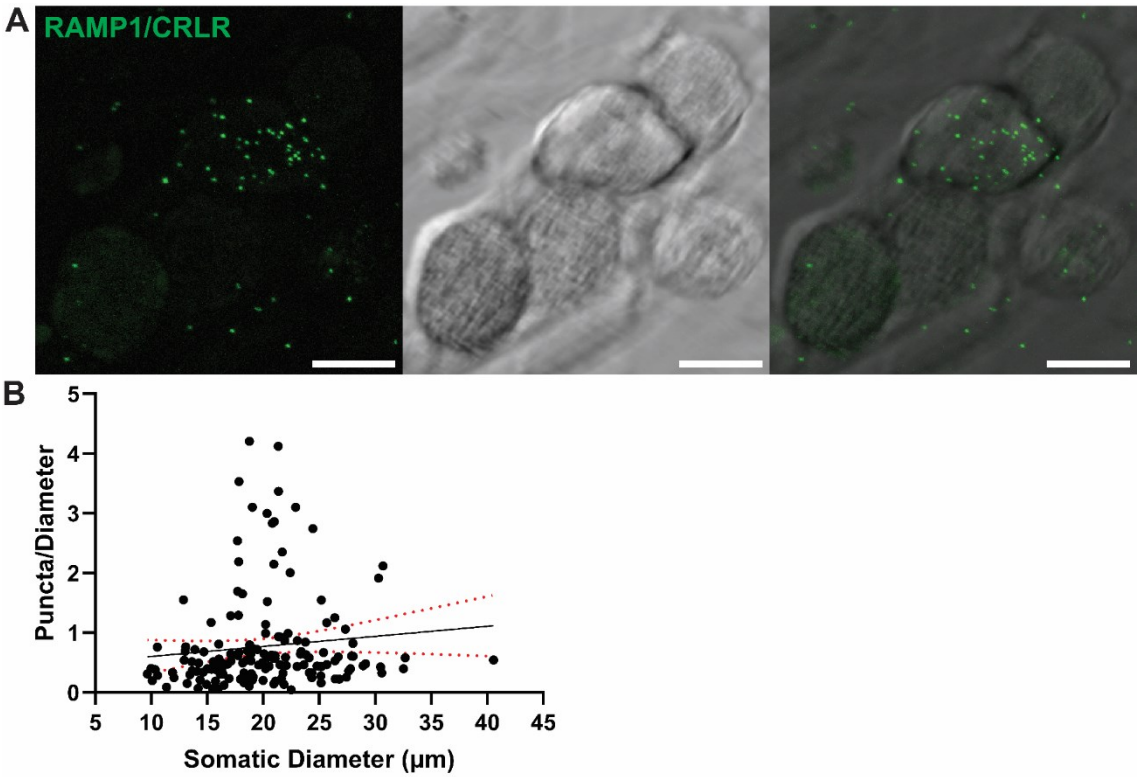

Figure 5.9: Positive control for PLA confirms nanodomain proximity between protein subunits of the canonical CGRP receptor, RAMP1 and CRLR. A) Robust punctate PLA signal observed between anti-RAMP1 and anti-CRLR antibodies in 4% PFA fixed primary trigeminal ganglion neuronal cultures prepared from neonatal (P1-7) rats. Left panel = PLA, middle panel = brightfield, right panel = overlay. **B)** Number of puncta was normalised to somatic diameter for each cell and plotted against its respective diameter to perform linear regression analysis. Error bars (red dotted lines) represent the 95% confidence intervals of the linear regression best-fit. Scale bars = 10 µm. PLA, proximity ligation assay; CGRP, calcitonin gene-related peptide; RAMP1, receptor activity modifying protein 1; CRLR, calcitonin receptor-like receptor.

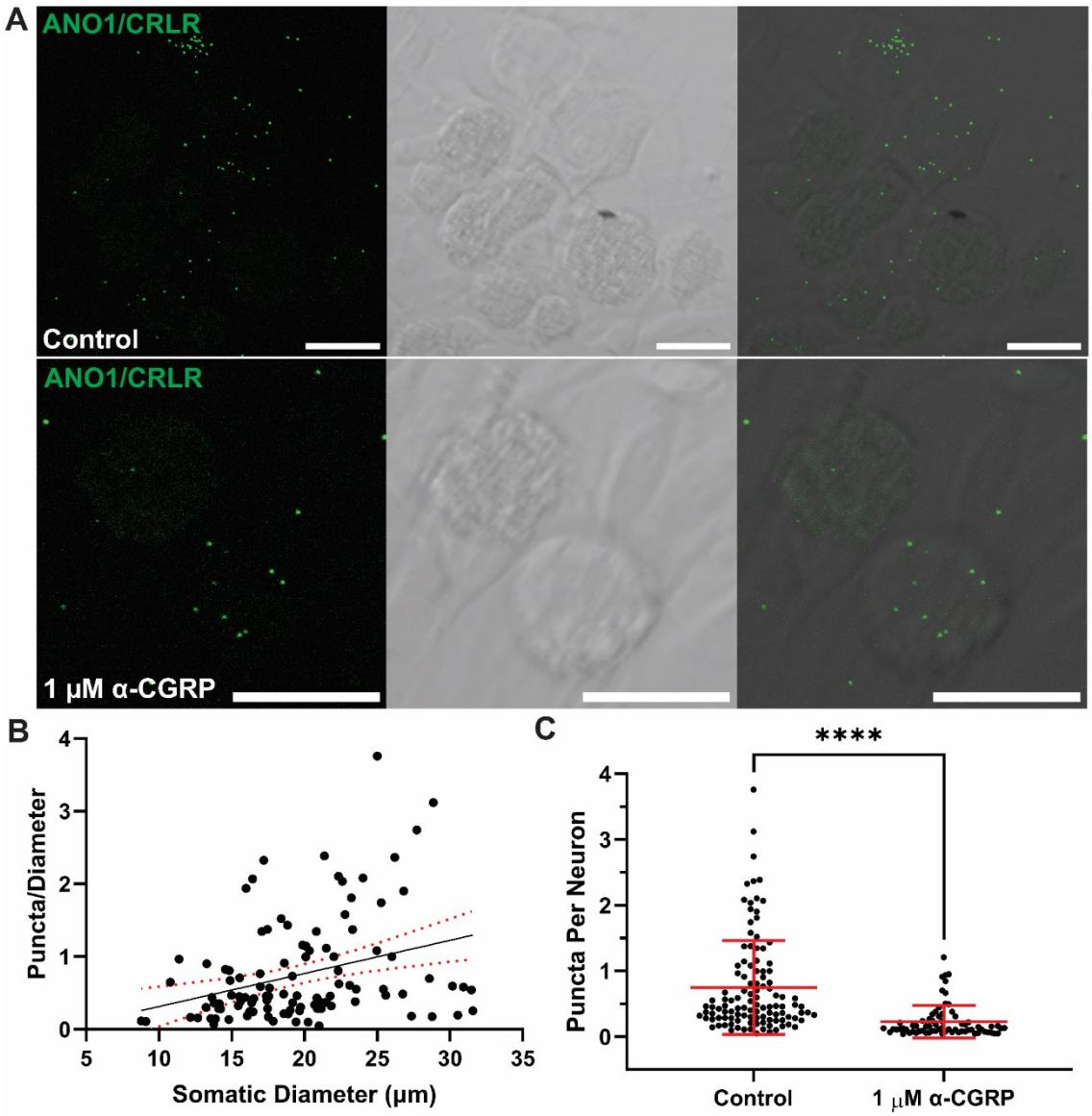

Figure 5.10: PLA supports nanodomain proximity between ANO1 and the canonical CGRP receptor component CRLR in TG neurons. A) Robust punctate PLA signal observed between anti-ANO1 and anti-CRLR antibodies in 4% PFA fixed primary trigeminal ganglion neuronal cultures prepared from neonatal (P1-7) rats. Cells were fixed before (top panels) or after (bottom panels) treatment with 1 μM α-CGRP. Left panel = PLA, middle panel = brightfield, right panel = overlay. **B)** Number of puncta was normalised to somatic diameter for each cell and plotted against its respective diameter to perform linear regression analysis for control neurons. **C)** Exposure to 1 μM α-CGRP significantly decreased the mean number of puncta per neuron for PLA between ANO1 and CRLR ($p < 0.0001$, Mann-Whitney test). Error bars (red dotted lines) represent the 95% confidence intervals of the linear regression best-fit **(B)** or the mean ± SD **(C)**. Scale bars = 10 μm. ****$p < 0.0001$. PLA, proximity ligation assay; ANO1, anoctamin 1; CRLR, calcitonin receptor-like receptor; CGRP, calcitonin gene-related peptide.

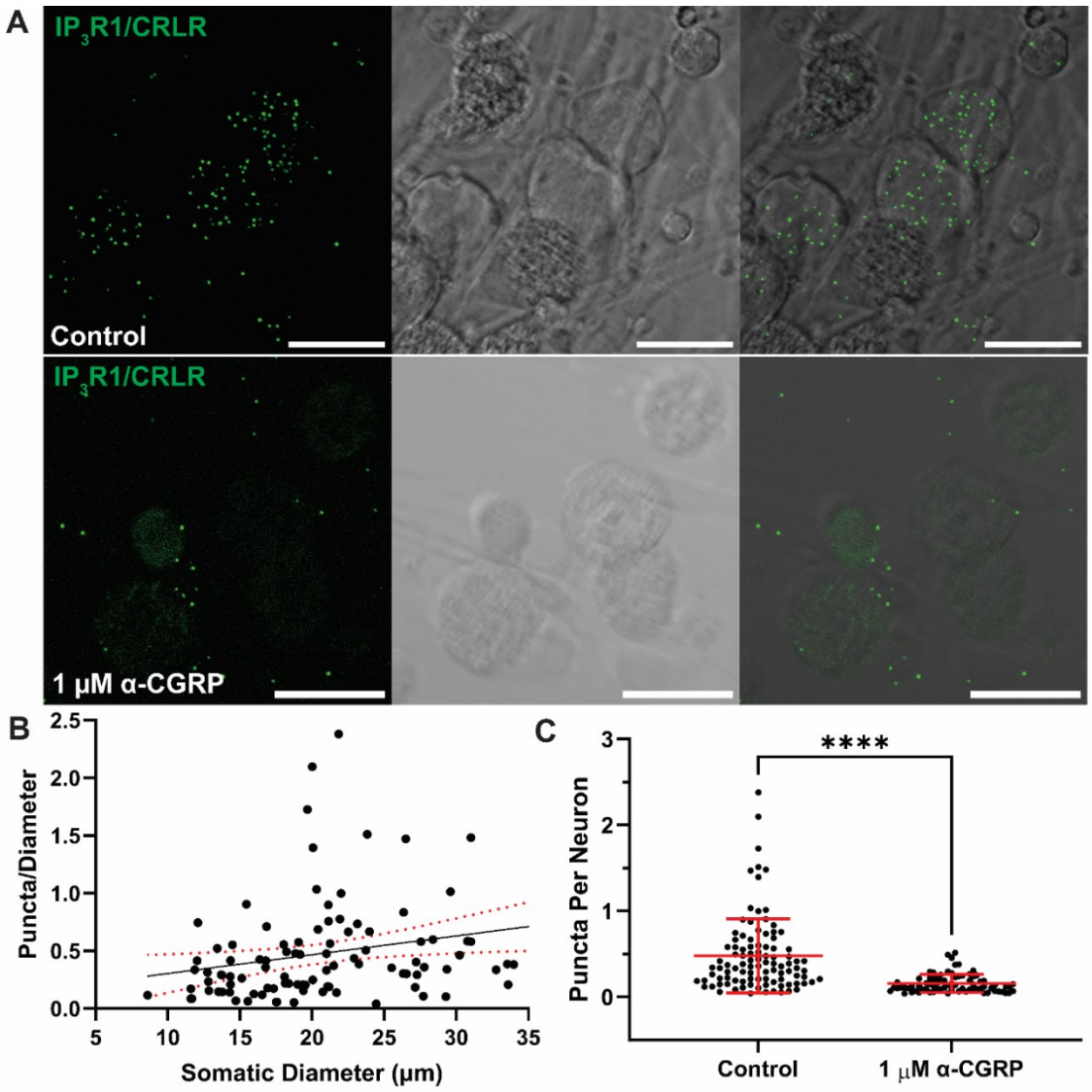

Figure 5.11: PLA supports nanodomain proximity between IP_3R1 and the canonical CGRP receptor component CRLR in TG neurons. A) Robust punctate PLA signal observed between anti-IP_3R1 and anti-CRLR antibodies in 4% PFA fixed primary trigeminal ganglion neuronal cultures prepared from neonatal (P1-7) rats. Cells were fixed before (top panels) or after (bottom panels) treatment with 1 μM α-CGRP. Left panel = PLA, middle panel = brightfield, right panel = overlay. **B)** Number of puncta was normalised to somatic diameter for each cell and plotted against its respective diameter to perform linear regression analysis for control neurons. **C)** Exposure to 1 μM α-CGRP significantly decreased the mean number of puncta per neuron for PLA between IP_3R1 and CRLR ($p < 0.0001$, Mann-Whitney test). Error bars (red dotted lines) represent the 95% confidence intervals of the linear regression best-fit **(B)** or the mean ± SD **(C)**. Scale bars = 10 μm. ****$p < 0.0001$. PLA, proximity ligation assay; IP_3R1, inositol tri-phosphate receptor type 1; CRLR, calcitonin receptor-like receptor; CGRP, calcitonin gene-related peptide.

5.2.6 No Evidence that CGRP Elicits Release of Intracellular Calcium Stores in Trigeminal Ganglion Neurons

The results presented thus far confirm protein expression of ANO1 in TG sensory neurons and are indicative of nanodomain proximity between ANO1 with known interactors in the DRG, IP_3R1 and TRPV1, and also suggest proximity between ANO1-IP_3R1 complexes with components of the canonical CGRP receptor, RAMP1 and CRLR. These data were confirmed in fixed TG neurons; therefore, to establish a functional coupling between ANO1 and these putative interactors, it was necessary to measure ANO1 activation in living cells.

While the canonical CGRP receptor primarily associates with G_s proteins, it has been reported to couple with G_q proteins in some instances (Walker et al., 2010), suggesting that the CGRP peptide could induce the release of intracellular ER Ca^{2+} stores downstream of the G_s signalling cascade. Previous studies involving expression of recombinant RAMP1 and CRLR in HEK293 cells reported both G_s (elevated cAMP levels) and G_q (intracellular accumulation of IP_3 and Ca^{2+} transients) signalling associated responses (Aiyar et al., 1999). To assess whether CGRP is capable of eliciting Ca^{2+} transients in primary trigeminal sensory neurons, cultures prepared from neonatal rats (N = 4) were maintained in vitro for 3 days before loading with 2 μM of the ratiometric Ca^{2+}-sensitive fluorescent dye, Fura-2 AM, 30 minutes prior to imaging. Cultures were perfused at room temperature for 60 seconds with standard extracellular solution (EC), followed by perfusion of 1 μM α-CGRP peptide in standard EC solution for 120 seconds, a washout period of 120 seconds with standard EC solution and a final perfusion of 50 mM K^+ EC solution as a positive control to differentiate sensory neurons from other cell types in culture (satellite glial cells, fibroblasts).

Ratiometric Fura-2 AM readings were recorded for 98 neurons (identified based on morphology) in total across 4 independent preparations and changes in $[Ca^{2+}]_i$ were measured as $\Delta R/R_0$ (change in 340/380 nm ratio normalised to ratio at t = 0 seconds). The maximum $\Delta R/R_0$ value following perfusion of 50 mM K^+ (to depolarise sensory neurons, inducing activation of VGCCs which promotes Ca^{2+} influx) was 5.52 while the mean response was 3.27 ± 0.105. To determine which neurons demonstrated a significant increase in $[Ca^{2+}]_i$ following perfusion of 1 μM α-CGRP, a threshold R/R_0 value was determined at 5% of the maximal response to K^+ (0.276). Therefore, neurons were deemed significantly CGRP-responsive if their maximum R/R_0 value during perfusion of α-CGRP exceeded 1.276.

Perfusion with 1 μM α-CGRP induced significant Ca^{2+} transients in 4 neurons out of 98, representing 4.08% of the neuronal population analysed (Figure 5.12A). The mean Ca^{2+}

response to CGRP was 1.410 ± 0.0407, significantly less than that observed following perfusion of 50 mM K^+ ($p = 0.0047$, paired t-test) (Figure 5.12B). The mean time to peak CGRP response was 10.5 ± 3.20 seconds, which was not significantly different than the mean time to peak K^+ response for those same 4 neurons (18.0 ± 8.68 seconds) ($p = 0.750$, Wilcoxon matched-pairs signed rank test).

Activation of G_q protein-coupled signalling cascades results in the downstream release of intracellular IP_3-sensitive Ca^{2+} stores. To confirm the source of α-CGRP-induced Ca^{2+} transients, Fura-2 AM recordings in primary TG neuronal cultures were repeated using Ca^{2+}-free EC solution to eliminate the influx of extracellular Ca^{2+}. In this experimental setup, any increase observed in $[Ca^{2+}]_i$ must, therefore, be due to the release of ER Ca^{2+} stores. However, perfusion of 1 μM α-CGRP in a 0 mM Ca^{2+} extracellular environment failed to induce significant Ca^{2+} transients in any of 140 trigeminal neurons (N = 5) (Figure 5.12C and D). This result would suggest that in TG sensory neurons, at least, CGRP does not elicit robust release of intracellular Ca^{2+} stores, such as those necessary to activate ANO1.

To confirm that noxious stimulation of TG sensory neurons can indeed induce the release of IP_3-sensitive Ca^{2+} stores, Fura-2 AM recordings were repeated during perfusion of the inflammatory mediator BK in Ca^{2+}-free EC solution, which has previously been shown to evoke significant Ca^{2+} transients in 0 mM Ca^{2+} extracellular conditions in both DRG and TG sensory neurons (Kawaguchi et al., 2015, Shah, 2017). In extracellular Ca^{2+}-free conditions, perfusion with 250 nM BK was sufficient to evoke robust Fura-2 AM Ca^{2+} transients in a total of 29 out of 57 neurons (N = 3), representing approximately 50% of the total trigeminal sensory neuronal population (Figure 5.12E and F). The mean maximum R/R_0 value in response to BK was 3.58 ± 0.237, and the mean time to peak was 49.9 ± 3.23 seconds, significantly longer than what was observed for CGRP-evoked Ca^{2+} transients ($p < 0.0001$, Mann-Whitney test).

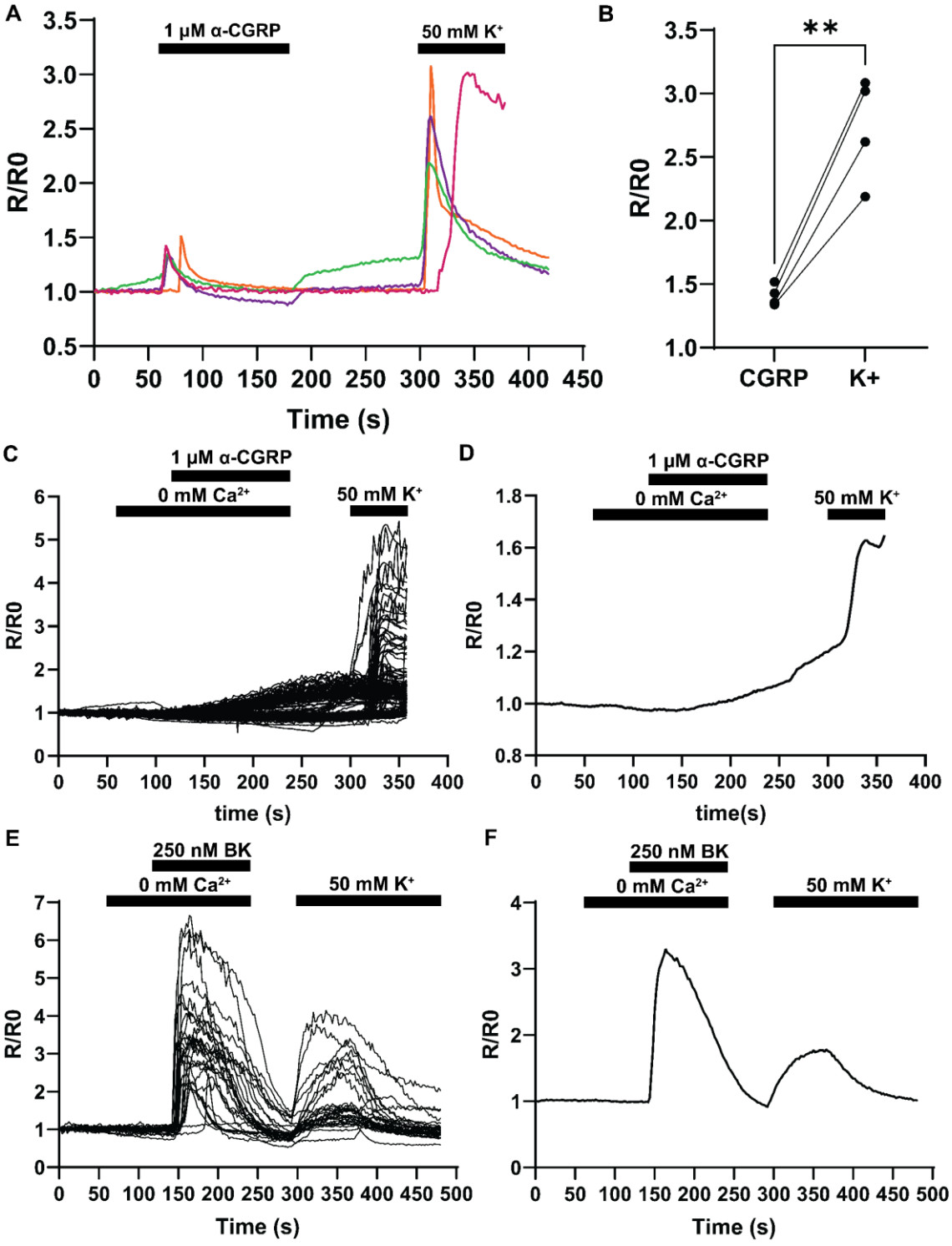

Figure 5.12: Ratiometric Fura-2 AM calcium imaging in primary cultured TG neurons. Continued on next page.

Figure 5.12: Ratiometric Fura-2 AM calcium imaging in primary cultured TG neurons. **A)** Bath application of 1 µM α-CGRP induced characteristic Ca^{2+} transients in 4 out of 98 (N = 5) primary cultured TG neurons prepared from neonatal rats (P1-7) loaded with the ratiometric Ca^{2+} indicator Fura-2 AM. Ca^{2+} response was measured as the ratio of fluorescence intensity with 340 nm excitation to 380 nm excitation and normalised to the value at t = 0 seconds. **B)** The mean Ca^{2+} response to 1 µM α-CGRP was significantly weaker than the response to a depolarising high (50 mM) K^+ stimulation (p = 0.0047, Wilcoxon matched-pairs signed rank test). **C)** Bath application of 1 µM α-CGRP under Ca^{2+}-free extracellular conditions did not induce a significant elevation of $[Ca^{2+}]_i$ in primary cultured TG neurons (n = 140, N = 5). **D)** Mean trace of all K^+-responsive TG neurons. **E)** Trigeminal ganglion neurons (50%, N = 3) showed robust Ca^{2+} transients in response to bath application of the inflammatory mediatory BK (250 nM) under Ca^{2+}-free extracellular conditions. **F)** Mean trace of all BK-responsive TG neurons. **p < 0.01. CGRP, calcitonin gene-related peptide; K^+, potassium cation; BK, bradykinin; Ca^{2+}, calcium cation.

5.2.7 Functional ANO1-TRPV1 Coupling May Potentiate CGRP Release from Small-Diameter Neurons in the Trigeminal Ganglion

Despite complementary co-localisation and PLA data suggestive of nanodomain proximity between the CaCC ANO1 and protein components of the canonical CGRP receptor, RAMP1 and CRLR, ratiometric in vitro Ca^{2+} imaging suggests stimulation of TG neurons with CGRP is insufficient to evoke the micromolar intracellular Ca^{2+} signals necessary for ANO1 activation and was unable to provide evidence for functional coupling between ANO1 and the CGRP receptor. On the other hand, PLA experiments support an alternative hypothesised role for ANO1 in the TG via functional coupling with TRPV1.

In small-diameter neurons of the TG, CAP-evoked CGRP release from TRPV1-expressing nociceptors is a well-established mechanism of trigeminal activation (Ulrich-Lai et al., 2001, Meng et al., 2009) and previous studies have demonstrated for TG neurons in vitro that non-selective inhibition of Ca^{2+}-activated Cl^- current activity is sufficient to significantly reduce the amplitude of CAP-evoked Ca^{2+} transients (Schöbel et al., 2012). Therefore, it stands to reason that a reduced Ca^{2+} signal will negatively impact Ca^{2+}-dependent exocytosis mechanisms, including SNARE-mediated exocytosis of large dense core vesicles (LDCVs) in which CGRP is stored (Meng et al., 2007).

In order to investigate this hypothesised contribution of ANO1 to CGRP release in the trigeminal system, several approaches were taken to quantify CGRP levels in primary sensory TG neurons following stimulation with CAP in the presence of the ANO1-selective inhibitor Ani9 (Seo et al., 2016). As a gold-standard approach, CAP-induced CGRP release was first measured by an ELISA as previously described (Pettinger et al., 2013). Primary TG cultures prepared from neonatal rats (N = 4) were maintained for 3 days *in vitro* prior to stimulation for 1 hour with 1 μM CAP alone or following pre-treatment for 30 minutes with the ANO1-selective inhibitor molecule, Ani9 (1 μM) (Seo et al., 2016). Protease inhibitor cocktail was included in all treatment solutions to prevent the degradation of CGRP peptide released into the extracellular space. Despite previous success, however, these results were not replicated as 1 μM CAP failed to significantly increase the amount of CGRP released from neurons compared to the control ($p = 0.665$, One-way ANOVA with Holm-Sidak's multiple comparisons tests) (Figure 5.13A, B). The mean baseline concentration of CGRP released from TG neurons at rest (normalised to total protein concentration) was 0.394 ± 0.134 pg/mL and this value was only slightly elevated for neurons treated with 1 μM CAP (0.808 ± 0.398 pg/mL). While pre-treatment with 1 μM Ani9 for 30 minutes did reduce mean CAP-induced CGRP release (0.277 ± 0.425 pg/mL), this was not significantly different compared to CAP alone ($p = 0.665$,

One-way ANOVA with Holm-Sidak's multiple comparisons tests), nor was the difference between the control and Ani9-treated conditions (p = 0.817, One-way ANOVA with Holm-Sidak's multiple comparisons tests).

The ELISA was repeated using an alternative *ex vivo* model of CGRP release in an effort to maximise neuron viability. This technique has been used successfully in the literature to demonstrate the effect of various pharmacological compounds on CAP-evoked CGRP release from the trigeminovascular system (Rasmussen et al., 2022). The left and right TG of neonatal rats (Control: N = 1; CAP and CAP + Ani9: N = 3) were dissected into standard growth media and allowed to acclimate at 37°C for 20 minutes prior to *ex vivo* stimulation with 1 μM CAP alone or following Ani9 (1 μM) pre-incubation as previous. Similarly, whole ganglia stimulation with 1 μM CAP failed to significantly increase the mean CGRP release into the bath solution compared to the control (p = 0.895, One-way ANOVA with Holm-Sidak's multiple comparisons tests) (Figure 5.13C, D). Although, one ganglion did appear to respond as expected to CAP stimulation with a CGRP concentration (normalised to dry weight of the ganglia) of 6.93 pg/mL, much greater than the overall mean for the group (3.32 ± 1.81 pg/mL). Pre-incubation with 1 μM Ani9 also did not significantly alter the concentration of CGRP release from the ex vivo TG preparation compared to the control group (p = 0.895, One-way ANOVA with Holm-Sidak's multiple comparisons tests): the mean normalised CGRP concentration released from ganglia pre-treated with Ani9 was 2.72 ± 0.252 pg/mL which was only slightly elevated compared to the control ganglia (1.55 pg/mL: due to limited availability of reagents only a single ganglia was used to measure baseline CGRP release).

Following the limited success with using ELISA to measure CAP-evoked CGRP release from trigeminal sensory neurons, an immunocytochemistry-based quantitative 'assay' was developed to quantify CGRP expression levels in trigeminal sensory neurons. Reports in the literature suggest immunostaining against CGRP can be successfully used to compare expression levels and localisation of the peptide in differentially treated tissue preparations. Stimulation of isolated sciatic nerve preparations with 1 μM CAP prior to fixation and immunostaining against CGRP revealed depletion of the peptide within axoplasmic vesicles of unmyelinated nerve fibres compared to untreated tissue (Bernardini et al., 2004). CGRP-like immunoreactivity has been quantified as a measure of integrated optical density in pulmonary neuroendocrine cells to demonstrate an upregulation of CGRP expression following chronic hypoxia (McBride et al., 1990). More recently, quantitative immunohistochemistry in the caudal trigeminal nucleus revealed significantly increased CGRP expression in response to acute treatment with an inflammatory cocktail (1 mM BK, 1 mM serotonin, 1 mM histamine and 0.1 mM prostaglandin in 10 mM HEPES buffer) at the dural surface compared to vehicle-treated

control tissue (Spekker et al., 2021). Therefore, while not as robust as ELISA-based quantification of CGRP release, quantitative analysis of immunostaining in fixed primary TG neuron cultures may reveal an effect of pharmacological intervention to CAP-evoked CGRP release.

Trigeminal neuron cultures (N = 3) were prepared on the same day from animals of the same age and cultures were maintained for 3 days *in vitro* prior to treatment with 1 μM CAP alone or following Ani9 (1 μM) pre-incubation as in the ELISA protocol. Fixed samples were co-immunostained with commercially available anti-CGRP and anti-ANO1 primary antibodies and confocal z stacks obtained alongside corresponding brightfield images which were used to identify neuronal ROIs based on the well-characterised morphology of primary cultured peripheral sensory neurons. Drug solutions, fixative, blocking buffer, and primary and secondary antibody dilutions were prepared as a single batch to treat all replicates identically and simultaneously to minimise the effects of intra-sample variability common with immunostaining experiments. Similarly, immunostained samples were visualised with confocal microscopy using identical settings and imaged within 24 hours of each other prior to identical post-processing, including background subtraction based on a secondary antibody-only negative control.

Figure 5.14 shows representative maximum intensity projections of ANO1 and CGRP immunoreactivity in control (Figure 5.14A), 1 μM CAP-treated (Figure 5.14B) and 1 μM Ani9 pre-treated (Figure 5.14C) trigeminal neurons. Due to the punctate nature of CGRP immunoreactivity observed in TG neuronal cultures, integrated density (ID) was taken as a more representative measure of immunofluorescence intensity. ID measures the sum fluorescence intensity for all pixels in the ROI, which, therefore, represents a more accurate measure of the amount of immunoreactive material per neuron in a heterogeneous population with respect to cell size. Neuronal size distribution analysis was performed to identify the target neuron sub-population (putative nociceptor C and Aδ neurons) and neurons were classified as either ANO1-positive, CGRP-positive or double-positive based on meeting a threshold 'Z score' set based on the mean ID calculated for ANO1- and CGRP-like immunoreactivity in the control neuronal sub-population with somatic diameters' equal to or less than 35 μm (see Chapter 2 for details). For both ANO1 and CGRP ID values, a Z score of at least 0.5 was deemed sufficient to distinguish between positive and negative neurons accurately. In order to investigate a hypothesised role for ANO1 in CAP-evoked CGRP release, it was necessary to identify neurons immunoreactive for both ANO1 and CGRP. Therefore, further analysis was restricted to this sub-population of double-positive trigeminal neurons.

A total population of 646 control neurons, 842 CAP-treated neurons, and 302 Ani9 pre-treated neurons were analysed. The respective mean somatic diameters for each treatment group were 14.2 ± 4.90 µm, 14.4 ± 4.51 µm and 15.0 ± 5.49 µm. The percentage of ANO1-positive, CGRP-positive and double-positive neurons identified in each treatment group is given in Table 5.1 and visualised in Figure 5.15A. There was no significant difference between treatment groups in the percentage of neurons classified as ANO1-positive ($p = 0.559$, Fisher's exact test), however, treatment with 1 µM CAP alone significantly reduced the percentage of neurons classified as CGRP-positive ($p = 0.0236$, Fisher's exact test) while pre-incubation with 1 µM Ani9 significantly increased the percentage of CGRP-positive neurons ($p = 0.0017$, Fisher's exact test). Accordingly, there was a highly significant difference in the percentages of CGRP-positive neurons treated with CAP alone and following Ani9 pre-treatment ($p < 0.0001$, Fisher's exact test). The percentage of neurons classified as significantly immunoreactive for both ANO1 and CGRP also was significantly decreased following exposure to 1 µM CAP ($p = 0.0448$, Fisher's exact test), although there was no difference between the control and Ani9 pre-treated groups ($p = 0.102$, Fisher's exact test).

Table 5.1: Percentages of the total trigeminal neuron population immunoreactive for ANO1, CGRP or both

	ANO1+	**CGRP+**	**Double+**
Control	24.5	20.3	14.1
1 µM CAP	22.4	15.7	10.6
1 µM CAP + 1 µM Ani9	24.8	29.8	18.2

The mean somatic diameter of double-positive neurons in TG cultures treated with either 1 µM CAP alone (20.64 ± 0.382 µm) or following pre-treatment with 1 µM Ani9 (22.4 ± 0.579 µm) did not significantly differ from that of control neurons (21.4 ± 0.410 µm) ($p = 0.340$ and $p > 1.00$), respectively; Kruskall-Wallis with Dunn's multiple comparisons tests), suggesting similar populations of neurons were compared within each treatment group (Figure 5.15B). Linear regression analysis revealed there was no significant correlation between somatic diameter and CGRP (slope = 0.0100, $p = 0.769$) or ANO1 (slope = 0.0279, $p = 0.299$) immunoreactivity in small-diameter trigeminal neurons (Figure 5.15C, D). Interestingly, although the mean percentage of ANO1-positive neurons did not differ between treatment conditions, pre-incubation with the ANO1 inhibitor Ani9 significantly increased the mean Z score for ANO1 immunoreactivity in double-positive neurons compared to both the control neurons ($p = 0.0004$, Kruskall-

Wallis with Dunn's multiple comparisons test) and neurons treated with CAP alone ($p = 0.0001$, Kruskall-Wallis with Dunn's multiple comparisons test).

Most relevant to consider, however, was the effect of treatment with CAP alone or following pre-incubation with the ANO1-selective inhibitor Ani9 on CGRP immunoreactivity in the population of ANO1- and CGRP-positive trigeminal neurons. As expected, exposure to 1 μM CAP significantly reduced the mean Z score for CGRP-like immunoreactive signal from 1.65 ± 0.131 in the control neuron population to 1.21 ± 0.0749 in the CAP-treated population ($p = 0.0455$, Kruskal-Wallis with Dunn's multiple comparisons tests) (Figure 5.15E). However, when trigeminal neuronal cultures were pre-incubated with the ANO1-selective inhibitor Ani9 (1 μM) prior to exposure to an equal concentration of CAP, this trend reversed, and the mean Z score for CGRP-immunoreactivity showed a significant increase compared to the control to 3.01 ± 0.419 ($p = 0.0055$, Kruskal-Wallis with Dunn's multiple comparisons tests). The difference in mean Z score for CGRP-like immunosignal between the CAP-treated neuronal sub-population and the Ani9-pre-treated sub-population was also found to be highly significant ($p < 0.0001$, Kruskal-Wallis with Dunn's multiple comparisons tests).

Overall, these data provide morphological evidence in support of a physiologically relevant functionality of ANO1 in CGRP-releasing small-diameter, putative nociceptor trigeminal neurons.

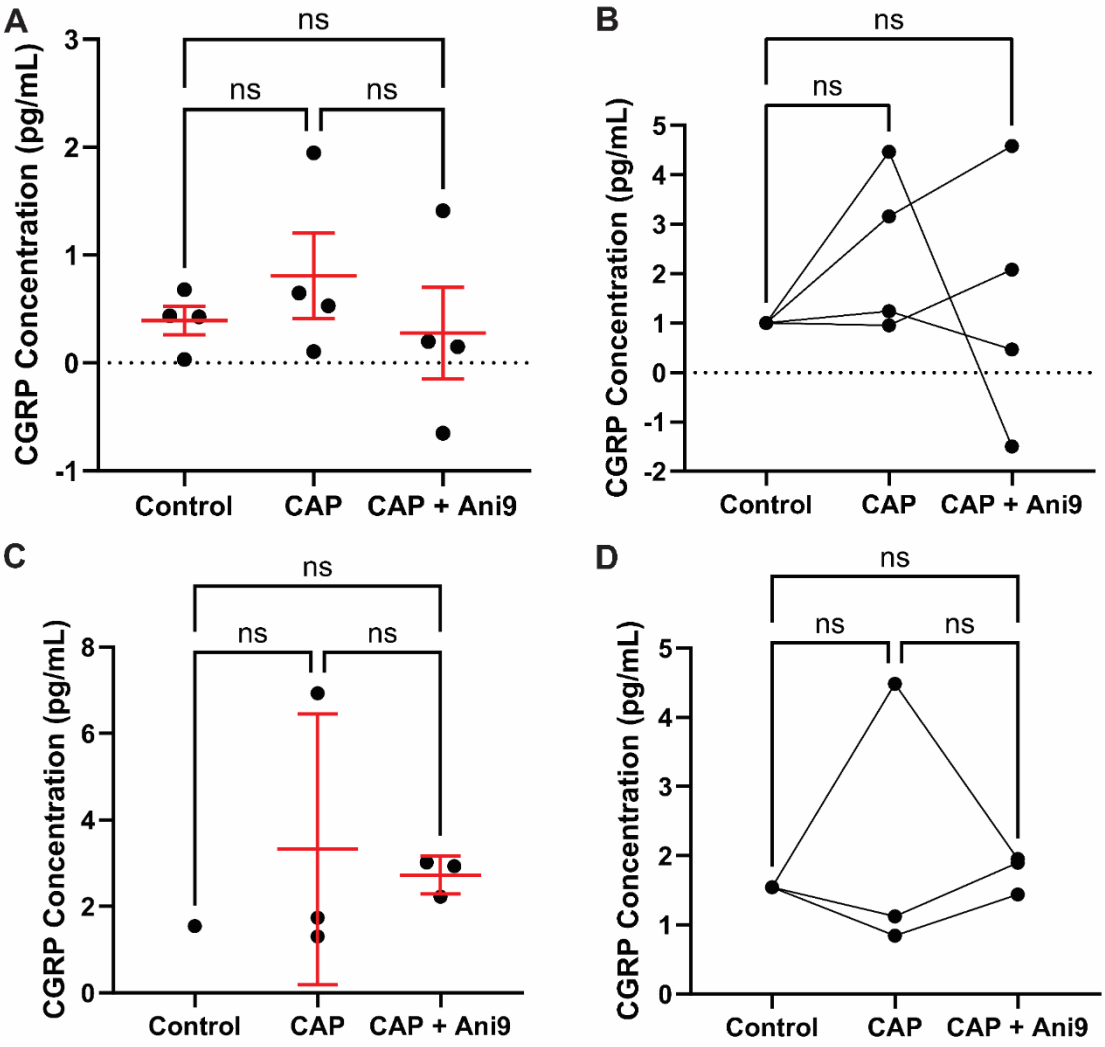

Figure 5.13: ELISA was not able to detect significant capsaicin-evoked CGRP release from in vitro or ex vivo trigeminal ganglion neuron preparations. CGRP release from TG neurons into the extracellular medium was measured using ELISA. Primary TG neuron cultures **(A** and **B)** or ex vivo dissected whole ganglia **(C** and **D)** were stimulated with 1 µM CAP alone in following pre-incubation with the ANO1-selective inhibitor molecule Ani9. CGRP concentration was normalised to total protein concentration **(A** and **B)** as measured by Micro BCA assay, or dry ganglia weight **(C** and **D)**. No significant differences in normalised CGRP concentration were observed between the control and treatment groups in either preparation (One-way ANOVA with Holm-Sidak's multiple comparisons tests). Error bars represent mean ± SD. ELISA, enzyme-linked immunosorbent assay; CAP, capsaicin; CGRP, calcitonin gene-related peptide; TG, trigeminal ganglion; BCA, biocinchoninic acid.

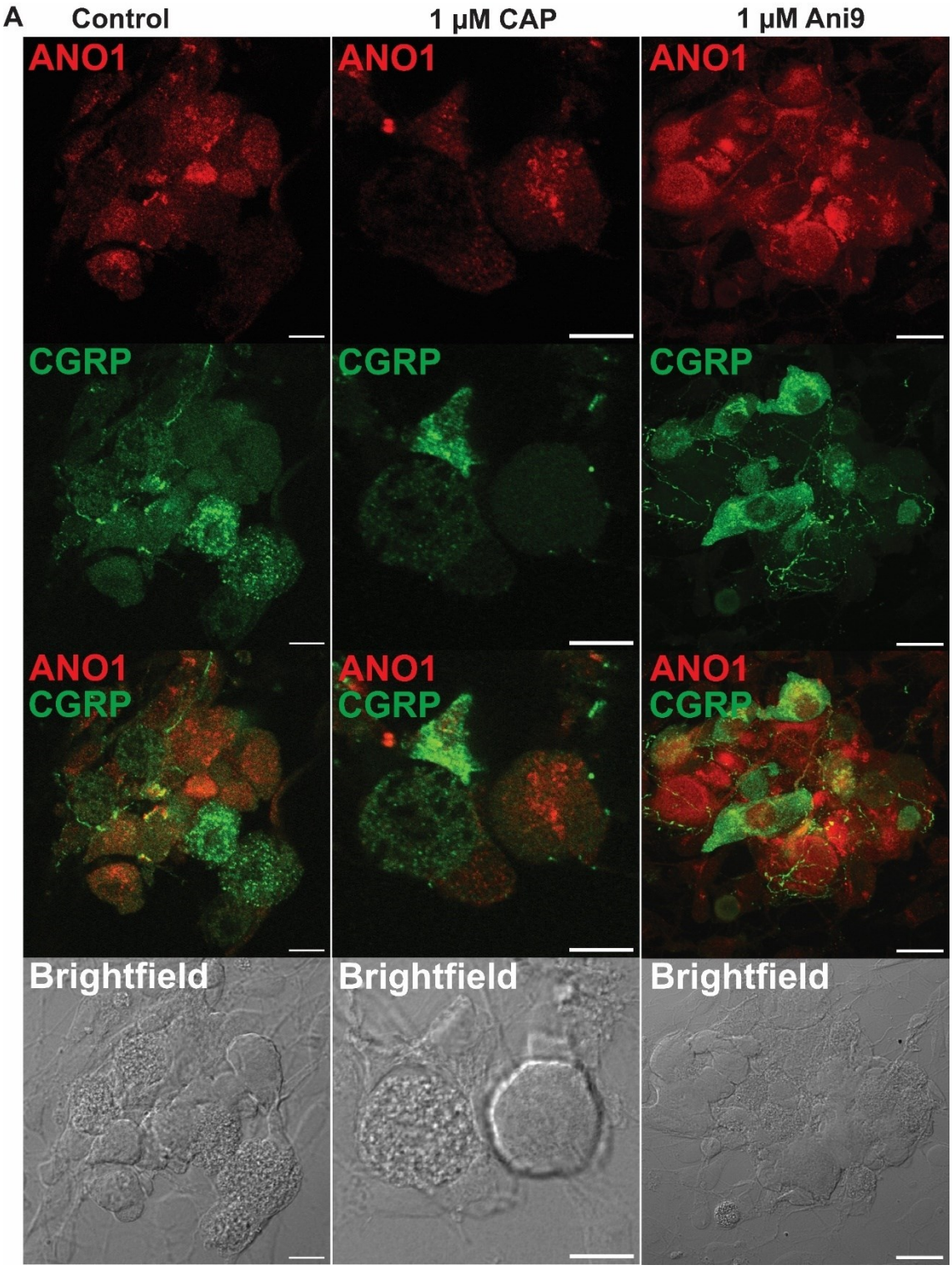

Figure 5.14: Immunocytochemistry of primary TG neuron cultures can detect significant treatment-dependent changes in CGRP levels in ANO1-immunoreactive neurons. Representative confocal micrographs depicting ANO1-like and CGRP-like immunoreactivity in primary neonate trigeminal neuron cultures. Neurons were fixed with 4% PFA at 3 days in vitro immediately following treatment with vehicle (left column), 1 µM CAP (middle column) or 1 µM CAP after pre-incubation with the ANO1-selective inhibitor molecule Ani9 (right column). The bottom row depicts the corresponding brightfield image of neuron cultures used to identify cellular ROIs. Scale bars = 10 µm. ANO1, anoctamin 1; CGRP, calcitonin gene-related peptide, CAP, capsaicin; ROI, region of interest.

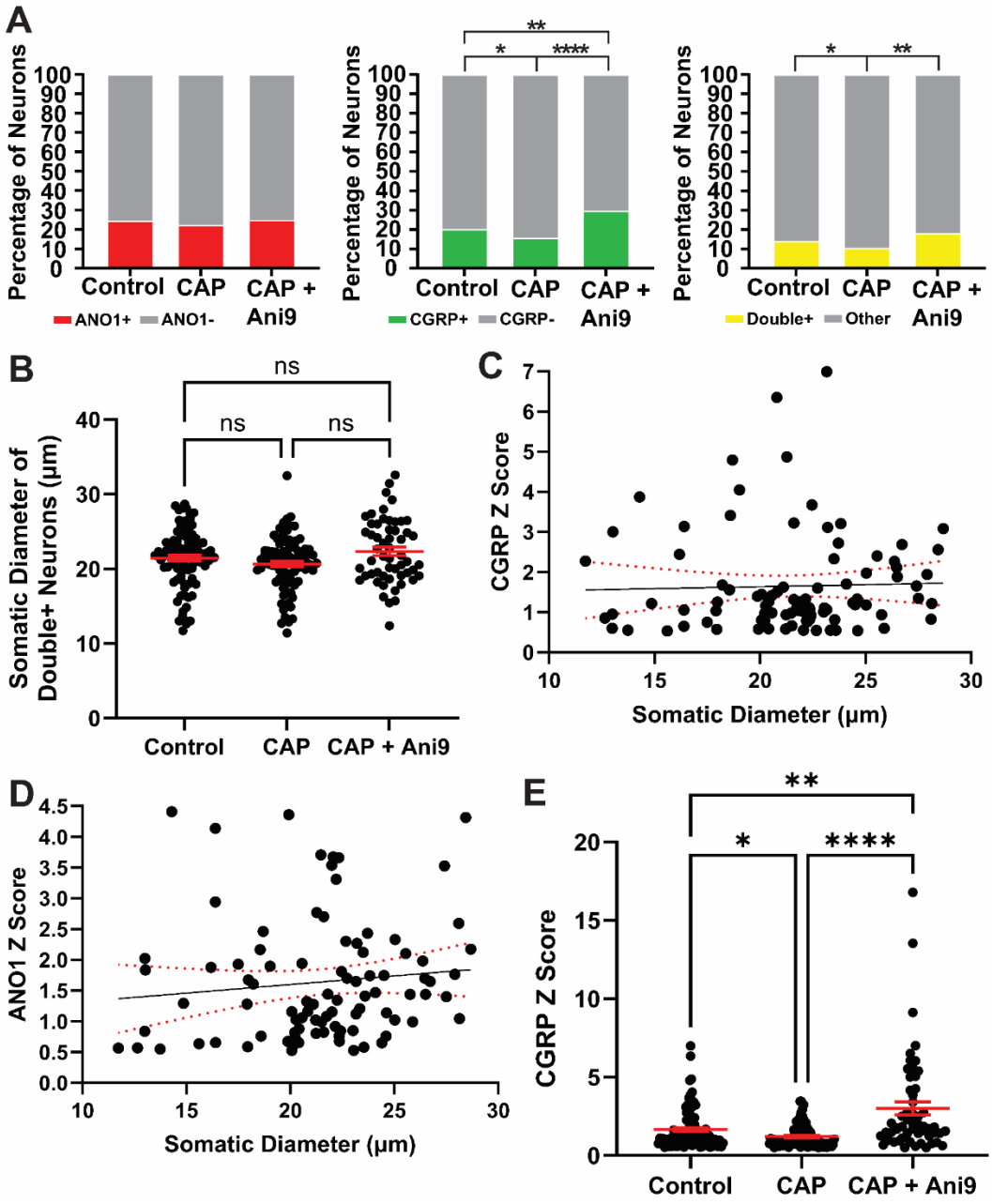

Figure 5.15: Pre-treatment with the ANO1-selective inhibitor Ani9 significantly attenuates capsaicin-evoked CGRP release in a sub-population of small-diameter TG neurons that co-express ANO1 and CGRP in vitro. **A)** Percentage of the total trigeminal neuronal population classified as significantly immunoreactive (Z score > 0.5) for ANO1 (red), CGRP (green) or both ANO1 and CGRP (yellow) (control, n = 646 neurons; CAP, n = 842 neurons; CAP + Ani9, n = 302 neurons; all conditions N = 3). **B)** Somatic diameters (µm) of trigeminal neurons classified as immunopositive for both ANO1 and CGRP in each of the experimental conditions. Z score for CGRP **(C)** and ANO1 **(D)** immunosignal in double-positive trigeminal neurons were plotted against somatic diameter for linear regression analysis. **E)** CGRP Z score for double-positive trigeminal neurons in each of the three experimental conditions. Significant differences were observed between the control and CAP-treated neurons ($p = 0.0455$), control and Ani9 pre-treated neurons ($p = 0.0055$) and between neurons treated with CAP alone or following Ani9 pre-treatment ($p < 0.0001$) (Kruskall-Wallis with Dunn's multiple comparisons tests). Error bars (red dotted lines) represent the 95% confidence intervals of the linear regression best-fit (C and D) or the mean ± SD (B and E). *$p < 0.05$, **$p < 0.01$, ****$p < 0.0001$. ANO1, anoctamin 1; ANO1+, ANO1-positive; CGRP, calcitonin gene-related peptide; CGRP+, CGRP-positive; CAP, capsaicin; TG, trigeminal ganglion.

5.3 Discussion

To date, ANO1-containing JMSCs have only been experimentally confirmed in DRG sensory neurons. Therefore, this thesis chapter sought to investigate ANO1 expression in TG nociceptive neurons and a potential mechanism of functional ANO1 coupling to trigeminal-specific nociceptive Ca^{2+} signals, including those necessary in the CGRP signalling cascade.

5.3.1 ANO1 Immunoreactivity in the Trigeminal System

Scattered reports in the literature provide limited immunohistochemical evidence of ANO1 protein expression in TG neurons. However, no comprehensive characterisation of this expression throughout the TG has been published at the time of writing. Several earlier studies have specifically failed to observe ANO1 immunoreactivity in trigeminal fibres innervating the nasal cavity, which originate from the V2 maxillary division of the TG (Dauner et al., 2012). It may be the case that ANO1 expression is confined to either the V1 (ophthalmic) or V3 (mandibular) divisions; indeed, both Kanazawa and Matsumoto (2014) and Suzuki et al. (2016) identified significant ANO1 immunoreactivity in the mandibular division of the TG in rats and mice. In the present study, sections for IHC analysis were obtained from all three divisions of the TG and neurons were analysed indiscriminately; however, at least some ANO1-immunopositive neurons were identified in every section, suggesting ANO1 may not show preferential distribution to any trigeminal division.

Immunohistochemistry revealed strong and specific ANO1-like immunoreactivity in soma-rich and fibre-rich regions of the TG. In the rat, nearly 90% of TG neurons are small-to-medium-diameter neurons with soma size ranging from 15-35 um (Messlinger and Russo, 2019, Ambalavanar and Morris, 1992). Therefore, it is unsurprising that such a large percentage of ANO1-immunoreactive neuron somas in the TG had diameters less than 35 μm (86.2%), considering ANO1's preferential expression in nociceptive neuronal subtypes in the DRG (Jin et al., 2013). Interestingly, however, ANO1 immunoreactivity in trigeminal afferent fibres appeared biased towards nerve fibres with diameters similar to NF200-positive nerve fibres, with only some limited colocalisation with peripherin-positive fibres. Although in the rodent DRG, there is clear differential expression of NF200 and peripherin to large-diameter and small-diameter neurons, respectively, with minimal overlap, such distinctions are less apparent among TG neurons. Comprehensive distribution analysis of trigeminal nerve fibres positive for common immunohistochemical markers revealed that while the majority of TG nerve fibres that were NF200-immunoreactive were myelinated, a significant percentage (23.9%) of such fibres were small, unmyelinated C-type fibres (Bae et al., 2015).

Conversely, Bae et al. found 15.5% of peripherin-positive fibres to be large myelinated Aβ-type fibres with diameters greater than 5 μm. These findings blur the lines on the traditional categorisation of sensory neurons into C and A subtypes based on their fibre diameter and certainly their expression of neurofilament markers including NF200 and peripherin, suggesting that in the TG, they may not be as reliable a marker for myelinated A- and unmyelinated C-fibres. Considering this, that ANO1 expression appears greater in trigeminal nerve fibres of the same size as NF200-positive fibres does not exclude ANO1 from a role in nociception in the TG.

In summary, neuronal size distribution analysis of ANO1 immunoreactive neurons supports the protein expression of ANO1 in small-diameter, putative nociceptive neurons of the TG. However, considering immunohistochemistry measures total protein content within this cell, this may not be representative of functional ANO1 channel expression at the PM. Indeed, immunosignal was detected throughout the cytoplasm in fixed tissue sections and primary trigeminal neuron cultures, likely representing ANO1 peptide in the ER, Golgi or trafficking vesicles. A simple alternative approach to investigate solely PM-inserted ANO1 could include the use of a primary antibody raised against an extracellular portion of the ANO1 protein. Combined without the use of permeabilising detergents such as TWEEN® 20 and Triton™ X-100 to prevent primary and secondary antibody entry into the cell, any resulting immunosignal should be confined to, putatively, functionally membrane-inserted ANO1 expression.

5.3.2 Alternative Splicing of ANO1 mRNA Gives Rise to Multiple Immunoreactive Bands Revealed by Western Blot Analysis

Alternative splicing is an important mechanism governing the modulation of both Ca^{2+} and voltage activation of ANO1 such that the inclusion or exclusion of particular exons in the mRNA transcript influences the physiological properties of ANO1 isoforms as differentially expressed Cl^- channels (Caputo et al., 2008). The differing prevalence of splice alternatives is likely responsible for the multiple ANO1-immunoreactive band sizes observed following western blot analysis of electrophoresed whole TG, dura mater and liver lysates. One such described splice variant in the mouse and human involves the exclusion of exon 18 (encoding the fifth transmembrane domain of ANO1). The exclusion of exon 18 results in a C-terminus truncation of the full protein from 956 amino acids to 596 amino acids due to a frame shift at I563, yielding a protein product of around 60 to 75 kDa (O'Driscoll et al., 2011). This is consistent with the approximately 75 kDa-sized ANO1 immunoreactive band observed in whole TG lysate, while the larger bands observed in dura mater and the liver lysates between 100 and 150 kDa more likely represent the full length ANO1 protein with an expected size of 114 kDa. Given that the

rat TMEM16A gene typically shares high homology with the mouse and human genes (Ayon et al., 2019, Yang et al., 2008), it is likely that such exon 18 exclusion splice variants occur in rat tissue as well, although this has not yet been experimentally confirmed.

It is not known for certain whether the exon 18 exclusion produces a functional truncated ANO1 variant, although prior studies have also identified approximately 75-85 kDa-sized ANO1-immunoreactive bands following western blot analysis of isolated cell lysates including smooth muscle cells from the murine hepatic portal vein (Davis et al., 2010) and guinea pig distal colonic epithelial cells (He et al., 2011). Indeed, functional ANO1 expression has been confirmed in murine portal vein smooth muscle cells (Kawata et al., 2022), suggesting that the exon 18 exclusion splice variant may produce a minimally functional ANO1 Cl^- channel.

5.3.3 Proximity Ligation Assay Reveals Noxious Stimuli-Induced Modulation of ANO1 Nanodomain Proximity to Putative Functional Partners in Small-Diameter Trigeminal Ganglion Neurons

Paramount to characterising ANO1-mediated nociceptive signalling mechanisms in the DRG was the use of PLA, enabling the sensitive detection of protein-protein interactions within a nanodomain scale (40 nm) (Söderberg et al., 2006, Söderberg et al., 2008, Weibrecht et al., 2010).

Given that the TG can be considered the cranial analogue to the DRG, it is not unsurprising that, indeed, a robust PLA signal was detected between ANO1 and its primary interactor, IP_3R1, exclusively in small-diameter (< 35 µm) TG neurons. Interestingly, this interaction was shown to respond dynamically to noxious stimuli: application of 1 µM CAP significantly increased the mean number of puncta per neuron for PLA between ANO1 and IP_3R1. Considering PLA detects discrete instances of protein pairs found within 40 nm, an increase in the number of puncta reflects an increase in the number of nanodomain interactions between ANO1 and IP_3R1. Such an outcome is likely to have a physiological impact considering current will be proportional to the number of active ion channels (up to the limiting factor of ion concentration on either side of the membrane): the greater the number of active ANO1 channels, the greater the Cl^- efflux from the neuron, the greater the membrane depolarisation and therefore, the more likely the neuron is to fire an action potential. As described for DRG nociceptive neurons in the previous chapter, this increase in proximity between ANO1 and IP_3R1 is also likely mediated by a Ca^{2+}-dependent translocation of the ER towards the PM, facilitating direct interaction between the two proteins.

PLA also revealed a sub-population of TG neurons with localised nanodomain proximity between ANO1 and TRPV1 that increased in response to CAP treatment, further supporting a hypothesised role for ANO1 in mediating amplification of nociception in small-diameter trigeminal neurons. This data is therefore the first example of dynamic nanodomain interactions for ANO1 in TG sensory neurons. To indisputably confirm the existence of ANO1-IP_3R1-TRPV1 multiprotein signalling complexes in the trigeminal system, however, it would be paramount to also confirm nanodomain proximity between TRPV1 and IP_3R1.Further evidence in support of a triple interaction between ANO1-IP_3R1-TRPV1 would be obtained through the use of a three-colour super-resolution microscopy approach, such as 3D stochastic optical reconstruction microscopy (STORM) as was performed in DRG sensory neurons (Shah et al., 2020).

In addition to known ANO1 interacting partners, this thesis sought to investigate multiple scenarios through which ANO1 activation may modulate mechanisms underlying trigeminal-specific signalling pathways, in particular, that of the major signalling neuropeptide, CGRP. Data presented in this thesis supports protein expression of ANO1 in both small-diameter C fibre and medium-diameter Aδ fibre neurons, laying the groundwork for multiple scenarios in which ANO1 modulation could function in CGRP-releasing (typically small-diameter) or CGRP-responding (typically medium-diameter) trigeminal neurons.

In Aδ neurons, heterodimerization of CRLR and RAMP1 protein components produces a high-affinity receptor for CGRP known to couple to G_q protein signalling pathways. Notably, PLA here identified significant nanodomain proximity between ANO1 and both RAMP1 and CRLR, and between IP_3R1 and CRLR in trigeminal sensory neurons. This novel finding offers strong support for a hypothesised functional coupling between ANO1 and the canonical CGRP receptor, opening up speculation that ANO1 may serve as an amplifier of any such signalling pathway culminating in the release of IP_3-sensitive Ca^{2+} stores, not only those downstream of the B2R G_qPCR and TRPV1. Similar to that observed between ANO1 and TRPV1 following CAP exposure, stimulation of TG neurons with 1 μM CGRP also significantly increased the number of PLA puncta per neuron between ANO1 and RAMP1 specifically in neurons whose diameter corresponded with the expected size for CGRP receptor-expressing Aδ neurons. Intriguingly, the converse was true for PLA signal between either ANO1 or IP_3R1 and CRLR; upon stimulation with CGRP, the mean number of PLA puncta per neuron showed a significant reduction, which would reflect a *loss* of proximity between ANO1-IP_3R1 complexes and the CGRP receptor.

This observation could be accounted for due to a dynamic stimulus-dependent rearrangement of ANO1-IP_3R1 complexes with respect to RAMP1/CRLR complexes or conformational changes to the CGRP receptor with ligand binding such that the respective primary antibodies are no longer within a 40 nm orientation necessary for PLA. Alternatively, this loss of interacting pairs may be the result of CGRP receptor internalisation, a well-documented phenomenon that occurs following CGRP binding (Gingell et al., 2020, Rees et al., 2020). This scenario, however, would not explain the increased PLA signal between ANO1 and RAMP1 following CGRP exposure.

Although dimerization of RAMP1 with CRLR confers the canonical CGRP receptor, a secondary CGRP-sensitive GPCR is formed by dimerization of RAMP1 with the calcitonin receptor (CTR) (Gingell et al., 2020). Known also as the amylin 1 (AMY1) receptor due to its affinity for the pancreatic peptide hormone amylin, this non-canonical CGRP receptor has been shown to be expressed in isolated rat TG neurons (Walker et al., 2015). AMY1 undergoes significantly less agonist-mediated internalisation, therefore, perhaps ANO1 functionally couples to AMY1, reflected in the increased proximity between ANO1 and RAMP1, rather than the canonical CGRP receptor, as suggested by the reduced proximity to CRLR, during CGRP stimulation. This highlights an intriguing question of whether ANO1 could be activated by amylin, particularly given amylin has demonstrated potency for intracellular Ca^{2+} mobilisation via affinity for RAMP1/CTR AMY1 receptors (Morfis et al., 2008). Interestingly, a recent in-depth immunohistochemical characterisation of AMY1 expression in the rat TG demonstrated colocalisation of CGRP-like and CTR-like immunoreactivity in small-to-medium-diameter C fibre neurons, which agrees well with the immunohistochemical characterisation of ANO1 expression presented in this thesis supporting a role for ANO1 in both CGRP-releasing and CGRP-responding neurons (Rees et al., 2022).

5.3.4 Does CGRP Evoke Mobilisation of Intracellular Ca^{2+} Stores in Trigeminal Ganglion Sensory Neurons?

Although it is commonly recited that canonical CGRP receptors are known to couple to G_q protein signalling cascades, there is limited evidence in the literature describing the ability of CGRP to evoke mobilisation of intracellular ER Ca^{2+} stores in peripheral sensory neurons. Furthermore, while immunohistochemical studies estimate the RAMP1/CRLR receptor is expressed in up to 32% of TG neurons (Lennerz et al., 2008), much smaller populations appear to respond to CGRP. This is likely due to the CGRP receptor's preferential coupling to G_s signalling pathways over G_q. An early study demonstrated significant Fluo-3 AM Ca^{2+} transients in approximately 20% of primary cultured DRG neurons following bath application of 1 μM CGRP (Segond von Banchet et al., 2002).

Pre-treatment with the Ca^{2+}-ATPase inhibitor thapsigargin to deplete ER Ca^{2+} stores or application of CGRP under Ca^{2+}-free extracellular conditions significantly attenuated CGRP-evoked Ca^{2+} transients, leading the authors to propose a mechanism of Ca^{2+}-induced Ca^{2+} release. Similarly, more recent evidence describes only “very few” TG neurons from female mice to show a significant Fura-2 Ca^{2+} transient in response to application of 1 μM CGRP (Guo et al., 2021). Earlier Ca^{2+} imaging studies similarly showed that cultured TG neurons failed to respond to acute application of 1 μM CGRP (Ceruti et al., 2011), or else only a small subset responded with a Ca^{2+} transient approximately 5% of the amplitude of response to high K^+ challenge (Fabbretti et al., 2006). For the Fura-2 AM Ca^{2+} imaging experiments described in this thesis, a CGRP concentration of 1 μM was used; therefore, perhaps it is not surprising that only 4% of neurons demonstrated a significant, albeit small, Ca^{2+} response.

The mean time to peak response observed was in concurrence with that described by Guo et al. (2021) (between 10 – 30 seconds), suggesting the few CGRP-evoked Ca^{2+} transients measured here were true responses. Furthermore, the mean peak R/R_0 measures were not dissimilar. Nonetheless, collating evidence from the literature and experiments described herein, it may be unlikely that CGRP is capable of inducing sufficiently high-concentration Ca^{2+} signals such as are necessary for ANO1 activation, particularly given that physiological CGRP concentrations rarely exceed 100 pM during a migraine attack (Goadsby et al., 1990). Hence it may be unlikely that ANO1-IP_3R1 nanodomain complexes meaningfully associate with the canonical CGRP receptor in the context of trigeminal activation.

5.3.5 ANO1-TRPV1 Coupling in Small-Diameter Trigeminal Ganglion Neurons is Necessary for CGRP Release

Having confirmed protein expression of ANO1 in a subpopulation of small and medium-diameter TG neurons, this thesis proposed two alternate hypothesised mechanisms through which ANO1 may functionally modulate CGRP signalling pathways acting at CGRP-releasing or CGRP-responding trigeminal neurons. Building on promising PLA data supporting CGRP-evoked nanodomain proximity between ANO1 and the canonical CGRP receptor subunit RAMP1, fluorescent Ca^{2+} imaging was performed to establish if acute CGRP application is capable of evoking release of micromolar IP_3-sensitive Ca^{2+} signals downstream of G_qPCR activation. In the current model, 1 μM CGRP was unable to elicit intracellular Ca^{2+} release, suggesting it was unlikely ANO1 would be activated downstream in CGRP-responding neurons. Alternatively, PLA confirmed CAP-sensitive nanodomain proximity between ANO1 with IP_3R1 and TRPV1. CAP-evoked CGRP release is a well-established measure of trigeminal neuron activation (Ulrich-Lai et al.,

2001), therefore, an immunocytochemistry-based CGRP assay was devised to measure the ability of CAP to induce CGRP release from cultured TG neurons in the presence of an ANO1-selective inhibitor, Ani9.

In small-diameter DRG nociceptive neurons, functional coupling between ANO1, IP_3R1 and TRPV1 at junctional signalling nanodomains is a well-characterised mechanism underlying ANO1-mediated amplification of CAP or noxious heat-evoked neuronal membrane depolarization. In this scenario, membrane depolarisation results from simultaneous Ca^{2+} and Na^{+} influx via TRPV1, and Cl^{-} efflux via ANO1. Importantly, TRPV1-associated membrane depolarisation leads to the activation of N-type VGCCs (Castro-Junior et al., 2013), Ca^{2+} influx through which has been linked to Ca^{2+}-sensitive exocytosis of CGRP-containing large dense core vesicles in the TG and trigeminal afferents innervating the dura mater (Amrutkar et al., 2011). Subsequently, it could be argued that ANO1-mediated amplification of membrane depolarisation promotes greater CGRP release.

Indeed, novel experimental evidence presented in this thesis confirms that antagonist inhibition of ANO1 activation results in a significant attenuation of CGRP release from cultured TG neurons that show immunoreactivity for both ANO1 and CGRP. TG neurons were treated with 1 μM CAP alone as a positive control, and as expected, acute stimulation with CAP significantly reduced the mean Z score for CGRP-like immunoreactivity in double-positive neurons. This measurement relates to the protein expression level, such that a higher Z score is indicative of greater intensity of immunosignal, which in turn is indicative of a greater concentration of immunoreactive material in the sample: a larger Z score is equivalent to a greater amount of CGRP present in the neuron. This is confirmed as stimulation of TG cultures with 1 μm CAP significantly reduced the mean Z score for CGRP immunoreactivity compared to the control, consistent with well-described mechanisms of CAP-evoked CGRP release. In this case, a higher degree of CGRP exocytosis from the cell subsequently leaves less immunoreactive CGRP within the cell. This also explains the significant reduction in the percentage of neurons classified as CGRP-positive following CAP stimulation, such that some cells may have depleted their CGRP stores and no longer contain sufficient immunoreactive peptides to classify as CGRP-positive according to the Z score analysis.

Most intriguingly, however, when trigeminal neuron cultures were pre-treated with the ANO1-selective inhibitor Ani9, the mean CGRP immunoreactivity was significantly elevated compared to the control, which may suggest a build-up of CGRP in large dense core vesicle stores within the cytoplasm. This raises the possibility that not only does ANO1-mediated neuronal depolarisation significantly contribute to CGRP release, but it

is essential for this mechanism. It is also likely that the described ANO1-TRPV1 functional coupling contributes directly to the peripheral sensitization described as a mechanism as headache in many trigeminal pain disorders, including migraine. Furthermore, inflammatory mediators including BK are known to be upregulated in the cerebrospinal fluid of chronic migraineurs, where they contribute to neurogenic inflammation and sensitisation. While not investigated in this thesis, functional coupling of ANO1 to B2R in trigeminal neurons could additionally contribute to inflammation-induced trigeminal hypersensitivity and as such pharmacological interventions to silence ANO1 or to disrupt junctional signalling in TG neurones may prove a possible treatment option to alleviate migraine-associated headache and other trigeminal neuralgic disorders. Therefore, greater understanding of the molecular mechanisms governing JMSC formation in primary sensory neurones is required to uncover novel therapeutic targets.

5.3.5 Conclusion

To summarise, the experiments described in this chapter support a putative functional role for ANO1 in small-diameter nociceptive neurons of the TG. Immunohistochemical analysis of fixed TG tissue samples and of primary dissociated trigeminal neuron cultures confirm the expression of ANO1 protein within sub-populations of small and medium-diameter neurons that also demonstrate immunoreactivity for IP_3R1, TRPV1, CGRP and RAMP1. PLA has confirmed nanodomain co-localisation of ANO1 with IP_3R1, TRPV1, and protein subunits of the canonical CGRP receptor. Although a hypothesised functional coupling of ANO1 to CGRP-evoked signalling pathways in medium-diameter TG neurons was not fully supported, morphological evidence suggests ANO1 functionality may be critical to the physiological release of CGRP in small-diameter C-fibre neurons. Release of CGRP from TG neurons and afferent nerve fibres is a well-characterised mechanism thought to be involved in the pathophysiological development of the headache component of migraine and other trigeminal pain disorders, therefore, ANO1 in the trigeminal system may pose a novel putative therapeutic target to attenuate CGRP-induced trigeminal sensitization.

Chapter 6: Discussion

In small-diameter neurons of the DRG, the CaCC ANO1 serves as a molecular amplifier of nociception via functional coupling to IP_3-sensitive release of intracellular ER Ca^{2+} stores from IP_3R1 (Jin et al., 2013, Liu et al., 2010). To date, experimental work towards uncovering the molecular mechanisms governing ANO1-mediated signalling in nociceptive neurons has been limited to the DRG where ANO1 has been shown to modulate both BK-induced inflammatory nociception via coupling to B2R and CAP-induced nociception via coupling to TRPV1 (Jin et al., 2016, Jin et al., 2013, Shah et al., 2020). Therefore, the question remains as to what extent ANO1 might be considered a generalised molecular mechanism for the amplification of other nociceptive signalling pathways or whether these established roles for ANO1 are conserved between peripheral sensory ganglia innervating other regions of the mammalian body. Further, prior work investigating ANO1 signalling complexes has only directly visualised nanoscale colocalisation between ANO1, IP_3R1 and B2R or TRPV1 through various antibody-based microscopy techniques in non-stimulated DRG neurons while ANO1 coupling to nociception has been inferred through functional in vitro imaging experiments; therefore, ANO1 nanodomains have been considered as static functional couplings. This thesis extends the characterization of the cellular ANO1 'interactome' to the trigeminal system and demonstrates for the first time that ANO1 nanodomain signalling complexes are, in fact, dynamically modulated by the nociceptive Ca^{2+} stimuli to which they are coupled, and that this mechanism is likely conserved across different nociceptive ganglia. Furthermore, this thesis presents novel evidence to support a hypothesised role for the ER-PM tether protein Esyt1 as a putative modulator of ANO1-IP_3R1 JMSC functionality in the DRG.

6.1 Novel Findings

6.1.1 ANO1 is Expressed in the Trigeminal Ganglion and Colocalises with IP_3R1

ANO1 is expressed by both excitable and non-excitable cell types, contributing to an impressive range of physiological functions from ion transport and fluid secretion to modulating electrical activity and muscle contraction (Dulin, 2020). Given the intrinsically low Ca^{2+} sensitivity of ANO1, it is unsurprising that functional coupling between ANO1 and highly localised, high-concentration Ca^{2+} release from intracellular stores is a generally well-conserved mechanism for ANO1 activation in both excitable and non-excitable cell types. Indeed, ANO1-mediated CaCCs have been observed downstream of IP_3-mediated Ca^{2+} release from the ER not only in DRG sensory neurons (Liu et al., 2010), but also in auditory spiral ganglion neurons (Zhang et al., 2015), pancreatic acinar cells (Wang et al., 2020), pulmonary arterial smooth muscle cells (Akin et al., 2023), and

the interstitial cells of Cajal (Zhu et al., 2015, Drumm et al., 2022). Therefore, given the well-established mechanism for functional coupling between ANO1 and IP_3R1, particularly in DRG sensory neurons (Jin et al., 2013, Shah et al., 2020), there is a surprising lack of interest in the literature to investigate whether this mechanism may be conserved in the cranial analogue to the DRG, the TG. While the DRG consists of primarily cutaneous nociceptive neurons innervating the body, TG sensory neurons provide sensory innervation to the intra- and extracranial structures of the head and neck (Darian-Smith, 1973). A considerable amount of recent single-cell transcriptomic data supports the expression of ANO1 in rodent TG neurons at the mRNA transcript level (Chu et al., 2023, Yang et al., 2022, Bhuiyan et al., 2024). Yet, the only available data towards confirmed protein expression of ANO1 in the TG has been limited to immunohistochemical characterisation of ANO1 co-expression with TRPV1 in a sub-population of TG neurons as weak evidence for functional coupling (Kanazawa and Matsumoto, 2014), although CAP-induced CaCCs *are* reported in TG neurons (Schöbel et al., 2012).

The experimental evidence described in the current thesis, therefore, represents the first attempt to describe nanodomain coupling between ANO1 and IP_3R1 in TG neurons and provides further evidence to support ANO1 protein expression in the TG and trigeminally innervated tissues. In Chapter 5, PLA was performed between ANO1 and IP_3R1 in primary TG neuronal cultures and indeed, a positive signal was identified exclusively in small-diameter (< 35 µm) neurons, representing discrete instances of at least 40 nm proximity between ANO1 and IP_3R1. This result was well-supported by quantitative colocalisation analysis of ANO1 and IP_3R1 immunoreactivity in TG neurons *in situ* (immunohistochemistry of fixed transverse tissue sections), where significantly greater colocalisation was observed in smaller-diameter compared to larger-diameter neurons. Unfortunately, due to technical limitations, further experimental work to confirm the functional coupling of ANO1 to IP_3-mediated Ca^{2+} signals in live TG neurons could not be completed. Therefore, the evidence presented here should be accepted as preliminary. However, it supports the hypothesis that canonical ANO1-IP_3R1 signalling nanodomains are a conserved molecular mechanism of nociceptive amplification across various somatosensory ganglia.

6.1.2 ANO1-IP_3R1 JMSCs in Peripheral Nociceptors are Dynamically Modulated

The compartmentalisation of specific signalling pathways into distinct nanodomains is an important mechanism by which Ca^{2+} signals are selectively localised, enabling precise spatial and temporal regulation of nociception (Berridge, 2006, Berridge, 1998). Functional coupling between PM-localised ANO1 and IP_3R1 at the ER in DRG

nociceptors is achieved via physical tethering of the ANO1 α2/3 loop and C-terminus to one or more undefined regions of IP_3R1 (Jin et al., 2013); therefore, close apposition of the ER and PM is essential to facilitate this interaction. Extensive ER-PM contact sites are present in peripheral sensory neurons at rest, covering up to 10% of the PM at the soma (Chen et al., 2019, Wu et al., 2017). Subsequently, these structures likely account for the previously documented nanodomain proximity between ANO1 and IP_3R1 observed using PLA and super-resolution STORM imaging in primary cultured DRG neurons at rest (Jin et al., 2013, Shah et al., 2020). However, activity-dependent expansion of ER-PM contact sites has also been well-documented in excitable cells, and this phenomenon is coupled to the recruitment of known junctional tether proteins, including JPHs and STIM-Orai JMSCs to ER-PM junctions (Yang et al., 2024, Gruszczynska-Biegala and Kuznicki, 2013, Zamponi et al., 2022). Therefore, it was logical to hypothesise that ANO1-IP_3R1 JMSCs may be similarly recruited at ER-PM contact sites in DRG neurons in response to noxious stimulation.

Indeed, this thesis presented novel evidence to that effect, demonstrating for the first time activity-dependent recruitment of ANO1-IP_3R1 JMSCs in peripheral sensory neurons. In primary cultured DRG neurons, quantitative analysis of PLA demonstrated that noxious stimulation with the inflammatory mediator BK was sufficient to significantly increase the number of nanodomain interactions between ANO1 and IP_3R1 compared to the control. Furthermore, this effect persisted when neurons were treated with BK in a Ca^{2+}-free extracellular environment, demonstrating ANO1-IP_3R1 JMSC interactions that are dependent on the release of intracellular ER Ca^{2+} stores mobilised via the BK-induced activation of G_q protein signalling cascades. Most interestingly, when DRG neurons were stimulated with BK for a progressively increasing duration of time, the resulting PLA 'time-course' very closely matched the kinetics of BK-induced mobilisation of PIP_2 and intracellular Ca^{2+} release (Jin et al., 2013, Liu et al., 2010), further evidencing that the release of intracellular Ca^{2+} facilitates ANO1-IP_3R1 nanodomain interaction via an as-yet-undetermined mechanism. While this increase in PLA signal may reflect the formation of *de novo* ANO1-IP_3R1 JMSCs, an alternate explanation is that ANO1 and IP_3R1 proteins are already present at ER-PM junctions and primed for interaction but are expressed at just over the 40 nm sensitivity for PLA to detect. Therefore, upon noxious stimulation, ANO1-IP_3R1 'pre-interactions' are tightened by intracellular Ca^{2+} release, thus gaining sufficient proximity for detection via PLA. Given that functional coupling between ANO1 and IP_3R1 occurs via their direct binding, ANO1 at ER-PM junctions is likely to already be within 40 nm of IP_3R1. Indeed, at ER-PM junctions, the inter-membrane distance has been reported to be on average between 10 and 25 nm apart (Wu et al., 2006, Chang et al., 2017); therefore, for ANO1 and IP_3R1 to be at a distance

apart greater than the sensitivity of PLA (40 nm) would indicate a loss of functional interaction and subsequently, increased PLA signal must represent the formation of ANO1-IP_3R1 interactions not already present at rest. However, that still does not necessarily suggest ANO1 and IP_3R1 are not already present at ER-PM contact sites before noxious stimulation. It may be that at rest, ANO1 and IP_3R1 are separated by greater than 40 nm along the length of the ER-PM junction (which can span up to 400 nm wide (Chang et al., 2017)) and undergo a lateral translocation to within nanodomain proximity. However, the molecular mechanism underlying such a movement is similarly undetermined.

6.1.3 ANO1 Coupling to Capsaicin-Evoked Nociception is Conserved in TG Neurons

Further to preliminary evidence in support of ANO1-IP_3R1 nanodomains in small-diameter neurons of the TG, PLA was used to demonstrate that functional coupling between ANO1 and IP_3R1 is similarly modulated in an activity-dependent manner as was observed in DRG neurons. When primary TG neuron cultures were stimulated with the TRPV1 agonist CAP, a significant increase in the mean PLA signal (normalised to somatic diameter) between ANO1 and IP_3R1 and between ANO1 and TRPV1 was observed, suggesting a mechanism of CAP-evoked nanodomain proximity. Interestingly, while the mean PLA signal between ANO1 and IP_3R1 did increase as a result of CAP stimulation, there was a much larger range in the number of PLA puncta normalised to diameter within the population of PLA-positive TG neurons in the control compared to the CAP treated group. Previous immunohistochemical studies characterising TRPV1 protein expression in the TG suggest TRPV1 is differentially expressed in each of the three divisions of the TG, where in the opthalamic (V1) and maxillary (V2) divisions, approximately 30% of neurons were TRPV1-immunoreactive compared to the mandibular (V3) division where only approximately 20% of the neurons are TRPV1-positive (Huang et al., 2012). Considering TRPV1 is expressed almost exclusively in small-diameter C-fibre nociceptors (Kobayashi et al., 2005), with a minority of Aδ and Aβ identified through RNA-Seq analysis(Bhuiyan et al., 2024), this differential distribution is unsurprising as while the V1 and V2 divisions of the TG consist of only sensory neurons, the V3 division contains both sensory and motor neurons (Williams et al., 2003). Previous immunohistochemical characterisation of ANO1 expression in the V3 division has reported that approximately 75% of ANO1-immunoreactive neurons were also immunoreactive for TRPV1 (Kanazawa and Matsumoto, 2014) Therefore, it is possible that ANO1-IP_3R1 JMSCs are present in small-diameter TG neurons that do not also express TRPV1 and are, therefore, non-responsive to CAP, however, this was not controlled for during PLA experiments between ANO1 and IP_3R1, nor was the division of

origin of TG neurons. It would be interesting to compare ANO1-IP_3R1 JMSC dynamics induced by BK in the TG and conversely, those induced by CAP in the DRG, particularly given the apparent preferential coupling of ANO1 to B2R over TRPV1 in the DRG. Differential regulation of ANO1 nanodomains, therefore, may represent an important difference in nociceptive signalling between different sensory ganglia, which could have consequences for therapeutic pharmacological interventions to target different sources of pain.

Alternatively, nanodomain coupling between ANO1 and TRPV1 may occur independent of functional coupling to IP_3R1. An alternate hypothesis for ANO1-TRPV1 functional coupling has been proposed by Takayama and colleagues whereby ANO1 is activated directly via Ca^{2+} influx through closely associated TRPV1 cation channels. Whole cell patch-clamp recordings in HEK293T cells observed CAP-induced CaCCs in cells co-expressing murine ANO1 and TRPV1, but not in cells expressing ANO1 or TRPV1 alone and CaCCs were abolished in Ca^{2+}-free extracellular bath solution, suggesting a necessity for extracellular Ca^{2+} influx (Takayama et al., 2015). This model proposes that noxious heat-evoked depolarization is the combined result of TRPV1-mediated cation influx and ANO1-mediated anion efflux. However, TRPV1 Ca^{2+} influx comprises only ~10% of the total CAP-evoked TRPV1 cation current (Samways et al., 2008), suggesting noxious activation of TRPV1 alone may not provide sufficient $[Ca^{2+}]_i$ to reach the micromolar $[Ca^{2+}]$ required for ANO1 activation (Yang et al., 2008, Xiao et al., 2011). On the other hand, ANO1-mediated CaCCs demonstrate synergistic Ca^{2+}-voltage gating; while the EC_{50} of ANO1 activation at hyperpolarized membrane potentials (-60 mV) is 2.6 μM, at depolarised membrane potentials (+ 60 mV) it is only 0.3 μM (Xiao et al., 2011). Therefore, it may be that following initial TRPV1-mediated depolarisation of the membrane potential, further Ca^{2+} influx via TRPV1 within nanodomain proximity of ANO1 is sufficient to mediate ANO1 activation independent of IP_3-sensitive release of intracellular Ca^{2+} stores.

Interestingly, Takayama and colleagues further proposed a role for functional coupling between ANO1 and TRPV1 in neurotransmission at synapses between the presynaptic terminals of primary DRG afferent neurons and first-order spinal neurons at the dorsal horn of the spinal cord. Pharmacological inhibition of ANO1 with the ANO1-selective inhibitor T16Ainh-A01 in a transverse spinal cord slice preparation almost completely abolished the generation of excitatory post-synaptic currents (EPSCs) at dorsal horn neurons in the substantia gelatinosa (SG) when CAP was applied at the dorsal root (Takayama et al., 2015). These results were hypothesised to demonstrate that ANO1-TRPV1 nanodomain interactions at peripheral synaptic terminals contribute to CAP-induced release of the major excitatory neurotransmitter, glutamate. Therefore, the

evidence presented in Chapter 5 of this thesis is not the first example of ANO1-mediated facilitation of CAP-evoked neurotransmitter release, lending further support to a hypothesised role for functional ANO1-TRPV1 coupling in CGRP release in the TG.

CGRP is a major excitatory neuropeptide abundantly expressed in sensory neurons of the trigeminal system including in the TG, although, the highest concentration of CGRP expression is localised to the central terminals of primary trigeminal afferent neurons in the trigeminal nucleus caudalis (TNC), consistent with the role of CGRP as a primary afferent neurotransmitter (Eftekhari and Edvinsson, 2011, Iyengar et al., 2017). CAP-evoked release of CGRP from trigeminally-innervated tissues and from the somata of neurons in the TG is a well-established model of trigeminal activation, and immunoassays are considered the gold standard to quantify neuropeptide release and is routinely used to investigate molecular mechanisms modulating CGRP signalling (Ulrich-Lai et al., 2001, Flores et al., 2001, Gupta et al., 2010, Jenkins et al., 2004, Dux et al., 2022, Gárate et al., 2024). In the present study, ELISA was used as an approach to evaluate the contribution of ANO1 activation to CAP-evoked CGRP release from primary cultured TG neurons and an *ex vivo* TG preparation; however, results from the literature were not replicated and ELISA did not detect significant CAP-induced release of CGRP. The short half-life of CGRP is commonly reported as a limitation to the collection and quantification of CGRP in biological samples by methods such as ELISA (Kraenzlin et al., 1985, Messlinger et al., 2021, Gárate et al., 2024), therefore, despite the inclusion of peptidase inhibitors, it could be that CAP-evoked CGRP release was undetectable by ELISA in the present study due to degradation from the time of collection to assay. Alternatively, the sensitivity of the ELISA kit used may have been insufficient to detect low concentrations of CGRP which could have resulted from low neuron viability in culture or sample volumes that were too large for the amount of biological material present. On the other hand, immunohistochemistry has also been used to successfully demonstrate CAP-induced differences in the expression levels of CGRP in the trigeminal system (Zhou et al., 2016, Spekker et al., 2021). Therefore, as an alternative method to investigate a functional role for ANO1 activation in TG neurons, an immunohistochemistry-based CGRP expression assay was devised.

Indeed, novel experimental evidence presented in this thesis confirmed that pharmacological inhibition of ANO1 with the selective antagonist Ani9 was sufficient to significantly attenuate CAP-induced CGRP release from TG neurons, suggesting that CAP-induced nanodomain proximity between ANO1 and TRPV1 reflects a functional interaction in the TG whereby ANO1-mediated amplification of TRPV1-associated membrane depolarisation contributes to depolarisation-evoked exocytosis of CGRP stores. While TRPV1-mediated membrane depolarisation has been directly linked to

Ca^{2+}-sensitive exocytosis of CGRP-containing vesicles via activation of high-voltage-activated N-type VGCCs (which have been shown to activated at membrane potentials of -13 mV (Helton et al., 2005, Dolphin, 2021)), Ca^{2+} influx via T-type Ca^{2+} channels has also been demonstrated to mediate a rapid, low-threshold exocytosis in an action potential-independent manner via functional coupling to syntaxin-1 (Weiss et al., 2012, Weiss and Zamponi, 2013, Jacus et al., 2012). T-type Ca^{2+} channels are activated by weak membrane depolarisation at approximately -45 mV (Dolphin, 2021, Klockner et al., 1999), which, is similar to that which is achieved via ANO1 activation in DRG neurons (depolarization to a range of -40 to -35 mV (Liu et al., 2010)). Therefore, it is tempting to speculate that moderate ANO1 activation-mediated depolarisation of the neuronal membrane is sufficient to activate T-type Ca^{2+} channel-mediated exocytosis, further contributing to CGRP release. Considering high voltage-activated VGCCs, including N-type, L-type and P/Q-types, rapidly undergo endocytosis-mediated downregulation in response to prolonged CAP stimulation (Ramgoolam and Dolphin, 2022), T-type VGCC-mediated vesicle exocytosis may serve as a molecular mechanism to amplify the functional range of CGRP signalling in the trigeminal system, similar to the role that T-type VGCCs mediate in photoreceptor cells of the retina, whereby sub-action potential-threshold activation of T-type channels contributes to a greater dynamic range of synaptic vesicle release in response to light (Davison et al., 2022). Given the extensive role established for T-type VGCCs in nociception in the PNS (Watanabe et al., 2015, Cai et al., 2021, Mustafá et al., 2022), this proposed signalling mechanism may be highly relevant to CGRP-related nociception in the trigeminal system and consequently, the functional role of ANO1 in the TG demands further elucidation as a potential therapeutic target for trigeminal-specific pain disorders such as migraine, headache and trigeminal neuralgia.

6.1.5 Esyt1 Expression in the DRG is Co-localised with ANO1 and IP_3R1

The Ca^{2+}-sensitive ER-PM junctional tether, Esyt1, was hypothesised to mediate functional coupling between ANO1 and IP_3R1 in small-diameter, nociceptive neurons of the DRG. Prior evidence for the expression of Esyt1 in the DRG comes from transcriptomic databases: in the rat, Esyt1 mRNA transcription is localised to sub-populations of Aδ mechanoreceptor neurons, although Esyt1 mRNA transcripts have been detected in a broader subset of neurons obtained from both mouse and human DRG samples (Bhuiyan et al., 2024). Earlier RNA-sequencing databases developed by the Denk laboratory reported Esyt1 mRNA expression in a dissociated mouse DRG purified nociceptor preparation (Lopes et al., 2017b, Thakur et al., 2014) which have since been independently verified by RNA-Seq (Li et al., 2016) and TRAP-Seq (Rozenbaum et al., 2018). To date, there is limited published evidence of Esyt1 protein

expression in the DRG other than a single study that demonstrated Esyt1 immunoreactivity in western blot analysis of lysate prepared from murine primary DRG culture (Megat et al., 2019a). The evidence presented in this thesis confirms the protein expression of Esyt1 in rodent DRG neurons and further demonstrates the sub-cellular localisation of Esyt1 protein immunoreactivity for the first time. Immunohistochemical analysis of perfusion-fixed DRG sections revealed protein expression for Esyt1 in DRG neurons similar in diameter to peripherin-positive, small-diameter neurons.

A time-resolved PLA approach was developed to characterise nanodomain proximity between Esyt1 with ANO1 and IP_3R1 to probe an activity-dependent interaction of Esyt1 with ANO1-IP_3R1 JMSC functionality in the DRG. Primary cultured DRG neurons were stimulated with the inflammatory mediator BK for progressively increasing durations of time prior to immediate fixation without washout and PLA was performed between Esyt1 with ANO1 and IP_3R1 independently. Quantitative analysis of the PLA signal between Esyt1 and ANO1 revealed an unexpected fluctuation in the mean number of puncta (normalised to diameter) which could indicate a multi-functionality whereby ANO1-Esyt1 nanodomain proximity is differentially modulated based on the intensity of noxious stimulation. Interestingly, stimulation of DRG neurons with BK for as little as 10 seconds was sufficient to significantly increase the mean normalised puncta, suggesting functional Esyt1-ANO1 interaction is not solely dependent on a noxious stimuli-induced release of intracellular Ca^{2+} stores but instead may be activated via another mechanism. Similarly, stimulation with BK for 10 seconds was sufficient to promote a short-lived, albeit significant increase in the mean PLA signal between Esyt1 and IP_3R1.

This observation may reflect either a nociception-induced increase in the frequency of ANO1-Esyt1 interactions, indicating the formation of de novo JMSC interactions, or it may result from a dynamic tightening of proximity between established protein pairs to which the PLA is more sensitive. It is relevant here to consider the previously reported role of Esyt1 in facilitating ANO1 protein trafficking (Lérias et al., 2018). Increased trafficking of ion channels to the PM in response to neuronal activity is a well-documented phenomenon in DRG neurons enabling a rapid, activity-dependent modulation of sensitivity to acute noxious stimuli and as a mechanism by which chronic pain hypersensitivity develops (Zhao et al., 2011, Davies et al., 2007, Ferron et al., 2021). For example, treatment of DRG sensory neurons with an inflammatory cocktail has been shown to promote increased expression of the voltage-gated sodium channel (VGSC) $Na_v1.7$ at the axonal PM via multiple mechanisms including increased vesicular loading, anterograde trafficking from the soma to distal axons, and membrane insertion via exocytosis (Higerd-Rusli et al., 2023). Similarly, proalgesic agents such as nerve growth factor (NGF) and adenosine triphosphate (ATP) have been shown to promote trafficking

and PM insertion via exocytosis of TRPV1 (Rivera et al., 2024, Stein et al., 2006, Camprubí-Robles et al., 2009). Historically, there has been limited research into molecular mechanisms regulating the expression of ANO1 in peripheral sensory neurons, with much of the work carried out on exogenously expressed ANO1 channels in cell lines or in smooth muscle cell types (Hawn et al., 2021). However, in bronchial epithelial cells, in which Esyt1 was first proposed as a positive regulator of ANO1 trafficking to the apical membrane, siRNA knockdown of Esyt1 was sufficient to significantly attenuate ANO1-mediated CaCC density (Lérias et al., 2018), supporting a role for Esyt1 in ANO1 functionality, albeit not necessarily confirming modulation of ANO1 trafficking in itself. Lerias and colleagues did, however, also observe reduced surface expression of GFP-tagged ANO1 following Esyt1 knockdown. Furthermore, Esyt1 has recently been implicated in the modulation of surface expression and function of STIM1 (Kang et al., 2019a), TRPC3 (Trothen et al., 2024) and the adhesion GPCR D1 (ADGRD1) (Stephan et al., 2023). Esyt1 has additionally been demonstrated to mediate trafficking of α-amino-3-hydroxy-5-methyl-4-isoxazolepropionic acid (AMPA) receptors to the neuronal surface membrane in response to long-term potentiation, which may point to a role for Esyt1 as a generalised activity-dependent trafficking chaperone in addition to mediating ER-PM tethering functions (Mao et al., 2023). Therefore, if Esyt1 does mediate a similar role in the DRG, it could prove a viable therapeutic target to disrupt ANO1 nociceptive signalling as a potential treatment avenue for pain disorders, although significant further experimental work will be required to fully elucidate the molecular mechanisms regulating ANO1 surface expression in nociceptive neurons to confirm if indeed Esyt1 mediates such a role as experiments demonstrating altered ANO1 functionality in response to manipulations of Esyt1 expression do not necessarily reflect an impact on ANO1 trafficking.

To further speculate on the hypothesised role of Esyt1 as an ANO1 trafficking regulator, it is interesting to note ANO1-Esyt1 PLA interactions were identified throughout the cytoplasm, (in contrast to IP_3R1-Esyt1 proximities identified by PLA, which were generally localised around the perimeter of the cell), therefore suggesting ANO1-Esyt1 couplings are not exclusively localised to ER-PM contact sites. Indeed, Esyt1 expression has been reported to localise throughout the ER, unlike its protein family members Esyt2 and Esyt3, which have been identified to localise to regions of the ER closely associated with the PM (Giordano et al., 2013, Min et al., 2007b). This localisation pattern for Esyt1 was confirmed in cultured DRG neurons (Figure 3.4A), where PLA performed using two separate primary antibodies against Esyt1 identified Esyt1 immunoreactivity throughout the cytoplasm. Furthermore, STED microscopy identified Esyt1-positive punctate immunoreactivity localised throughout the neuron, although this showed an apparent

translocation towards the PM upon neuronal stimulation with BK. PLA puncta reflecting discrete instances of nanodomain proximity between Esyt1 with ANO1 and Esyt1 with IP_3R1 were observed at the PM following stimulation with BK for 40 – 50 seconds, coinciding with the observed kinetics of BK-evoked Ca^{2+} mobilisation (Jin et al., 2013). As Esyt1 and IP_3R1 are ER-resident proteins, their apparent localisation at the PM suggests functionality at ER-PM contact sites. Together, the PLA data demonstrating activity-dependent dynamic nanodomain interactions between Esyt1 with ANO1 and IP_3R1 implies that the Ca^{2+}-sensitive Esyt1 C2 domains are sufficiently activated by BK-evoked release of intracellular Ca^{2+} to promote a dynamic rearrangement of these three proteins with respect to one another. Of course, it is entirely plausible that a putative Esyt1-ANO1 coupling reflects a multi-faceted functional role whereby Esyt1 both positively modulates ANO1 trafficking to the PM and mediates ANO1 JMSC dynamics at ER-PM contact sites which could account for the multiple 'peaks' in interaction observed in PLA signal between Esyt1 and ANO1 during the time course of BK stimulation in DRG neurons.

Given the apparent preferential coupling of ANO1-IP_3R1 JMSCs with B2R over TRPV1, it would be interesting to perform further STED imaging for ANO1 and Esyt1 immunoreactivity in DRG neurons stimulated with CAP. Indeed, PLA signal between ANO1 and Esyt1 in CAP-stimulated was significantly less compared to signal in BK-stimulated neurons, albeit still significantly elevated above that of control neurons. If Esyt1 is responsible for either ANO1 trafficking to ER-PM junctions or for tethering the ER to PM to facilitate ANO1 JMSC interactions, this may reflect the underlying mechanism for why CAP appears less capable of inducing ANO1 nanodomain formation over BK. Although it is interesting to note that CAP stimulation did not significantly modulate nanodomain proximity between Esyt1 and IP_3R1 compared to control DRG neurons, which could otherwise reflect a functional role for Esyt1-ANO1 interactions in CAP-evoked nociception that is independent of ANO1-IP_3R1 JMSC activity. To further elucidate such a role, it would also be relevant to probe for nanodomain proximity between Esyt1 and TRPV1 following CAP stimulation in DRG neurons.

6.1.7 Hypothesising on the Modulation of ANO1 Nanodomains by Esyt1 in Sensory Neurons

This thesis proposed a novel hypothesis to explain the observed increase in PLA signal between ANO1 and IP_3R1 following noxious stimulation with the inflammatory mediator BK in primary cultured DRG neurons and by CAP in TG neurons. Prior work investigating functional coupling between ANO1 and IP_3R1 has identified nanodomain proximity between both ligand-gated ion channels mediated by their direct binding in non-

stimulated DRG neurons (Jin et al., 2013, Shah et al., 2020) and those findings are corroborated in the present study. Therefore, a population of ANO1-IP_3R1 JMSCs are functional in sensory neurons independent of noxious stimulation-evoked intracellular Ca^{2+} release, while a secondary population gains nanodomain proximity upon noxious stimulation. As this hypothesis is based on data in fixed cells, of course, these two populations may not be mutually exclusive but, for the purposes of this discussion, can be putatively classified as Ca^{2+}-dependent and Ca^{2+}-independent ANO1-IP_3R1 JMSCs. Furthermore, Ca^{2+}-dependent ANO1-IP_3R1 JMSCs appear to possess a range of Ca^{2+} sensitivities based on the observation that the mean PLA signal between ANO1 and IP_3R1 appears to display a gradual 'rundown' with prolonged BK stimulation suggesting some JMSCs remain active for longer than others and are likely require lower $[Ca^{2+}]_i$ signals to activate. Alternatively, this variability may reflect differential Ca^{2+} dynamics between individual neurons. It may be the case that ANO1-IP_3R1 JMSCs are differentially controlled by a combination of multiple molecular mechanisms with a range of Ca^{2+} sensitivities, further increasing the dynamic range and specificity of ANO1-mediated amplification of nociceptive signalling. Proximity between ANO1 and IP_3R1 at Ca^{2+}-independent JMSCs may simply be mediated by the direct binding of ANO1 itself to IP_3R1. Indeed, the homologue of mammalian ANO1 in yeast *Saccharomyces cerevisiae*, Ist2, is selectively localised to regions of the ER in close apposition to the PM and is known to function as a ER-PM junctional tether (Wolf et al., 2012), suggesting the formation of ER-PM contact sites is not solely dependent on scaffolding proteins not directly involved in JMSC activity themselves. Similarly, oligomerisation of CRAC channel STIM and Orai subunits mediates ER-PM contact sites necessary for SOCE (Derler et al., 2016), although JPH tether proteins are also necessary for that process (Hogea et al., 2021). The data presented in this thesis, however, lends support to a hypothesised role for the ER-PM tether protein Esyt1 to mediate Ca^{2+}-dependent ANO1-IP_3R1 JMSC interactions. Further experimental work will therefore be required to fully elucidate the mechanisms by which Esyt1 might functionally modulate ANO1-IP_3R1 JMSCs in the DRG.

6.2 Limitations and Considerations

Throughout this thesis, protein expression levels were quantified in fixed neurons as a measure of the mean fluorescence intensity across each cell in relation to an overall mean calculated per technical replicate in an effort to control for variability in the quality of immunostaining between samples. Technically, immunofluorescence intensity should only be regarded as a semi-quantitative approach to determining protein expression levels with sufficient standardisation of protocols across experiments yet may still be subject to significant variability in sensitivity and reproducibility. Mass spectrometry is

commonly considered the gold standard for measures of protein expression levels in tissue, and quantitative immunofluorescence has only demonstrated comparable accuracy when specific antibodies giving high signal-to-noise ratios are used (Toki et al., 2017). Despite optimization of immunostaining protocols, antibodies against ANO1 typically have poor specificity and low signal-to-noise ratio, therefore, colocalisation analysis methods based on correlating pixel intensity as a representation of protein expression are likely not the most appropriate method to accurately quantify proximity. It is for this reason that objects-based nearest neighbour analysis was performed for STED data to utilise a variety of approaches to characterise ANO1 interaction to target proteins, in combination with PLA as a more objective measure of nanodomain proximity.

It is important, however, to also consider the limitations associated with STED microscopy. Throughout this thesis, DRG neurons were fixed prior to volumetric STED imaging, which was achieved through the optical sectioning (z stack imaging) and reconstruction of individual 2D STED images captured of the PM. Volumetric STED imaging has been shown to produce cumulative photobleaching effects, reducing the signal-to-noise ratio achievable and importantly, may induce a shift in the apparent axial localisation of fluorescence signal which will have obvious ramifications for investigations requiring accurate protein localisation (Srambickal et al., 2021). While deconvolution can mitigate these effects to an extent, and is capable of increasing the signal-to-noise ratio by up-to eight-fold while further increasing resolution (Schoonderwoert et al., 2013), care should still be taken when interpreting localisation results. Given the problematic limitations with respect to the volumetric STED approach used in the present study, it is difficult to draw confident and accurate conclusions regarding the ‘true’ proximity between ANO1 and putative nanodomain interactors TRPV1 and Esyt1 based on this alone, however, the evidence presented certainly brings to light intriguing scientific questions for future development.

Throughout this thesis, experiments investigating the nanodomain proximity between paired membrane-bound proteins were performed exclusively in fixed biological samples, therefore, it is important to consider the ways in which fixation can affect protein localisation data. Refractive index (RI) is an important principle in microscopy, as it determines how light propagates through different media, influencing image contrast and resolution when imaging biological tissue (Khan et al., 2021). Mismatched RI can increase light scattering and spherical aberration during imaging (Diel et al., 2020), however, while it is standard practice to match the RI of the mounting medium (ProLong Gold AntiFade – 1.47) and immersion medium (Immersol™ – 1.518) as closely as possible, what is less commonly considered is the refractive index of the biological sample itself. Fixation of cells in 4% PFA has been shown to reduce their refractive index

relative to live cells to approximately 1.34 (Baczewska et al., 2021). The surface area of cells within the optimum plane of focus was also shown to significantly reduce in most cell types following fixation. Furthermore, 4% PFA fixation of cells has been shown to distort the topography of cell surface membranes, and likely alter protein position relative to their true in situ localisation (Kim et al., 2017) – indeed, fixed DRG neurons take on a 'rough' appearance compared to live cells but even the PM of living cells is non-homogenous (Adler et al., 2010). Such variations in membrane topography are known to create the appearance of molecular clustering, that is, an apparent greater concentration of labelled proteins at regions of the PM that are more dense, and further implies for quantitative STED localisation analysis that the measured nearest neighbour may be incorrectly attributed to a protein expressed in an adjacent membrane fold rather than the 'true' nearest neighbour expressed in the same membrane region (Adler et al., 2024).

These considerations would emphasise the importance for future investigations of protein-protein interactions in DRG neurons to be conducted in living cells. Why, then, were ANO1 nanodomains investigated in fixed neurons for the experiments described herein? Typically, the clustering of proteins in response to stimuli is transient and the principle of dynamic protein-protein interactions is an important mechanism by which signalling pathways rapidly and adaptively respond to extracellular stimuli (Acuner Ozbabacan et al., 2011). However, the transient nature of such protein-protein interactions increases the complexity of visualising such interactions in living cells; thus the use of fixed biological specimens is convenient, although it then becomes relevant to consider how effectively fixation with 4% PFA preserves potential protein-protein interactions. Fixation quality is, in fact, impacted by protein binding dynamics and typically, proteins undergoing rapid binding/un-binding dynamics are more poorly preserved by cross-linking fixatives including PFA. Furthermore, transmembrane proteins in particular are subject to fixation-induced clustering, which presents a particular complication when studying protein nanodomain interactions (Yoshida et al., 2023, Stanly et al., 2016). To combat this, it is necessary that the fixation rate occurs more rapidly than the protein binding-unbinding rate. Given that the PLA signal between ANO1 and IP_3R1 in response to progressively increasing duration of BK stimulation appears to conform to a physiologically relevant stimulus (BK-evoked intracellular Ca^{2+} mobilisation) it could be argued that in the case of ANO1-IP_3R1, fixation with PFA is sufficient to stabilise the nanodomain interaction, however, perhaps the same could not be said for ANO1-Esyt1 or IP_3R1-Esyt1 interactions which may be weaker or more transient.

In order to study intracellular protein dynamics in living cells, a typical approach would be to exogenously overexpress a fluorescently tagged version of the protein of interest in order to visualise stimulus-induced protein translocation with a fluorescence microscopy. For example, in the Gamper laboratory, nucleofection of primary DRG neurons with a GFP-tagged Esyt1 construct has been used to demonstrate BK-induced translocation of Esyt1 towards the PM using a total internal reflection (TIRF) microscopy setup (unpublished data). However, in order to study protein-protein interactions, such an approach would firstly require the co-transfection of multiple recombinant plasmids, which is unlikely to be a viable approach considering the generally low transfection efficiency in primary neurons (typically between 5 and 20% (Yu et al., 2015, Dib-Hajj et al., 2009)) and secondly, overexpression of proteins introduces non-physiological protein-protein interaction artifacts as protein clustering is non-linearly dependent on concentration (Li et al., 2012). Therefore, to suggest an alternative approach to studying dynamic ANO1 interactions *in vitro,* recent advances have been made for the direct labelling of endogenous proteins with fluorophores enabling live-cell fluorescent microscopy, including super-resolution microscopy. Arsic et al demonstrate the direct coupling of small organic fluorophores to unnatural amino acids (UAAs) using click chemistry in their recent 2022 *Nature Communications* paper. Click chemistry-reactive UAAs can be incorporated into target proteins of interest via clustered regularly interspaced short palindromic repeats (CRISPR)-Cas9 genome engineering, subsequently allowing for fluorescent tagging of endogenously-expressed proteins in primary neurons and live-cell STED imaging (Arsić et al., 2022). A similar approach could therefore be used to fluorescently label endogenous ANO1 and putative interacting partners to study their dynamic interactions in living neurons, circumventing the limitations associated with poor ANO1 antibody specificity, exogenous overexpression of proteins and quantifying protein localisation in fixed cells. However, the most efficient and simple approach to studying protein-protein interactions in primary cells likely remains a combination of antibody-based fluorescent imaging techniques in fixed cells and supporting functional live cell imaging experiments. Therefore, it will be of paramount importance to further apply the hypothesised mechanisms governing ANO1 nanodomain modulation to functional *in vitro* studies to fully elucidate their functionality in peripheral sensory neurons.

6.3 Future Directions

6.3.1 Approaches to Measuring ANO1 Activation in Peripheral Sensory Neurons

The experimental data described in this thesis provide indirect evidence towards a putative role for functional coupling between ANO1 and TRPV1, and ANO1 and IP_3R1

in small-diameter nociceptive neurons of the TG. To fully elucidate ANO1 functionality in TG nociceptors it will be essential to demonstrate CAP-induced activation of ANO1 similar to that described for DRG neurons (Shah et al., 2020). Unfortunately, due to technical limitations, key *in vitro* functional imaging experiments were unsuccessful in primary cultured TG neurons. Previously in the Gamper laboratory, anion channel activation has been measured using an iodide (I^-)-sensitive double-mutant of the enhanced yellow fluorescent protein (EYFP-H148Q/I152L) (Jin et al., 2013, Shah et al., 2020, Du et al., 2017, Hao et al., 2023, Li et al., 2024). EYFP-H148Q/I152L has a high I^- sensitivity with an affinity for I^- as low as 2 mM, whereby binding of I^- results in a quenching of the EYFP fluorescence up to 50% (Galietta et al., 2001). ANO1 is similarly permeable to I^- as it is for Cl^- (Twyffels et al., 2014), therefore by substituting a portion of the NaCl concentration for NaI in standard extracellular bath solution during live-cell imaging, anion channel activation is inferred through the influx of I^-, measured as a quenching of EYFP-H148Q/I152L which is typically transfected into primary neuron cultures via electroporation (Chen et al., 2006). High transfection efficiencies are typically difficult to achieve in primary sensory neurons through electroporation or other non-viral gene delivery methods (Yu et al., 2015), and electroporation of dissociated neuron cultures using a commercially available electroporation device (Nucleofector™, Lonza) requires a relatively large number of cells (at least 2 x 10^5 in 100 µL is recommended by the manufacturer) (Yu et al., 2015). A single rat TG neuron preparation yields approximately 3.5 x 10^4 neurons (Lagares and Avendaño, 2000), compared to a single DRG neuron preparation which can yield up to the required 2 x 10^5 neurons (Shen et al., 2019). Therefore, while DRG neuron transfections are routinely performed in the Gamper laboratory in primary neuron cultures prepared from two animals, the number of animals required to yield an equivalent number of cells from a TG neuron preparation is less viable. While attempts to transfect primary TG neurons with EYFP-H148Q/I152L were made, poor cell survivability adversely impacted efforts to record ANO1 activation in TG neurons. Therefore, alternative transfection methods such as viral gene delivery or lipofection may be more efficacious in expressing EYFP-H148Q/I152L in primary TG neuronal cultures (Chong et al., 2021). For ongoing investigation into the modulation of ANO1 activity not only in the TG but also in the DRG, a useful approach may be to develop a transgenic mouse line that constitutively and selectively expresses EYFP-H148Q/I152L in peripheral sensory neurons. A similar approach has previously proven successful whereby recombinant genomic sequences for GFP and yellow fluorescent protein (YFP) were inserted under the control of the promotor for the S100β gene, enabling selective fluorescent protein expression in Schwann cells (Zuo et al., 2004). Interestingly, Zuo and colleagues demonstrated GFP expression in myelinating

Schwann cells surrounding peripheral axons teased from the sciatic nerve and in the skin. There is considerable interest in the development novel *in vivo* Ca^{2+} imaging techniques and their application to the study of nociception (Stratton et al., 2024, Gedeon et al., 2024, Ingram et al., 2024). In particular, the ability to measure afferent sensory nerve activity at the peripheral nerve endings is relevant as this is the initial site for transduction of noxious stimuli in cutaneous nociceptors (Dubin and Patapoutian, 2010b). Therefore, the addition of a genetically encoded halide-sensitive imaging approach could be invaluable to the study of not only ANO1-mediated Cl^- signalling in peripheral sensory nerve terminals but also for future investigations of GABAergic signalling.

As a progression of the hypothesis presented in the current work, it will be essential to further investigate the functionality of ANO1-containing signalling nanodomains in the peripheral nerve terminals. The presence of tubular ER within neuronal processes is well described in the literature (Yperman and Kuijpers, 2023, Öztürk et al., 2020) so there is strong basis to suggest ER-PM contact sites play an essential role in Ca^{2+} signalling dynamics at the sensory nerve terminals as well as in the soma. Indeed, in the CNS, extensive axonal ER-PM contact sites mediated by STIM1-Orai JMSCs have been reported in the peripheral axons of cortical pyramidal neurons (Zamponi et al., 2022) and activity-dependent SOCE at axonal ER-PM junctions modulates presynaptic function in hippocampal neurons (de Juan-Sanz et al., 2017).

6.3.2 Dysregulation of ER-PM JMSCs as a Pathophysiological Mechanism Underlying Chronic Pain

Chapter 3 raised important findings that functional couplings between ANO1 and interacting proteins IP_3R1 and TRPV1 at ER-PM junctions in DRG nociceptive neurons are not static or permanent complexes but are dynamically and differentially regulated by noxious stimuli. A series of 'time-resolved' PLA experiments revealed ANO1-IP_3R1 proximity may be regulated by the release of intracellular Ca^{2+} stores. For the experiments described in this thesis, DRG neuron cultures were stimulated with acute application of 250 nM BK, and ANO1-IP_3R1 proximity was shown to undergo desensitization after 5 minutes. It is uncertain, therefore, what the effect on ANO1-IP_3R1 complexing prolonged, or chronic exposure to BK, may be, or in other words, what is the lifecycle of an individual interaction between an ANO1 Cl^- channel and an IP_3R1 Ca^{2+} channel? Would prolonged exposure to BK eliciting a larger release of intracellular Ca^{2+} promote the formation of more ANO1-IP_3R1 interactions or prolong the contact time between those channels already present at ER-PM junctions and primed to interact? Would either of these mechanisms have an equivalent physiological effect? Additionally,

how might the sensitivity of ANO1-IP_3R1 JMSCs change in response to chronic pain? Interestingly, ANO1 has been demonstrated to be upregulated in multiple *in vivo* models of inflammatory and neuropathic chronic pain (García et al., 2014, García et al., 2018, Pineda-Farias et al., 2015). Therefore, with increased ANO1 expression it is likely that upon noxious stimulation, an increased number of ANO1-IP_3R1 JMSCs are formed, thus contributing to the hyperalgesia observed in chronic pain models as it follows that a greater number of ANO1 Cl^- channels activated will lead to a more pronounced Cl^- efflux and resulting depolarisation of the neuron in response to a coupled noxious stimulus such as BK or CAP. This hypothesis is further supported by evidence for the upregulation of IP_3 alongside ANO1 in the rat L4-6 DRG following chronic constriction injury of the sciatic nerve, suggesting ANO1-IP_3R1 interactions are critical to the development of neuropathic pain (Zhang et al., 2018).

Given the substantial amount of published evidence suggesting Ca^{2+} activation of Esyt1 induces a conformational change in shape that brings the ER and PM into closer proximity (Chang et al., 2013, Bian et al., 2018, Fernández-Busnadiego et al., 2015a, Giordano et al., 2013, Idevall-Hagren et al., 2015, Ge et al., 2022), the most likely hypothesis to explain the results presented herein are that an established subset of ANO1-nanodomains are mediated by Esyt1 and stimulation with an inflammatory mediator induces translocation of the ER towards the PM, facilitating ANO1-IP_3R1 coupling and bringing ANO1 and Esyt1 within closer proximity (Figure 6.1). To verify this hypothesis, it will be important to test whether disruption of Esyt1 influences the ability of ANO1 to couple with IP_3R1 or whether Esyt1 knockdown inhibits ANO1 activation in the context of nociception. It is important to note that the sub-population of ANO1-containing nanodomains modulated by Esyt1 may not be restricted to ANO1-IP_3R1-B2R complexes; indeed, the TRPV1 agonist CAP was also capable of inducing a significant increase in the observed PLA signal between ANO1 and Esyt1. Therefore, further investigations into how Esyt1 may modulate functional coupling between ANO1, IP_3R1 and TRPV1 in response to noxious heat or stimulation with the TRPV1 agonist CAP would be relevant.

It would also be of interest to investigate a potential role for Esyt1 as an ANO1 trafficking facilitator in the DRG, particularly given that single-cell transcriptomic evidence suggests Esyt1 is similarly upregulated in DRG C-fibre neurons in response to sciatic nerve crush injury and sciatic nerve ligation *in vivo* models of chronic pain (Renthal et al., 2020). Furthermore, Esyt1 mRNA transcription and protein expression was shown to significantly increase in nociceptive DRG neurons in a paclitaxel model of chemotherapy-induced peripheral neuropathy (CIPN) (Megat et al., 2019a), further supporting a role for Esyt1 in nociception and development of chronic pain. Increased expression of Esyt1

could contribute to the development of hyperalgesia through facilitating increased trafficking of ANO1 to the PM or by strengthening ER-PM contact sites, promoting greater JMSC-like interactions between ANO1 and IP_3R1. Returning to the proposed hypothesis of ANO1-IP_3R1 JMSCs of differing Ca^{2+} sensitivities, elevated Esyt1 expression could also contribute to the development of allodynia, that is a pain response to innocuous stimuli, if it promotes the formation of ANO1-IP_3R1 interactions independent of intracellular Ca^{2+} release, effectively maladaptively increasing the sensitivity of nociceptive JMSCs. Over-expression of Esyt1 was shown to significantly increase the area over which the ER and PM were in close apposition and reduce the mean distance between apposed membranes (Giordano et al., 2013, Fernández-Busnadiego et al., 2015a). It follows that increased ER-PM contact sites would also substantially increase ANO1-IP_3R1 JMSC formation.

To summarise, pharmacological interventions aimed at disrupting ER-PM JMSCs either between ANO1 and IP_3R1 or between ANO1 and Esyt1 may provide a viable avenue for the development of novel therapeutic strategies to combat both acute and chronic pain.

6.4 Conclusion

In conclusion, this thesis provides new insights into the dynamic modulation of ANO1 nanodomain signalling complexes in peripheral nociceptive neurons. The evidence presented expands the understanding of ANO1's functional role in both DRG and TG neurons, demonstrating that ANO1-IP_3R1 JMSCs are not static but are dynamically regulated by activity-dependent noxious stimulation. These findings challenge previous assumptions of constitutive ANO1-IP_3R1 coupling and suggests a broader role for ANO1 in amplifying nociceptive signals across different sensory ganglia. The potential involvement of Esyt1 as a modulator of these interactions highlights a novel mechanism through which ER-PM junctions may facilitate or regulate nociceptive amplification, especially in chronic pain conditions. These findings demand further investigation into the modulation of ANO1 nanodomains as therapeutic strategies in pain management, offering a promising approach to address various forms of acute and chronic pain, including trigeminal disorders.

References

ABBE, E. 1873. Beiträge zur Theorie des Mikroskops und der mikroskopischen Wahrnehmung. *Archiv für Mikroskopische Anatomie,* 9**,** 413-468.

ACUNER OZBABACAN, S. E., ENGIN, H. B., GURSOY, A. & KESKIN, O. 2011. Transient protein–protein interactions. *Protein Engineering, Design and Selection,* 24**,** 635-648.

ADLER, J., BERNHEM, K. & PARMRYD, I. 2024. Membrane topography and the overestimation of protein clustering in single molecule localisation microscopy – identification and correction. *Communications Biology,* 7**,** 791.

ADLER, J. & PARMRYD, I. 2010. Quantifying colocalization by correlation: The Pearson correlation coefficient is superior to the Mander's overlap coefficient. *Cytometry Part A,* 77A**,** 733-742.

ADLER, J. & PARMRYD, I. 2013. Colocalization analysis in fluorescence microscopy. *Methods Mol Biol,* 931**,** 97-109.

ADLER, J., SHEVCHUK, A. I., NOVAK, P., KORCHEV, Y. E. & PARMRYD, I. 2010. Plasma membrane topography and interpretation of single-particle tracks. *Nature Methods,* 7**,** 170-171.

ADNAN, M., ISLAM, W., ZHANG, J., ZHENG, W. & LU, G. D. 2019. Diverse Role of SNARE Protein Sec22 in Vesicle Trafficking, Membrane Fusion, and Autophagy. *Cells,* 8.

AGNATI, L. F., FUXE, K., TORVINEN, M., GENEDANI, S., FRANCO, R., WATSON, S., NUSSDORFER, G. G., LEO, G. & GUIDOLIN, D. 2005. New Methods to Evaluate Colocalization of Fluorophores in Immunocytochemical Preparations as Exemplified by a Study on A2A and D2 Receptors in Chinese Hamster Ovary Cells. *Journal of Histochemistry & Cytochemistry,* 53**,** 941-953.

AIRY, G. B. 1835. On the Diffraction of an Object-glass with Circular Aperture. *Transactions of the Cambridge Philosophical Society,* 5**,** 283.

AIYAR, N., DISA, J., STADEL, J. M. & LYSKO, P. G. 1999. Calcitonin gene-related peptide receptor independently stimulates 3',5'-cyclic adenosine monophosphate and Ca2+ signaling pathways. *Mol Cell Biochem,* 197**,** 179-85.

AKIN, E. J., AOUN, J., JIMENEZ, C., MAYNE, K., BAECK, J., YOUNG, M. D., SULLIVAN, B., SANDERS, K. M., WARD, S. M., BULLEY, S., JAGGAR, J. H., EARLEY, S., GREENWOOD, I. A. & LEBLANC, N. 2023. ANO1, CaV1.2, and IP3R form a localized unit of EC-coupling in mouse pulmonary arterial smooth muscle. *Journal of General Physiology,* 155**,** e202213217.

ALKHANI, H., ASE, A. R., GRANT, R., O'DONNELL, D., GROSCHNER, K. & SÉGUÉLA, P. 2014. Contribution of TRPC3 to Store-Operated Calcium Entry and Inflammatory Transductions in Primary Nociceptors. *Molecular Pain,* 10**,** 1744-8069-10-43.

ALLEN, V., SWIGART, P., CHEUNG, R., COCKCROFT, S. & KATAN, M. 1997. Regulation of inositol lipid-specific phospholipase cdelta by changes in Ca2+ ion concentrations. *Biochem J,* 327 (Pt 2)**,** 545-52.

AMBALAVANAR, R. & MORRIS, R. 1992. The distribution of binding by isolectin I-B4 from Griffonia simplicifolia in the trigeminal ganglion and brainstem trigeminal nuclei in the rat. *Neuroscience,* 47**,** 421-9.

AMRUTKAR, D. V., PLOUG, K. B., OLESEN, J. & JANSEN-OLESEN, I. 2011. Role for voltage gated calcium channels in calcitonin gene-related peptide release in the rat trigeminovascular system. *Neuroscience,* 172**,** 510-7.

ARNOLD, D. P., XU, Y. & TAKATORI, S. C. 2023. Antibody binding reports spatial heterogeneities in cell membrane organization. *Nat Commun,* 14**,** 2884.
ARREOLA, J., LÓPEZ-ROMERO, A. E., HUERTA, M., GUZMÁN-HERNÁNDEZ, M. L. & PÉREZ-CORNEJO, P. 2024. Insights into the function and regulation of the calcium-activated chloride channel TMEM16A. *Cell Calcium,* 121.
ARSIĆ, A., HAGEMANN, C., STAJKOVIĆ, N., SCHUBERT, T. & NIKIĆ-SPIEGEL, I. 2022. Minimal genetically encoded tags for fluorescent protein labeling in living neurons. *Nature Communications,* 13**,** 314.
ASHRAF, A. P. K. & GERKE, V. 2022. The resealing factor S100A11 interacts with annexins and extended synaptotagmin-1 in the course of plasma membrane wound repair. *Front Cell Dev Biol,* 10**,** 968164.
AYON, R. J., HAWN, M. B., AOUN, J., WIWCHAR, M., FORREST, A. S., CUNNINGHAM, F., SINGER, C. A., VALENCIK, M. L., GREENWOOD, I. A. & LEBLANC, N. 2019. Molecular mechanism of TMEM16A regulation: role of CaMKII and PP1/PP2A. *Am J Physiol Cell Physiol,* 317**,** C1093-c1106.
BACZEWSKA, M., EDER, K., KETELHUT, S., KEMPER, B. & KUJAWIŃSKA, M. 2021. Refractive Index Changes of Cells and Cellular Compartments Upon Paraformaldehyde Fixation Acquired by Tomographic Phase Microscopy. *Cytometry Part A,* 99**,** 388-398.
BADER, C. R., BERTRAND, D. & SCHLICHTER, R. 1987. Calcium-activated chloride current in cultured sensory and parasympathetic quail neurones. *J Physiol,* 394**,** 125-48.
BAE, J. Y., KIM, J. H., CHO, Y. S., MAH, W. & BAE, Y. C. 2015. Quantitative analysis of afferents expressing substance P, calcitonin gene-related peptide, isolectin B4, neurofilament 200, and Peripherin in the sensory root of the rat trigeminal ganglion. *J Comp Neurol,* 523**,** 126-38.
BAE, Y. C., OH, J. M., HWANG, S. J., SHIGENAGA, Y. & VALTSCHANOFF, J. G. 2004. Expression of vanilloid receptor TRPV1 in the rat trigeminal sensory nuclei. *Journal of Comparative Neurology,* 478**,** 62-71.
BARBER, R. D., HARMER, D. W., COLEMAN, R. A. & CLARK, B. J. 2005. GAPDH as a housekeeping gene: analysis of GAPDH mRNA expression in a panel of 72 human tissues. *Physiol Genomics,* 21**,** 389-95.
BARISH, M. E. 1983. A transient calcium-dependent chloride current in the immature Xenopus oocyte. *J Physiol,* 342**,** 309-25.
BASBAUM, A. I., BAUTISTA, D. M., SCHERRER, G. & JULIUS, D. 2009. Cellular and molecular mechanisms of pain. *Cell,* 139**,** 267-84.
BATADA, N. N., SHEPP, L. A. & SIEGMUND, D. O. 2004. Stochastic model of protein–protein interaction: Why signaling proteins need to be colocalized. *Proceedings of the National Academy of Sciences,* 101**,** 6445-6449.
BELINSKAIA, M., ZURAWSKI, T., KAZA, S. K., ANTONIAZZI, C., DOLLY, J. O. & LAWRENCE, G. W. 2022. NGF Enhances CGRP Release Evoked by Capsaicin from Rat Trigeminal Neurons: Differential Inhibition by SNAP-25-Cleaving Proteases. *International Journal of Molecular Sciences,* 23**,** 892.
BERNARDINI, N., NEUHUBER, W., REEH, P. W. & SAUER, S. K. 2004. Morphological evidence for functional capsaicin receptor expression and calcitonin gene-related peptide exocytosis in isolated peripheral nerve axons of the mouse. *Neuroscience,* 126**,** 585-590.
BERRIDGE, M. J. 1998. Neuronal calcium signaling. *Neuron,* 21**,** 13-26.

BERRIDGE, M. J. 2006. Calcium microdomains: organization and function. *Cell Calcium,* 40**,** 405-12.
BERRIDGE, M. J. 2016. The Inositol Trisphosphate/Calcium Signaling Pathway in Health and Disease. *Physiological Reviews,* 96**,** 1261-1296.
BERTA, T., QADRI, Y., TAN, P. H. & JI, R. R. 2017. Targeting dorsal root ganglia and primary sensory neurons for the treatment of chronic pain. *Expert Opin Ther Targets,* 21**,** 695-703.
BHAVE, G., HU, H.-J., GLAUNER, K. S., ZHU, W., WANG, H., BRASIER, D. J., OXFORD, G. S. & GEREAU, R. W. 2003. Protein kinase C phosphorylation sensitizes but does not activate the capsaicin receptor transient receptor potential vanilloid 1 (TRPV1). *Proceedings of the National Academy of Sciences,* 100**,** 12480-12485.
BHUIYAN, S. A., XU, M., YANG, L., SEMIZOGLOU, E., BHATIA, P., PANTALEO, K. I., TOCHITSKY, I., JAIN, A., ERDOGAN, B., BLAIR, S., CAT, V., MWIRIGI, J. M., SANKARANARAYANAN, I., TAVARES-FERREIRA, D., GREEN, U., MCILVRIED, L. A., COPITS, B. A., BERTELS, Z., DEL ROSARIO, J. S., WIDMAN, A. J., SLIVICKI, R. A., YI, J., SHARIF-NAEINI, R., WOOLF, C. J., LENNERZ, J. K., WHITED, J. L., PRICE, T. J. & RENTHAL, W. 2024. Harmonized cross-species cell atlases of trigeminal and dorsal root ganglia. *Science Advances,* 10**,** eadj9173.
BIAN, X., SAHEKI, Y. & DE CAMILLI, P. 2018. Ca(2+) releases E-Syt1 autoinhibition to couple ER-plasma membrane tethering with lipid transport. *Embo j,* 37**,** 219-234.
BILLIG, G. M., PÁL, B., FIDZINSKI, P. & JENTSCH, T. J. 2011. Ca2+-activated Cl− currents are dispensable for olfaction. *Nature Neuroscience,* 14**,** 763-769.
BOISSEAU, P., BENE, M. C., BESNARD, T., PACHCHEK, S., GIRAUD, M., TALARMAIN, P., ROBILLARD, N., GOURLAOUEN, M. A., BEZIEAU, S. & FOUASSIER, M. 2018. A new mutation of ANO6 in two familial cases of Scott syndrome. *British journal of haematology.* England: Wiley-Blackwell.
BOLTE, S. & CORDELIERES, F. P. 2006. A guided tour into subcellular colocalization analysis in light microscopy. *Journal of Microscopy,* 224**,** 213-232.
BOSCO, R., ALVARADO, S., QUIROZ, D. & EBLEN-ZAJJUR, A. 2010. Digital Morphometric Characterization of Lumbar Dorsal Root Ganglion Neurons in Rats. *Journal of Histotechnology,* 33**,** 113-118.
BRADFORD, M. M. 1976. A rapid and sensitive method for the quantitation of microgram quantities of protein utilizing the principle of protein-dye binding. *Analytical Biochemistry,* 72**,** 248-254.
BRÜCKNER, A., POLGE, C., LENTZE, N., AUERBACH, D. & SCHLATTNER, U. 2009. Yeast two-hybrid, a powerful tool for systems biology. *Int J Mol Sci,* 10**,** 2763-2788.
CAI, S., GOMEZ, K., MOUTAL, A. & KHANNA, R. 2021. Targeting T-type/CaV3.2 channels for chronic pain. *Translational Research,* 234**,** 20-30.
CAIN, D. M., KHASABOV, S. G. & SIMONE, D. A. 2001. Response properties of mechanoreceptors and nociceptors in mouse glabrous skin: an in vivo study. *J Neurophysiol,* 85**,** 1561-74.
CAMPBELL, J. N. & LAMOTTE, R. H. 1983. Latency to detection of first pain. *Brain Res,* 266**,** 203-8.
CAMPRUBÍ-ROBLES, M., PLANELLS-CASES, R. & FERRER-MONTIEL, A. 2009. Differential contribution of SNARE-dependent exocytosis to inflammatory potentiation of TRPV1 in nociceptors. *The FASEB Journal,* 23**,** 3722-3733.

CAPUTO, A., CACI, E., FERRERA, L., PEDEMONTE, N., BARSANTI, C., SONDO, E., PFEFFER, U., RAVAZZOLO, R., ZEGARRA-MORAN, O. & GALIETTA, L. J. 2008. TMEM16A, a membrane protein associated with calcium-dependent chloride channel activity. *Science,* 322**,** 590-4.

CASTONGUAY, A. & ROBITAILLE, R. 2002. Xestospongin C is a potent inhibitor of SERCA at a vertebrate synapse. *Cell Calcium,* 32**,** 39-47.

CASTRO-JUNIOR, C. J., MILANO, J., SOUZA, A. H., SILVA, J. F., RIGO, F. K., DALMOLIN, G., CORDEIRO, M. N., RICHARDSON, M., BARROS, A. G. A., GOMEZ, R. S., SILVA, M. A. R., KUSHMERICK, C., FERREIRA, J. & GOMEZ, M. V. 2013. Phα1β toxin prevents capsaicin-induced nociceptive behavior and mechanical hypersensitivity without acting on TRPV1 channels. *Neuropharmacology,* 71**,** 237-246.

CATERINA, M. J., SCHUMACHER, M. A., TOMINAGA, M., ROSEN, T. A., LEVINE, J. D. & JULIUS, D. 1997. The capsaicin receptor: a heat-activated ion channel in the pain pathway. *Nature,* 389**,** 816-824.

CERUTI, S., FUMAGALLI, M., VILLA, G., VERDERIO, C. & ABBRACCHIO, M. P. 2008. Purinoceptor-mediated calcium signaling in primary neuron-glia trigeminal cultures. *Cell Calcium,* 43**,** 576-90.

CERUTI, S., VILLA, G., FUMAGALLI, M., COLOMBO, L., MAGNI, G., ZANARDELLI, M., FABBRETTI, E., VERDERIO, C., VAN DEN MAAGDENBERG, A. M. J. M., NISTRI, A. & ABBRACCHIO, M. P. 2011. Calcitonin Gene-Related Peptide-Mediated Enhancement of Purinergic Neuron/Glia Communication by the Algogenic Factor Bradykinin in Mouse Trigeminal Ganglia from Wild-Type and R192Q Ca_v2.1 Knock-In Mice: Implications for Basic Mechanisms of Migraine Pain. *The Journal of Neuroscience,* 31**,** 3638-3649.

CHANDRA, G., SREETAMA, S. C., MÁZALA, D. A. G., CHARTON, K., VANDERMEULEN, J. H., RICHARD, I. & JAISWAL, J. K. 2021. Endoplasmic reticulum maintains ion homeostasis required for plasma membrane repair. *Journal of Cell Biology,* 220**,** e202006035.

CHANG, C.-L., CHEN, Y.-J. & LIOU, J. 2017. ER-plasma membrane junctions: Why and how do we study them? *Biochimica et Biophysica Acta (BBA) - Molecular Cell Research,* 1864**,** 1494-1506.

CHANG, C. L., HSIEH, T. S., YANG, T. T., ROTHBERG, K. G., AZIZOGLU, D. B., VOLK, E., LIAO, J. C. & LIOU, J. 2013. Feedback regulation of receptor-induced Ca2+ signaling mediated by E-Syt1 and Nir2 at endoplasmic reticulum-plasma membrane junctions. *Cell Rep,* 5**,** 813-25.

CHEN, C., SMYE, S. W., ROBINSON, M. P. & EVANS, J. A. 2006. Membrane electroporation theories: a review. *Medical and Biological Engineering and Computing,* 44**,** 5-14.

CHEN, F., TILLBERG, P. W. & BOYDEN, E. S. 2015. Expansion microscopy. *Science,* 347**,** 543-548.

CHEN, Y.-J., QUINTANILLA, C. G. & LIOU, J. 2019. Recent insights into mammalian ER–PM junctions. *Current Opinion in Cell Biology,* 57**,** 99-105.

CHIPPERFIELD, A. R. & HARPER, A. A. 2000. Chloride in smooth muscle. *Prog Biophys Mol Biol,* 74**,** 175-221.

CHO, H. & OH, U. 2013. Anoctamin 1 mediates thermal pain as a heat sensor. *Curr Neuropharmacol,* 11**,** 641-51.

CHO, H., YANG, Y. D., LEE, J., LEE, B., KIM, T., JANG, Y., BACK, S. K., NA, H. S., HARFE, B. D., WANG, F., RAOUF, R., WOOD, J. N. & OH, U. 2012. The calcium-activated chloride channel anoctamin 1 acts as a heat sensor in nociceptive neurons. *Nature Neuroscience,* 15**,** 1015-1021.

CHOI, J. W., LIM, S., OH, Y.-S., KIM, E.-K., KIM, S.-H., KIM, Y.-H., HEO, K., KIM, J., KIM, J. K., YANG, Y. R., RYU, S. H. & SUH, P.-G. 2010. Subtype-specific role of phospholipase C-β in bradykinin and LPA signaling through differential binding of different PDZ scaffold proteins. *Cellular Signalling,* 22**,** 1153-1161.

CHONG, Z. X., YEAP, S. K. & HO, W. Y. 2021. Transfection types, methods and strategies: a technical review. *PeerJ,* 9**,** e11165.

CHU, Y., WU, Y., JIA, S., XU, K., LIU, J., MAI, L., FAN, W. & HUANG, F. 2023. Single-nucleus transcriptome analysis reveals transcriptional profiles of circadian clock and pain related genes in human and mouse trigeminal ganglion. *Frontiers in Neuroscience,* 17.

COX, G. & SHEPPARD, C. J. 2004. Practical limits of resolution in confocal and non-linear microscopy. *Microsc Res Tech,* 63**,** 18-22.

D'AMICO-MARTEL, A. & NODEN, D. M. 1983. Contributions of placodal and neural crest cells to avian cranial peripheral ganglia. *American Journal of Anatomy,* 166**,** 445-468.

DANG, S., FENG, S., TIEN, J., PETERS, C. J., BULKLEY, D., LOLICATO, M., ZHAO, J., ZUBERBÜHLER, K., YE, W., QI, L., CHEN, T., CRAIK, C. S., JAN, Y. N., MINOR, D. L., CHENG, Y. & JAN, L. Y. 2017. Cryo-EM structures of the TMEM16A calcium-activated chloride channel. *Nature,* 552**,** 426-429.

DARIAN-SMITH, I. 1973. The Trigeminal System. *In:* ALBE-FESSARD, D., ANDRES, K. H., BATES, J. A. V., BESSON, J. M., BROWN, A. G., BURGESS, P. R., DARIAN-SMITH, I., V. DÜRING, M., GORDON, G., HENSEL, H., JONES, E., LIBET, B., OSCARSSON, O., PERL, E. R., POMPEIANO, O., POWELL, T. P. S., RÉTHELYI, M., SCHMIDT, R. F., SEMMES, J., SKOGLUND, S., SZENTÁGOTHAI, J., TOWE, A. L., WALL, P. D., WERNER, G., WHITSEL, B. L., ZOTTERMAN, Y. & IGGO, A. (eds.) *Somatosensory System.* Berlin, Heidelberg: Springer Berlin Heidelberg.

DAUNER, K., LIßMANN, J., JERIDI, S., FRINGS, S. & MÖHRLEN, F. 2012. Expression patterns of anoctamin 1 and anoctamin 2 chloride channels in the mammalian nose. *Cell and Tissue Research,* 347**,** 327-341.

DAVIES, A., HENDRICH, J., VAN MINH, A. T., WRATTEN, J., DOUGLAS, L. & DOLPHIN, A. C. 2007. Functional biology of the alpha(2)delta subunits of voltage-gated calcium channels. *Trends Pharmacol Sci,* 28**,** 220-8.

DAVIS, A. J., FORREST, A. S., JEPPS, T. A., VALENCIK, M. L., WIWCHAR, M., SINGER, C. A., SONES, W. R., GREENWOOD, I. A. & LEBLANC, N. 2010. Expression profile and protein translation of TMEM16A in murine smooth muscle. *Am J Physiol Cell Physiol,* 299**,** C948-59.

DAVISON, A., LUX, U. T., BRANDSTÄTTER, J. H. & BABAI, N. 2022. T-Type Ca2+ Channels Boost Neurotransmission in Mammalian Cone Photoreceptors. *The Journal of Neuroscience,* 42**,** 6325-6343.

DE BEER, M. A. & GIEPMANS, B. N. G. 2020. Nanobody-Based Probes for Subcellular Protein Identification and Visualization. *Frontiers in Cellular Neuroscience,* 14.

DE JUAN-SANZ, J., HOLT, G. T., SCHREITER, E. R., DE JUAN, F., KIM, D. S. & RYAN, T. A. 2017. Axonal Endoplasmic Reticulum Ca2+ Content Controls Release Probability in CNS Nerve Terminals. *Neuron,* 93**,** 867-881.e6.

DEBA, F. & BESSAC, B. F. 2015. Anoctamin-1 Cl− Channels in Nociception: Activation by an N-Aroylaminothiazole and Capsaicin and Inhibition by T16A[inh]-A01. *Molecular Pain,* 11**,** s12990-015-0061-y.

DELMAS, P. & BROWN, D. A. 2002. Junctional signaling microdomains: bridging the gap between the neuronal cell surface and Ca2+ stores. *Neuron,* 36**,** 787-90.

DELMAS, P., WANAVERBECQ, N., ABOGADIE, F. C., MISTRY, M. & BROWN, D. A. 2002. Signaling microdomains define the specificity of receptor-mediated InsP(3) pathways in neurons. *Neuron,* 34**,** 209-20.

DENT, M., RAISMAN, G. & LAI, F. A. 1996. Expression of type 1 inositol 1,4,5-trisphosphate receptor during axogenesis and synaptic contact in the central and peripheral nervous system of developing rat. *Development (Cambridge, England),* 122**,** 1029-39.

DERLER, I., JARDIN, I. & ROMANIN, C. 2016. Molecular mechanisms of STIM/Orai communication. *Am J Physiol Cell Physiol,* 310**,** C643-62.

DIB-HAJJ, S. D., CHOI, J. S., MACALA, L. J., TYRRELL, L., BLACK, J. A., CUMMINS, T. R. & WAXMAN, S. G. 2009. Transfection of rat or mouse neurons by biolistics or electroporation. *Nature Protocols,* 4**,** 1118-1127.

DICKSON, E. J. & HILLE, B. 2019. Understanding phosphoinositides: rare, dynamic, and essential membrane phospholipids. *Biochemical Journal,* 476**,** 1-23.

DIEL, E. E., LICHTMAN, J. W. & RICHARDSON, D. S. 2020. Tutorial: avoiding and correcting sample-induced spherical aberration artifacts in 3D fluorescence microscopy. *Nature Protocols,* 15**,** 2773-2784.

DJOUHRI, L., BLEAZARD, L. & LAWSON, S. N. 1998. Association of somatic action potential shape with sensory receptive properties in guinea-pig dorsal root ganglion neurones. *J Physiol,* 513 (Pt 3)**,** 857-72.

DJOUHRI, L. & LAWSON, S. N. 2004. Aβ-fiber nociceptive primary afferent neurons: a review of incidence and properties in relation to other afferent A-fiber neurons in mammals. *Brain Research Reviews,* 46**,** 131-145.

DOLPHIN, A. C. 2021. Functions of Presynaptic Voltage-gated Calcium Channels. *Function,* 2**,** zqaa027.

DOYLE, J. P., DOUGHERTY, J. D., HEIMAN, M., SCHMIDT, E. F., STEVENS, T. R., MA, G., BUPP, S., SHRESTHA, P., SHAH, R. D., DOUGHTY, M. L., GONG, S., GREENGARD, P. & HEINTZ, N. 2008. Application of a translational profiling approach for the comparative analysis of CNS cell types. *Cell,* 135**,** 749-62.

DRUMM, B. T., HANNIGAN, K. I., LEE, J. Y., REMBETSKI, B. E., BAKER, S. A., KOH, S. D., COBINE, C. A. & SANDERS, K. M. 2022. Ca(2+) signalling in interstitial cells of Cajal contributes to generation and maintenance of tone in mouse and monkey lower oesophageal sphincters. *J Physiol,* 600**,** 2613-2636.

DU, X., HAO, H., GIGOUT, S., HUANG, D., YANG, Y., LI, L., WANG, C., SUNDT, D., JAFFE, D. B., ZHANG, H. & GAMPER, N. 2014. Control of somatic membrane potential in nociceptive neurons and its implications for peripheral nociceptive transmission. *Pain,* 155**,** 2306-22.

DU, X., HAO, H., YANG, Y., HUANG, S., WANG, C., GIGOUT, S., RAMLI, R., LI, X., JAWORSKA, E., EDWARDS, I., DEUCHARS, J., YANAGAWA, Y., QI, J., GUAN, B., JAFFE, D. B., ZHANG, H. & GAMPER, N. 2017. Local GABAergic signaling within sensory ganglia controls peripheral nociceptive transmission. *The Journal of Clinical Investigation,* 127**,** 1741-1756.

DUBIN, A. E. & PATAPOUTIAN, A. 2010a. Nociceptors: the sensors of the pain pathway. *The Journal of Clinical Investigation,* 120**,** 3760-3772.
DUBIN, A. E. & PATAPOUTIAN, A. 2010b. Nociceptors: the sensors of the pain pathway. *J Clin Invest,* 120**,** 3760-72.
DULIN, N. O. 2020. Calcium-Activated Chloride Channel ANO1/TMEM16A: Regulation of Expression and Signaling. *Frontiers in Physiology,* 11.
DUNST, S. & TOMANCAK, P. 2019. Imaging Flies by Fluorescence Microscopy: Principles, Technologies, and Applications. *Genetics,* 211**,** 15-34.
DURAN, C. & HARTZELL, H. C. 2011. Physiological roles and diseases of tmem16/anoctamin proteins: are they all chloride channels? *Acta Pharmacologica Sinica,* 32**,** 685-692.
DUTTA, A. K., KHIMJI, A.-K., KRESGE, C., BUGDE, A., DOUGHERTY, M., ESSER, V., UENO, Y., GLASER, S. S., ALPINI, G., ROCKEY, D. C. & FERANCHAK, A. P. 2011. Identification and Functional Characterization of TMEM16A, a Ca2+-activated Cl− Channel Activated by Extracellular Nucleotides, in Biliary Epithelium*. *Journal of Biological Chemistry,* 286**,** 766-776.
DUX, M., VOGLER, B., KUHN, A., MACKENZIE, K. D., STRATTON, J. & MESSLINGER, K. 2022. The Anti-CGRP Antibody Fremanezumab Lowers CGRP Release from Rat Dura Mater and Meningeal Blood Flow. *Cells,* 11**,** 1768.
EBERHARD, D. A. & HOLZ, R. W. 1988. Intracellular Ca2+ activates phospholipase C. *Trends in Neurosciences,* 11**,** 517-520.
EDVINSSON, J. C. A., WARFVINGE, K., KRAUSE, D. N., BLIXT, F. W., SHEYKHZADE, M., EDVINSSON, L. & HAANES, K. A. 2019. C-fibers may modulate adjacent Aδ-fibers through axon-axon CGRP signaling at nodes of Ranvier in the trigeminal system. *The Journal of Headache and Pain,* 20**,** 105.
EDVINSSON, L., GRELL, A. S. & WARFVINGE, K. 2020. Expression of the CGRP Family of Neuropeptides and their Receptors in the Trigeminal Ganglion. *J Mol Neurosci,* 70**,** 930-944.
EFTEKHARI, S. & EDVINSSON, L. 2011. Calcitonin gene-related peptide (CGRP) and its receptor components in human and rat spinal trigeminal nucleus and spinal cord at C1-level. *BMC Neuroscience,* 12**,** 112.
EFTEKHARI, S., WARFVINGE, K., BLIXT, F. W. & EDVINSSON, L. 2013. Differentiation of nerve fibers storing CGRP and CGRP receptors in the peripheral trigeminovascular system. *J Pain,* 14**,** 1289-303.
FABBRETTI, E., D'ARCO, M., FABBRO, A., SIMONETTI, M., NISTRI, A. & GINIATULLIN, R. 2006. Delayed upregulation of ATP P2X3 receptors of trigeminal sensory neurons by calcitonin gene-related peptide. *J Neurosci,* 26**,** 6163-71.
FALZONE, M. E., MALVEZZI, M., LEE, B. C. & ACCARDI, A. 2018. Known structures and unknown mechanisms of TMEM16 scramblases and channels. *J Gen Physiol,* 150**,** 933-947.
FERNÁNDEZ-BUSNADIEGO, R. 2016. Supramolecular architecture of endoplasmic reticulum–plasma membrane contact sites. *Biochemical Society Transactions,* 44**,** 534-540.
FERNÁNDEZ-BUSNADIEGO, R., SAHEKI, Y. & DE CAMILLI, P. 2015a. Three-dimensional architecture of extended synaptotagmin-mediated endoplasmic reticulum-plasma membrane contact sites. *Proc Natl Acad Sci U S A,* 112**,** E2004-13.
FERNÁNDEZ-BUSNADIEGO, R., SAHEKI, Y. & DE CAMILLI, P. 2015b. Three-dimensional architecture of extended synaptotagmin-mediated endoplasmic reticulum–

plasma membrane contact sites. *Proceedings of the National Academy of Sciences,* 112**,** E2004-E2013.
FERRI, G.-L., SABANI, A., ABELLI, L., POLAK, J. M., DAHL, D. & PORTIER, M.-M. 1990. Neuronal intermediate filaments in rat dorsal root ganglia: differential distribution of peripherin and neurofilament protein immunoreactivity and effect of capsaicin. *Brain Research,* 515**,** 331-335.
FERRON, L., KOSHTI, S. & ZAMPONI, G. W. 2021. The life cycle of voltage-gated Ca2+ channels in neurons: an update on the trafficking of neuronal calcium channels. *Neuronal Signaling,* 5.
FLEGEL, C., SCHÖBEL, N., ALTMÜLLER, J., BECKER, C., TANNAPFEL, A., HATT, H. & GISSELMANN, G. 2015. RNA-Seq Analysis of Human Trigeminal and Dorsal Root Ganglia with a Focus on Chemoreceptors. *PLoS One,* 10**,** e0128951.
FLORES, C. M., LEONG, A. S., O. DUSSOR, G., CATHERINE, H.-R., HARGREAVES, K. M. & KILO, S. 2001. Capsaicin-evoked CGRP release from rat buccal mucosa: development of a model system for studying trigeminal mechanisms of neurogenic inflammation. *European Journal of Neuroscience,* 14**,** 1113-1120.
FORTELNY, N., OVERALL, C. M., PAVLIDIS, P. & FREUE, G. V. C. 2017. Can we predict protein from mRNA levels? *Nature,* 547**,** E19-E20.
FREDRIKSSON, S., GULLBERG, M., JARVIUS, J., OLSSON, C., PIETRAS, K., GÚSTAFSDÓTTIR, S. M., OSTMAN, A. & LANDEGREN, U. 2002. Protein detection using proximity-dependent DNA ligation assays. *Nat Biotechnol,* 20**,** 473-7.
FRINGS, S., REUTER, D. & KLEENE, S. J. 2000. Neuronal Ca2+-activated Cl− channels — homing in on an elusive channel species. *Progress in Neurobiology,* 60**,** 247-289.
FULLER, A. M., LUIZ, A., TIAN, N., ARCANGELETTI, M., ISEPPON, F., SEXTON, J. E., MILLET, Q., CAXARIA, S., KETABI, N., CELIK, P., WOOD, J. N. & SIKANDAR, S. 2023. Gate control of sensory neurotransmission in peripheral ganglia by proprioceptive sensory neurons. *Brain,* 146**,** 4033-4039.
GALIETTA, L. J. 2009. The TMEM16 protein family: a new class of chloride channels? *Biophys J,* 97**,** 3047-53.
GALIETTA, L. J., HAGGIE, P. M. & VERKMAN, A. S. 2001. Green fluorescent protein-based halide indicators with improved chloride and iodide affinities. *FEBS Lett,* 499**,** 220-4.
GAMPER, N. & SHAH, S. 2022. Inferiority complex: why do sensory ion channels multimerize? *Biochemical Society Transactions,* 50**,** 213-222.
GAO, Y., ZORMAN, S., GUNDERSEN, G., XI, Z., MA, L., SIRINAKIS, G., ROTHMAN, J. E. & ZHANG, Y. 2012. Single reconstituted neuronal SNARE complexes zipper in three distinct stages. *Science,* 337**,** 1340-3.
GÁRATE, G., PASCUAL, J., PASCUAL-MATO, M., MADERA, J., MARTÍN, M. M.-S. & GONZÁLEZ-QUINTANILLA, V. 2024. Untangling the mess of CGRP levels as a migraine biomarker: an in-depth literature review and analysis of our experimental experience. *The Journal of Headache and Pain,* 25**,** 69.
GARCÍA, G., MARTÍNEZ-ROJAS, V. A., OVIEDO, N. & MURBARTIÁN, J. 2018. Blockade of anoctamin-1 in injured and uninjured nerves reduces neuropathic pain. *Brain Research,* 1696**,** 38-48.
GARCÍA, G., MARTÍNEZ-ROJAS, V. A., ROCHA-GONZÁLEZ, H. I., GRANADOS-SOTO, V. & MURBARTIÁN, J. 2014. Evidence for the participation of Ca2+-activated chloride channels in formalin-induced acute and chronic nociception. *Brain Research,* 1579**,** 35-44.

GASSER, H. S. & ERLANGER, J. 1929. THE RÔLE OF FIBER SIZE IN THE ESTABLISHMENT OF A NERVE BLOCK BY PRESSURE OR COCAINE. *American Journal of Physiology-Legacy Content,* 88**,** 581-591.

GE, J., BIAN, X., MA, L., CAI, Y., LI, Y., YANG, J., KARATEKIN, E., DE CAMILLI, P. & ZHANG, Y. 2022. Stepwise membrane binding of extended synaptotagmins revealed by optical tweezers. *Nat Chem Biol,* 18**,** 313-320.

GEDEON, J. Y., PINEDA-FARIAS, J. B. & GOLD, M. S. 2024. *JoVE***,** e65978.

GINGELL, J. J., REES, T. A., HENDRIKSE, E. R., SIOW, A., RENNISON, D., SCOTTER, J., HARRIS, P. W. R., BRIMBLE, M. A., WALKER, C. S. & HAY, D. L. 2020. Distinct Patterns of Internalization of Different Calcitonin Gene-Related Peptide Receptors. *ACS Pharmacology & Translational Science,* 3**,** 296-304.

GIORDANO, F., SAHEKI, Y., IDEVALL-HAGREN, O., COLOMBO, S. F., PIRRUCCELLO, M., MILOSEVIC, I., GRACHEVA, E. O., BAGRIANTSEV, S. N., BORGESE, N. & DE CAMILLI, P. 2013. PI(4,5)P(2)-dependent and Ca(2+)-regulated ER-PM interactions mediated by the extended synaptotagmins. *Cell,* 153**,** 1494-509.

GOADSBY, P. J., EDVINSSON, L. & EKMAN, R. 1990. Vasoactive peptide release in the extracerebral circulation of humans during migraine headache. *Annals of Neurology,* 28**,** 183-187.

GOLINI, L., CHOUABE, C., BERTHIER, C., CUSIMANO, V., FORNARO, M., BONVALLET, R., FORMOSO, L., GIACOMELLO, E., JACQUEMOND, V. & SORRENTINO, V. 2011. Junctophilin 1 and 2 proteins interact with the L-type Ca2+ channel dihydropyridine receptors (DHPRs) in skeletal muscle. *J Biol Chem,* 286**,** 43717-43725.

GÖTTFERT, F., WURM, CHRISTIAN A., MUELLER, V., BERNING, S., CORDES, VOLKER C., HONIGMANN, A. & HELL, STEFAN W. 2013. Coaligned Dual-Channel STED Nanoscopy and Molecular Diffusion Analysis at 20 nm Resolution. *Biophysical Journal,* 105**,** L01-L03.

GRUSZCZYNSKA-BIEGALA, J. & KUZNICKI, J. 2013. Native STIM2 and ORAI1 proteins form a calcium-sensitive and thapsigargin-insensitive complex in cortical neurons. *Journal of Neurochemistry,* 126**,** 727-738.

GUO, Z., CZERPANIAK, K., ZHANG, J. & CAO, Y. Q. 2021. Increase in trigeminal ganglion neurons that respond to both calcitonin gene-related peptide and pituitary adenylate cyclase-activating polypeptide in mouse models of chronic migraine and posttraumatic headache. *Pain,* 162**,** 1483-1499.

GUPTA, S., AMRUTKAR, D. V., MATAJI, A., SALMASI, H., HAY-SCHMIDT, A., SHEYKHZADE, M., MESSLINGER, K., OLESEN, J. & JANSEN-OLESEN, I. 2010. Evidence for CGRP re-uptake in rat dura mater encephali. *British Journal of Pharmacology,* 161**,** 1885-1898.

HAANES, K. A. & EDVINSSON, L. 2019. Pathophysiological Mechanisms in Migraine and the Identification of New Therapeutic Targets. *CNS Drugs,* 33**,** 525-537.

HABERBERGER, R. V., KURAMATILAKE, J., BARRY, C. M. & MATUSICA, D. 2023. Ultrastructure of dorsal root ganglia. *Cell Tissue Res,* 393**,** 17-36.

HANNA, M. G., BLOCK, S., FRANKEL, E. B., HOU, F., JOHNSON, A., YUAN, L., KNIGHT, G., MORESCO, J. J., YATES, J. R., 3RD, ASHTON, R., SCHEKMAN, R., TONG, Y. & AUDHYA, A. 2017. TFG facilitates outer coat disassembly on COPII transport carriers to promote tethering and fusion with ER-Golgi intermediate compartments. *Proc Natl Acad Sci U S A,* 114**,** E7707-e7716.

HAO, H., RAMLI, R., WANG, C., LIU, C., SHAH, S., MULLEN, P., LALL, V., JONES, F., SHAO, J., ZHANG, H., JAFFE, D. B., GAMPER, N. & DU, X. 2023. Dorsal root ganglia control nociceptive input to the central nervous system. *PLOS Biology,* 21**,** e3001958.

HARKE, B., KELLER, J., ULLAL, C. K., WESTPHAL, V., SCHÖNLE, A. & HELL, S. W. 2008. Resolution scaling in STED microscopy. *Optics Express,* 16**,** 4154-4162.

HARTLINE, D. K. & COLMAN, D. R. 2007. Rapid Conduction and the Evolution of Giant Axons and Myelinated Fibers. *Current Biology,* 17**,** R29-R35.

HARTZELL, C., PUTZIER, I. & ARREOLA, J. 2005. Calcium-activated chloride channels. *Annu Rev Physiol,* 67**,** 719-58.

HAWN, M. B., AKIN, E., HARTZELL, H. C., GREENWOOD, I. A. & LEBLANC, N. 2021. Molecular mechanisms of activation and regulation of ANO1-Encoded Ca(2+)-Activated Cl(-) channels. *Channels (Austin),* 15**,** 569-603.

HE, Q., HALM, S. T., ZHANG, J. & HALM, D. R. 2011. Activation of the basolateral membrane Cl- conductance essential for electrogenic K+ secretion suppresses electrogenic Cl- secretion. *Exp Physiol,* 96**,** 305-16.

HEIMAN, M., SCHAEFER, A., GONG, S., PETERSON, J. D., DAY, M., RAMSEY, K. E., SUÁREZ-FARIÑAS, M., SCHWARZ, C., STEPHAN, D. A., SURMEIER, D. J., GREENGARD, P. & HEINTZ, N. 2008. A translational profiling approach for the molecular characterization of CNS cell types. *Cell,* 135**,** 738-48.

HELL, S. W. & WICHMANN, J. 1994. Breaking the diffraction resolution limit by stimulated emission: stimulated-emission-depletion fluorescence microscopy. *Optics Letters,* 19**,** 780-782.

HELLIWELL, R. J. A., MCLATCHIE, L. M., CLARKE, M., WINTER, J., BEVAN, S. & MCINTYRE, P. 1998. Capsaicin sensitivity is associated with the expression of the vanilloid (capsaicin) receptor (VR1) mRNA in adult rat sensory ganglia. *Neuroscience Letters,* 250**,** 177-180.

HELTON, T. D., XU, W. & LIPSCOMBE, D. 2005. Neuronal L-Type Calcium Channels Open Quickly and Are Inhibited Slowly. *The Journal of Neuroscience,* 25**,** 10247-10251.

HENRY, C., CARRERAS-SUREDA, A. & DEMAUREX, N. 2022. Enforced tethering elongates the cortical endoplasmic reticulum and limits store-operated Ca2+ entry. *Journal of Cell Science,* 135.

HIGERD-RUSLI, G. P., TYAGI, S., BAKER, C. A., LIU, S., DIB-HAJJ, F. B., DIB-HAJJ, S. D. & WAXMAN, S. G. 2023. Inflammation differentially controls transport of depolarizing Nav versus hyperpolarizing Kv channels to drive rat nociceptor activity. *Proceedings of the National Academy of Sciences,* 120**,** e2215417120.

HOFFMANN, J., BACA, S. M. & AKERMAN, S. 2019. Neurovascular mechanisms of migraine and cluster headache. *J Cereb Blood Flow Metab,* 39**,** 573-594.

HOGAN, P. G. 2015. The STIM1–ORAI1 microdomain. *Cell Calcium,* 58**,** 357-367.

HOGEA, A., SHAH, S., JONES, F., CARVER, C. M., HAO, H., LIANG, C., HUANG, D., DU, X. & GAMPER, N. 2021. Junctophilin-4 facilitates inflammatory signalling at plasma membrane-endoplasmic reticulum junctions in sensory neurons. *J Physiol,* 599**,** 2103-2123.

HUANG, D., LI, S., DHAKA, A., STORY, G. M. & CAO, Y.-Q. 2012. Expression of the Transient Receptor Potential Channels TRPV1, TRPA1 and TRPM8 in Mouse Trigeminal Primary Afferent Neurons Innervating the Dura. *Molecular Pain,* 8**,** 1744-8069-8-66.

HUANG, F., WANG, X., OSTERTAG, E. M., NUWAL, T., HUANG, B., JAN, Y.-N., BASBAUM, A. I. & JAN, L. Y. 2013. TMEM16C facilitates Na+-activated K+ currents in rat sensory neurons and regulates pain processing. *Nature Neuroscience,* 16**,** 1284-1290.

HUANG, P., LIU, J., DI, A., ROBINSON, N. C., MUSCH, M. W., KAETZEL, M. A. & NELSON, D. J. 2001. Regulation of human CLC-3 channels by multifunctional Ca2+/calmodulin-dependent protein kinase. *J Biol Chem,* 276**,** 20093-100.

HUFF, J. 2015. The Airyscan detector from ZEISS: confocal imaging with improved signal-to-noise ratio and super-resolution. *Nature Methods,* 12.

HURLEY, M. E., SHAH, S. S., SHEARD, T. M. D., KIRTON, H. M., STEELE, D. S., GAMPER, N. & JAYASINGHE, I. 2023. Super-Resolution Analysis of the Origins of the Elementary Events of ER Calcium Release in Dorsal Root Ganglion Neurons. *Cells,* 13.

IDEVALL-HAGREN, O., LÜ, A., XIE, B. & DE CAMILLI, P. 2015. Triggered Ca2+ influx is required for extended synaptotagmin 1-induced ER-plasma membrane tethering. *Embo j,* 34**,** 2291-305.

INGOLIA, N. T. 2016. Ribosome Footprint Profiling of Translation throughout the Genome. *Cell,* 165**,** 22-33.

INGRAM, S., CHISHOLM, K. I., WANG, F., DE KONINCK, Y., DENK, F. & GOODWIN, G. L. 2024. Assessing spontaneous sensory neuron activity using in vivo calcium imaging. *PAIN,* 165.

IYENGAR, S., OSSIPOV, M. H. & JOHNSON, K. W. 2017. The role of calcitonin gene–related peptide in peripheral and central pain mechanisms including migraine. *PAIN,* 158.

JACUS, M. O., UEBELE, V. N., RENGER, J. J. & TODOROVIC, S. M. 2012. Presynaptic Cav3.2 channels regulate excitatory neurotransmission in nociceptive dorsal horn neurons. *J Neurosci,* 32**,** 9374-82.

JARVIUS, J., MELIN, J., GÖRANSSON, J., STENBERG, J., FREDRIKSSON, S., GONZALEZ-REY, C., BERTILSSON, S. & NILSSON, M. 2006. Digital quantification using amplified single-molecule detection. *Nat Methods,* 3**,** 725-7.

JENG, G., AGGARWAL, M., YU, W.-P. & CHEN, T.-Y. 2016. Independent activation of distinct pores in dimeric TMEM16A channels. *Journal of General Physiology,* 148**,** 393-404.

JENKINS, D. W., LANGMEAD, C. J., PARSONS, A. A. & STRIJBOS, P. J. 2004. Regulation of calcitonin gene-related peptide release from rat trigeminal nucleus caudalis slices in vitro. *Neuroscience Letters,* 366**,** 241-244.

JHA, A., CHUNG, W. Y., VACHEL, L., MALETH, J., LAKE, S., ZHANG, G., AHUJA, M. & MUALLEM, S. 2019. Anoctamin 8 tethers endoplasmic reticulum and plasma membrane for assembly of Ca(2+) signaling complexes at the ER/PM compartment. *Embo j,* 38.

JIN, X., SHAH, S., DU, X., ZHANG, H. & GAMPER, N. 2016. Activation of Ca2+-activated Cl− channel ANO1 by localized Ca2+ signals. *The Journal of Physiology,* 594**,** 19-30.

JIN, X., SHAH, S., LIU, Y., ZHANG, H., LEES, M., FU, Z., LIPPIAT, J. D., BEECH, D. J., SIVAPRASADARAO, A., BALDWIN, S. A., ZHANG, H. & GAMPER, N. 2013. Activation of the Cl- channel ANO1 by localized calcium signals in nociceptive sensory neurons requires coupling with the IP3 receptor. *Sci Signal,* 6**,** ra73.

KANAZAWA, T. & MATSUMOTO, S. 2014. Expression of transient receptor potential vanilloid 1 and anoctamin 1 in rat trigeminal ganglion neurons innervating the tongue. *Brain Res Bull,* 106**,** 17-20.

KANEKO, H., PUTZIER, I., FRINGS, S. & GENSCH, T. 2002. Determination of intracellular chloride concentration in dorsal root ganglion neurons by fluorescence lifetime imaging. *Current Topics in Membranes.* Academic Press.

KANEKO, H., PUTZIER, I., FRINGS, S., KAUPP, U. B. & GENSCH, T. 2004. Chloride Accumulation in Mammalian Olfactory Sensory Neurons. *The Journal of Neuroscience,* 24**,** 7931.

KANG, F., ZHOU, M., HUANG, X., FAN, J., WEI, L., BOULANGER, J., LIU, Z., SALAMERO, J., LIU, Y. & CHEN, L. 2019a. E-syt1 Re-arranges STIM1 Clusters to Stabilize Ring-shaped ER-PM Contact Sites and Accelerate Ca(2+) Store Replenishment. *Sci Rep,* 9**,** 3975.

KANG, F., ZHOU, M., HUANG, X., FAN, J., WEI, L., BOULANGER, J., ZENGZHEN, L., SALAMERO, J., LIU, Y. & CHEN, L. 2019b. E-syt1 Re-arranges STIM1 Clusters to Stabilize Ring-shaped ER-PM Contact Sites and Accelerate Ca2+ Store Replenishment. *Scientific Reports,* 9.

KATANOSAKA, K., BANIK, R. K., GIRON, R., HIGASHI, T., TOMINAGA, M. & MIZUMURA, K. 2008. Contribution of TRPV1 to the bradykinin-evoked nociceptive behavior and excitation of cutaneous sensory neurons. *Neuroscience Research,* 62**,** 168-175.

KAWAGUCHI, A., SATO, M., KIMURA, M., YAMAZAKI, T., YAMAMOTO, H., TAZAKI, M., ICHINOHE, T. & SHIBUKAWA, Y. 2015. Functional expression of bradykinin B1 and B2 receptors in neonatal rat trigeminal ganglion neurons. *Front Cell Neurosci,* 9**,** 229.

KAWATA, N., KONDO, R., SUZUKI, Y. & YAMAMURA, H. 2022. Increased TMEM16A-Mediated Ca²⁺-Activated Cl[−] Currents in Portal Vein Smooth Muscle Cells of Caveolin 1-Deficient Mice. *Biological and Pharmaceutical Bulletin,* 45**,** 1692-1698.

KC, E., ISLAM, J. & PARK, Y. S. 2022. Trigeminal ganglion itself can be a viable target to manage trigeminal neuralgia. *The Journal of Headache and Pain,* 23**,** 150.

KHAN, R., GUL, B., KHAN, S., NISAR, H. & AHMAD, I. 2021. Refractive index of biological tissues: Review, measurement techniques, and applications. *Photodiagnosis and Photodynamic Therapy,* 33**,** 102192.

KIM, H., KIM, H., LEE, J., LEE, B., KIM, H. R., JUNG, J., LEE, M. O. & OH, U. 2018. Anoctamin 9/TMEM16J is a cation channel activated by cAMP/PKA signal. *Cell Calcium,* 71**,** 75-85.

KIM, H., KIM, H., NGUYEN, L. T., HA, T., LIM, S., KIM, K., KIM, S. H., HAN, K., HYEON, S. J., RYU, H., PARK, Y. S., KIM, S. H., KIM, I.-B., HONG, G.-S., LEE, S. E., CHOI, Y., COHEN, L. B. & OH, U. 2022. Amplification of olfactory signals by Anoctamin 9 is important for mammalian olfaction. *Progress in Neurobiology,* 219**,** 102369.

KIM, H., SHIM, W.-S. & OH, U. 2024. Anoctamin 1, a multi-modal player in pain and itch. *Cell Calcium,* 123**,** 102924.

KIM, S.-O., KIM, J., OKAJIMA, T. & CHO, N.-J. 2017. Mechanical properties of paraformaldehyde-treated individual cells investigated by atomic force microscopy and scanning ion conductance microscopy. *Nano Convergence,* 4**,** 5.

KIM, S., MA, L., UNRUH, J., MCKINNEY, S. & YU, C. R. 2015. Intracellular chloride concentration of the mouse vomeronasal neuron. *BMC Neuroscience,* 16**,** 90.

KLOCKNER, U., LEE, J.-H., CRIBBS, L. L., DAUD, A., HESCHELER, J., PEREVERZEV, A., PEREZ-REYES, E. & SCHNEIDER, T. 1999. Comparison of the Ca2+ currents induced by expression of three cloned a1 subunits, a1G, a1H and a1I, of low-voltage-activated T-type Ca2+ channels. *European Journal of Neuroscience,* 11**,** 4171-4178.

KOBAYASHI, K., FUKUOKA, T., OBATA, K., YAMANAKA, H., DAI, Y., TOKUNAGA, A. & NOGUCHI, K. 2005. Distinct expression of TRPM8, TRPA1, and TRPV1 mRNAs in rat primary afferent neurons with aδ/c-fibers and colocalization with trk receptors. *Journal of Comparative Neurology,* 493**,** 596-606.

KOGELMAN, L. J. A., CHRISTENSEN, R. E., PEDERSEN, S. H., BERTALAN, M., HANSEN, T. F., JANSEN-OLESEN, I. & OLESEN, J. 2017. Whole transcriptome expression of trigeminal ganglia compared to dorsal root ganglia in Rattus Norvegicus. *Neuroscience,* 350**,** 169-179.

KORCZENIEWSKA, O. A., HUSAIN, S., HOQUE, M., SOTEROPOULOS, P., KHAN, J., ELIAV, E. & BENOLIEL, R. 2024. Time-Course Progression of Whole Transcriptome Expression Changes of Trigeminal Ganglia Compared to Dorsal Root Ganglia in Rats Exposed to Nerve Injury. *The Journal of Pain,* 25**,** 101-117.

KORCZENIEWSKA, O. A., KATZMANN RIDER, G., GAJRA, S., NARRA, V., RAMAVAJLA, V., CHANG, Y.-J., TAO, Y., SOTEROPOULOS, P., HUSAIN, S., KHAN, J., ELIAV, E. & BENOLIEL, R. 2020. Differential gene expression changes in the dorsal root versus trigeminal ganglia following peripheral nerve injury in rats. *European Journal of Pain,* 24**,** 967-982.

KRAENZLIN, M. E., CH'NG, J. L. C., MULDERRY, P. K., GHATEI, M. A. & BLOOM, S. R. 1985. Infusion of a novel peptide, calcitonin gene-related peptide (CGRP) in man. Pharmacokinetics and effects on gastric acid secretion and on gastrointestinal hormones. *Regulatory Peptides,* 10**,** 189-197.

KRAUß, S. D., PETERSEN, D., NIEDIEKER, D., FRICKE, I., FREIER, E., EL-MASHTOLY, S. F., GERWERT, K. & MOSIG, A. 2015. Colocalization of fluorescence and Raman microscopic images for the identification of subcellular compartments: a validation study. *Analyst,* 140**,** 2360-2368.

KRISPIN, S., NITZAN, E. & KALCHEIM, C. 2010. The dorsal neural tube: A dynamic setting for cell fate decisions. *Developmental Neurobiology,* 70**,** 796-812.

KUNZELMANN, K., OUSINGSAWAT, J. & SCHREIBER, R. 2024. Anoctamins in epithelial transport. *Cell Calcium,* 120**,** 102888.

KUROKAWA, K., OKAMOTO, M. & NAKANO, A. 2014. Contact of cis-Golgi with ER exit sites executes cargo capture and delivery from the ER. *Nature Communications,* 5**,** 3653.

KUWASHIMA, Y., YANAGAWA, M., ABE, M., HIROSHIMA, M., UEDA, M., ARITA, M. & SAKO, Y. 2021. Comparative Analysis of Single-Molecule Dynamics of TRPV1 and TRPV4 Channels in Living Cells. *Int J Mol Sci,* 22.

KYRIAKOPOULOU, E. 2019. *Reciprocal regulation of the Fibroblast Growth Factor Receptor 2 (FGFR2) and the Transient Receptor Potential Ankyrin 1 (TRPA1) through their direct interaction.* Doctor of Philosophy, University of Leeds.

LAGARES, A. & AVENDAÑO, C. 2000. Lateral asymmetries in the trigeminal ganglion of the male rat. *Brain Research,* 865**,** 202-210.

LAM, A. K. M., RHEINBERGER, J., PAULINO, C. & DUTZLER, R. 2021. Gating the pore of the calcium-activated chloride channel TMEM16A. *Nature Communications,* 12**,** 785.

LE PICHON, C. E. & CHESLER, A. T. 2014. The functional and anatomical dissection of somatosensory subpopulations using mouse genetics. *Frontiers in Neuroanatomy,* 8.

LE, S. C. & YANG, H. 2020. An Additional Ca2+ Binding Site Allosterically Controls TMEM16A Activation. *Cell Reports,* 33**,** 108570.

LENNERZ, J. K., RÜHLE, V., CEPPA, E. P., NEUHUBER, W. L., BUNNETT, N. W., GRADY, E. F. & MESSLINGER, K. 2008. Calcitonin receptor-like receptor (CLR), receptor activity-modifying protein 1 (RAMP1), and calcitonin gene-related peptide (CGRP) immunoreactivity in the rat trigeminovascular system: Differences between peripheral and central CGRP receptor distribution. *Journal of Comparative Neurology,* 507**,** 1277-1299.

LÉRIAS, J. R., PINTO, M. C., BOTELHO, H. M., AWATADE, N. T., QUARESMA, M. C., SILVA, I. A. L., WANITCHAKOOL, P., SCHREIBER, R., PEPPERKOK, R., KUNZELMANN, K. & AMARAL, M. D. 2018. A novel microscopy-based assay identifies extended synaptotagmin-1 (ESYT1) as a positive regulator of anoctamin 1 traffic. *Biochim Biophys Acta Mol Cell Res,* 1865**,** 421-431.

LI, C. L., LI, K. C., WU, D., CHEN, Y., LUO, H., ZHAO, J. R., WANG, S. S., SUN, M. M., LU, Y. J., ZHONG, Y. Q., HU, X. Y., HOU, R., ZHOU, B. B., BAO, L., XIAO, H. S. & ZHANG, X. 2016. Somatosensory neuron types identified by high-coverage single-cell RNA-sequencing and functional heterogeneity. *Cell Res,* 26**,** 83-102.

LI, P., BANJADE, S., CHENG, H. C., KIM, S., CHEN, B., GUO, L., LLAGUNO, M., HOLLINGSWORTH, J. V., KING, D. S., BANANI, S. F., RUSSO, P. S., JIANG, Q. X., NIXON, B. T. & ROSEN, M. K. 2012. Phase transitions in the assembly of multivalent signalling proteins. *Nature,* 483**,** 336-40.

LI, X., PRUDENTE, A. S., PRATO, V., GUO, X., HAO, H., JONES, F., FIGOLI, S., MULLEN, P., WANG, Y., TONELLO, R., LEE, S. H., SHAH, S., MAFFEI, B., BERTA, T., DU, X. & GAMPER, N. 2024. Peripheral gating of mechanosensation by glial diazepam binding inhibitor. *The Journal of Clinical Investigation,* 134.

LIM, N. K., LAM, A. K. M. & DUTZLER, R. 2016. Independent activation of ion conduction pores in the double-barreled calcium-activated chloride channel TMEM16A. *Journal of General Physiology,* 148**,** 375-392.

LIPSCOMBE, D., HELTON, T. D. & XU, W. 2004. L-Type Calcium Channels: The Low Down. *Journal of Neurophysiology,* 92**,** 2633-2641.

LIU, B., LINLEY, J. E., DU, X., ZHANG, X., OOI, L., ZHANG, H. & GAMPER, N. 2010. The acute nociceptive signals induced by bradykinin in rat sensory neurons are mediated by inhibition of M-type K+ channels and activation of Ca2+-activated Cl– channels. *The Journal of Clinical Investigation,* 120**,** 1240-1252.

LIU, H. 2019. Receptor Mediated Activation of TRPC3 Channel When at ER PM Junctions. *Biophysical Journal,* 116**,** 537a.

LIU, Y., BEYER, A. & AEBERSOLD, R. 2016. On the Dependency of Cellular Protein Levels on mRNA Abundance. *Cell,* 165**,** 535-550.

LOPES, D. M., DENK, F. & MCMAHON, S. B. 2017a. The Molecular Fingerprint of Dorsal Root and Trigeminal Ganglion Neurons. *Front Mol Neurosci,* 10**,** 304.

LOPES, D. M., MALEK, N., EDYE, M., JAGER, S. B., MCMURRAY, S., MCMAHON, S. B. & DENK, F. 2017b. Sex differences in peripheral not central immune responses to pain-inducing injury. *Sci Rep,* 7**,** 16460.

LUKACS, V., THYAGARAJAN, B., VARNAI, P., BALLA, A., BALLA, T. & ROHACS, T. 2007. Dual regulation of TRPV1 by phosphoinositides. *J Neurosci,* 27**,** 7070-80.

LUKACS, V., YUDIN, Y., HAMMOND, G. R., SHARMA, E., FUKAMI, K. & ROHACS, T. 2013. Distinctive changes in plasma membrane phosphoinositides underlie differential regulation of TRPV1 in nociceptive neurons. *J Neurosci,* 33**,** 11451-63.

LYTTON, J., WESTLIN, M. & HANLEY, M. R. 1991. Thapsigargin inhibits the sarcoplasmic or endoplasmic reticulum Ca-ATPase family of calcium pumps. *Journal of Biological Chemistry,* 266**,** 17067-17071.

MACDONALD, L., BALDINI, G. & STORRIE, B. 2015. Does super-resolution fluorescence microscopy obsolete previous microscopic approaches to protein co-localization? *Methods Mol Biol,* 1270**,** 255-75.

MAIDORN, M., RIZZOLI, S. O. & OPAZO, F. 2016. Tools and limitations to study the molecular composition of synapses by fluorescence microscopy. *Biochemical Journal,* 473**,** 3385-3399.

MAIER, T., GÜELL, M. & SERRANO, L. 2009. Correlation of mRNA and protein in complex biological samples. *FEBS Letters,* 583**,** 3966-3973.

MALIN, S. A., DAVIS, B. M. & MOLLIVER, D. C. 2007. Production of dissociated sensory neuron cultures and considerations for their use in studying neuronal function and plasticity. *Nature Protocols,* 2**,** 152-160.

MANIERO, C., SCUDIERI, P., HARIS SHAIKH, L., ZHAO, W., GURNELL, M., GALIETTA, L. J. V. & BROWN, M. J. 2019. ANO4 (Anoctamin 4) Is a Novel Marker of Zona Glomerulosa That Regulates Stimulated Aldosterone Secretion. *Hypertension,* 74**,** 1152-1159.

MANTENIOTIS, S., LEHMANN, R., FLEGEL, C., VOGEL, F., HOFREUTER, A., SCHREINER, B. S., ALTMÜLLER, J., BECKER, C., SCHÖBEL, N., HATT, H. & GISSELMANN, G. 2013. Comprehensive RNA-Seq expression analysis of sensory ganglia with a focus on ion channels and GPCRs in Trigeminal ganglia. *PLoS One,* 8**,** e79523.

MAO, R., TONG, C. & LIU, J.-J. 2023. E-Syt1 Regulates Neuronal Activity-Dependent Endoplasmic Reticulum–Plasma Membrane Junctions and Surface Expression of AMPA Receptors. *Contact,* 6**,** 25152564231185011.

MATSUDA, S., KOBAYASHI, N., MOMINOKI, K., WAKISAKA, H., MORI, M. & MURAKAMI, S. 1998. [Morphological transformation of sensory ganglion neurons and satellite cells]. *Kaibogaku zasshi. Journal of anatomy,* 73**,** 603-613.

MCBRIDE, J. T., SPRINGALL, D. R., WINTER, R. J. & POLAK, J. M. 1990. Quantitative immunocytochemistry shows calcitonin gene-related peptide-like immunoreactivity in lung neuroendocrine cells is increased by chronic hypoxia in the rat. *Am J Respir Cell Mol Biol,* 3**,** 587-93.

MCMANUS, J., CHENG, Z. & VOGEL, C. 2015. Next-generation analysis of gene expression regulation – comparing the roles of synthesis and degradation. *Molecular BioSystems,* 11**,** 2680-2689.

MEGAT, S., RAY, P. R., MOY, J. K., LOU, T.-F., BARRAGÁN-IGLESIAS, P., LI, Y., PRADHAN, G., WANGHZOU, A., AHMAD, A., BURTON, M. D., NORTH, R. Y., DOUGHERTY, P. M., KHOUTORSKY, A., SONENBERG, N., WEBSTER, K. R., DUSSOR, G., CAMPBELL, Z. T. & PRICE, T. J. 2019a. Nociceptor Translational Profiling Reveals the Ragulator-Rag GTPase Complex as a Critical Generator of Neuropathic Pain. *The Journal of Neuroscience,* 39**,** 393-411.

MEGAT, S., RAY, P. R., TAVARES-FERREIRA, D., MOY, J. K., SANKARANARAYANAN, I., WANGHZOU, A., FANG LOU, T., BARRAGAN-IGLESIAS, P., CAMPBELL, Z. T., DUSSOR, G. & PRICE, T. J. 2019b. Differences between Dorsal Root and

Trigeminal Ganglion Nociceptors in Mice Revealed by Translational Profiling. *J Neurosci,* 39**,** 6829-6847.
MELZACK, R. & WALL, P. D. 1965. Pain mechanisms: a new theory. *Science,* 150**,** 971-9.
MENDELL, L. M. 2014. Constructing and deconstructing the gate theory of pain. *PAIN®,* 155**,** 210-216.
MENG, J., OVSEPIAN, S. V., WANG, J., PICKERING, M., SASSE, A., AOKI, K. R., LAWRENCE, G. W. & DOLLY, J. O. 2009. Activation of TRPV1 Mediates Calcitonin Gene-Related Peptide Release, Which Excites Trigeminal Sensory Neurons and Is Attenuated by a Retargeted Botulinum Toxin with Anti-Nociceptive Potential. *The Journal of Neuroscience,* 29**,** 4981.
MENG, J., WANG, J., LAWRENCE, G. & DOLLY, J. O. 2007. Synaptobrevin I mediates exocytosis of CGRP from sensory neurons and inhibition by botulinum toxins reflects their anti-nociceptive potential. *Journal of Cell Science,* 120**,** 2864-2874.
MERCHANT, F. A. & PERIASAMY, A. 2023. Chapter Ten - Multispectral Fluorescence Imaging. *In:* MERCHANT, F. A. & CASTLEMAN, K. R. (eds.) *Microscope Image Processing (Second Edition).* Academic Press.
MERSKEY, H. 1994. Task force on taxonomy. *Classification of Chronic Pain : Descriptions of Chronic Pain Syndromes and Definitions of Pain Terms*.
MESSLINGER, K., BALCZIAK, L. K. & RUSSO, A. F. 2020. Cross-talk signaling in the trigeminal ganglion: role of neuropeptides and other mediators. *Journal of Neural Transmission,* 127**,** 431-444.
MESSLINGER, K. & RUSSO, A. F. 2019. Current understanding of trigeminal ganglion structure and function in headache. *Cephalalgia,* 39**,** 1661-1674.
MESSLINGER, K., VOGLER, B., KUHN, A., SERTEL-NAKAJIMA, J., FRANK, F. & BROESSNER, G. 2021. CGRP measurements in human plasma – a methodological study. *Cephalalgia,* 41**,** 1359-1373.
MEYER, L., WILDANGER, D., MEDDA, R., PUNGE, A., RIZZOLI, S. O., DONNERT, G. & HELL, S. W. 2008. Dual-Color STED Microscopy at 30-nm Focal-Plane Resolution. *Small,* 4**,** 1095-1100.
MIKOSHIBA, K. 2007. IP3 receptor/Ca2+ channel: from discovery to new signaling concepts. *Journal of Neurochemistry,* 102**,** 1426-1446.
MIN, S.-W., CHANG, W.-P. & SÜDHOF, T. C. 2007a. E-Syts, a family of membranous Ca²⁺-sensor proteins with multiple C₂ domains. *Proceedings of the National Academy of Sciences,* 104**,** 3823-3828.
MIN, S. W., CHANG, W. P. & SÜDHOF, T. C. 2007b. E-Syts, a family of membranous Ca2+-sensor proteins with multiple C2 domains. *Proc Natl Acad Sci U S A,* 104**,** 3823-8.
MOISEENKOVA-BELL, V. Y., STANCIU, L. A., SERYSHEVA, I. I., TOBE, B. J. & WENSEL, T. G. 2008. Structure of TRPV1 channel revealed by electron cryomicroscopy. *Proceedings of the National Academy of Sciences,* 105**,** 7451-7455.
MORENILLA-PALAO, C., PLANELLS-CASES, R., GARCÍA-SANZ, N. & FERRER-MONTIEL, A. 2004. Regulated exocytosis contributes to protein kinase C potentiation of vanilloid receptor activity. *J Biol Chem,* 279**,** 25665-72.
MORFIS, M., TILAKARATNE, N., FURNESS, S. G., CHRISTOPOULOS, G., WERRY, T. D., CHRISTOPOULOS, A. & SEXTON, P. M. 2008. Receptor activity-modifying proteins differentially modulate the G protein-coupling efficiency of amylin receptors. *Endocrinology,* 149**,** 5423-31.

MUSTAFÁ, E. R., GAMBETA, E., STRINGER, R. N., SOUZA, I. A., ZAMPONI, G. W. & WEISS, N. 2022. Electrophysiological and computational analysis of Cav3.2 channel variants associated with familial trigeminal neuralgia. *Molecular Brain,* 15**,** 91.

NAVE, K.-A. 2010. Myelination and support of axonal integrity by glia. *Nature,* 468**,** 244-252.

NISHI, M., SAKAGAMI, H., KOMAZAKI, S., KONDO, H. & TAKESHIMA, H. 2003. Coexpression of junctophilin type 3 and type 4 in brain. *Brain Res Mol Brain Res,* 118**,** 102-10.

NUMAZAKI, M., TOMINAGA, T., TOYOOKA, H. & TOMINAGA, M. 2002. Direct Phosphorylation of Capsaicin Receptor VR1 by Protein Kinase Cε and Identification of Two Target Serine Residues *. *Journal of Biological Chemistry,* 277**,** 13375-13378.

O'DRISCOLL, K. E., PIPE, R. A. & BRITTON, F. C. 2011. Increased complexity of Tmem16a/Anoctamin 1 transcript alternative splicing. *BMC Molecular Biology,* 12**,** 35.

OLAUSSON, H., MARSHALL, A., NAGI, S. S. & COLE, J. 2024. Slow touch and ultrafast pain fibres: Revisiting peripheral nerve classification. *Clinical Neurophysiology,* 163**,** 255-262.

ORCI, L., RAVAZZOLA, M., LE COADIC, M., SHEN, W. W., DEMAUREX, N. & COSSON, P. 2009. From the Cover: STIM1-induced precortical and cortical subdomains of the endoplasmic reticulum. *Proc Natl Acad Sci U S A,* 106**,** 19358-62.

OUSINGSAWAT, J., MARTINS, J. R., SCHREIBER, R., ROCK, J. R., HARFE, B. D. & KUNZELMANN, K. 2009. Loss of TMEM16A Causes a Defect in Epithelial Ca2+-dependent Chloride Transport*. *Journal of Biological Chemistry,* 284**,** 28698-28703.

ÖZTÜRK, Z., O'KANE, C. J. & PÉREZ-MORENO, J. J. 2020. Axonal Endoplasmic Reticulum Dynamics and Its Roles in Neurodegeneration. *Front Neurosci,* 14**,** 48.

PARMRYD, I., ADLER, J., PATEL, R. & MAGEE, A. I. 2003. Imaging metabolism of phosphatidylinositol 4,5-bisphosphate in t-cell GM1-enriched domains containing Ras proteins☆. *Experimental Cell Research,* 285**,** 27-38.

PAULINO, C., KALIENKOVA, V., LAM, A. K. M., NELDNER, Y. & DUTZLER, R. 2017. Activation mechanism of the calcium-activated chloride channel TMEM16A revealed by cryo-EM. *Nature,* 552**,** 421-425.

PEDEMONTE, N. & GALIETTA, L. J. V. 2014. Structure and Function of TMEM16 Proteins (Anoctamins). *Physiological Reviews,* 94**,** 419-459.

PETKOVIC, M., JEMAIEL, A., DASTE, F., SPECHT, C. G., IZEDDIN, I., VORKEL, D., VERBAVATZ, J. M., DARZACQ, X., TRILLER, A., PFENNINGER, K. H., TARESTE, D., JACKSON, C. L. & GALLI, T. 2014. The SNARE Sec22b has a non-fusogenic function in plasma membrane expansion. *Nat Cell Biol,* 16**,** 434-44.

PETRESCU, A. D., PAYNE, H. R., BOEDECKER, A., CHAO, H., HERTZ, R., BAR-TANA, J., SCHROEDER, F. & KIER, A. B. 2003. Physical and Functional Interaction of Acyl-CoA-binding Protein with Hepatocyte Nuclear Factor-4α *. *Journal of Biological Chemistry,* 278**,** 51813-51824.

PETRUSKA, J. C., NAPAPORN, J., JOHNSON, R. D., GU, J. G. & COOPER, B. Y. 2000. Subclassified Acutely Dissociated Cells of Rat DRG: Histochemistry and Patterns of Capsaicin-, Proton-, and ATP-Activated Currents. *Journal of Neurophysiology,* 84**,** 2365-2379.

PETTINGER, L., GIGOUT, S., LINLEY, J. & GAMPER, N. 2013. Bradykinin Controls Pool Size of Sensory Neurons Expressing Functional -Opioid Receptors. *The Journal of neuroscience : the official journal of the Society for Neuroscience,* 33**,** 10762-10771.

PHANSALKAR, N., MORE, S., SABALE, A. & JOSHI, M. Adaptive local thresholding for detection of nuclei in diversity stained cytology images. 2011 International Conference on Communications and Signal Processing, 10-12 Feb. 2011 2011. 218-220.

PHILLIPS, M. J. & VOELTZ, G. K. 2016. Structure and function of ER membrane contact sites with other organelles. *Nature Reviews Molecular Cell Biology,* 17**,** 69-82.

PHIMISTER, A. J., LANGO, J., LEE, E. H., ERNST-RUSSELL, M. A., TAKESHIMA, H., MA, J., ALLEN, P. D. & PESSAH, I. N. 2007. Conformation-dependent stability of junctophilin 1 (JP1) and ryanodine receptor type 1 (RyR1) channel complex is mediated by their hyper-reactive thiols. *J Biol Chem,* 282**,** 8667-77.

PINEDA-FARIAS, J. B., BARRAGÁN-IGLESIAS, P., LOEZA-ALCOCER, E., TORRES-LÓPEZ, J. E., ROCHA-GONZÁLEZ, H. I., PÉREZ-SEVERIANO, F., DELGADO-LEZAMA, R. & GRANADOS-SOTO, V. 2015. Role of anoctamin-1 and bestrophin-1 in spinal nerve ligation-induced neuropathic pain in rats. *Molecular Pain,* 11.

POTESER, M., LEITINGER, G., PRITZ, E., PLATZER, D., FRISCHAUF, I., ROMANIN, C. & GROSCHNER, K. 2016. Live-cell imaging of ER-PM contact architecture by a novel TIRFM approach reveals extension of junctions in response to store-operated Ca2+-entry. *Scientific Reports,* 6.

PRABAHAR, A., ZAMORA, R., BARCLAY, D., YIN, J., RAMAMOORTHY, M., BAGHERI, A., JOHNSON, S. A., BADYLAK, S., VODOVOTZ, Y. & JIANG, P. 2024. Unraveling the complex relationship between mRNA and protein abundances: a machine learning-based approach for imputing protein levels from RNA-seq data. *NAR Genomics and Bioinformatics,* 6**,** lqae019.

PREMKUMAR, L. S. & AHERN, G. P. 2000. Induction of vanilloid receptor channel activity by protein kinase C. *Nature,* 408**,** 985-90.

PRICE, D. D. & DUBNER, R. 1977. Mechanisms of first and second pain in the peripheral and central nervous systems. *J Invest Dermatol,* 69**,** 167-71.

PRICE, T. J. & FLORES, C. M. 2007. Critical Evaluation of the Colocalization Between Calcitonin Gene-Related Peptide, Substance P, Transient Receptor Potential Vanilloid Subfamily Type 1 Immunoreactivities, and Isolectin B4 Binding in Primary Afferent Neurons of the Rat and Mouse. *The Journal of Pain,* 8**,** 263-272.

PRICE, T. J., HARGREAVES, K. M. & CERVERO, F. 2006. Protein expression and mRNA cellular distribution of the NKCC1 cotransporter in the dorsal root and trigeminal ganglia of the rat. *Brain Research,* 1112**,** 146-158.

PURVES, D., AUGUSTINE, G., J. , FITZPATRICK, D., HALL, W. C., LAMANTIA, A.-S., MCNAMARA, J. O. & WILLIAMS, S. M. 2004. *Neuroscience (3rd Edition)*, Sunauer Associates.

QU, Z., WEI, R. W., MANN, W. & HARTZELL, H. C. 2003. Two bestrophins cloned from Xenopus laevis oocytes express Ca(2+)-activated Cl(-) currents. *J Biol Chem,* 278**,** 49563-72.

RAJA, S. N., MEYER, R. A. & CAMPBELL, J. N. 1988. Peripheral mechanisms of somatic pain. *Anesthesiology,* 68**,** 571-590.

RAMGOOLAM, K. H. & DOLPHIN, A. C. 2022. Capsaicin-Induced Endocytosis of Endogenous Presynaptic CaV2.2 in DRG-Spinal Cord Co-Cultures Inhibits Presynaptic Function. *Function,* 4.

RASMUSSEN, R. H., JANSEN-OLESEN, I., KRISTENSEN, D. M. & CHRISTENSEN, S. L. 2022. Ex Vivo Release of Calcitonin Gene-Related Peptide from the Trigeminovascular System in Rodents. *JoVE***,** e63723.

REES, T. A., GINGELL, J., SIOW, A., HARRIS, P., BRIMBLE, M., HAY, D. & WALKER, C. 2020. Differential internalisation of the CGRP and AMY1 receptor. *The FASEB Journal,* 34**,** 1-1.

REES, T. A., RUSSO, A. F., O'CARROLL, S. J., HAY, D. L. & WALKER, C. S. 2022. CGRP and the Calcitonin Receptor are Co-Expressed in Mouse, Rat and Human Trigeminal Ganglia Neurons. *Frontiers in Physiology,* 13.

REISNER, A. H., NEMES, P. & BUCHOLTZ, C. 1975. The use of Coomassie Brilliant Blue G250 perchloric acid solution for staining in electrophoresis and isoelectric focusing on polyacrylamide gels. *Anal Biochem,* 64**,** 509-16.

RENTHAL, W., TOCHITSKY, I., YANG, L., CHENG, Y. C., LI, E., KAWAGUCHI, R., GESCHWIND, D. H. & WOOLF, C. J. 2020. Transcriptional Reprogramming of Distinct Peripheral Sensory Neuron Subtypes after Axonal Injury. *Neuron,* 108**,** 128-144.e9.

RETSKY, R., ASHINA, S., OVED, D. & SHARON, R. 2023. Calcitonin Gene-Related Peptide and Trigeminal Neuralgia. *SN Comprehensive Clinical Medicine,* 5**,** 75.

RHEE, S. G. & BAE, Y. S. 1997. Regulation of phosphoinositide-specific phospholipase C isozymes. *J Biol Chem,* 272**,** 15045-8.

RIENECKER, K. D. A., POSTON, R. G. & SAHA, R. N. 2020. Merits and Limitations of Studying Neuronal Depolarization-Dependent Processes Using Elevated External Potassium. *ASN Neuro,* 12**,** 1759091420974807.

RINGKAMP, M., DOUGHERTY, P. M. & RAJA, S. N. 2018. Chapter 1 - Anatomy and Physiology of the Pain Signaling Process. *In:* BENZON, H. T., RAJA, S. N., LIU, S. S., FISHMAN, S. M. & COHEN, S. P. (eds.) *Essentials of Pain Medicine (Fourth Edition).* Elsevier.

RIVERA, B., ORELLANA-SERRADELL, O., SERVILI, E., SANTOS, R., BRAUCHI, S. & CERDA, O. 2024. The odyssey of the TR(i)P journey to the cellular membrane. *Frontiers in Cell and Developmental Biology,* 12.

ROCK, J. R., O'NEAL, W. K., GABRIEL, S. E., RANDELL, S. H., HARFE, B. D., BOUCHER, R. C. & GRUBB, B. R. 2009. Transmembrane Protein 16A (TMEM16A) Is a Ca2+-regulated Cl– Secretory Channel in Mouse Airways*. *Journal of Biological Chemistry,* 284**,** 14875-14880.

ROHACS, T. 2015. Phosphoinositide regulation of TRPV1 revisited. *Pflugers Arch,* 467**,** 1851-69.

ROZENBAUM, M., RAJMAN, M., RISHAL, I., KOPPEL, I., KOLEY, S., MEDZIHRADSZKY, K. F., OSES-PRIETO, J. A., KAWAGUCHI, R., AMIEUX, P. S., BURLINGAME, A. L., COPPOLA, G. & FAINZILBER, M. 2018. Translatome Regulation in Neuronal Injury and Axon Regrowth. *eNeuro,* 5.

RUAN, H. Z. & BURNSTOCK, G. 2003. Localisation of P2Y1 and P2Y4 receptors in dorsal root, nodose and trigeminal ganglia of the rat. *Histochem Cell Biol,* 120**,** 415-26.

SAHEKI, Y., BIAN, X., SCHAUDER, C. M., SAWAKI, Y., SURMA, M. A., KLOSE, C., PINCET, F., REINISCH, K. M. & DE CAMILLI, P. 2016a. Control of plasma membrane lipid homeostasis by the extended synaptotagmins. *Nat Cell Biol,* 18**,** 504-15.

SAHEKI, Y., BIAN, X., SCHAUDER, C. M., SAWAKI, Y., SURMA, M. A., KLOSE, C., PINCET, F., REINISCH, K. M. & DE CAMILLI, P. 2016b. Control of plasma membrane lipid homeostasis by the extended synaptotagmins. *Nature Cell Biology,* 18**,** 504-515.

SAMPIERI, A., SANTOYO, K., ASANOV, A. & VACA, L. 2018. Association of the IP3R to STIM1 provides a reduced intraluminal calcium microenvironment, resulting in enhanced store-operated calcium entry. *Scientific Reports,* 8**,** 13252.

SAMWAYS, D. S., KHAKH, B. S. & EGAN, T. M. 2008. Tunable calcium current through TRPV1 receptor channels. *J Biol Chem,* 283**,** 31274-8.

SCHINDELIN, J., ARGANDA-CARRERAS, I., FRISE, E., KAYNIG, V., LONGAIR, M., PIETZSCH, T., PREIBISCH, S., RUEDEN, C., SAALFELD, S., SCHMID, B., TINEVEZ, J.-Y., WHITE, D. J., HARTENSTEIN, V., ELICEIRI, K., TOMANCAK, P. & CARDONA, A. 2012. Fiji: an open-source platform for biological-image analysis. *Nature Methods,* 9**,** 676-682.

SCHMOLZE, D., STANDLEY, C., FOGARTY, K. & FISCHER, A. 2011. Advances in Microscopy Techniques. *Archives of pathology & laboratory medicine,* 135**,** 255-63.

SCHÖBEL, N., RADTKE, D., LÜBBERT, M., GISSELMANN, G., LEHMANN, R., CICHY, A., SCHREINER, B. S. P., ALTMÜLLER, J., SPECTOR, A. C., SPEHR, J., HATT, H. & WETZEL, C. H. 2012. Trigeminal Ganglion Neurons of Mice Show Intracellular Chloride Accumulation and Chloride-Dependent Amplification of Capsaicin-Induced Responses. *PLOS ONE,* 7**,** e48005.

SCHOONDERWOERT, V., DIJKSTRA, R., LUCKINAVICIUS, G., KOBLER, O. & VAN DER VOORT, H. 2013. Huygens STED Deconvolution Increases Signal-to-Noise and Image Resolution towards 22 nm. *Microscopy Today,* 21**,** 38-44.

SCHOU, W. S., ASHINA, S., AMIN, F. M., GOADSBY, P. J. & ASHINA, M. 2017. Calcitonin gene-related peptide and pain: a systematic review. *The Journal of Headache and Pain,* 18**,** 34.

SCHROEDER, B. C., CHENG, T., JAN, Y. N. & JAN, L. Y. 2008. Expression cloning of TMEM16A as a calcium-activated chloride channel subunit. *Cell,* 134**,** 1019-29.

SCHWANHÄUSSER, B., BUSSE, D., LI, N., DITTMAR, G., SCHUCHHARDT, J., WOLF, J., CHEN, W. & SELBACH, M. 2011. Global quantification of mammalian gene expression control. *Nature,* 473**,** 337-342.

SEDMAK, J. J. & GROSSBERG, S. E. 1977. A rapid, sensitive, and versatile assay for protein using Coomassie brilliant blue G250. *Anal Biochem,* 79**,** 544-52.

SEGOND VON BANCHET, G., PASTOR, A., BISKUP, C., SCHLEGEL, C., BENNDORF, K. & SCHAIBLE, H. G. 2002. Localization of functional calcitonin gene-related peptide binding sites in a subpopulation of cultured dorsal root ganglion neurons. *Neuroscience,* 110**,** 131-145.

SEO, Y., LEE, H. K., PARK, J., JEON, D.-K., JO, S., JO, M. & NAMKUNG, W. 2016. Ani9, A Novel Potent Small-Molecule ANO1 Inhibitor with Negligible Effect on ANO2. *PLOS ONE,* 11**,** e0155771.

SHAH, S. 2017. Mechanisms of ANO1 channel activation in sensory neurons. *PhD Thesis, University of Leeds*.

SHAH, S., CARVER, C. M., MULLEN, P., MILNE, S., LUKACS, V., SHAPIRO, M. S. & GAMPER, N. 2020. Local Ca(2+) signals couple activation of TRPV1 and ANO1 sensory ion channels. *Sci Signal,* 13.

SHEN, H., GAN, M., YANG, H. & ZOU, J. 2019. An integrated cell isolation and purification method for rat dorsal root ganglion neurons. *J Int Med Res,* 47**,** 3253-3260.

SHEN, W. W., FRIEDEN, M. & DEMAUREX, N. 2011. Remodelling of the endoplasmic reticulum during store-operated calcium entry. *Biol Cell,* 103**,** 365-80.

SHERMAN, D. L. & BROPHY, P. J. 2005. Mechanisms of axon ensheathment and myelin growth. *Nature Reviews Neuroscience,* 6**,** 683-690.

SHIHAN, M. H., NOVO, S. G., LE MARCHAND, S. J., WANG, Y. & DUNCAN, M. K. 2021. A simple method for quantitating confocal fluorescent images. *Biochem Biophys Rep,* 25**,** 100916.

SIMMS, J., ROUTLEDGE, S., UDDIN, R. & POYNER, D. 2019. The Structure of the CGRP and Related Receptors. *Handb Exp Pharmacol,* 255**,** 23-36.

SLEIGH, J. N., DAWES, J. M., WEST, S. J., WEI, N., SPAULDING, E. L., GÓMEZ-MARTÍN, A., ZHANG, Q., BURGESS, R. W., CADER, M. Z., TALBOT, K., YANG, X. L., BENNETT, D. L. & SCHIAVO, G. 2017. Trk receptor signaling and sensory neuron fate are perturbed in human neuropathy caused by Gars mutations. *Proc Natl Acad Sci U S A,* 114**,** E3324-e3333.

SÖDERBERG, O., GULLBERG, M., JARVIUS, M., RIDDERSTRÅLE, K., LEUCHOWIUS, K. J., JARVIUS, J., WESTER, K., HYDBRING, P., BAHRAM, F., LARSSON, L. G. & LANDEGREN, U. 2006. Direct observation of individual endogenous protein complexes in situ by proximity ligation. *Nat Methods,* 3**,** 995-1000.

SÖDERBERG, O., LEUCHOWIUS, K. J., GULLBERG, M., JARVIUS, M., WEIBRECHT, I., LARSSON, L. G. & LANDEGREN, U. 2008. Characterizing proteins and their interactions in cells and tissues using the in situ proximity ligation assay. *Methods,* 45**,** 227-32.

SOONTRAPA, P. & LIEWLUCK, T. 2022. Anoctamin 5 (ANO5) Muscle Disorders: A Narrative Review. *Genes* [Online], 13.

SPECTOR, T. 1978. Refinement of the coomassie blue method of protein quantitation. A simple and linear spectrophotometric assay for less than or equal to 0.5 to 50 microgram of protein. *Anal Biochem,* 86**,** 142-6.

SPEHR, J., SPEHR, M., HATT, H. & WETZEL, C. H. 2004. Subunit-specific P2X-receptor expression defines chemosensory properties of trigeminal neurons. *Eur J Neurosci,* 19**,** 2497-510.

SPEKKER, E., LABORC, K., BOHAR, Z., NAGY-GRÓCZ, G., FEJES-SZABÓ, A., SZŰCS, M., VECSEI, L. & PÁRDUTZ, Á. 2021. Effect of dural inflammatory soup application on activation and sensitization markers in the caudal trigeminal nucleus of the rat and the modulatory effects of sumatriptan and kynurenic acid. *The Journal of Headache and Pain,* 22.

SRAMBICKAL, C. V., BERGSTRAND, J. & WIDENGREN, J. 2021. Cumulative effects of photobleaching in volumetric STED imaging-artefacts and possible benefits. *Methods Appl Fluoresc,* 9.

STANLY, T. A., FRITZSCHE, M., BANERJI, S., GARCÍA, E., BERNARDINO DE LA SERNA, J., JACKSON, D. G. & EGGELING, C. 2016. Critical importance of appropriate fixation conditions for faithful imaging of receptor microclusters. *Biology Open,* 5**,** 1343-1350.

STATHOPULOS, P. B., LI, G. Y., PLEVIN, M. J., AMES, J. B. & IKURA, M. 2006. Stored Ca2+ depletion-induced oligomerization of stromal interaction molecule 1 (STIM1)

via the EF-SAM region: An initiation mechanism for capacitive Ca2+ entry. *J Biol Chem,* 281**,** 35855-62.
STEIN , A. T., UFRET-VINCENTY , C. A., HUA , L., SANTANA , L. F. & GORDON , S. E. 2006. Phosphoinositide 3-Kinase Binds to TRPV1 and Mediates NGF-stimulated TRPV1 Trafficking to the Plasma Membrane. *Journal of General Physiology,* 128**,** 509-522.
STEPHAN, A. B., SHUM, E. Y., HIRSH, S., CYGNAR, K. D., REISERT, J. & ZHAO, H. 2009. ANO2 is the cilial calcium-activated chloride channel that may mediate olfactory amplification. *Proceedings of the National Academy of Sciences,* 106**,** 11776-11781.
STEPHAN, G., ERDJUMENT-BROMAGE, H., LIU, W., FRENSTER, J. D., RAVN-BOESS, N., BREADY, D., CAI, J., FENYO, D., NEUBERT, T. & PLACANTONAKIS, D. G. 2023. Modulation of GPR133 (ADGRD1) Signaling by its Intracellular Interaction Partner Extended Synaptotagmin 1 (ESYT1). *bioRxiv*.
STONEY, S. D. 1990. Limitations on impulse conduction at the branch point of afferent axons in frog dorsal root ganglion. *Experimental Brain Research,* 80**,** 512-524.
STRATTON, H. J., WARWICK, C., KOERBER, H. R. & ROSS, S. E. 2024. Population Level Profiling of Primary Afferent Neuronal Activity in Response to Epinephrine Using Two-Photon Calcium Imaging. *The Journal of Pain,* 25**,** 19-20.
STRINGER, C., WANG, T., MICHAELOS, M. & PACHITARIU, M. 2021. Cellpose: a generalist algorithm for cellular segmentation. *Nature Methods,* 18**,** 100-106.
SUGIURA, T., TOMINAGA, M., KATSUYA, H. & MIZUMURA, K. 2002. Bradykinin Lowers the Threshold Temperature for Heat Activation of Vanilloid Receptor 1. *Journal of Neurophysiology,* 88**,** 544-548.
SUN, H., TSUNENARI, T., YAU, K. W. & NATHANS, J. 2002. The vitelliform macular dystrophy protein defines a new family of chloride channels. *Proc Natl Acad Sci U S A,* 99**,** 4008-13.
SUZUKI, A., SHINODA, M., HONDA, K., SHIRAKAWA, T. & IWATA, K. 2016. Regulation of transient receptor potential vanilloid 1 expression in trigeminal ganglion neurons via methyl-CpG binding protein 2 signaling contributes tongue heat sensitivity and inflammatory hyperalgesia in mice. *Molecular Pain,* 12.
SUZUKI, J., FUJII, T., IMAO, T., ISHIHARA, K., KUBA, H. & NAGATA, S. 2013. Calcium-dependent Phospholipid Scramblase Activity of TMEM16 Protein Family Members*. *Journal of Biological Chemistry,* 288**,** 13305-13316.
SUZUKI, J., UMEDA, M., SIMS, P. J. & NAGATA, S. 2010. Calcium-dependent phospholipid scrambling by TMEM16F. *Nature,* 468**,** 834-8.
SUZUKI, M. & MIZUNO, A. 2004. A Novel Human Cl- Channel Family Related to Drosophila flightless Locus*. *Journal of Biological Chemistry,* 279**,** 22461-22468.
TAJTI, J., UDDMAN, R., MÖLLER, S., SUNDLER, F. & EDVINSSON, L. 1999. Messenger molecules and receptor mRNA in the human trigeminal ganglion. *Journal of the Autonomic Nervous System,* 76**,** 176-183.
TAKAYAMA, Y. & TOMINAGA, M. 2024. Interaction between TRP channels and anoctamins. *Cell Calcium,* 121**,** 102912.
TAKAYAMA, Y., UTA, D., FURUE, H. & TOMINAGA, M. 2015. Pain-enhancing mechanism through interaction between TRPV1 and anoctamin 1 in sensory neurons. *Proceedings of the National Academy of Sciences,* 112**,** 5213-5218.

TALLEY, E. M., CRIBBS, L. L., LEE, J. H., DAUD, A., PEREZ-REYES, E. & BAYLISS, D. A. 1999. Differential distribution of three members of a gene family encoding low voltage-activated (T-type) calcium channels. *J Neurosci,* 19**,** 1895-911.

THAKUR, M., CROW, M., RICHARDS, N., DAVEY, G. I. J., LEVINE, E., KELLEHER, J. H., AGLEY, C. C., DENK, F., HARRIDGE, S. D. R. & MCMAHON, S. B. 2014. Defining the nociceptor transcriptome. *Frontiers in Molecular Neuroscience,* 7.

TOKI, M. I., CECCHI, F., HEMBROUGH, T., SYRIGOS, K. N. & RIMM, D. L. 2017. Proof of the quantitative potential of immunofluorescence by mass spectrometry. *Lab Invest,* 97**,** 329-334.

TROTHEN, S. M., TEPLITSKY, J. E., ARMSTONG, R. E., ZANG, R. X., LURIE, A., MUMBY, M. J., EDGAR, C. R., GROL, M. W. & DIKEAKOS, J. D. 2024. PACS-1 Interacts with TRPC3 and ESyt1 to Mediate Protein Trafficking while Promoting SOCE and Cooperatively Regulating Hormone Secretion. *ACS Omega,* 9**,** 35014-35027.

TRUCKENBRODT, S., MAIDORN, M., CRZAN, D., WILDHAGEN, H., KABATAS, S. & RIZZOLI, S. O. 2018. X10 expansion microscopy enables 25-nm resolution on conventional microscopes. *EMBO reports,* 19**,** e45836.

TWYFFELS, L., STRICKAERT, A., VIRREIRA, M., MASSART, C., VAN SANDE, J., WAUQUIER, C., BEAUWENS, R., DUMONT, J. E., GALIETTA, L. J., BOOM, A. & KRUYS, V. 2014. Anoctamin-1/TMEM16A is the major apical iodide channel of the thyrocyte. *Am J Physiol Cell Physiol,* 307**,** C1102-12.

UHLÉN, M., FAGERBERG, L., HALLSTRÖM, B. M., LINDSKOG, C., OKSVOLD, P., MARDINOGLU, A., SIVERTSSON, Å., KAMPF, C., SJÖSTEDT, E., ASPLUND, A., OLSSON, I., EDLUND, K., LUNDBERG, E., NAVANI, S., SZIGYARTO, C. A.-K., ODEBERG, J., DJUREINOVIC, D., TAKANEN, J. O., HOBER, S., ALM, T., EDQVIST, P.-H., BERLING, H., TEGEL, H., MULDER, J., ROCKBERG, J., NILSSON, P., SCHWENK, J. M., HAMSTEN, M., VON FEILITZEN, K., FORSBERG, M., PERSSON, L., JOHANSSON, F., ZWAHLEN, M., VON HEIJNE, G., NIELSEN, J. & PONTÉN, F. 2015. Tissue-based map of the human proteome. *Science,* 347**,** 1260419.

ULRICH-LAI, Y. M., FLORES, C. M., HARDING-ROSE, C. A., GOODIS, H. E. & HARGREAVES, K. M. 2001. Capsaicin-evoked release of immunoreactive calcitonin gene-related peptide from rat trigeminal ganglion: evidence for intraganglionic neurotransmission. *Pain,* 91**,** 219-226.

UPMANYU, N., JIN, J., EMDE, H. V., GANZELLA, M., BÖSCHE, L., MALVIYA, V. N., ZHULEKU, E., POLITI, A. Z., NINOV, M., SILBERN, I., LEUTENEGGER, M., URLAUB, H., RIEDEL, D., PREOBRASCHENSKI, J., MILOSEVIC, I., HELL, S. W., JAHN, R. & SAMBANDAN, S. 2022. Colocalization of different neurotransmitter transporters on synaptic vesicles is sparse except for VGLUT1 and ZnT3. *Neuron,* 110**,** 1483-1497.e7.

USOSKIN, D., FURLAN, A., ISLAM, S., ABDO, H., LÖNNERBERG, P., LOU, D., HJERLING-LEFFLER, J., HAEGGSTRÖM, J., KHARCHENKO, O., KHARCHENKO, P. V., LINNARSSON, S. & ERNFORS, P. 2015. Unbiased classification of sensory neuron types by large-scale single-cell RNA sequencing. *Nature Neuroscience,* 18**,** 145-153.

VALDES, P. A., YU, C. J., ARONSON, J., GHOSH, D., ZHAO, Y., AN, B., BERNSTOCK, J. D., BHERE, D., FELICELLA, M. M., VIAPIANO, M. S., SHAH, K., CHIOCCA, E. A. & BOYDEN, E. S. 2024. Improved immunostaining of nanostructures and cells in human brain specimens through expansion-mediated protein decrowding. *Sci Transl Med,* 16**,** eabo0049.

VAN HEES, J. & GYBELS, J. 1981. C nociceptor activity in human nerve during painful and non painful skin stimulation. *J Neurol Neurosurg Psychiatry,* 44**,** 600-7.
VAN SLAGEREN, R., DEN BOEF, G. & VAN DER LINDEN, W. E. 1973. The signal vs. concentration relationships in fluorimetry. *Talanta,* 20**,** 501-512.
VELLANI, V., MAPPLEBECK, S., MORIONDO, A., DAVIS, J. B. & MCNAUGHTON, P. A. 2001. Protein kinase C activation potentiates gating of the vanilloid receptor VR1 by capsaicin, protons, heat and anandamide. *J Physiol,* 534**,** 813-25.
VERMEIREN, S., BELLEFROID, E. J. & DESIDERIO, S. 2020. Vertebrate Sensory Ganglia: Common and Divergent Features of the Transcriptional Programs Generating Their Functional Specialization. *Front Cell Dev Biol,* 8**,** 587699.
VULLHORST, D., BLOOM, M. S., AKELLA, N. & BUONANNO, A. 2023. ER-PM Junctions on GABAergic Interneurons Are Organized by Neuregulin 2/VAP Interactions and Regulated by NMDA Receptors. *International Journal of Molecular Sciences,* 24**,** 2908.
WALKER, C. S., CONNER, A. C., POYNER, D. R. & HAY, D. L. 2010. Regulation of signal transduction by calcitonin gene-related peptide receptors. *Trends in Pharmacological Sciences,* 31**,** 476-483.
WALKER, C. S., EFTEKHARI, S., BOWER, R. L., WILDERMAN, A., INSEL, P. A., EDVINSSON, L., WALDVOGEL, H. J., JAMALUDDIN, M. A., RUSSO, A. F. & HAY, D. L. 2015. A second trigeminal CGRP receptor: function and expression of the AMY1 receptor. *Ann Clin Transl Neurol,* 2**,** 595-608.
WANG, Q., BAI, L., LUO, S., WANG, T., YANG, F., XIA, J., WANG, H., MA, K., LIU, M., WU, S., WANG, H., GUO, S., SUN, X. & XIAO, Q. 2020. TMEM16A Ca(2+)-activated Cl(-) channel inhibition ameliorates acute pancreatitis via the IP(3)R/Ca(2+)/NFκB/IL-6 signaling pathway. *J Adv Res,* 23**,** 25-35.
WARD, R. J. & MILLIGAN, G. 2014. Structural and biophysical characterisation of G protein-coupled receptor ligand binding using resonance energy transfer and fluorescent labelling techniques. *Biochimica et Biophysica Acta (BBA) - Biomembranes,* 1838**,** 3-14.
WATANABE, M., UEDA, T., SHIBATA, Y., KUMAMOTO, N., SHIMADA, S. & UGAWA, S. 2015. Expression and Regulation of Cav3.2 T-Type Calcium Channels during Inflammatory Hyperalgesia in Mouse Dorsal Root Ganglion Neurons. *PLOS ONE,* 10**,** e0127572.
WEIBRECHT, I., LEUCHOWIUS, K. J., CLAUSSON, C. M., CONZE, T., JARVIUS, M., HOWELL, W. M., KAMALI-MOGHADDAM, M. & SÖDERBERG, O. 2010. Proximity ligation assays: a recent addition to the proteomics toolbox. *Expert Rev Proteomics,* 7**,** 401-9.
WEISS, N., HAMEED, S., FERNÁNDEZ-FERNÁNDEZ, J. M., FABLET, K., KARMAZINOVA, M., POILLOT, C., PROFT, J., CHEN, L., BIDAUD, I., MONTEIL, A., HUC-BRANDT, S., LACINOVA, L., LORY, P., ZAMPONI, G. W. & DE WAARD, M. 2012. A Cav3.2/Syntaxin-1A Signaling Complex Controls T-type Channel Activity and Low-threshold Exocytosis*. *Journal of Biological Chemistry,* 287**,** 2810-2818.
WEISS, N. & ZAMPONI, G. W. 2013. Control of low-threshold exocytosis by T-type calcium channels. *Biochimica et Biophysica Acta (BBA) - Biomembranes,* 1828**,** 1579-1586.
WESTON, C., WINFIELD, I., HARRIS, M., HODGSON, R., SHAH, A., DOWELL, S. J., MOBAREC, J. C., WOODLOCK, D. A., REYNOLDS, C. A., POYNER, D. R., WATKINS, H. A. & LADDS, G. 2016. Receptor Activity-modifying Protein-directed G Protein

Signaling Specificity for the Calcitonin Gene-related Peptide Family of Receptors * . *Journal of Biological Chemistry,* 291**,** 21925-21944.
WILLIAMS, L. S., SCHMALFUSS, I. M., SISTROM, C. L., INOUE, T., TANAKA, R., SEOANE, E. R. & MANCUSO, A. A. 2003. MR imaging of the trigeminal ganglion, nerve, and the perineural vascular plexus: normal appearance and variants with correlation to cadaver specimens. *AJNR Am J Neuroradiol,* 24**,** 1317-23.
WILLIAMSON, P. 2015. Phospholipid Scramblases. *Lipid Insights,* 8s1**,** LPI.S31785.
WILLIG, K. I., KELLER, J., BOSSI, M. & HELL, S. W. 2006. STED microscopy resolves nanoparticle assemblies. *New Journal of Physics,* 8**,** 106.
WOLF, W., KILIC, A., SCHRUL, B., LORENZ, H., SCHWAPPACH, B. & SEEDORF, M. 2012. Yeast Ist2 recruits the endoplasmic reticulum to the plasma membrane and creates a ribosome-free membrane microcompartment. *PLoS One,* 7**,** e39703.
WOO, J. S., SUN, Z., SRIKANTH, S. & GWACK, Y. 2020. The short isoform of extended synaptotagmin-2 controls Ca(2+) dynamics in T cells via interaction with STIM1. *Sci Rep,* 10**,** 14433.
WOOLF, C. J. & MA, Q. 2007. Nociceptors—Noxious Stimulus Detectors. *Neuron,* 55**,** 353-364.
WU, M. M., BUCHANAN, J., LUIK, R. M. & LEWIS, R. S. 2006. Ca2+ store depletion causes STIM1 to accumulate in ER regions closely associated with the plasma membrane. *J Cell Biol,* 174**,** 803-13.
WU, X. & HAMMER, J. A. 2021. ZEISS Airyscan: Optimizing Usage for Fast, Gentle, Super-Resolution Imaging. *Methods Mol Biol,* 2304**,** 111-130.
WU, Y., WHITEUS, C., XU, C. S., HAYWORTH, K. J., WEINBERG, R. J., HESS, H. F. & DE CAMILLI, P. 2017. Contacts between the endoplasmic reticulum and other membranes in neurons. *Proceedings of the National Academy of Sciences,* 114**,** E4859-E4867.
XIAO, Q., YU, K., PEREZ-CORNEJO, P., CUI, Y., ARREOLA, J. & HARTZELL, H. C. 2011. Voltage- and calcium-dependent gating of TMEM16A/Ano1 chloride channels are physically coupled by the first intracellular loop. *Proceedings of the National Academy of Sciences,* 108**,** 8891-8896.
YAMAGATA, K., SUGIMURA, M., YOSHIDA, M., SEKINE, S., KAWANO, A., OYAMAGUCHI, A., MAEGAWA, H. & NIWA, H. 2016. Estrogens Exacerbate Nociceptive Pain via Up-Regulation of TRPV1 and ANO1 in Trigeminal Primary Neurons of Female Rats. *Endocrinology,* 157**,** 4309-4317.
YANG, L., JIN, M., DU, P., CHEN, G., ZHANG, C., WANG, J., JIN, F., SHAO, H., SHE, Y., WANG, S., ZHENG, L. & WANG, J. 2015. Study on Enhancement Principle and Stabilization for the Luminol-H2O2-HRP Chemiluminescence System. *PLoS One,* 10**,** e0131193.
YANG, L., XU, M., BHUIYAN, S. A., LI, J., ZHAO, J., COHRS, R. J., SUSTERICH, J. T., SIGNORELLI, S., GREEN, U., STONE, J. R., LEVY, D., LENNERZ, J. K. & RENTHAL, W. 2022. Human and mouse trigeminal ganglia cell atlas implicates multiple cell types in migraine. *Neuron,* 110**,** 1806-1821.e8.
YANG, Y., VALENCIA, L. A., LU, C.-H., NAKAMOTO, M. L., TSAI, C.-T., LIU, C., YANG, H., ZHANG, W., JAHED, Z., LEE, W.-R., SANTORO, F., LIOU, J., WU, J. C. & CUI, B. 2024. Plasma membrane curvature regulates the formation of contacts with the endoplasmic reticulum. *Nature Cell Biology*.

YANG, Y. D., CHO, H., KOO, J. Y., TAK, M. H., CHO, Y., SHIM, W.-S., PARK, S. P., LEE, J., LEE, B., KIM, B.-M., RAOUF, R., SHIN, Y. K. & OH, U. 2008. TMEM16A confers receptor-activated calcium-dependent chloride conductance. *Nature,* 455**,** 1210-1215.

YOSHIDA, S. R., MAITY, B. K. & CHONG, S. 2023. Visualizing Protein Localizations in Fixed Cells: Caveats and the Underlying Mechanisms. *The Journal of Physical Chemistry B,* 127**,** 4165-4173.

YPERMAN, K. & KUIJPERS, M. 2023. Neuronal endoplasmic reticulum architecture and roles in axonal physiology. *Mol Cell Neurosci,* 125**,** 103822.

YU, L., REYNAUD, F., FALK, J., SPENCER, A., DING, Y. D., BAUMLÉ, V., LU, R., CASTELLANI, V., YUAN, C. & RUDKIN, B. B. 2015. Highly efficient method for gene delivery into mouse dorsal root ganglia neurons. *Front Mol Neurosci,* 8**,** 2.

ZAMPONI, E., MEEHL, J. B. & VOELTZ, G. K. 2022. The ER ladder is a unique morphological feature of developing mammalian axons. *Developmental Cell,* 57**,** 1369-1382.e6.

ZHANG, M., GAO, C. X., WANG, Y. P., MA, K. T., LI, L., YIN, J. W., DAI, Z. G., WANG, S. & SI, J. Q. 2018. The association between the expression of PAR2 and TMEM16A and neuropathic pain. *Molecular Medicine Reports,* 17**,** 3744-3750.

ZHANG, X.-D., LEE, J.-H., LV, P., CHEN, W. C., KIM, H. J., WEI, D., WANG, W., SIHN, C.-R., DOYLE, K. J., ROCK, J. R., CHIAMVIMONVAT, N. & YAMOAH, E. N. 2015. Etiology of distinct membrane excitability in pre- and posthearing auditory neurons relies on activity of Cl[−] channel TMEM16A. *Proceedings of the National Academy of Sciences,* 112**,** 2575-2580.

ZHAO, B., WANG, H.-B., LU, Y.-J., HU, J.-W., BAO, L. & ZHANG, X. 2011. Transport of receptors, receptor signaling complexes and ion channels via neuropeptide-secretory vesicles. *Cell Research,* 21**,** 741-753.

ZHOU, Y., LONG, H., YE, N., LIAO, L., YANG, X., JIAN, F., WANG, Y. & LAI, W. 2016. The effect of capsaicin on expression patterns of CGRP in trigeminal ganglion and trigeminal nucleus caudalis following experimental tooth movement in rats. *J Appl Oral Sci,* 24**,** 597-606.

ZHU, M. H., SUNG, T. S., O'DRISCOLL, K., KOH, S. D. & SANDERS, K. M. 2015. Intracellular Ca2+ release from endoplasmic reticulum regulates slow wave currents and pacemaker activity of interstitial cells of Cajal. *American Journal of Physiology-Cell Physiology,* 308**,** C608-C620.

ZUO, Y., LUBISCHER, J. L., KANG, H., TIAN, L., MIKESH, M., MARKS, A., SCOFIELD, V. L., MAIKA, S., NEWMAN, C., KRIEG, P. & THOMPSON, W. J. 2004. Fluorescent proteins expressed in mouse transgenic lines mark subsets of glia, neurons, macrophages, and dendritic cells for vital examination. *J Neurosci,* 24**,** 10999-1009.